Technische Universität München
TUM School of Natural Sciences

Aqueous Sodium-Ion Batteries Based on Prussian Blue Analogs: From a Model System Towards an Optimized Design

Xaver Lamprecht

Vollständiger Abdruck der von der TUM School of Natural Sciences der Technischen Universität München zur Erlangung des akademischen Grades eines

Doktors der Naturwissenschaften (Dr. rer. nat)

genehmigten Dissertation.

Vorsitz:	Prof. Dr. Nora Brambilla
Prüfer der Dissertation:	1. Prof. Dr. Aliaksandr Bandarenka
	2. Prof. Dr. Pekka Peljo

Die Dissertation wurde am 26.07.2023 bei der Technischen Universität München eingereicht und durch die TUM School of Natural Sciences am 26.09.2023 angenommen.

Abstract

Safe and scalable battery technologies based on sustainable and highly available resources constitute the backbone of transforming the global energy provision to renewable sources. Sodium-ion batteries with water-based electrolytes (ASIB) and active materials from the class of Prussian blue analogs (PBA) are considered as a promising alternative to modern lithium-ion batteries (LIB). Whereas the intercalation-based charge storage mechanism is overall very similar to state-of-the-art LIBs, the involved materials have the potential to make this technology a low-cost, non-flammable and environmentally benign alternative for mass market adoption. Even though the lower energy density of < 100 Wh/kg might exclude ASIBs from mobile applications, they appear as an auspicious solution for large-scale stationary usage to allow the integration of decentralized and highly fluctuating renewable power sources into the electricity grid. However, certain challenges remain to be solved on the way towards market readiness. This work focusses on optimizing battery performance by studying different PBAs as active materials for both cathode and anode in combination with water-based electrolytes. The main objectives are enhancing cycling stability and enabling fast-charging capability. Electrodeposited thin-film model electrodes are employed, as they offer precise control over composition and thickness. Such a model system allows the investigation of specific material aspects, avoiding the complexities associated with "traditional" composite-type electrodes.

A major pathway for capacity decay in PBAs is found to follow a complex mechanism involving transition metal dissolution and subsequent partial re-deposition. Whereas active material loss causes an irreversible capacity fade, impaired kinetics and mass transport properties of the re-deposited material corrupt the rate capability during extended cycling. The composition of the electrolyte highly governs the electrode stability against dissolution. Strongly adsorbing anions, as well as high OH^- and H_3O^+ availability should be avoided, while the usage of strongly concentrated electrolytes guarantees exceeding stability. Furthermore, PBA thin-film model electrodes show an extremely fast, loss-free charging behavior of less than one minute. Whereas quasi-reversible kinetics enable remarkably high power densities, solid-state diffusion of Na^+ within the host material ultimately limits the charging speed. The film thickness can accordingly be used to precisely tune the rate capability. The usage of microstructured templates for the electrodeposition is discussed as an outlook to achieve commercially viable footprint mass loadings for thin-film electrodes and thereby transfer the presented model system towards a practical hybrid battery-supercapacitor device.

Zusammenfassung

Sichere und skalierbare Batterietechnologien auf der Basis von nachhaltigen und reichlich vorhandenen Ressourcen bilden das Rückgrat für die Umstellung der globalen Energieversorgung auf erneuerbare Quellen. Natrium-Ionen-Batterien mit wasserbasierten Elektrolyten (ASIB) und Aktivmaterialien aus der Klasse der Preußischblau-Analoga (PBA) werden als vielversprechende Alternative zu modernen Lithium-Ionen-Batterien (LIB) betrachtet. Während der Interkalationsmechanismus zur Speicherung von Ladung insgesamt sehr ähnlich zu herkömmlichen LIBs ist, haben die verwendeten Materialien das Potenzial, diese Technologie zu einer kostengünstigen, nicht brennbaren und umweltfreundlichen Alternative für den Massenmarkt zu machen. Obwohl deren niedrigere Energiedichte von weniger als 100 Wh/kg ein Ausschlusskriterium für mobile Anwendungen darstellen dürfte, erscheinen ASIBs als vielversprechende Lösung für den großflächigen stationären Einsatz, um die Integration dezentraler und stark schwankender erneuerbarer Energiequellen in das Stromnetz zu ermöglichen. Es gibt jedoch noch zu lösende Herausforderungen auf dem Weg zur Marktreife. Diese Arbeit konzentriert sich darauf, die Leistungsfähigkeit der Batterien durch die Untersuchung verschiedener PBAs als Aktivmaterialien für Kathode und Anode in Kombination mit wasserbasierten Elektrolyten zu optimieren. Die Hauptziele sind die Verbesserung der Zyklenstabilität und die Ermöglichung von Schnellladefähigkeit. Dazu werden elektrochemisch abgeschiedene Dünnschicht-Modellelektroden verwendet, da dies eine präzise Kontrolle über die Zusammensetzung und Schichtdicke zulässt. Ein solches Modellsystem ermöglicht die Untersuchung spezifischer Materialeigenschaften und umgeht die Komplexitäten, die mit "traditionellen" Kompositelektroden verbunden sind.

Es wurde festgestellt, dass Kapazitätsverlust bei PBAs im Wesentlichen durch einen komplexen Mechanismus erfolgt, der das Auslösen von Übergangsmetallen und die anschließende teilweise Wiederabscheidung umfasst. Während der Verlust von Aktivmaterial zu irreversiblen Kapazitätseinbußen führt, beeinträchtigen die verschlechterte Kinetik und Massentransporteigenschaften des wieder abgeschiedenen Materials die Leistungsfähigkeit bei langem Zyklieren. Die Widerstandsfähigkeit der Elektrode gegen Auflösung wird in hohem Maße durch die Zusammensetzung des Elektrolyten beeinflusst. Stark adsorbierende Anionen, sowie eine hohe Verfügbarkeit von OH^- und H_3O^+ sollten vermieden werden, während die Verwendung von stark konzentrierten Elektrolyten außerordentliche Stabilität gewährleistet. Darüber hinaus zeigen PBA-Dünnschicht-Modellelektroden ein extrem schnelles, verlustfreies

Ladeverhalten innerhalb weniger als einer Minute. Während die quasi-reversible Elektrodenkinetik bemerkenswert hohe Leistungsdichten ermöglicht, begrenzt die Festkörperdiffusion von Na^+ innerhalb des Aktivmaterials letztendlich die mögliche Ladegeschwindigkeit. Die Schichtdicke kann dementsprechend verwendet werden, um die Ratenfestigkeit präzise einzustellen. Die Verwendung von mikrostrukturierten Substraten für die elektrochemische Abscheidung des Aktivmaterials wird ausblickend diskutiert, um kommerziell tragfähige Massenbelegungen der Dünnschichtelektroden zu erreichen und somit das vorgestellte Modellsystem in eine praxisnahe, hybride Batterie-Superkondensator-Konstruktion zu überführen.

Acknowledgments

This work would not have been possible without the help and support of many people. I would like to express my deepest gratitude to

- **Prof. Aliaksandr Bandarenka** for supervising my PhD project and giving me the opportunity to work on such an exciting topic with maximum autonomy and freedom to pursue interesting research directions. I am also particularly grateful for his help in proofreading and submitting our manuscripts for publication.

- **Prof. Dr. Pekka Peljo** for agreeing and taking the time to be the second examiner of this thesis.

- **Manuela Ritter** and **Sigfried Schreier** for their everyday work and support on all administrative and technical issues. The chair would not function without the two of them.

- Our collaboration partners and co-authors for their contribution to our published articles and beyond: **Dr. Jan M. Macak** and **Ludek Hromadko** (both Brno University of Technology and University of Pardubice) for performing SEM and XRD measurements and their continuous support over several projects. **Dr. Serhiy Cherevko** and **Dr. Florian Speck** (both Forschungszentrum Jülich) for the dissolution experiments with their innovative flow-cell ICP-MS technique. **Prof. Dr. Vitaly Alexandrov** and **Dr. Iman Evazzade** (both University of Nebraska-Lincoln) for their efforts to examine PBA degradation mechanisms with DFT and AIMD calculations.

- All fellow members from the ECS group for the pleasant working environment, the fruitful discussions and scientific collaboration, but also the fun time outside the lab during football games, group events, while being at international conferences and several too-hot Chinese dinners. I am grateful for the evolved friendships beyond our time as colleagues. I would like to specifically express my sincere gratitude to: **Dr. Regina Kluge**, **Dr. Elena Gubanova**, **Dr. Sebastian Watzele** and **Dr. Batyr Garlyyev** for their great support in the daily doing as a PhD student. **Philipp Marzak**, **Dr. Jeongsik Yun** and **Philipp Moser** for introducing me to the topic of Prussian blue analogs and aqueous sodium-ion batteries during my Master's project, as well as the good advice during my PhD time and our collaboration on several publications. **Raphael Streng** for the inspiring discussions and collaboration on new battery materials, as well as for keeping the torch of aqueous batteries

burning at the ECS chair. **Göktug Yesilbas** for his help with preparing composite-type electrodes and our interesting discussions on data and various battery topics. **Dr. Richard Haid** for his help with AFM measurements. **Dr. Leon Katzenmeier** for being a great sparing partner for impedance analysis. **Dr. Shujin Hou** for his help with SEM and XRD measurements. **Leif Carstensen**, **Thorsten Schmidt**, **Kun-Ting Song**, **Peter Schneider**, **Rainer Götz**, **Christian Schott**, **Dr. Rohit R. Gaddam**, **Theophilus K. Sarpey**, **Xiaoxin Ma** and all other colleagues for their support and the great time in our laboratory and office.

- The many people from the preceding list, as well as my cousin **Felix Michel**, for supporting me with proofreading this thesis.

- All students I had the pleasure to support as an advisor for their BSc and MSc theses during their time at the chair, namely **Philipp Zellner**, **Nina Thomsen**, **Florian Steinberger**, **Andreas Grasser**, **Raphael Streng**, **Roman List**, **Iago Ungerer Fraga**, **Tim Steeger** and **Max Labandowski**. Thanks for your hard work and contribution to our joint research projects.

- **Dr. Tom Pehl** and **Dr. Mian Zahid Hussain** (both TUM Chemistry Department) for their scientific advice and support with wet chemical experiments during the synthesis and treatment of new materials.

I am especially grateful to my family for their unconditional love, support, and everlasting understanding:

- my partner **Melanie**, without whom my life would not be the same.
- my parents **Claudia** and **Bernhard**, who always enable me the freedom to pursue my personal goals and dreams.
- my sister **Antonia**, who is always around for having a great time.
- my grandparents **Linde** and **Hans**, as well as **Moni** and **Peter**, from whom I learned ambition, diligence, humbleness, and courage.
- my parents-in-law-to-be **Roswitha** and **Lothar**, for welcoming me in your family.

List of Publications

R. R. Gaddam,♠ L. Katzenmeier,♠ X. Lamprecht,♠ A. S. Bandarenka. Review on physical impedance models in modern battery research. *Physical Chemistry Chemical Physics* **2021**, *23*(23), 12926-12944.

X. Lamprecht, F. Speck, P. Marzak, S. Cherevko, A.S. Bandarenka. Electrolyte effects on the stabilization of Prussian blue analog electrodes in aqueous sodium-ion batteries. *ACS Applied Materials and Interfaces* **2022**, *14*, 3515-3525.

X. Lamprecht,♠ P. Marzak,♠ A. Wieczorek, N. Thomsen, J. Kim, B. Garlyyev, Y. Liang, A. S. Bandarenka, J. Yun. High voltage and superior cyclability of indium hexacyanoferrate cathodes for aqueous Na-ion batteries enabled by superconcentrated $NaClO_4$ electrolytes. *Energy Advances* **2022**, *1*, 623-631.

X. Lamprecht, I. Evazzade, I. Ungerer, L. Hromadko, J. M. Macak, A. S. Bandarenka, V. Alexandrov. Mechanisms of degradation of $Na_2Ni[Fe(CN)_6]$ functional electrodes in aqueous media: a combined theoretical and experimental study. *The Journal of Physical Chemistry C* **2023**, *127*(5), 2204–2214.

X. Lamprecht, P. Zellner, G. Yesilbas, L. Hromadko, P. Moser, P. Marzak, S. Hou, R. W. Haid, F. Steinberger, T. Steeger, J. M. Macak, A. S. Bandarenka. Fast charging capability of thin-film Prussian blue analogue electrodes for aqueous sodium-ion batteries. *ACS Applied Materials and Interfaces* **2023**, *15(19)*, 23951–23962.

♠ The authors have contributed equally.

Conference Contributions

X. Lamprecht, A. S. Bandarenka. Anion induced dissolution mechanism of PBA electrodes for aqueous Na^+ batteries during super-fast cycling. 72nd Annual Meeting of the International Society of Electrochemistry. August 29 – September 3, 2021, Hybrid Meeting: Jeju Island, Korea/Online. *Oral Presentation*.

X. Lamprecht, A. S. Bandarenka. Degradation mechanism of Prussian blue analog electrodes in aqueous sodium-ion batteries. 5th International Conference on Applied Surface Science. April 25 – 28, 2022, Palma de Mallorca, Spain. *Poster Presentation*.

X. Lamprecht, A. S. Bandarenka. Degradation mechanism of Prussian blue analog electrodes in aqueous sodium-ion batteries. 32nd Topical Meeting of the International Society of Electrochemistry. June 19 – 22, 2022, Stockholm, Sweden. *Oral Presentation*.

X. Lamprecht, A. S. Bandarenka. Fast-charging Prussian blue analog electrodes for aqueous sodium-ion batteries. 73rd Annual Meeting of the International Society of Electrochemistry. September 12 – 16, 2022, Online Meeting. *Oral Presentation*.

Advised Student Projects

P. Zellner. Scalability of fast-charging properties in aqueous sodium-ion batteries. *BSc Thesis*, **2021**.

N. M. Thomsen. Aqueous sodium ion batteries: conceptualizing the commercial uptake of a scalable energy storage system. *MSc Thesis*, **2021**.

F. Steinberger. Aqueous sodium ion batteries: stability and self-discharge of manganese hexacyanomanganate electrodes. *MSc Thesis*, **2021**.

A. Grasser. Molecular crowding electrolytes as a way towards high-energy aqueous sodium-ion batteries. *MSc Thesis*, **2022**.

R. Streng. Investigation of alizarin and its derivatives as anode materials for aqueous sodium ion batteries. *MSc Thesis*, **2022**.

R. List. Carbon cloth as a high-area current collector for thin-film electrodes in aqueous sodium ion batteries. *BSc Thesis*, **2022**.

I. Ungerer Fraga. Role of the electrolyte composition on the stability of NiHCF electrodes for aqueous sodium-ion batteries. *BSc Thesis*, **2022**.

T. Steeger. Self-discharge, degradation and characterization of manganese hexacyanomanganate thin films in aqueous sodium ion batteries. *BSc Thesis*, **2022**.

M. Labandowski. Characterization of ink-coated nickel hexacyanoferrate battery-cathodes in aqueous sodium ion batteries. *BSc Thesis*, **2022**.

Table of Contents

1 Introduction

When the invention of the steam engine kicked off the industrial revolution in the late 18th century and laid the ground for the development of our world as we know it today, no one would have imagined that this also provoked one of the most severe threats that humanity has ever seen: the climate change. The combustion of carbon-based fuels, such as natural gas, coal, and oil, as well as its derivatives, has become the main scheme for modern energy provision over the last 200 years. However, this has resulted in a massive release of CO_2 and other so-called greenhouse gases into the atmosphere. Up to this day, this process appears unstoppable, especially in light of the economic emergence of highly populated developing countries. As it is well-known nowadays, the increasing presence of CO_2 and other so-called greenhouse gases in the earth's atmosphere changes the net power equilibrium of in- and outbound heat radiation, which in turn causes the main earth's temperature to rise.[1,2,3,4,5]

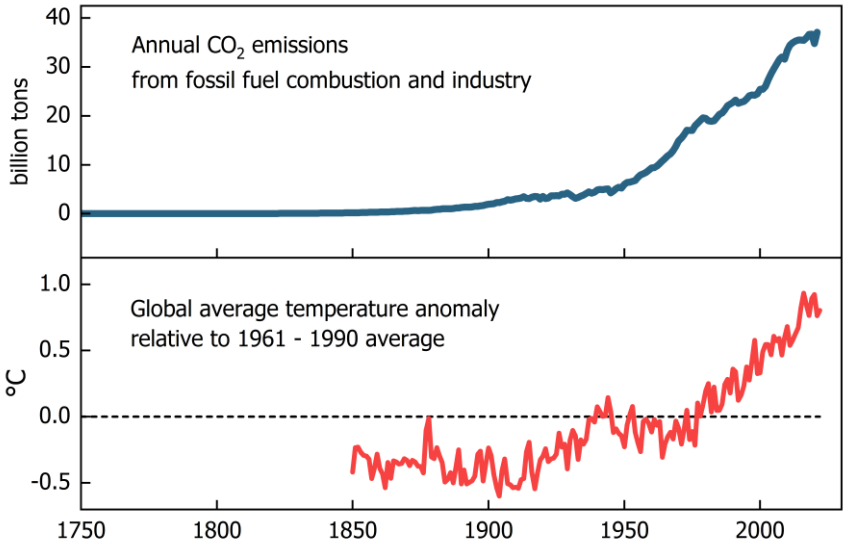

***Figure 1**. Correlation of the global temperature anomaly and annual CO_2 emission since the industrial revolution. Data source for CO_2 emissions: ref. 6. Data source for temperature anomaly: ref. 7.*

Figure 1 shows the distinctive correlation between the annual CO_2 emissions caused by human activity and the earth's global average temperature. The impact of the "Anthropocene", the most recent geological epoch where human activity dictates the earth's macroscopic state, is easily visible. Similar correlations can be drawn involving deforestation, meat production, global wealth, energy consumption and other factors on one side, and polar ice caps, glacier extents, sea level increase, ocean acidity, wildfire and extreme weather events on the other

side.[8] If this development continuous likewise in the future, scientists unanimously project that climate change will have catastrophic consequences leading to a radical change of our environment and lives as we know it today.[9,10,11,12]

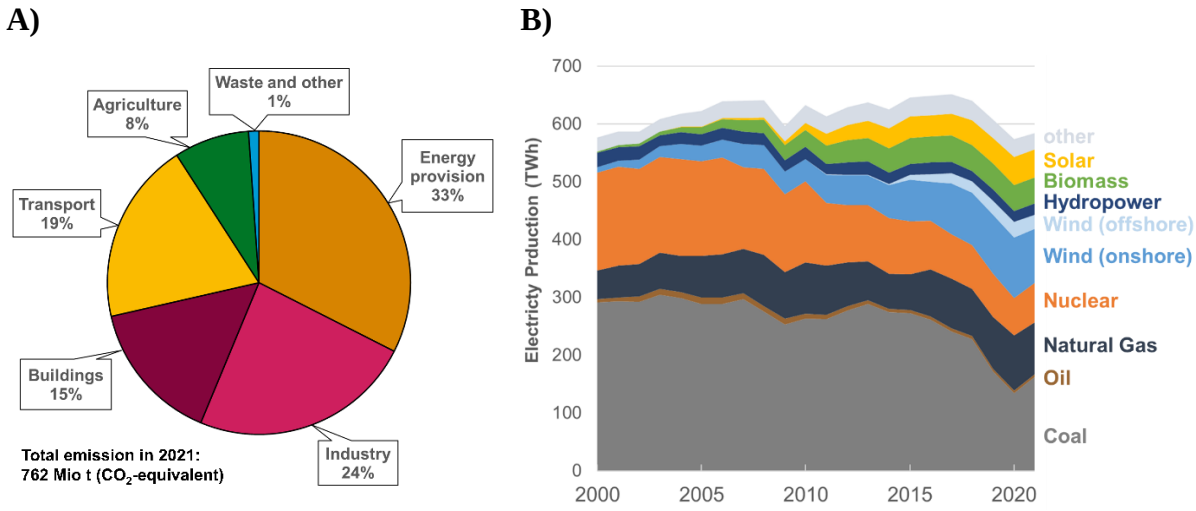

***Figure 2**..(**A**) Sectoral emission of greenhouse gases (CO_2-equivalent) in Germany in 2021. Data source: ref. 15. (**B**) Electricity production in Germany from 2000 – 2021. Data source: ref.16.*

After decades of political and societal ignorance, policies and commitments for decarbonizing our energy provision toward sustainability are on the agenda of almost any country in the world. The Paris Climate Agreement from 2015, along with its amendments from the international climate summits in recent years, aims at drastically regulating greenhouse gas emissions in the coming decades to limit global warming to a maximum of 1.5 °C compared to pre-industrial times.[13] As a result, Germany, which currently ranks #7 with its total CO_2 emissions,[14] will need to transform its energy provision schemes drastically. As shown in **Figure 2A**, the relative sectoral emission related to the provision of energy (electricity and heating) in Germany in 2021 amounts to 33%,[15] while around 42% of the electricity was produced from renewable sources (see **Figure 2B**).[16] In the meantime, the German government has concluded that its share will have to be increased to 80% by 2030 to reach the CO_2 emission reduction goals deduced from the climate agreements.[17] The amount of required electric energy is predicted to increase heavily in the future due to the ongoing electrification of the mobility sector, industrial processes (steel, cement, chemicals), and building up the hydrogen economy based on electrolysis. For Germany, electricity consumption could almost double by 2050 from its current level.[18] The urgency for a fast transition away from fossil fuels was furthermore exemplified under the impression of the recent war avalanched by Russia against Ukraine,

which led to the abandoned provision of natural gas and threatened power supply insecurity in many European countries. Renewable energies, on the other hand, have the potential to reduce international resource dependencies from a few countries and increase the autonomy of the European states.

So far, this has been mainly approached by ramping up the construction of photovoltaic and wind power production systems. As shown in **Figure 3A**, a cumulative installed solar and wind capacity of 120 GW was in place in Germany in 2021.[19] For comparison, the average electricity demand was 58 GW.[20] Whereas this results already in full coverage of electricity demand by renewables on some days throughout the year, there will be a significant mismatch of generation *vs.* consumption most of the time. This strategy has led to major challenges regarding the electric power grid in terms of distribution, stability and quality of power provision.[21,22] By nature, the production of renewable energies strongly fluctuates according to the weather, daytime and season (see **Figure 3B**). However, the production of electric power must always match its consumption to maintain a net power flux balance in the grid, while even small deviations can result in a system collapse and failure of electric equipment. The uneven distribution of wind production sites poses another challenge. Differing local conditions and political considerations lead to local overproduction as well as shortages across the grid. Countermeasures to these problems, such as curtailment, withholding short-term operation reserve power, redispatch, as well as building immense power transmission lines have the potential to be massive cost drivers in the energy transition.[23,24,25] It is questionable if such measures alone will be enough to operate the power grid with almost 100% renewable energies.

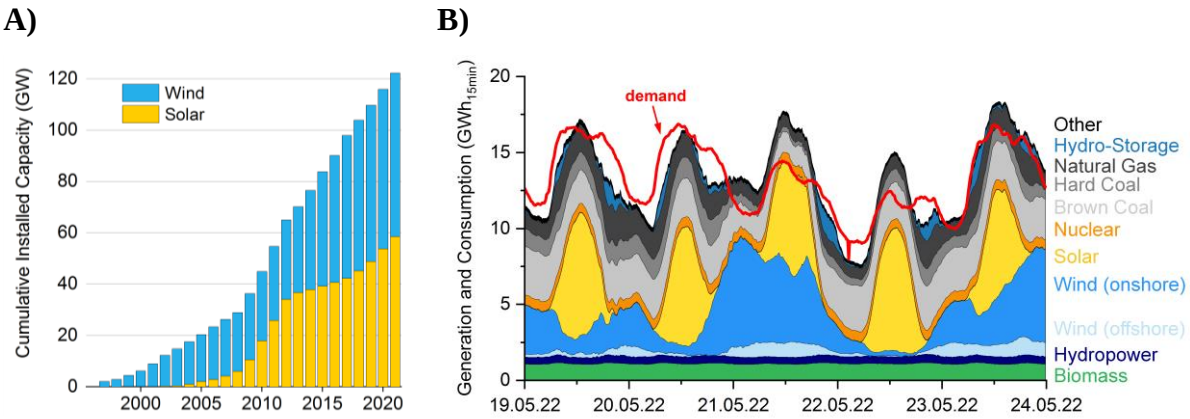

***Figure 3**. (**A**) Cumulative capacity for electricity generation from solar and wind energy installed in Germany. Data source: ref. 19. (**B**) Generation vs. consumption of electricity in Germany from 19. May 2022 to 24. May 2022. Data source: ref. 20.*

It is therefore believed that stationary energy storage systems will play a key role in enabling the integration of renewable energies.[26,27,28,29] Rechargeable batteries are among the best options for compensating temporal misbalance of supply and demand of electricity, as well as the arbitrage of local production gradients to avoid redispatch measures. Thereby, they can significantly support the grid's flexibility and transmission capacity.[30,31,32,33] The advantages of battery energy storage include their easy deployment across the grid from small to large system units. Furthermore, they are not dependent on local conditions like, for example, pumped-hydro storage or compressed-air energy storage. Additional selling points are their high energy efficiency and fast response time. It is thus believed that batteries cannot only enable a high degree of utilization of electricity from renewable sources, but also contribute to their integration into the electricity grid while maintaining reliable power provision.[34,35,36,37,38]

Today, the leading battery technology available on the market is based on lithium-ion chemistries with organic electrolytes, commonly known as lithium-ion batteries (LIB).[39,40] While these high cell-voltage (> 3 – 4 V) systems were developed for the high energy density demand of electric cars and portable electronics (> 200 – 300 Wh/kg based on all materials),[41] their adoption for stationary storage raises serious concerns regarding scalability and safety.[42] Lithium resources are unevenly distributed across the world with major deposits in South America, Australia and China.[43] The limited resource availability and unsustainable mining of lithium potentially cause high material price levels and price instability, supply insecurity and environmental concerns.[43,44,45,46,47] Another critical material for automotive high energy density NMC and NCA cells is cobalt, a rare transition metal mainly sourced in the D. R. Congo, with its mining conditions being highly criticized for lacking humanitarian standards.[48] However, even if ethically less concerned, cobalt-free $LiFePO_4$ (LFP)-based cells would be used, the large-scale adoption of LIBs for stationary applications will further increase the pressure on this pioneering technology. One of the largest stationary battery systems worldwide is the Hornsdale Power Reserve, which is shown in **Figure 4**. This 193.5 MWh plant equipped with lithium-ion cells equals over 3,200 Tesla Model 3 fully-electric cars (for a 60 kWh battery).[49] For Germany, it is expected that between 100 to 500 GWh of stationary battery storage will be needed by 2045.[35] This implies at least a 30 to 150-fold increase of the large-scale and home-scale capacity installed in 2021, which was almost entirely deployed by LIBs.[50] If future stationary energy storage systems will continuously rely on lithium-based batteries, rising prizes could become an elevating obstacle for the electrification of the transport sector, which is equally important to achieve the climate goals. On the other site, various failure modes

can result in a thermal runaway or short-circuit of LIBs and therefore pose a severe safety risk related to the flammable organic electrolyte.[51] Footage of burning electric cars has repeatedly been on the media over the last years. Considering both home-scale and large-scale stationary battery systems, safety concerns could seriously impact the procurement decision.

***Figure 4**. Hornsdale Power Reserve in South Australia. The grid-connected battery energy storage system provides a capacity of 193.5 MWh at 150 MW. Picture reproduced from ref. 52.*

Aqueous sodium-ion batteries (ASIB) could be a suitable alternative for stationary storage applications.[53,54,55] Whereas they intrinsically come with a lower energy density due to the restricted cell voltage limited by water electrolysis, scalability and safety can be considered more important metrics for stationary systems. Resource availability would be guaranteed by employing sodium instead of lithium, which is much more abundant and also evenly distributed across the world in the form of mineral rock and salt water.[43,56,57] Furthermore, the use of an aqueous electrolyte has the potential for environmentally benign chemistry and makes the cell non-flammable, allowing its safe operation.[55,58,59,60] When developing a scalable, low-cost and environmentally benign sodium-ion battery technology, these prerequisites, of course, also apply to the active material employed for the battery's electrodes. The material class of Prussian blue analogs (PBA) has attracted considerable interest for being a promising candidate for ASIBs.[53,54,55,61,62,63,64,65] Prussian blue was first discovered by accident in 1706 in Berlin as a product from a failed synthesis procedure based on cattle blood, pot ash and green vitriol (iron sulfate).[66] This new pigment found almost immediate application for paintings and cloth

dying due to its appealing color and lower price compared to alternatives. As an example, **Figure 5** shows the oil-on-canvas painting "The Starry Night" by Vincent van Gogh.

***Figure 5**. "La nuit étoilée" (The Starry Night) by Vincent van Gogh, 1889, was created using Prussian blue pigment. Public Domain – Image downloaded from ref. 67.*

Prussian blue analogs are derivatives from the historical pigment, where the incorporation of different transition metals strongly influences their (electro)chemical and physical properties.[63,68,69,70,71,72] They are nowadays widely used and investigated as functional materials in various disciplines, involving (electro)sensorics,[73,74,75] heterogeneous (electro)catalysis,[76,77,78] desalination and selective ion removal,[79,80,81] as well as electrochromic devices.[82,83] Over the last decades, PBAs have also been extensively studied as active materials for batteries.[53,54,55,61,62,63,64,65,84,85,86,87,88] The interest in this battery material class originates from their facile and inexpensive synthesis relying on abundant precursor materials, which are based on nitrogen and carbon together with iron, manganese, copper, zinc or other transition metals. Further advantages are their tunability and reversible (alkali-)metal ion insertion kinetics associated with their redox activity. Next to *CATL*, a leading Chinese battery manufacturer, several companies are working on commercializing Prussian blue and its derivatives for organic SIBs.[89,90,91] The California-based start-up *Natron Energy* recently introduced an all-PBA-based aqueous SIB to the market,[92] exploiting the ≈ 50 Wh/kg achievable for aqueous batteries.

Despite their stage of development, there is still a lack of fundamental understanding and potential for optimizing critical aspects in terms of viability and performance of PBA-based

ASIBs. This thesis aims at discussing the following aspects and findings, which are vital for the successful large-scale adoption of this innovative battery technology:

After almost 50 years of research on LIBs, its cost significantly decreased to ≈ 100 – 150 $/kWh (cell level).[41,93,94] Despite the cheaper precursor materials of PBA-based ASIBs, their upfront capital cost per kWh is estimated to result in the same range as LIBs. This is mainly due to its 5 – 10 times lower energy density.[95] However, when used for stationary applications, cycling stability[37,38] and the resulting amortized cost over lifetime undoubtedly outweighs energy density as a major critical metric for consideration.[31,57,96] Suppose PBA-based ASIBs could be operated for more than 10,000 cycles without significant capacity loss. On the market, this threshold currently constitutes the warranty-limit of LFP-based LIBs.[97,98,99] Correspondingly, such performance strongly surpasses NMC- and NCA-based LIBs.[100] This high cycling stability would result in levelized costs of 0.01 − 0.02 $/(kWh/cycle) on a cell level.[95] Even when added to the generation cost of wind and solar energy to solve the generation *vs.* consumption problem, a battery-supported electricity provision will not only defeat fossil fuels in terms of sustainability, but also in economic standards.[101]

These considerations make clear that cycling stability is assigned the utmost importance for stationary battery systems to be economically viable. In this work, the degradation mechanism of PBA electrodes in aqueous electrolytes will be elucidated in detail. It will be shown that a major degradation pathway follows a complex mechanism involving transition metal dissolution and subsequent partial re-deposition. Whereas mass loss causes an irreversible capacity decay, impaired kinetics and mass transport properties of the re-deposited material corrupt the rate capability, thereby representing an additional power fade. The individual elemental dissolution of electrode constituents and its correlation to the electrode potential and current will be investigated by employing an innovative *in-operando* online dissolution monitoring technique. Furthermore, it will be shown with the help of DFT calculations, how the composition of the electrolyte, namely the pH, Na^+ concentration and involved anions, impacts the dissolution behavior and stability of PBA electrodes. This will allow to explain the extremely high stability of PBAs in some strongly concentrated electrolytes. Such stabilization measure was already known before, but so far lacked a fundamental understanding of the underlying physico-chemical processes driving the electrode degradation. This work aims to provide a profound perception of these mechanisms.

Another aspect that could significantly impact the viability of ASIBs as stationary energy storage systems is their ability to provide grid stabilization services. Historically, the electricity grid was designed for a limited amount of centralized large power generation sites, like coal and nuclear power plants, with steady and highly predictable output. A few hydroelectric systems were enough to react to marginal load fluctuations, and therefore high-quality power provision was ensured.[102] The ongoing integration of the immanently fluctuating and intermittent renewable energy sources from decentralized production sites comes along with an increased need for stabilization measures to maintain grid reliability.[103,104] Such short-term ancillary services especially include frequency regulation by balancing net power flux in the grid. This application requires high power loads within a few seconds to maintain grid stability, flexibility, and supply continuity. Large-scale batteries with the capability to provide and sink such high-power profiles could therefore not only enable the full and reliable integration of renewable energies to the grid, but also provide surpassing revenue streams for such stationary storage systems.[28,105,106,107] Suitable hybrid electrochemical devices combine a sufficient energy density, usually associated with batteries, with a high power capability typical for supercapacitors.[108,109] Apart from the above-described grid stabilization services, they could even enable applications like urban short-distance electric mobility.[110] Busses, for example, only require power for short intervals between two stations while offering frequent recharging possibilities with durations of approximately one minute while passengers board and disembark at each station.[111,112,113] Of course, such applications need an appropriate infrastructure, especially for recharging the busses, but first pilot projects, *e.g.*, in Minsk and many other cities[114,115] provide a promising perspective on electrifying street-bound public transport by using high-power electrochemical energy storage systems.

In this work, pathways for customizing PBA-based ASIBs for high-power applications will be explored. In contrast to the traditional synthesis routine of composite electrodes, an easy, single-step electrochemical deposition is employed to obtain binder- and additive-free thin-film model electrodes. Their fast-charging capability is investigated with regard to the electrochemically active material thickness. Their performance is analyzed to identify the rate-determining steps governing the interfacial mass and charge transport processes. Furthermore, the detrimental role of parasitic processes for low-mass-loading electrodes will be outlined and assessed. Prototypical all-PBA-based ASIBs will be presented, highlighting a direction towards hybrid battery-supercapacitor systems combining sufficient energy density with high power density. By employing conductive, microstructured high-surface area substrates as templates

for the electrodeposition, the scalability of such model systems towards commercially relevant mass-loadings will be discussed.

2 Theoretical Background

In the following chapter, the relevant fundamentals of electrochemistry will be introduced, focusing on the concepts necessary to understand the content of this work. This is followed by an explanation of the general working principle of intercalation-type batteries, charge-discharge characteristics, and considerations on the employed electrolyte. Furthermore, metrics to evaluate the performance of the involved materials will be introduced. The descriptions, derivations and explanations in this chapter follow the standard textbooks "Handbook of Battery Materials" by C. Daniel and J. O. Besenhard,[116] "Linden's Handbook of Batteries" by T. B. Reddy and D. Linden,[117] "Elektrochemie" by C. H. Hamann and W. Vielstich,[118] as well as "Electrochemical Methods: Fundamentals and Applications" by A. J. Bard and L. R. Faulkner.[119] For the sake of fluid readability, not every instance will be referenced to the mentioned sources.

2.1 Introduction to Electrochemistry

The history of electrochemistry dates back over two hundred years to the pioneering experiments of Luigi Galvani and Alessandro Volta. Today, it is one of the most important science disciplines encountered in everyday life, as well as for our present and future basis of the economy. It provides the fundamentals of many critical technologies like batteries, fuel cells, electroplating, corrosion, sensors or electrolysis.

2.1.1 The Electrochemical Cell

Electrochemistry describes the phenomena happening at the interface between different chemical phases. In the most common sense, it is concerned with the interrelation of chemical and electrical processes between an electronic conductor (electrode) in contact with an ionic conductor (electrolyte). A simple electrochemical cell consists of two electrodes (I and II) immersed in a liquid electrolyte. Current flow is enabled by providing an external pathway for electrons, while ions are conducted through the solution. The current flow can be either forced by connecting an external power source and driving a current through the cell or proceed spontaneously due to an internal driving force capable of providing power to an external load. In general, currents can either be associated with capacitive effects or redox reactions. While the former result from the re-arrangement of mobile ions at the electrode-electrolyte interface counteracting the electrode charge, the latter involve the conversion of species at the electrode-

electrolyte interface by the transfer of electrons or ions. These processes are schematically represented in **Figure 6** and will be explained in the following sections.

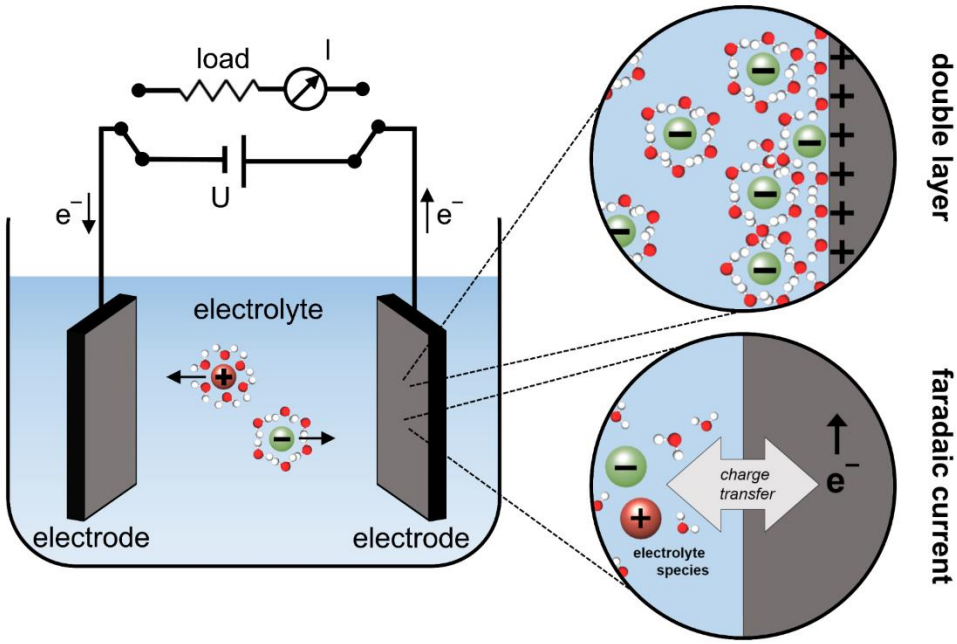

***Figure 6**. Schematic representation of an electrochemical cell. Current flow is enabled via the (re-)arrangement of the electrical double layer, which results in a capacitive current contribution, or interfacial charge transfer, the so-called faradaic current.*

Furthermore, each phase in the electrochemical cell can be assigned a so-called Galvani potential φ, which describes the respective electrostatic potential within the bulk of each phase. For the cell introduced above, the Galvani potential of each electrode ($\varphi(I)$ and $\varphi(II)$) and the solution ($\varphi(S)$) must be considered. If a phase is in electrochemical equilibrium with its adjacent phase, then $\varphi = \varphi_{eq}$. The resulting difference of the Galvani potential between a metal electrode and a solution, $\Delta\varphi = \varphi(I) - \varphi(S)$, is, however, not measurable. Rather, a measured potential difference always refers to a second electrode, according to **Equation 1** (neglecting the contact potential differences between the metal wires and phases I and II of an actual measurement device):

$$\Delta\varphi = [\varphi(I) - \varphi(S)] - [\varphi(II) - \varphi(S)] = \varphi(I) - \varphi(II) \qquad \textbf{Equation 1}$$

Assuming that the Galvani potential of phase II remains constant and in equilibrium ($\varphi(II) = \varphi(II)_{eq} = const$), we can refer to all determined or applied potential differences $\Delta\varphi$ of the investigated electrode I against this reference and define its electrode potential E as given in **Equation 2**:

$$\Delta\varphi = \varphi(I) - \varphi(II) = \varphi(I) - \varphi(II)_{eq} \equiv E \qquad \textbf{Equation 2}$$

Experimentally, this situation is approximated by employing a so-called reference electrode, as it will be introduced later, from which the electrode potential is sensed through a high-impedance voltmeter (no current flow), while all cell current is guided through a different electrode. Despite the impossibility of measuring it, the electrode potential can mathematically be related to an absolute potential scale using electron energy levels with regard to the vacuum. This was discussed in great detail by S. Trasatti.[120]

2.1.2 Electrical Double Layer

First, assume that two metal electrodes (A and B) are immersed into an electrochemically inert aqueous solution, with no interfacial charge transfer occurring at either electrode (ideal polarizable electrode). Nevertheless, a transient current pulse can be observed when applying a voltage *U* between the two electrodes. As interfacial charge transfer is omitted, the voltage across the cell will lead to an accumulation of charge *Q* on the electrode, which is localized at its surface due to the high inherent electronic conductivity. This surface charge subsequently attracts oppositely charged ions in the electrolyte vicinity, which approach the electrode and accumulate at the interface. This arrangement of accumulated opposing charges across the electrode-electrolyte interface is called the electrical double layer (EDL), and it is always observed in electrochemical systems regardless of other processes.

Hydrated ions approach the electrode surface as close as their solvation shell allows. The plane through the centers of the accumulated hydrated ions is called the outer Helmholtz plane (OHP). In this most simple treatment, the potential drops linearly between the electrode surface and the OHP. Accordingly, the EDL can be represented as a capacitor with a distance between its planes equivalent to the radius *r* of the hydrated ions. It should be assumed that the nature of electrode B and the electrolyte causes the voltage to drop entirely at the interface of electrode A and the electrolyte. Its capacitance *C* is then obtained by **Equation 3**:

$$\frac{Q}{U} = C = \varepsilon_0 \varepsilon_r \cdot \frac{A}{r} \qquad \textbf{Equation 3}$$

Here, *A* is the area of the interface. Furthermore, ε_0 is the vacuum permittivity, and ε_r is the relative permittivity of the dielectric medium, with $\varepsilon_r \approx 80$ in the case of water as the solvent.[121] Considering an aqueous KCl solution, the radius of the solvation shell of K^+ is approximately 3.6 Å.[122] The resulting areal capacitance would be $C/A \approx 200$ µF/cm^2. However, experimentally

determined values are usually one order of magnitude lower.[123] This overestimation results from the too-simplified model of the double layer. In reality, a more complex structure must be considered, including surface-oriented solvent molecules with a static dipole or adsorbed (partially) de-solvated ions, which mark the so-called inner Helmholtz plane in direct vicinity to the electrode. This causes that $\varepsilon_{r,effective}$ is significantly smaller than in the simple model introduced above. Furthermore, in sufficiently diluted solutions, a diffusive extension of the accumulated countercharges is observed at a further distance from the electrode, which increases the effective distance in the capacitor model.[124,125,126] In general, the double layer capacitance is a function of the electrode potential due to the potential-dependent composition of the closest layer of adsorbed species. Therefore, the double-layer capacitance is usually determined as a differential capacity according to **Equation 4**:

$$C_{dl} = \frac{dQ}{dE} = \frac{1}{\frac{1}{C_{IHP}} + \frac{1}{C_{OHP}} + \frac{1}{C_{diffuse}}} = \mathrm{f}(E) \qquad \textbf{Equation 4}$$

2.1.3 Origin of Electrode Potentials and Faradaic Reactions

So far, only capacitive charge accumulation at the electrode-electrolyte interface upon a change of the electrode potential has been considered as the source of current flow. However, an electrochemical cell also enables the conversion of chemical energy from a redox reaction into electrical energy and *vice versa*. This process is facilitated by spatially separating the oxidation and reduction reactions at the two electrodes while closing the electrical circuit through the ionically conducting electrolyte and the external electron conductor. This, in turn, requires the transfer of charge (electrons or ions) across the interface at each electrode. The driving force for this process is expressed by the respective electrode potential. For the sake of simplicity, half-cell reactions will be considered in the following, *i.e.*, only the processes happening at one electrode-electrolyte interface with a given electrode potential. It will be assumed that current flow is conserved and not influenced by the processes occurring at the second electrode.

Consider the following half-cell redox reaction taking place at an electrode involving the conversion of species *S* in the solution under the exchange of *n* electrons across the interface (**Equation 5**):

$$\mathrm{S_{ox}} + \mathrm{ne^-} \rightleftharpoons \mathrm{S_{red}} \qquad \textbf{Equation 5}$$

If no net current flow is allowed, which means that the oxidation and reduction proceed at equal rates, an electrochemical equilibrium will exist with an associated Galvani potential φ_{eq}. The standard Galvani potential φ_0 of an associated redox couple is the value of the Galvani potential obtained under standard conditions in equilibrium. Before, we had already introduced the potential of electrode I, which is determined using a second electrode II, as the difference between their respective Galvani potentials. If each electrode is in equilibrium with its adjacent phase and under standard conditions, this is expressed by the difference of the standard Galvani potentials as given by **Equation 6**:

$$E_0 = \Delta\varphi_0 = \varphi(I)_0 - \varphi(II)_0 \qquad \textbf{Equation 6}$$

The Galvani potential scale can be arbitrarily set and has been defined as φ_0 = 0.0V for the proton reduction reaction $2H^+ + 2e^- \rightleftharpoons H_2$. This is the so-called standard hydrogen electrode (SHE), against which all standard potentials are reported. The electrochemical series lists the standard potentials of redox couples and is tabulated in standard textbooks.[127] A selection is exemplarily provided in **Table 1**.

Table 1. Standard potentials of selected redox pairs.[127]

Reaction	E_0 *vs.* SHE
$Li^+ + e^- \rightleftharpoons Li$	– 3.04 V
$Na^+ + e^- \rightleftharpoons Na$	– 2.71 V
$Fe^{2+} + 2e^- \rightleftharpoons Fe$	– 0.45 V
$2H_2O + 2e^- \rightleftharpoons H_2 + 2OH^-$	– 0.41 V at pH = 7
$2H^+ + 2e^- \rightleftharpoons H_2$	0.0 V
$AgCl + e^- \rightleftharpoons Ag + Cl^-$	0.22 V
$Cu^{2+} + 2e^- \rightleftharpoons Cu$	0.34 V
$[Fe(CN)_6]^{3-} + e^- \rightleftharpoons [Fe(CN)_6]^{4-}$	0.36 V
$O_2 + 2H_2O + 4e^- \rightleftharpoons 4OH^-$	0.82 V at pH = 7
$O_2 + 4H^+ + 4e^- \rightleftharpoons 2H_2O$	1.23 V

Apparently, the standard potential is an especially important characteristic of a redox couple. In the following, its origin should be briefly discussed on a practical, simplified example describing the corrosion of iron in the air involving atmospheric humidity as expressed in **Equation 7**:

$$2Fe + O_2 + 2H_2O \rightarrow 2Fe^{2+} + 4OH^- \qquad \textbf{Equation 7}$$

The products of this reaction eventually form local precipitates of iron oxide/hydroxide. The corresponding change of the standard Gibbs free energy ΔG of the reaction is directly related to the difference of the respective standard potentials according to **Equation 8**:

$$\Delta G_0 = -\frac{\Delta E_0}{nF} \qquad \textbf{Equation 8}$$

As seen in **Table 1**, the standard oxidation potential of iron is much lower than the standard reduction potential of oxygen and therefore $\Delta G_0 < 0$, which means that the reaction proceeds spontaneously. For comparison, copper can still be oxidized by oxygen, whereas the smaller difference in their standard potentials reflects its lower proneness to corrosion in the air compared to iron. In contrast, the standard oxidation potential of gold is much higher than the standard reduction potential of oxygen, from which it results that it cannot be corroded in air or acids (see standard reduction potential of H^+ in **Table 1**). This resistance against corrosion is reflected in its notation as a "noble" metal. In simple terms, the standard potential represents the ability of a species to consume or release electrons, so basically reflecting its reducing or oxidative power relative to another species. It should be noted that the thermodynamic stability of metals in a solution, in general, strongly depends on the pH and corrosion pathway involving different species under the influence of the electrode potential. So-called Pourbaix diagrams well describe these relations.[128]

For non-standard conditions, the equilibrium potential E_{eq} is related to the activity a_i of the involved species. This correlation is expressed by the Nernst equation, which can be derived from thermodynamics (**Equation 9**):

$$E_{eq} = E_0 + \frac{RT}{nF}\ln\left(\frac{a_{ox}}{a_{red}}\right) \qquad \textbf{Equation 9}$$

Here, R is the gas constant, T is the temperature, and F is the Faraday constant. For sufficiently diluted solutions, the activity can be approximated by the respective concentrations c_i. As described above, the electrode potential is determined with respect to a reference. However, the SHE reference is often impractical to use in experimental systems and is many times replaced by a silver-silver chloride (SSC) half-cell from which the potential against SHE can be calculated. This implies that an electrode potential referenced against SSC, for instance, 0.5 V *vs*. SSC, is equivalent to 0.5 V + 0.22 V *vs*. SHE. Practically, it is more useful to replace

the SHE with the so-called reversible hydrogen electrode (RHE) as a reference for reporting measured or applied electrode potentials in aqueous electrolytes, which is directly linked to the pH of the employed solution according to **Equation 10**:

$$E_{RHE} = E_{SHE} + 59\ \text{mV} \cdot pH \qquad \text{at } 25°\text{C} \qquad \textbf{Equation 10}$$

This relation also explains the values for both the hydrogen and oxygen oxidation/reduction at pH = 7 listed in **Table 1**. It should be noted that the according standard potential difference always remains at 1.23 V, which resembles the theoretical thermodynamic stability of water. This will be further discussed in **Section 2.2.4**.

Let us return to the redox reaction considered in **Equation 5**. The Nernst equation allows us to relate the ratio of a_{ox}/a_{red} to the electrode potential. However, activity coefficients are usually unknown, and it is more convenient to work with the so-called formal potential E'_0, especially at higher electrolyte concentrations (see **Equation 11**).

$$E_{eq} = E_0 + \frac{RT}{nF}\ln\left(\frac{a_{ox}}{a_{red}}\right) = E'_0 + \frac{RT}{nF}\ln\left(\frac{c_{ox}}{c_{red}}\right) \qquad \textbf{Equation 11}$$

E'_0 is, however, not a constant but specific for an investigated system. It can be easily determined experimentally when $c_{ox} = c_{red}$. For a battery material, this corresponds to an electrode in equilibrium at 50% state-of-charge.

The previous considerations applied to equilibrium conditions without net current flow, where both oxidation and reduction direction in **Equation 5** proceed equally fast. Let us assume the electrode potential is externally forced away from the initial equilibrium potential $E_{eq,i}$. To reach a new equilibrium state at $E_{eq,f}$ the ratio of c_{ox}/c_{red} must adapt according to the Nernst equation. This, in turn, requires the conversion of S by either electrochemical oxidation or reduction. So-called Faradaic current i must flow, which effectively means that charge, *i.e.*, electrons or ions, crosses the electrode-electrolyte interface. This current flow can potentially (but not necessarily) drive the electrode out of equilibrium resulting in a corresponding so-called overpotential or polarization η as shown in **Equation 12**, the magnitude of which strongly depends on the current:

$$\eta(i) = E(i) - E_{eq} \qquad \textbf{Equation 12}$$

The amount of transferred charge ΔQ is directly linked to the number and thereby the mass Δm of converted species by Faraday's law, as shown in **Equation 13**, where F denotes the Faraday constant and M is the molar mass of the converted species.

$$\Delta Q = \frac{nF}{M}\Delta m \qquad \textbf{Equation 13}$$

2.2 Fundamentals of Batteries

Today, more than thirty years after its commercialization in 1991,[129] lithium-ion batteries are considered as one of the most disruptive technologies in human history,[130] with the potential to significantly contribute to solving the imminent climate crisis.[131] For their fundamental work in developing LIBs, J. B. Goodenough, M. S Whittingham and A. Yoshino were awarded the Nobel Prize in Chemistry in 2019.[132] The underlying phenomenon of so-called ion intercalation is also the basis of many "post-LIB" alternative technologies, such as aqueous sodium-ion batteries based on Prussian blue analogs, the material class discussed in this thesis.

2.2.1 What is a Battery

A battery is an electrochemical cell, or more precisely, a galvanic cell with a limited amount of internally stored reactants. It converts chemical energy into electrical energy by spontaneous, spatially separated redox reactions. This process is called discharging, and the electrode where the oxidation occurs is called an anode, while the electrode where a reactant is reduced is called a cathode.[i] Suppose the respective electrode reactions (half-cell reactions) are chemically reversible. In that case, the battery is rechargeable (secondary cell) by providing an external electrical driving force, in contrast to non-rechargeable batteries (primary cell). In this work, only the former will be considered. Therefore, a rechargeable battery is a device capable of storing energy *via* reversible conversion processes employing internally stored active materials. The amount of energy that can be stored is directly given by the Gibbs free energy change ΔG for the pure chemical reaction of the reactants. For an electrochemical cell including redox-active materials, an electromotive force U_{oc}, also denoted as cell voltage, is observed between the two electrodes under no current flow (open-circuit). This quantity is directly related to the Gibbs free energy change as expressed in **Equation 14**:

[i] Strictly speaking, the denotation should switch upon charging the cell. However, the terms anode and cathode have been established in the battery community as derived from the discharge direction.

$$U_{oc} = E_{eq,cathode} - E_{eq,anode} = -\frac{\Delta G}{nF}$$ **Equation 14**

The respective half-cell reaction determines the equilibrium potentials of the cathode and anode and, in each case, are described by the Nernst equation. Under standard conditions, the open-circuit voltage is therefore equal to the difference of the respective standard electrode potentials. At a specific state-of-charge, U_{oc} is equal to the maximum voltage that a cell can deliver during discharging and, inversely, the minimum voltage needed from an external source to recharge the cell. Importantly, a battery can provide power at a more or less constant voltage level over the entire state-of-discharge (SOD) range, in contrast to capacitive storage devices. The exact charge-discharge characteristics under current flow strongly depend on the employed materials and conditions and will be discussed in **Section 2.2.3**.

2.2.2 Intercalation-type Batteries

The involved active materials, together with the electrolyte, are the main components defining the properties of a battery. This work focuses on so-called intercalation-type active materials, most famously known from LIBs, which enabled the spectacular breakthrough of battery-powered mobile consumer-electronic devices and electric vehicles in the last decade.[133] The term "intercalation" was probably used for the first time in 1951 by McDonnell *et al.*[134] and then in 1959 by W. Rüdorff,[135] describing the capability of graphite derivatives to take up foreign (ionic) species within their lattice. Today, the term is commonly used by the battery community to describe the phenomenon of mobile species insertion into both structural elements like 2D/layered materials and 3D frameworks containing channels and cavities.[116,136,137]

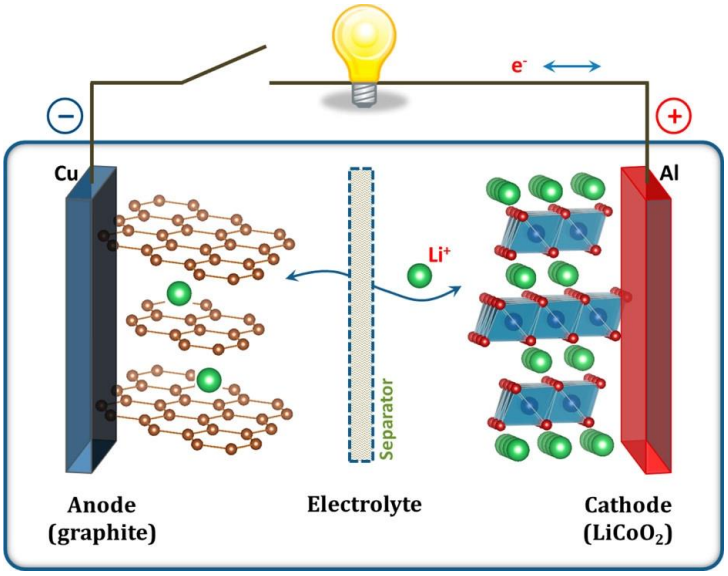

***Figure 7**. Schematic representation of a $LiCoO_2$/graphite lithium-ion battery to illustrate the mechanism of ion intercalation. Reprinted with permission from ref. 140. Copyright © 2013, American Chemical Society.*

The "mother" of the modern-day lithium-ion battery was first fabricated in 1985 and later commercialized by *Sony* based on a lithiated transition-metal oxide cathode and a carbonaceous anode.[129,138,139] **Figure 7** schematically shows a $LiCoO_2$/graphite cell with an organic Li^+-electrolyte to illustrate the mechanism of ion intercalation. The respective half-cell discharge reactions are given in **Equation 15** with $0 \leq x \leq 1$, where $x = 1$ represents the fully charged state and $x = 0$ the fully discharged state:[140]

cathode:	$Li_{1-x}CoO_2 + xe^- + xLi^+ \rightarrow LiCoO_2$	
anode:	$Li_xC_6 \rightarrow 6C + xLi^+ + xe^-$	**Equation 15**
overall cell reaction:	$Li_{1-x}CoO_2 + Li_xC_6 \rightarrow LiCoO_2 + 6C$	

As seen from these reactions, lithium ions are extracted (deintercalated) from the anode by an oxidation process, which drives electrons towards the cathode side trough an external load. At the cathode, the reduction of the active material proceeds, which leads to the insertion (intercalation) of lithium ions for charge compensation. Li^+-ion shuttling between the cathode and anode is enabled through the liquid electrolyte using an organic solvent. Both graphite and lithium cobalt oxide allow the intercalation of the small lithium ions into their interplanar structural layers, as depicted in **Figure 7**. The resulting electromotive force is between 3 – 4 V, depending on the state-of-discharge. An intercalation-type active material considered for a battery application must allow reversible ion insertion and extraction with minimal to no corresponding lattice deformation for a long cycling lifetime. Furthermore, the material must

support mixed ion and electron conduction.[116] The underlying kinetics and mass transport properties largely determine the fast-charging capability, which will be further discussed in the next section.

2.2.3 Charge-Discharge Characteristics

As discussed in great detail by M. D. Levi and D. Aurbach, the intercalation phenomenon can be described in analogy to an ion-adsorption process.[141] To understand this, we first need to establish the following properties of an intercalation reaction as represented for a cation A^+ into an empty host intercalation site $[\ ]_{host}$ as in **Equation 16**, with the number of transferred electrons $n = 1$ per intercalated ion:[142]

$$A^+ + e^- + [\ ]_{host} \rightarrow [A]_{host}$$
$$X = \frac{[A]_{host}}{[\ ]_{host} + [A]_{host}} = f(E) \qquad \textbf{Equation 16}$$

Accordingly, guest ions can occupy a fixed number of intercalation sites within the host lattice, and the relative occupation X is related to the electrode potential. For a cathode material, which is considered as fully charged in its maximum deintercalated state, the relative occupation resembles its state-of-discharge (X = SOD = *1* – SOC), with 0 < SOD < 1. Naturally, the SOD is inversely related to the state-of-charge (SOC). Treating the intercalation material as a quasi-metal, one can expect that the electrode potential remains constant within its extension and drops at the electrode-electrolyte interface. This is in great similarity to the electrical double layer effect discussed in **Section 2.1.2**. Therefore, the three-dimensional, spatially distributed intercalation sites within the lattice can be treated in analogy to ion-adsorption sites. Assuming that all lattice intercalation positions are equal and the interaction between intercalation sites/ions can be neglected, the equilibrium electrode potential E_{eq} is described in analogy to the Nernst equation using the Langmuir adsorption isotherm (see **Equation 17**):[141,142,143]

$$E_{eq} = E_0' + \frac{RT}{F} \ln\left(\frac{1 - X}{X}\right) \qquad \textbf{Equation 17}$$

As before, E'_0 can be identified as the equilibrium potential of the electrode with an equal amount of empty and occupied intercalation sites, which corresponds to SOC = 50%. **Figure 8** shows an exemplary intercalation isotherm for an ideal, single-phase active material considered as cathode, as expressed by the indicated (dis)charging directions. It is entirely equivalent to the charge-discharge characteristics (potential *vs.* charge plot) for an electrode

which transitions from SOD = 0 to SOD = 1 under current flow along continuous quasi-equilibrium states. Such a process is also called "Nernstian", with totally reversible kinetics.

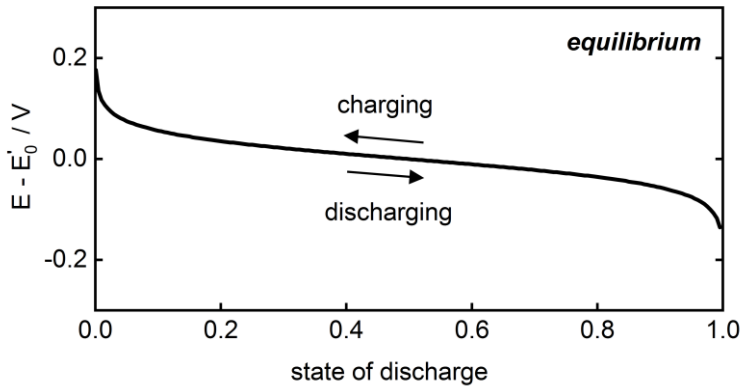

***Figure 8**. Exemplary intercalation isotherm according to **Equation 17**.*

So far, we have neglected that the flow of faradaic current inevitably requires the transfer of charge, as well as the transport of reactants. Therefore, a non-negligible overpotential (see **Equation 12** in **Section 2.1.3**) is usually observed during the charge and discharge processes of a battery electrode. The associated characteristics are described by non-equilibrium kinetics. A very comprehensive treatment of potential rate limitations resulting charge-discharge characteristics is provided in refs. 142, 143 and 144. A brief, phenomenological excerpt strongly aligned with the mentioned sources will be provided in the following. For the sake of fluid readability, not every instance will be referenced. Without the restriction of generality, the following introduction will focus on active materials with $n = 1$.

First of all, the flow of faradaic current associated with an intercalation process requires the transfer of electrons from the current collector to an active material redox center, as well as the insertion of a cation from the solution into the host lattice. Both processes are coupled to each other and involve an interfacial charge transfer across the boundary of two different phases, which is associated with a certain activation barrier that needs to be overcome. The resulting dependence of the charge-transfer overpotential η_{ct} (also called activation overpotential) on the current i can, phenomenologically, be described in terms of Butler-Volmer kinetics (see **Equation 18**) as schematically illustrated in **Figure 9A**.[118]

$$i = i_+ + i_- = i_0 \cdot \left[\exp\left(\frac{\alpha F}{RT}\eta_{ct}\right) - \exp\left(-\frac{(1-\alpha)F}{RT}\eta_{ct}\right)\right] \qquad \textbf{Equation 18}$$

$$\text{with} \quad \frac{i_0}{S} = j_0 = Fk_0(c_{ox}^*)^{\alpha}(c_{red}^*)^{1-\alpha}$$

The transfer coefficient $0 < \alpha < 1$ describes the symmetry of the activation barrier between the potential energy curves of the initial and final states and is usually close to 0.5. Furthermore, S is the total active material surface, and k_0 is the apparent rate constant, which contains information on the activation energy for the specific redox system as well as the concentration of the intercalate in the electrolyte. A high activation barrier for charge transfer leads to a small k_0 and therefore a small i_0 and *vice versa*. The value of the exchange current density j_0 is equal to the current density in anodic (j_+) and cathodic (j_-) directions in equilibrium ($\eta_{ct} = 0$), where $j = j_+ + j_- = 0$ and therefore $j_{+,eq} = |j_{-,eq}| \equiv j_0$. In general, j_0 strongly depends on the surface concentration of oxidized and reduced active redox centers (c^*_{ox} and c^*_{red}), where an oxidized center refers to an unoccupied intercalation site in the lattice and *vice versa* for a reduced center. In the absence of concentration gradients ($c^* = c^{bulk}$), the surface concentrations are directly linked to the state-of-discharge, and therefore the electrode potential, as given by **Equation 19**:[143]

$$c^*_{ox} = (1 - X) \cdot \frac{\rho}{M} \quad \text{and} \quad c^*_{red} = X \cdot \frac{\rho}{M} \qquad \textbf{Equation 19}$$

Here, ρ is the density of the active material, and M is its molar mass. Therefore, ρ/M is equal to the total concentration of intercalation sites in the electrode material in the case of one intercalation site existing per unit-formula. It follows that the exchange current density is maximum when SOC = SOD = 50%. As seen in **Figure 9B**, the charge transfer polarization causes a SOD-dependent hysteresis of the charge-discharge curves. However, the obtainable capacity remains mostly unchanged if the allowed electrode potential window is large enough.

It is important to note that the exchange current density is a system-specific property, *i.e.*, a constant for a given electrode material in a given electrolyte (ρ/M and k_0), which does not depend on the amount of material. However, the absolute exchange current is proportional to the total active material surface. Therefore, suppose the latter is increased by adding more material, i_0 will also increase, which results in a smaller overpotential for a given absolute current because i/i_0 gets smaller. Or, if this is put the other way, an active material geometry with a high area-to-mass ratio (for example, many small nanoparticles or a thin film *vs.* one single large particle with the same mass) will be more beneficial from a kinetic point of view. A system with facile kinetics (large k_0 and/or S, therefore large i_0) will only require a small overpotential to unbalance the current flow in equilibrium and effectively drive a large net current in the direction of the slight overpotential. In this case, we return to the equilibrium charge-discharge curve (current flow along continuous quasi-equilibrium states). In contrast, a

process with very sluggish kinetics (small k_0 and/or S, therefore small i_0) and a resultingly large activation overpotential is called totally irreversible.[119] This term should not be confused with the fact that a reaction can still be chemically reversed, *i.e.*, forced back to its initial state by reversing the current and accepting an (equally) high overpotential in the other direction.

So far, we have assumed that the mass transport properties of the investigated electrode-electrolyte system are very fast and can therefore be neglected. For an intercalation reaction to proceed, cations from the electrolyte need to cross the interface ($x = 0$) into an empty lattice site and move further into the bulk electrode by ionic diffusion as the determinant transport mechanism. This process proceeds until they ultimately reach the "deepest" intercalation site at the current collector interface in the case of a thin-film or the center of a particle ($x = l$). Accordingly, the flow of faradaic current is associated with a concentration gradient of the intercalate extending from the electrode surface into the material bulk, as described by Fick's first law (**Equation 20**):[118,142]

$$c^* = c_x = c^{bulk} \text{ with } 0 \leq x \leq l \qquad \text{for } t = 0$$
$$i = FS \cdot D \left(\frac{\partial c}{\partial x}\right)_{x=0} \quad \text{and} \quad \left(\frac{\partial c}{\partial x}\right)_{x=l} = 0 \qquad \text{for } t > 0$$

Equation 20

Here, D is the diffusion coefficient of a species in a specific phase, c^{bulk} is its concentration in the bulk of the phase, and c^* is its concentration at the electrode-electrolyte interface. For solid-state diffusion (*i.e.*, diffusion of intercalated ions inside the active material host), the concentration gradient at the center of a particle or at a current collector - thin-film interface ($x = l$) must vanish as expressed by the boundary condition for **Equation 20** (finite-length diffusion, reflective boundary). Assuming very fast charge transfer kinetics, the anodic (during oxidation) electrode potential is expressed by **Equation 21**:

$$E = E_{eq} + \frac{RT}{F} \ln\left(\frac{c^*}{c^{bulk}}\right) = E_{eq} + \eta_{diff} \qquad \textbf{Equation 21}$$

Mass transport limitations therefore result in a diffusion overpotential η_{diff}, which is related to the ratio c^*/c^{bulk}. The dependence of the diffusion overpotential on the current is schematically shown in **Figure 9C**, which reveals only a rather moderate deviation from the equilibrium potential at a specific SOD up to a certain current, where the overpotential suddenly increases drastically.

For the herein-discussed case of thin-film intercalation-type battery electrodes, the planar diffusivity of ions in the liquid electrolyte bulk is usually sufficient (*D* large) and can therefore be neglected, as the concentration profile can be considered constant. Furthermore, electrolytes usually contain a high concentration of intercalating ions. Therefore, their concentration at the surface is easily replenished. These assumptions can potentially become invalid in the case of porous electrolyte diffusion in composite-type or nanostructured electrodes. In comparison, the solid-state diffusion of an inserted cation is usually significantly lower (*D* small) and can therefore lead to the buildup of a concentration gradient within the solid electrode. Considering an exemplary case of electrode reduction, we will initially have an entirely empty lattice. If now cations start being inserted at a rate higher than they can diffuse away from the interface towards the electrode bulk, their surface concentration will significantly rise, while the concentration of empty sites decreases accordingly. As a result, the electrode potential appears to be lower than E_{eq}. Similar considerations explain an increase in the electrode potential during oxidation. This is schematically shown in **Figure 9D**. In general, two types of diffusive behavior regimes can be differentiated for the transport of an intercalate within a solid host material: semi-infinite diffusion, as long as the concentration gradient does not reach the center of a particle or the current collector in the case of a thin film, and finite diffusion beyond this point. In the case of too high currents, uncomplete (dis)charging can be observed. For a desired (dis)charging time τ, the maximum active material dimension l for full utilization can be estimated by **Equation 22**:[144]

$$l < \sqrt{D \cdot \tau} \qquad \textbf{Equation 22}$$

Accordingly, the material size should be as small as possible to achieve fast rates. Nevertheless, for an exact treatment c^* and c^{bulk} must be known, which are strongly time-dependent. The exact shape of the charge-discharge curve will depend on the specific applied conditions (*e.g.*, potential or current control). In general, the *E(t)-i(t)-SOC(t)* and deduced rate capability characteristics can be obtained by solving Fick's second law (see **Equation 23**) with the respective boundary conditions.

$$\frac{\partial c}{\partial t} = D \frac{\partial^2 c}{\partial x^2} \qquad \textbf{Equation 23}$$

This will, however, not be discussed in more detail herein and the interested reader is referred to the literature.[118,119,144,145] For the case of vanishing concentration gradients (fast transport

properties) and facile charge transfer kinetics, we return to the equilibrium intercalation isotherm.

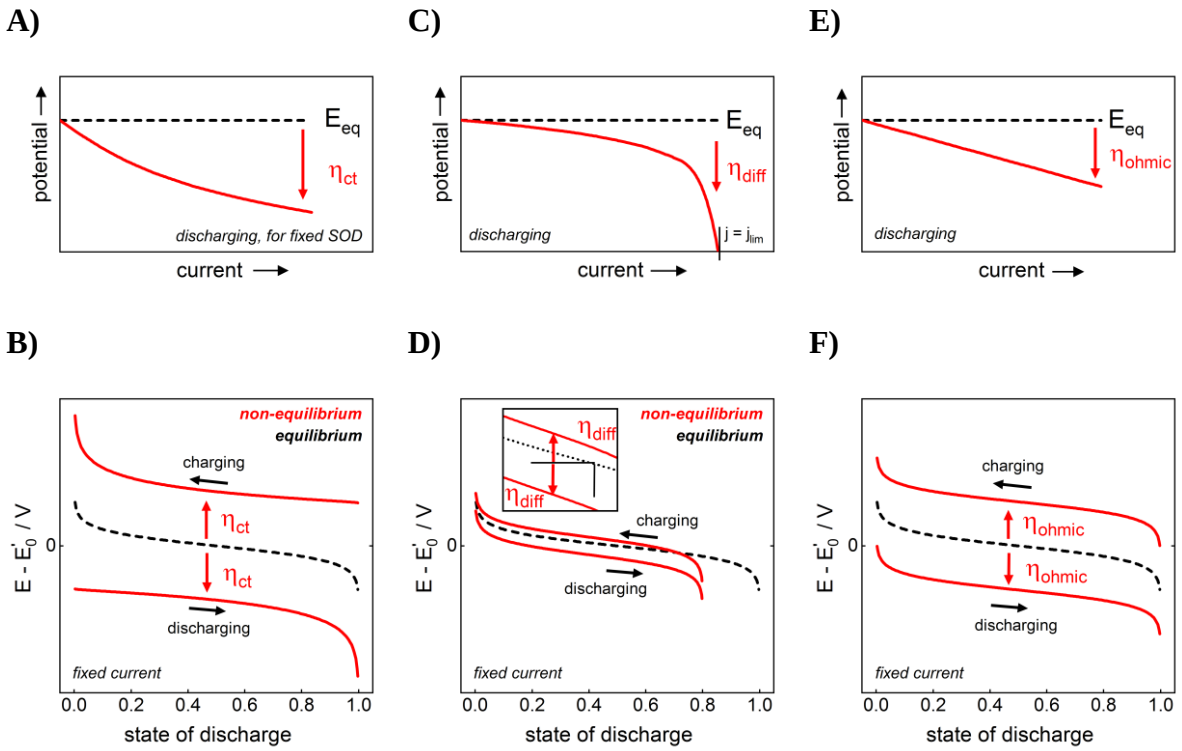

***Figure 9**. (**A**,**C**,**E**) Schematic illustration of the different contributions to polarization for an intercalation-type battery electrode as a function of the current. (**B**,**D**,**F**) Resulting schematic deviation of the charge-discharge curves from equilibrium.*

Lastly, it should be mentioned that the flow of current will, in any case, lead to an ohmic deviation of the potential, which increases linearly with the current according to **Equation 24** (see **Figure 9E**):

$$\eta_{ohm} = i \cdot R_i \qquad \textbf{Equation 24}$$

The ohmic polarization is characterized by the internal resistance R_i. This is mainly associated with the conductivity of the electrolyte and leads to a constant down- or upwards shift of the discharge and charge curves regardless of the SOD (**Figure 9F**).

The total deviation of the electrode potential from its equilibrium value at a given SOD is the sum of the individual contributions according to **Equation 25**:

$$\eta_{total} = \eta_{ct} + \eta_{diff} + \eta_{ohm} \qquad \textbf{Equation 25}$$

For active materials involving the formation of a so-called solid-electrolyte-interphase (SEI), multistep reaction pathways or nucleation processes, their respective contributions must also be considered, which will however be omitted here. The process (charge transfer or mass transport), which mostly determines the charge-discharge characteristics of a battery electrode, is called rate-limiting, as the slowest process constitutes the maximum current for an accepted total overpotential. Nevertheless, it should be noted that individual overpotentials might be interdependent, especially in the case of mixed rate control. Further treatment of the experimentally available diagnostic features for the specific rate limitations will be discussed in **Section 3.1**.

For a battery, the respective overpotentials of the cathode (cat) and anode (an) add up. The total voltage *U* is given in **Equation 26**:

$$U = E_{cat} - E_{an}$$
$$U_{discharge} = U_{oc} - \left(\eta_{ct,cat} + \eta_{ct,an} + \eta_{diff,cat} + \eta_{diff,an}\right) - |i|R_i$$
$$U_{charge} = U_{oc} + \left(\eta_{ct,cat} + \eta_{ct,an} + \eta_{diff,cat} + \eta_{diff,an}\right) + |i|R_i$$

Equation 26

2.2.4 Electrolyte Considerations

The employed electrolyte has a strong impact on the characteristics of a battery. Its likely most important property is the stability of the active material in the electrolyte, which is one of the main research topics of this work. Another essential aspect is the so-called stability window, which reflects the potential range where the electrolyte can be considered inert.[146] Beyond these limits, faradaic reactions decomposing the solution's constituents set in. For organic LIBs, this commonly leads to the formation of an SEI at the anode during the initial cycles. While this process is accompanied by irreversible loss of capacity (≈ 10%) and results in impaired kinetics, it also protects the electrolyte from further decomposition.[147,148] The main disadvantage of organic electrolytes, however, is safety concerns related to their flammability.[149]

Aqueous electrolytes are a low-cost, safe, and environmentally friendly alternative, but they come with inherently smaller attainable voltages.[60] The choice of electrode materials is limited by the oxygen evolution reaction at the cathode and the hydrogen evolution reaction at the anode side. Thermodynamically, the theoretical voltage limit for a battery is therefore 1.23 V (see **Table 1**). As a result, the individual electrode potentials must remain within these pH-

dependent limits to avoid parasitic currents stemming from the electrolyte decomposition. Practical stability windows in conventional aqueous solutions can reach up to ≈ 2.0 V due to sluggish water decomposition kinetics at the electrodes and other effects.[60,150,151] Nevertheless, the real operational voltage still depends on the accepted rate of persistent parasitic OER/HER currents.[152,153] In general, it is especially challenging to inhibit the HER for the use of low-electrode-potential anodes, whereas the OER is usually rather sluggish by itself, allowing the operation of high-electrode-potential cathode materials.[154]

Promising advances to increase the real stability window > 2.0 V involve the usage of highly-concentrated, so-called "water-in-salt", electrolytes.[59,150,155,156,157,158] Some of these support the formation of SEI-like protective layers on electrodes even in aqueous media under the decomposition of organic fluorinated anions. Compared to such rather costly salts, $NaClO_4$ is considered an effective candidate.[159,160,161,162,163] The widened electrochemical stability of highly-concentrated non-SEI forming electrolytes involving $NaClO_4$ or $LiNO_3$ solutions is mainly ascribed to the absence of free water molecules and the strong interaction of the electrolyte species, which increase the kinetic barrier for electrochemical solvent decomposition.[159,164,165] Another beneficial side-effect of highly concentrated $NaClO_4$ solutions is its significantly lowered freezing point, allowing a wide operational temperature range for the battery.[166] Furthermore, it effectively reduces the dissolution of active electrode materials, as discussed in **Section 6.3.2.3**. Another approach involves the concept of so-called "molecular crowding", where water molecules are virtually confined by the use of a crowding agent as an additive in the electrolyte to reduce their activity toward decomposition reactions. A voltage window above 3 V could be achieved in low-concentrated LiTFSI with 94% polyethylene glycol as an additive.[167] This strategy has been investigated for use in aqueous Na^+-electrolytes in the advised Master's thesis research project by A. Grasser,[168] which will however not be further discussed in this thesis.

Furthermore, as already discussed in **Section 2.2.3**, an important property of a battery is its internal resistance, which is usually dominated by the electrolyte as given by **Equation 27**:[118]

$$R = \rho_s \frac{L}{A} \qquad \textbf{Equation 27}$$

Here, L is the distance between the two electrodes, and A is the geometric area perpendicular to the current flow. The resistivity of the solution ρ_s is the inverse of the ionic conductivity κ. For practical batteries, κ should at least be a few mS/cm over the entire operating temperature

range,[169] which is easily met by reasonably concentrated aqueous solutions. For example, the conductivity of aqueous 8 M $NaClO_4$ is ≈ 140 mS/cm at 25°C.[170] For comparison, the conductivity of 1 M $LiPF_6$ in organic solvents typical for LIBs is around 10 mS/cm at room temperature.[117,171] The diffusion coefficient of alkali metal cations in the electrolyte is usually in the order of 10^{-6} cm^2/s under battery-relevant conditions.[143,172] Again, for the specific case of Na^+ diffusivity in aqueous 8 M $NaClO_4$, $D_{Na+} \approx 0.4 \cdot 10^{-5}$ cm^2/s was found.[164] Apart from this, a good wettability of the electrolyte with the electrodes is also an important aspect.[173]

Further considerations regarding an aqueous electrolyte involve the choice of a suitable, electrochemically inert current collector. For organic LIBs, copper and aluminum are usually used for the anode and cathode, respectively.[174] However, corrosion is an intrinsic threat to many metallic substrates in aqueous media. Whereas gold serves well for research applications, its high cost prevents usage for real-world systems, where rather stainless-steel or titanium are considered, as aluminum is not stable over a wide pH range even at only moderate cathode potentials.[60,175,176] Recently, there has also been increasing interest in carbon-based current collectors for electrochemical applications due to their flexibility, light weight, potentially low cost, and large specific surface area.[177,178]

2.2.5 Metrics and Performance Indicators

A couple of experimentally available properties will be presented in the following along refs. 116, 140 and 173 to allow an understanding of the terms and quantities used in this work.

The capacity Q of an electrode during (dis)charging is obtained according to **Equation 28**:

$$Q = \int i(t) \cdot dt \qquad \textbf{Equation 28}$$

For constant current conditions, the so-called C-rate is defined by **Equation 29**:

$$C\text{-}rate = \frac{i}{Q_{max}}, \quad 1\mathrm{C} = \frac{1}{\mathrm{h}} \qquad \textbf{Equation 29}$$

A rate of 1C corresponds to a time of 1 hour for full charge or full discharge. Q_{max} should be measured at a low rate where no limitations are observed. Q can significantly drop at high rates due to mass transport limitations (see **Section 2.2.3**). The rate capability describes the capacity retention for different applied rates. A high share of the theoretical capacity should be available up to very high C-rates for fast-cycling capability. For comparison, the time needed to refuel a

car with gasoline is ≈ 5 minutes, which corresponds to a rate of 12C for charging a battery. The coulombic efficiency (CE) represents the ratio of *Q* during electrode discharging compared to charging. It is defined according to **Equation 30** and is significantly affected by parasitic currents in the cell, for example, from electrolyte decomposition or other side reactions.

$$CE = \frac{Q_{discharging}}{Q_{charging}} \quad \rightarrow \text{ cathode: } CE = \frac{Q_{red}}{Q_{ox}}, \text{ anode: } CE = \frac{Q_{ox}}{Q_{red}} \qquad \textbf{Equation 30}$$

The specific capacity q_{max} relates the total capacity Q_{max} to the mass of active material (see **Equation 31**), and its theoretical value can be estimated from the reaction equation taking the number of involved electrons per unit formula.

$$q_{max} = \frac{Q_{max}}{m_{active}} \qquad \textbf{Equation 31}$$

During (dis)charging, the ratio of the specific charge *q* (also the total charge *Q*) and q_{max} (also the total capacity Q_{max}) yields the SOD, from which the lattice occupation *X* can be obtained (SOD = *X* for a cathode material, SOC = *X* for an anode material):

$$q = q_{max} \cdot SOD \text{ and } Q = Q_{max} \cdot SOD \qquad \textbf{Equation 32}$$

The stability of an electrode is assessed by the evolution of the available capacity over a continuous number of cycles and/or time. It therefore reflects how often a battery can be cycled. Often, the number of cycles until 80% capacity remains is considered as an important benchmark. Usually, the dissolution/loss of active material leads to an irreversible capacity loss. The self-discharge of an electrode is observed as the evolution of the potential over time under open-circuit conditions since the potential reflects the SOD *via* **Equation 17**.

The open-circuit voltage of a battery was already introduced above (see **Equation 14**). It should be as high as possible by combining active materials with a high standard potential for the cathode and a low standard potential for the anode. However, these must remain within the stability window of the electrolyte. Without optimized electrolytes (see **Section 2.2.4**), the achievable voltage is limited to 1 – 2 V for ASIBs compared to ≈ 4 V for "traditional" LIBs. Due to the time-variant battery voltage under operation, the (dis)charging power *P* can be given at SOC = 0.5 (see **Equation 33**):

$$P = V_{SOC=0.5} \cdot i \qquad \textbf{Equation 33}$$

The energy *W* provided by or stored in a battery is calculated according to **Equation 34**:

$$W = \int_{SOC=0}^{SOC=1} V(Q) \cdot dQ \approx V_{SOC=0.5} \cdot Q \qquad \textbf{Equation 34}$$

Energy efficiency is the ratio of the output energy yielded during discharge and the input energy needed for charging. Due to the overpotentials observed at the cathode and anode (see **Section 2.2.3**), a higher voltage is required for charging the cell than the voltage provided during discharging (see **Equation 26**). Therefore, the energy efficiency can be significantly smaller than 100% depending on the specific rate-limiting processes and the internal resistance. A low coulombic efficiency translates into even lower energy efficiency.

The capacity, energy, and power can be represented as their respective gravimetric densities by dividing by the total active material mass or by the total volume to obtain their volumetric characteristics. However, for a comparison beyond the active materials on a so-called cell-level, the masses of the electrolyte, current collector, and inactive electrode components, as well as the housing, must be considered and can significantly lower the final power and energy density of a battery. The exact factor strongly depends on the battery technology, cell geometry, and loading. However, as a rule of thumb, a reduction of 50% of the specific values can be assumed when going from the pure active-material level (reversibly obtained capacity, not theoretical) to the cell level. The system/pack-level involves the assembly of many cells in their final application (for example, in a car or a stationary storage system) and comprises additional components like cooling, structural elements or electronics, which add additional weight and further reduce the gravimetric characteristics.[94,179,180]

3 Techniques and Methods

3.1 Electrochemical Techniques

All described techniques refer to the usage in a three-electrode configuration, which allows both measuring and controlling the potential of the working electrode (WE) with regard to a fixed potential reference. While the latter is established by a reference electrode (RE), all current is entirely provided or sunk by a counter electrode. The WE potential is usually reported against the employed reference, for example, *E vs*. SSC for a silver-silver chloride RE. Furthermore, the explanations in this chapter will focus on applying the techniques in battery research. The descriptions and explanations are primarily based on the standard textbooks "Elektrochemie" by C. H. Hamann and W. Vielstich[118] and "Electrochemical Methods: Fundamentals and Applications" by A. J. Bard and L. R. Faulkner.[119]

3.1.1 Cyclic Voltammetry

Cyclic voltammetry (CV) is a potentiodynamic technique widely used in electrochemistry, as it is a fast and straightforward way to investigate an electrochemical system.[181] It is helpful to quickly determine the potential range of redox activity for an electrode immersed into an electrolyte or assess the stability window of an electrolyte. It further provides insights into the reversibility and stability of electron-transfer initiated processes and allows drawing conclusions on the kinetic properties of a system. In general, the potential E of the WE is linearly ramped over time at a specific rate (scan rate $v = dE/dt$) between a lower and upper potential vertex, reversing its direction when hitting the vertices (see **Figure 10A**). The resulting current i is plotted against the applied potential, which yields the so-called cyclic voltammogram as shown in **Figure 10B**.[119] It should be noted that CVs represent the overall response of the system to a variation of the electrode potential, which involves (possibly overlapping) faradaic currents next to capacitive currents from double-layer charging. Following the commonly used IUPAC convention, the potential is shown on the x-axis from low to high values, referring to positive currents for oxidation (anodic scan) and negative currents for reduction (cathodic scan).

Interesting diagnostic features that can be obtained from cyclic voltammetry are the peak current values $i_{p,ox/red}$ with the associated potentials of peak current $E_{p,ox/red}$ and the corresponding peak-to-peak separation ΔE_{pp}. In general, both the value and position of the

current waves' maximum can be a function of the scan rate. For the peak current this is relation represented in **Equation 35** using the two arbitrary factors *a* and *b*:[182,183]

$$i_{p,ox/red} = b \cdot \nu^a \rightarrow \log(i_{p,ox/red}) = a \cdot \log(\nu) + \log(b) \qquad \textbf{Equation 35}$$

The transferred charge *Q* is shown against the potential in **Figure 10C**. Its extrema indicate the potentials of complete oxidation or reduction of the investigated species available for reaction at the electrode. The half-charge potentials $E_{1/2,ox/red}$ are obtained at 50% SOC of the battery material.

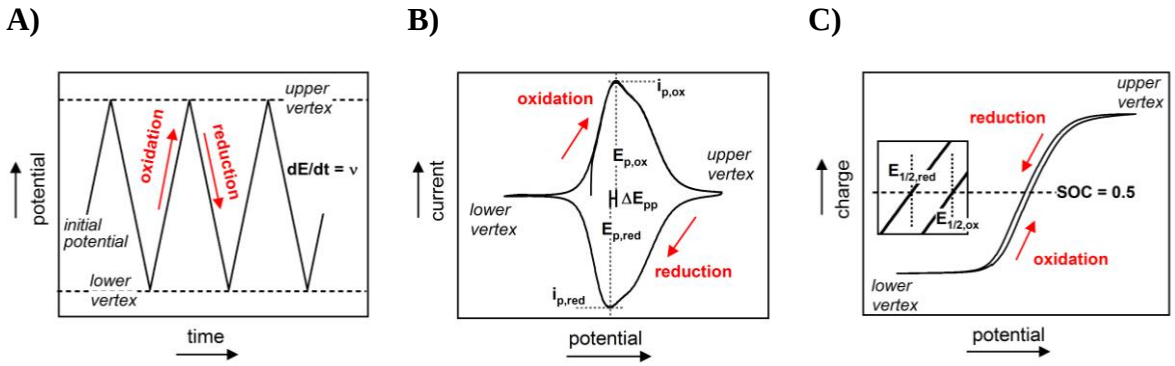

***Figure 10**. Cyclic Voltammetry: imposed potential vs. time (**A**), typical cyclic voltammogram showing the resulting current waves vs. potential (**B**) and transferred charge vs. potential (**C**) curves.*

In battery research, CV can be a powerful tool to investigate kinetics and transport limitations during (dis)charging, especially when it is subsequently probed by various scan rates. According to the rate-limiting processes described in **Section 2.2.3**, the following cases will be distinguished for the analysis of the systems' response in this work. In the ideal case, without any mass transport limitation, a linear relationship between the peak current and scan rate (a = 1) is obtained. Furthermore, a high symmetry of the cathodic and anodic curves with vanishing peak-to-peak separation is characteristic for reversible reaction rate control in quasi-equilibrium (fast kinetics). If the system is controlled by slow mass transport, *e.g.*, the diffusion of intercalated species in the bulk of the solid electrode, the linear dependency of the peak current on the scan rate breaks down (a = 0.5). This is accompanied by a peak-to-peak separation of up to 59 mV at 25°C and the appearance of an asymmetric current decay after the peak. For the case of slow charge transfer, the peaks' height is still proportional to the scan rate. While the overall shape of the anodic and cathodic waves remains undisturbed, increasing the scan rate results in an increasing peak-to-peak separation (irreversibility). Mixed

intercalation rate control refers to the case when both mass transport and charge transfer kinetics proceed on similarly slow time scales to contribute to rate limitations.[119,142,184]

3.1.2 Galvanostatic Cycling

Galvanostatic cycling (GC) is a constant-current technique that is also part of the standard charging protocols of batteries in commercial applications (so-called "CCCV" protocol, meaning constant current during initial charging, followed by a constant voltage period).[185] A constant current is applied to the electrode for a certain time interval (see C-rate, **Equation 29**) while recording its potential (see **Figure 11A**).[119] The available capacity of the active material determines the duration of the current pulse. **Figure 11B** correlates the electrode potential to the transferred charge. The charge-discharge potential hysteresis, which strongly depends on the applied current, is determined at 50% state-of-charge respectively (see **Equation 36**) and serves as a measure for the total polarization η.

$$\Delta E_{1/2} = E_{1/2,charge} - E_{1/2,discharge} \quad \text{and} \quad \eta = E - E_{eq} \approx \frac{\Delta E_{1/2}}{2} \qquad \textbf{Equation 36}$$

Similar to the cases described above for CV, several diagnostic features related to the limiting processes described in **Section 2.2.3** can be obtained from GC by current variation experiments. If the intercalation reaction rate is not limited by sluggish charge transfer or slow mass transport, the total capacity of the active material can be attained during cycling. Furthermore, the absence of respective overpotentials associated with these limitations leads to a hysteresis-free charge-discharge behavior. In this case, the half-charge potentials converge to the equilibrium intercalation potential curve. The equilibrium charge-discharge curves resemble the intercalation isotherm for a single-phase electrode material. If the system's response is governed by slow reactant diffusion, the available electrode capacity gradually decreases when increasing the imposed current. The concentration polarization slightly shifts the charge-discharge curves in the vertical direction. Charge transfer limitations due to sluggish kinetics result in a strong potential hysteresis caused by a significant electrode polarization at higher currents. The obtained capacity remains almost unchanged if the potential window for cycling is large enough to overcome the polarization and allow a complete material (dis)charge.[142,186]

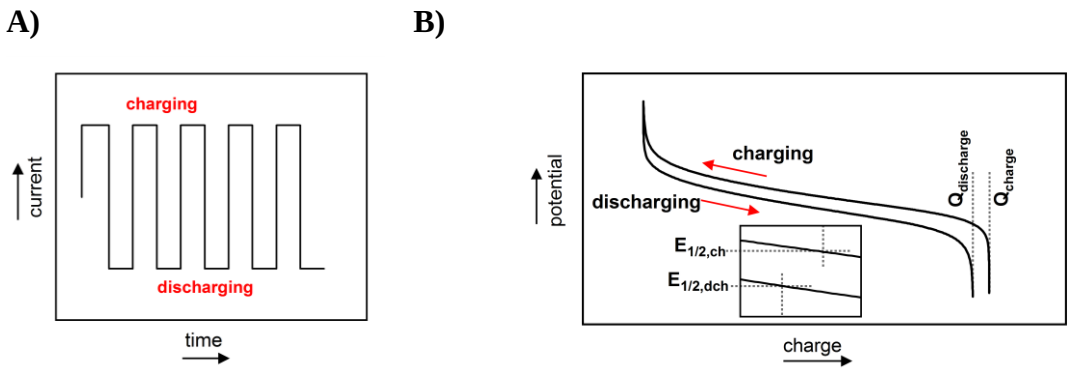

***Figure 11**. Galvanostatic cycling of a cathode material, where oxidation refers to charging and reduction to discharging: Imposed current vs. time (**A**) and a resulting charge-discharge curve showing the electrode potential vs. transferred charge (**B**).*

3.1.3 Electrochemical Impedance Spectroscopy

In battery research, electrochemical impedance spectroscopy (EIS) is a powerful method to study the processes occurring at the electrode-electrolyte interfaces. The technique is based on analyzing the response of a system in a steady state to a small-amplitude perturbation. Due to the different specific time constants of the individual (intermediate) steps of an electrochemical reaction, it is capable of isolating processes like double layer effects, adsorption, charge transfer or mass transport by varying the frequency of the probing signal from the MHz to mHz range. A model involving classical electrical network elements can represent the investigated system with its possibly unknown processes ("black box"). Mechanistic insights and system parameters can be obtained by finding and fitting such a physical model to interpret the (likely) complicated impedance response. The technique is schematically summarized in **Figure 12**. The reader is referred to the literature for further reading beyond the following introductory excerpt.[118,119,187,188,189]

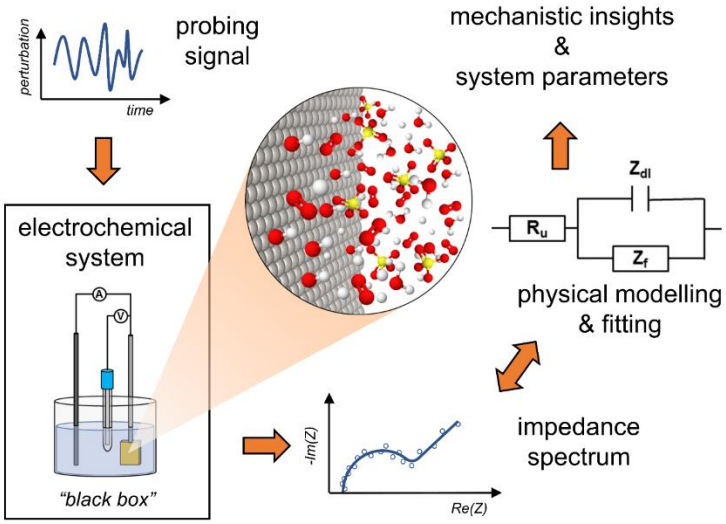

***Figure 12**. Overview of an EIS experiment. The response of an electrochemical system in steady-state to an external small-amplitude perturbation is analyzed using a physical model of the involved processes. Adapted and reproduced from ref. 190 with permission from the PCCP Owner Societies. Copyright © 2021, The Authors.*

3.1.3.1 General Principle

In potentiostatic electrochemical impedance spectroscopy (PEIS), a system is typically probed while holding a constant potential E_c. Initially, non-stationary currents will flow until the system equilibrates according to the applied potential (see **Figure 13A**). Once a steady state is reached, the electrode potential is modulated with a perturbating sinusoidal signal ΔE with an angular frequency ω and amplitude E_P as given by **Equation 37**:

$$E(t) = E_c + \Delta E(t) = E_C + E_P \cdot \sin(\omega t) \quad \text{with} \quad \omega = 2\pi f \qquad \textbf{Equation 37}$$

In general, the current-potential characteristics of an electrochemical system are very complex and highly non-linear. However, by choosing a sufficiently small amplitude E_P (usually a few mV), the current response of a stationary system can be linearized and therefore follows the perturbation with an amplitude I_P and a phase shift φ as described by **Equation 38**:

$$\Delta I(t) = I_P \cdot \sin(\omega t + \varphi) \qquad \textbf{Equation 38}$$

This linear response allows to calculate the impedance Z as shown in **Equation 39** in similarity to Ohm's law and by using complex expressions for the current and potential:

$$Z(\omega) = \frac{\Delta E(t)}{\Delta I(t)} = \frac{E_P \cdot \sin(\omega t)}{I_P \cdot \sin(\omega t + \varphi)} = Z_P \cdot (\cos(\varphi) + j \cdot \sin(\varphi))$$
$$= \mathrm{Re}(Z(\omega)) + j \cdot \mathrm{Im}(Z(\omega))$$
$$\text{with} \quad Z_P = \frac{E_P}{I_P} = |Z| = \sqrt{\mathrm{Re}(Z)^2 + \mathrm{Im}(Z)^2} = \sqrt{R^2 + B^2}$$

Equation 39

Accordingly, the impedance can be described by its real part (Re(*Z*)), the so-called resistance *R*, and imaginary part (Im(*Z*)), the so-called reactance *B*, as well as its magnitude |*Z*| and the phase shift φ. The imaginary unit is represented by *j*. Generally, a purely reactive load causes a phase-shift of 90° between the current and voltage while no power is dissipated. The current through a purely resistive load always follows the voltage, therefore active power is transferred. Usual graphical representations of the impedance involve a Nyquist plot (-Im(*Z*) *vs*. Re(*Z*)) or Bode plot (log(|*Z*|) and φ *vs*. log(*f*)). The self-consistency and validity of the acquired impedance spectra can be assessed by the so-called Kramers-Kronig (KK) check using software for impedance data analysis.

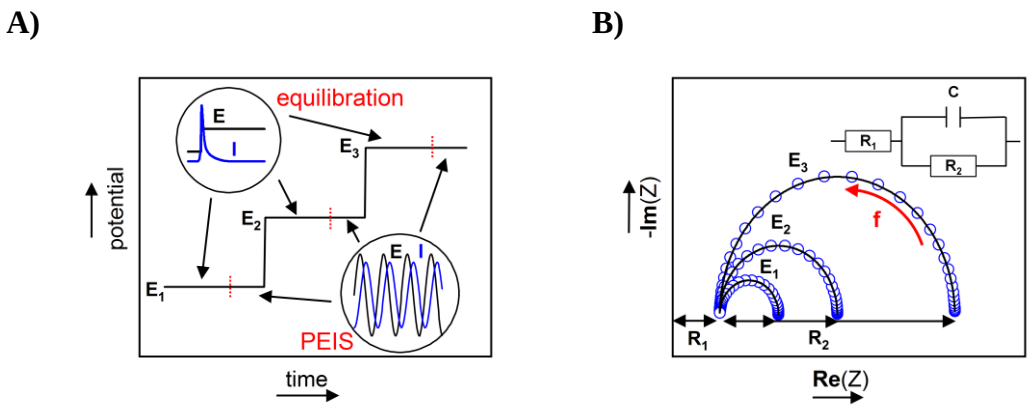

***Figure 13**. Potentiostatic impedance spectroscopy: (**A**) Applied staircase potential with equilibration and perturbation periods. (**B**) Impedance spectra in a Nyquist-plot representation of an arbitrary electrical circuit with the constant resistance R_1 and capacitor C, while the magnitude of resistor R_2 depends on the electrode potential.*

In analogy to an electric network, the overall impedance of an electrochemical system can be modelled by an electrical equivalent circuit (EEC). The impedance response of an arbitrary EEC is exemplarily shown in **Figure 13B**, which consists of a capacitor *C* and two resistors R_1 and R_2, where R_2 is potential-dependent. Whereas the parallel connection of R_2 and *C* (*RC*-element) yields a semicircle with a diameter of R_2, the spectrum is shifted on the Re(*Z*) axis by the series resistance R_1. In general, a variety of empirical EECs can fit an impedance response. It should, however, be kept in mind that such a model must describe the physico-chemical

processes of the investigated system to allow drawing conclusions or calculating quantities from its results. In contrast to an empirical EEC, which might be able to perfectly fit the data without having physico-chemical meaning, a physical EEC is built from a mechanistic understanding and is evaluated and verified by fitting the data. The approach of modelling by means of a physical EEC can either help to understand the unknown mechanisms of an electrochemical reaction ("black box") and/or extract kinetic parameters and other properties of the investigated system from a (known) model.[191] Impedance spectra are usually fitted to an EEC employing available software to check for its applicability and determine the values of its constituent elements as, for example, described in ref. 192.

3.1.3.2 Modelling a Simple Electrochemical System

A large variety of physical EECs is discussed in the literature to describe complex electrochemical systems, including double layer effects, charge transfer, mass transport and adsorption.[187,190,193] In the following, a brief and simple description of the general approach is given. In the simplest case of an electrode immersed in an electrolyte under conditions where no electrochemical reaction occurs, current flow is associated with a capacitive charging of the double layer with the current passing through the ionically conducting electrolyte. The resistance of the solution is of a purely ohmic nature and can therefore be represented by a resistor R_u (uncompensated resistance in the case of a three-electrode configuration). Its value can be easily read from the Nyquist plot as the shift of the spectra on the Re(Z)-axis. The double-layer ideally behaves like an electrical capacitor and therefore C_{dl} is used for modelling. Consequently, the impedance of such an ideal polarizable electrode (blocking condition) is given by **Equation 40**, and its model is shown in **Figure 14A**:

$$Z = R_u + \frac{1}{j\omega C_{dl}} \qquad \textbf{Equation 40}$$

For conditions that allow faradaic reactions (non-blocking condition) to occur, an associated faradaic current can be observed, which in general can depend on the electrode potential E, surface concentration of redox species $C_{ox}(0)$ and $C_{red}(0)$ or surface coverage of adsorbed intermediate reactants θ. The potential perturbation applied during an EIS experiment will lead to a perturbation of the faradaic current, as well as the surface concentration and coverage. For a sufficiently small amplitude of the perturbation signal, this dependence can be linearized (see **Equation 41**):

$$\Delta i = \left(\frac{\partial i}{\partial E}\right)\Delta E + \left(\frac{\partial i}{\partial c_{ox}}\right)\Delta c_{ox} + \left(\frac{\partial i}{\partial c_{red}}\right)\Delta c_{red} + \left(\frac{\partial i}{\partial \theta}\right)\Delta\theta$$
$$\text{with} \quad \left(\frac{\partial i}{\partial E}\right) = \frac{1}{R_{ct}(E)} \qquad \textbf{Equation 41}$$

Here, the charge-transfer resistance R_{ct} is a measure for the kinetic facility of the charge-transfer step. It results from the linearization of the Butler-Volmer equation for low overpotentials and is related to the potential-dependent exchange current ($j_0 \cdot S$) according to **Equation 42**.[194] For an intercalation reaction, the minimum of R_{ct} is obtained at $E_{SOC=50\%}$, because i_0 reaches its maximum at this potential.[143]

$$i \approx i_0 \frac{nF}{RT}\eta \quad \text{and therefore} \quad R_{ct}(E) = \frac{RT}{nFi_0(E)} \qquad \textbf{Equation 42}$$

In general, Δi can be obtained by calculating the respective partial derivatives, which can however become extremely complicated depending on the boundary conditions and specifics of the investigated reaction, including mass transport properties or intermediate/consecutive steps. For an overly simple reaction that neglects mass transport or adsorption effects, the faradaic path of impedance reduces to the charge-transfer resistance. The overall impedance of such a system is given by **Equation 43**:

$$Z = R_u + \frac{1}{j\omega C_{dl} + \frac{1}{R_{ct}}} \qquad \textbf{Equation 43}$$

The corresponding equivalent circuit is given in **Figure 14B**, where R_{ct} was, however, replaced by Z_f for a more inclusive representation of the faradaic impedance. In this general model, the faradaic current can be interpreted as a leakage of the double layer. This approximation dates to Randles[195] in 1947 and has been commonly used until today.

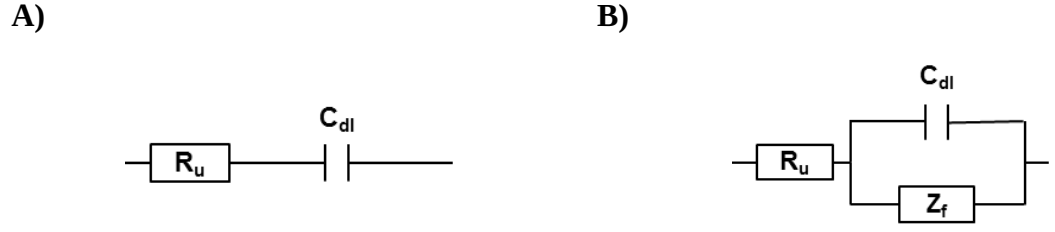

***Figure 14**. Simple EECs for an electrode immersed in an electrolyte (**A**) under blocking conditions and (**B**) under conditions that allow faradaic processes.*

Usually, the double-layer cannot be modelled by a simple capacitor, and it is therefore typically approximated by the so-called constant phase element (CPE) to account for its non-ideality. The impedance of a CPE is presented in **Equation 44**:

$$Z(CPE) = \frac{1}{P(j\omega)^n}$$
$$\text{with} \quad \alpha = 90° \cdot (1 - n), \quad 0 \leq n \leq 1 \quad \text{and} \quad [P] = F \cdot s^{n-1} \qquad \textbf{Equation 44}$$

Here, the exponent *n* describes the non-ideal phase shift α deviating from the usually expected 90° associated with a capacitor. *P* is related to the capacitance. For $n = 1$, the CPE behaves like a perfect capacitor, and for $n = 0$ like a pure resistor. The CPE can be conceived as a leaking capacitor, as it involves both a resistive (energy dissipation) and a reactive part (energy conservation). For a discussion of the origin of the CPE, the reader is referred to the literature.[196]

3.1.3.3 Physical Impedance Model for Intercalation-type Battery Electrodes

The following description of a physical model describing the impedance response of a wide range of intercalation-type battery electrodes is based on the work of Yun *et al.*[197,198] and Ventosa *et al.*[199] It has successfully been applied to various investigated systems, including the intercalation of Li^+, Na^+, K^+ or even Mg^{2+} into Prussian blue analogs from aqueous and organic solutions,[197,199,200,201,202,203,204,205] as well as the "traditional" LIB-materials graphite[206] and $LiFePO_4$[199] in common $LiPF_6$ – EC:DEC electrolytes. The underlying mechanism and EEC were discussed along with the role of physical EIS models in battery research in a published review article: "R. R. Gaddam, L. Katzenmeier, X. Lamprecht, A. S. Bandarenka. **Review on physical impedance models in modern battery research**. *Physical Chemistry Chemical Physics* **2021**, *23*(23), 12926-12944". A reprint of the article is attached in the appendix.

In the literature, the reversible deintercalation of alkali metal cations is usually represented as a single-step reaction, where the ion extraction immediately follows the electron transfer in the active material. This is exemplarily shown for the deintercalation of Na^+ from NiHCF in **Equation 45**:[54]

$$Na_2Ni[Fe^{II}(CN)_6] \rightarrow NaNi[Fe^{III}(CN)_6] + Na^+ + e^- \qquad \textbf{Equation 45}$$

However, it was argued by Yun *et al.*[197] that the underlying charge and mass transfer processes are likely more complex than represented by this simple description and rather follow a multistage mechanism involving at least three quasi-reversible steps. For the example of NiHCF, the deintercalation reaction is initiated by a fast electronic charge transfer leading to the oxidation of the iron centers (**Equation 46**):

step 1: $$Na_2Ni[Fe^{II}(CN)_6] \rightarrow Na_2Ni[Fe^{III}(CN)_6]^+ + e^- \quad \textbf{Equation 46}$$

The cation extraction cannot immediately follow due to the considerably slower solid-state diffusion in the host lattice, which leads to the appearance of excess surface charge at the electrode. This is intermediately balanced by the specific adsorption of highly mobile anions (A^-) from the electrolyte side on the electrode surface (**Equation 47**):

step 2: $$Na_2Ni[Fe^{III}(CN)_6]^+ + A^- \rightarrow \left[Na_2Ni[Fe^{III}(CN)_6]\right]^* A \quad \textbf{Equation 47}$$

Finally, the adsorbed anions desorb from the electrode surface once the cation has reached the interface and transfers into the solution (**Equation 48**):

step 3: $$\left[Na_2Ni[Fe^{III}(CN)_6]\right]^* A \rightarrow NaNi[Fe^{III}(CN)_6] + Na^+ + A^- \quad \textbf{Equation 48}$$

The impedance model of this multistep reaction, as proposed by Yun *et al.*[197] and Ventosa *et al.*,[199] is shown in **Figure 15A**. It is clearly seen that this EEC is, in its general form, similar to the generic EEC for any electrochemical process presented in **Figure 14B**. However, the faradaic impedance is replaced by the charge-transfer resistance R_{ct} and a ladder-type arrangement of two *GX*-elements to represent the intermediate reaction steps described above. The impedance of the circuit elements $G_{1,2}$ and $X_{1,2}$ is given in **Equation 49**:

$$Z(G_{1,2}) = G_{1,2} \quad \text{and} \quad Z(X_{1,2}) = \frac{1}{j\omega X_{1,2}} \quad \textbf{Equation 49}$$

Mathematically, $G_{1,2}$ and $X_{1,2}$ are equal to a resistor and capacitor and have the units Ohm and Farad. However, in contrast to these "real" circuit elements, they can take on negative values. This allows to fit the "loop"-shaped impedance spectra as obtained for some intercalation-type battery electrodes in the mid-to-low frequency region, as exemplarily shown in **Figure 15B**. In fact, such features have occasionally been observed in the past, as for example, for a commercial $LiCoO_2$/carbon cell from Sony as early as 2000,[207] but have mostly been ignored or considered as artefacts. As discussed above, they can, however, represent an important

characteristic to describe the physico-chemical behavior of intercalation-type battery electrodes. The overall impedance for this EEC is presented in **Equation 50**:

$$Z = R_u + \cfrac{1}{(j\omega)^{n\cdot Q} + \cfrac{1}{R_{ct} + \cfrac{1}{j\omega G_1 + \cfrac{1}{X_1 + \cfrac{1}{j\omega G_2 + \cfrac{1}{X_2}}}}}}$$

Equation 50

It must be kept in mind that the individual elements of the EEC are related to the complex rate equations of the interconnected multistep mechanism described above. A detailed, general treatment of faradaic reactions involving intermediate surface adsorbed species can be found in the literature.[187]

A) **B)**

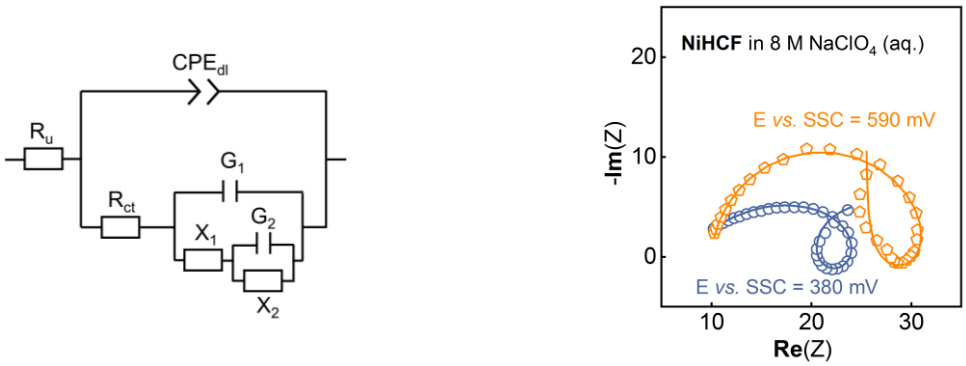

***Figure 15**. (**A**) EEC representing a physical model for the reversible intercalation of cations in battery materials involving the intermediate adsorption of electrolyte anions. (**B**) Exemplary impedance spectra fitted with the presented EEC.*

It should be noted that this model does not consider contributions to the impedance associated with the mass transport of charge carriers. This is related to the investigated frequency range in this work. Stationarity issues were usually observed during the experiments starting from a few hundred mHz downward. This can be explained by the electrode-electrolyte-geometry involving very low mass loadings (< 100 µg/cm^2) within the large electrolyte volume provided by the electrochemical cell (see **Section 4.1**) fostering parasitic side reactions (see **Section 7.4**). For analysis, only data with acceptable KK-check were considered. However, significant features in the Nyquist plot associated with solid-state diffusion are not expected above frequencies of approximately 100 mHz for the PBA thin-film electrodes investigated herein. This can be estimated using the diffusion coefficient of Na^+ within the PBA lattice (< 10^{-11} cm^2/s)[208] and the order of magnitude of the highest investigated film thickness *l* and, thereby, diffusion length (100 nm):

$$\frac{1}{\tau} = \omega_D = \frac{D_{Na^+,NiHCF}}{l^2} \approx 100 \text{ mHz}$$

Here, ω_D marks the characteristic frequency, where the diffusional regime transits from quasi-semi-infinite to reflective-boundary behavior within the confined active material dimensions. For $\omega \ll \omega_D$, the attainable penetration depth of Na^+ during probing exceeds the film thickness, and the active material is effectively filled and emptied during the impedance measurement. This would result in a straight vertical line in the Nyquist plot (φ = 90°), similar to the impedance response of a capacitor (reflective boundary). For $\omega \gg \omega_D$, the penetration depth is much shorter than the film thickness and the impedance theoretically approaches a semi-infinite-like behavior similar to a classic Warburg element (φ = 45° for planar case). However, such behavior is rarely observed in the measurements, which could be caused by overlapping with the frequency domain of the other processes involved in the introduced model for intercalation. It should be noted that non-planar or irregular diffusion geometries result in a significant deviation from φ = 45°. An extensive theoretical treatment of the solid-state diffusion impedance is available in ref. 209 from which the brief discussion presented above was extracted.

3.1.4 Electrochemical Quartz Crystal Microbalance

Electrochemical quartz crystal microbalance (EQCM) refers to the application of the quartz crystal microbalance technique in electrochemistry. By being able to resolve mass changes of an electrode precisely, it allows to monitor and analyze processes like electrodeposition, interfacial flux of species, dissolution, adsorption, or self-assembled monolayers.[210,211]

Its working principle is based on the piezoelectric properties of quartz crystals, which can react to an external electric field through mechanical deformation and *vice versa* relative to preferred crystallographic directions. As shown in **Figure 16A**, a standing thickness-shear wave can be stimulated by an external probing signal, which is applied across the crystal *via* opposing metal contacts (*e.g.*, evaporated gold). The material-dependent resonant frequency f_0 of the standing wave is inversely proportional to the thickness d_Q of the quartz crystal. It follows that a change of the thickness Δd_Q results in a proportional variation of the resonant frequency Δf_0 as elaborated in **Equation 51**.

$$f \propto \frac{1}{d} \quad \rightarrow \quad \frac{\partial f}{\partial d} = -\frac{f}{d}$$
$$\rightarrow \quad \frac{\Delta f_0}{f_0} = -\frac{\Delta d_Q}{d_Q}, \qquad d_Q = \frac{m_Q}{S_Q\,\rho_Q}$$

Equation 51

Here, m_Q is the mass of the crystal, S_Q is its area and ρ_Q the density of quartz. The amplitude of a standing wave is always maximum on the top and bottom of the oscillating plate. Its surface, therefore, only contributes to f_0 by its inertia, not by its elastic properties, as it is assumed to not experience any shear distortion. Correspondingly, a thin layer of a different material with a thickness of Δd_t can be treated as an extension of the quartz crystal, and by using **Equation 51** the Sauerbrey equation is obtained (**Equation 52**).

$$\Delta f_0 = -\frac{\Delta d_t}{d_Q} \cdot f_0 = -\frac{1}{d_Q\,S_Q\,\rho_Q} \cdot f_0 \cdot \Delta m_t = -c_f \cdot \frac{\Delta m_t}{S_Q}$$

Equation 52

The areal mass loading $\Delta m_t/S_Q$ of a thin layer on top of the crystal surface can therefore be obtained by measuring the reduction of the resonant frequency Δf_0 as described below. The sensitivity factor c_f is a material constant for the used quartz crystal independent of the investigated thin layer.[212]

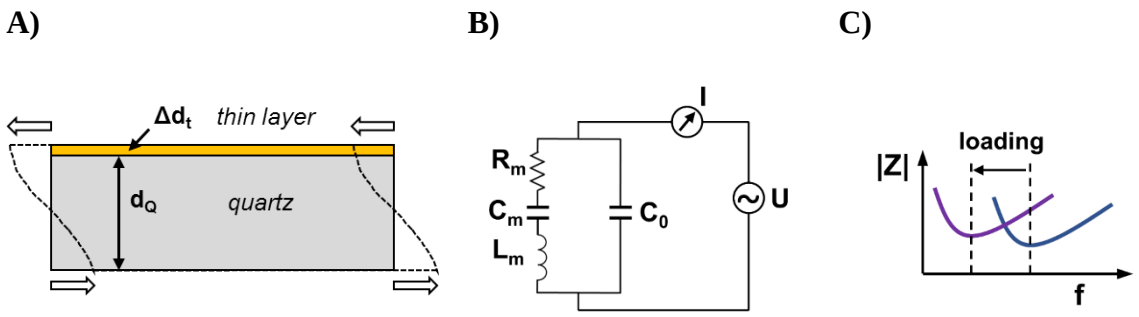

***Figure 16**. (**A**) Schematic representation of a standing thickness-shear wave in a quartz crystal oscillator. (**B**) Electrical equivalent circuit model of a QCM. (**C**) Schematic impedance analysis of an RLC oscillator as a function of the stimulation frequency upon increasing its inductance.*

The oscillating crystal can be modeled by an electrical equivalent circuit, as shown in **Figure 16B**. The "motional" resistance R_m characterizes mechanical and dissipative losses, the capacitor C_m is related to the elasticity of the quartz and the inductor L_m characterizes the mass displacement by vibrational stimulation. The parasitic element C_0 is the electric capacitance across the crystal. The resonant frequency of the system can be found by probing its impedance

response. For the series *RLC* path, it can be easily understood that the magnitude of its impedance reduces to its minimum ($|Z| = R_m$) at $f = f_0$, since the individual reactance of C_m and L_m cancel under resonance conditions. This situation is represented in **Equation 53** with the resistance *R* and reactance *B* and schematically illustrated in **Figure 16C**:

$$|Z(f)| = \sqrt{R^2 + B^2} = \sqrt{(R_m)^2 + \left(2\pi f L_m - \frac{1}{2\pi f C_m}\right)^2}$$
$$|Z(f_0)| = R_m \quad \text{with} \quad f_0 = \frac{1}{2\pi\sqrt{L_m C_m}} \qquad \textbf{Equation 53}$$

For the sake of completeness, it should be noted that a second resonant frequency exists due to the parallel path across C_0. Therefore, complex measurement circuitry is required to compensate for its effects, which is, however, beyond the scope of this introduction.[213] Upon loading the oscillator with an additional mass Δm_t, its motional inertia increases, which is reflected in a higher value of L_m, leading to a new, lower resonant frequency.

In theory, the technique can achieve extremely high precision in the order of a few ng/cm^2. However, limitations due to temperature drift, noise, and the resolution of detectable frequency shifts must be considered in reality.[212,213] Furthermore, the Sauerbrey equation only applies to thin, uniform, and rigid ad-layers neglecting viscoelastic effects. Therefore, thick coatings and operation in a liquid environment can lead to deviations and reduced precision. Surface roughness and viscous coupling of the coating with the liquid medium cause additional damping of the oscillator, leading to an overestimation of the mass of the investigated layer.[210,214,215]

3.2 X-Ray Photoelectron Spectroscopy

X-ray photoelectron spectroscopy (XPS) is a surface analysis tool that allows the investigation of a material's elemental composition and the physico-chemical bonding environment of its constituting atoms. The technique is based on the photoelectric effect, which results in the emission of electrons from a sample upon radiation with x-rays with an energy of *hν*. By measuring their kinetic energy E_{kin} with a spectrometer in a vacuum chamber, the electron binding energy E_b can be calculated according to **Equation 54**.

$$E_b = h\nu - E_{kin} - \Phi \qquad \textbf{Equation 54}$$

E_b is characteristic of the atomic orbital from which the electron originates. Φ is a correction term that accounts for the work function of the spectrometer and the sample, if the binding

energy is taken with respect to the sample's Fermi level. The acquired spectrum relates the intensity of the collected photoelectrons to their binding energy. As each element has a unique set of binding energies, XPS allows to identify the different constituents of a sample. The exact position and shape of a photoelectron peak reveal information on the chemical bonding environment and oxidation state of an element. Due to the low mean free path of electrons in solids, only electrons from the top few nanometers of the sample's surface are detected as peaks in the spectrum. Electrons undergoing inelastic scattering before leaving the sample add to the background signal.[216] The quality of the acquired spectra as well as conclusions drawn from its analysis should be carefully assessed to avoid misinterpretation.[217,218]

3.3 X-Ray Diffraction

X-ray diffraction (XRD) experiments allow the identification and analysis of crystalline phases in a sample, which can be either in powder form or a thin film. The technique is based on the diffraction of x-rays within a crystal's periodic structure if the spacing between crystal planes is in the same order of magnitude as the radiation wavelength. The x-rays are elastically scattered by the electron cloud of the atomic lattice. Constructive interference of the scattered x-rays can occur for certain incident angles which fulfill the Bragg condition (**Equation 55**), with 2ϑ being the angle between the incident and scattered beams.

$$2 \cdot d_{hkl} \cdot \sin(\vartheta) = n \cdot \lambda \qquad \textbf{Equation 55}$$

Here, d_{hkl} is the distance between two adjacent lattice planes described by the so-called Miller indices (*hkl*). The wavelength of the incoming x-rays is λ, and *n* is an integer representing the order of the reflection. Experimentally, a unique diffraction pattern is obtained as a function of 2ϑ for each crystal phase in the sample, which allows to draw conclusions on its composition and crystallinity. Furthermore, the lattice constant *a* of a present crystal phase can be determined, which is shown in **Equation 56** for the specific case of cubic lattices.[219,220]

$$a = d_{hkl} \cdot \sqrt{h^2 + k^2 + l^2} \qquad \textbf{Equation 56}$$

3.4 Scanning Electron Microscopy

Scanning electron microscopy (SEM) is a highly informative and popular technique to investigate the morphology of micro- and nanostructured materials. As for any microscopical technique, it gives an enlarged visual representation of small features of a specimen, which are

invisible to the human eye. In general, the achievable resolution of a microscope, which is the minimum distance of two objects which can be distinguished from one another, is limited by the employed wavelength of the probing wave signal. Therefore, SEM operates with high-energy electrons, which possess much smaller wavelengths than visible light used in optical microscopy. The experiment is performed in a vacuum chamber to maintain a high flux intensity of the electron beam and avoid scattering. To obtain an image, electrons are accelerated towards the sample using a strong electric field (tens of kV) while the surface is scanned with the focused electron beam in a raster pattern. As the electrons penetrate a few micrometers into the surface, a variety of signals is generated from the interaction with the specimen atoms. These include secondary and backscattered electrons, as well as characteristic x-rays. While the gray-scale image representing the surface morphology is processed based on the collected electron signal, the composition of the specimen can be assessed by analyzing the emitted x-ray spectrum. The lateral resolution of SEM ultimately depends on the spot size of the electron beam and is in the order of nanometers.[221]

3.5 Atomic Force Microscopy

The surface topology of a sample can be probed by using atomic force microscopy (AFM). In this technique, the surface is scanned by a very sharp tip sitting on the free end of a cantilever. When approaching the sample with the tip, an attractive van der Waals force builds up. However, the overall force becomes strongly repulsive at an even closer distance. This results from an overlap of the electron wave functions of the atoms sitting on the apex of the tip and on the sample surface. A three-dimensional image of the surface can be reconstructed by measuring the resulting cantilever deflection with a laser and using feedback-controlled electronics. It should be mentioned that there are several AFM operation modes with detailed descriptions in the literature. In general, a remarkably high resolution down to the sub-nanometer range is achievable for this technique. The surface roughness can be quantified by using **Equation 57**.[222]

$$R_a = \frac{1}{N}\sum_{i=1}^{N} |h_i(x,y) - \bar{h}| \qquad \textbf{Equation 57}$$

N is the total number of pixels in the image, with $h_i(x,y)$ being the corresponding height at this position, while $\bar{h}$ is the average height.

4 Experimental

4.1 Description of the Setup for Electrochemical Experiments

Electrochemical experiments were performed in a custom glass setup, as depicted in **Figure 17A**. The main cell accommodates a three-electrode configuration. The electrode terminals are connected to a potentiostat for controlling the electrochemical experiments. For the WE, mostly an Au-QCM was used. However, the modular design of the cell also allows to employ other electrodes *via* an alligator clip fixed to a metallic rod, such as carbon cloth, stainless-steel foil or Au-arrandee^{TM} chips. In such a case, particular care was taken to avoid contact of the alligator clip with the electrolyte to prevent corrosive processes. An Ag/AgCl (SSC, 3 M KCl) RE is connected to the main cell using a Luggin capillary filled with 0.1 M H_2SO_4 to establish a sensing point close to the WE and thereby minimize the ohmic drop associated with the uncompensated resistance.[223] Depending on the employed electrolyte, the uncompensated resistance was in the range of 2 – 30 Ω. A Pt-wire usually served as the counter electrode. For experiments involving high-capacity WEs (*e.g.*, composite electrodes), a symmetric electrode configuration was set up to avoid counter electrode overloads or pH variations within the bulk electrolyte. A detailed discussion of this case can be found in **Section 4.3.1**.

The setup was continuously flushed with argon gas to remove residual oxygen and provide an inert atmosphere to avoid side reactions. Similarly, the electrolyte and precursor solutions were purged in the preconditioning cell for at least 10 minutes before being poured into the main cell for experiments. The gas outlets were connected to gas-washing bottles to capture HCN gas in the unlikely case of its formation from $Fe(CN)_6$-decomposition in the main cell. The setup was located in a laboratory fume hood, and an HCN gas detector was in place during the experiments to ensure safe working conditions. The glass setup was regularly cleaned with "Piranha solution" (2:1 vol., H_2SO_4:H_2O_2) and extensively flushed with ultrapure water.

Whereas the described setup allows to individually investigate battery materials as cathode or anode in half-cell configuration, full-cell battery prototypes can be examined by the "double-cell" shown in **Figure 17B**. This configuration was introduced by Marzak *et al*. and consisted of two of the previously described electrochemical cells connected *via* an attached, lockable glass tube building an electrolyte bridge.[224] It should be mentioned that the large spatial

distance between the two electrodes in the opposing cells results in a high uncompensated resistance across the electrolyte bridge of ≈ 153.5 Ω in 8 M $NaClO_4$, as determined by EIS.

A) **B)**

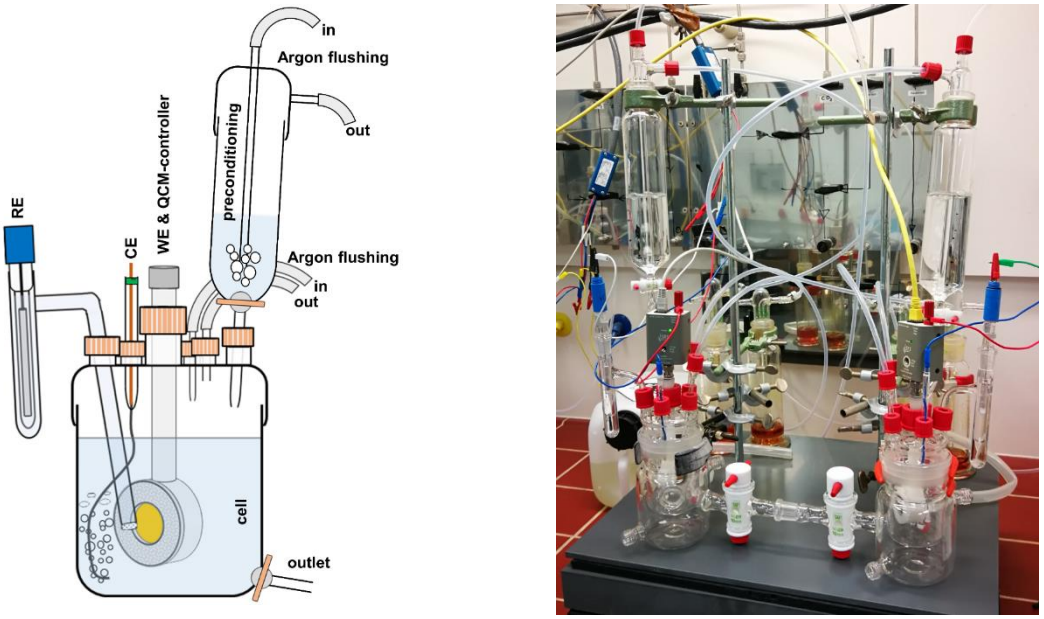

***Figure 17**. (**A**) Schematic illustration of the custom glass setup used for electrochemical experiments of battery half-cells. (**B**) Photograph of the setup, showing the "double-cell" configuration to investigate prototypical battery full-cells.*

4.2 Sample Preparation

For this work, PBA battery electrodes were mainly prepared as thin films *via* direct electrochemical deposition on conductive substrates. Bulky composite electrodes with a high-capacity loading were obtained *via* the slurry casting of PBA active material powder. The two synthesis routines are schematically illustrated in (**Figure 18**) and will be described in detail in the following.

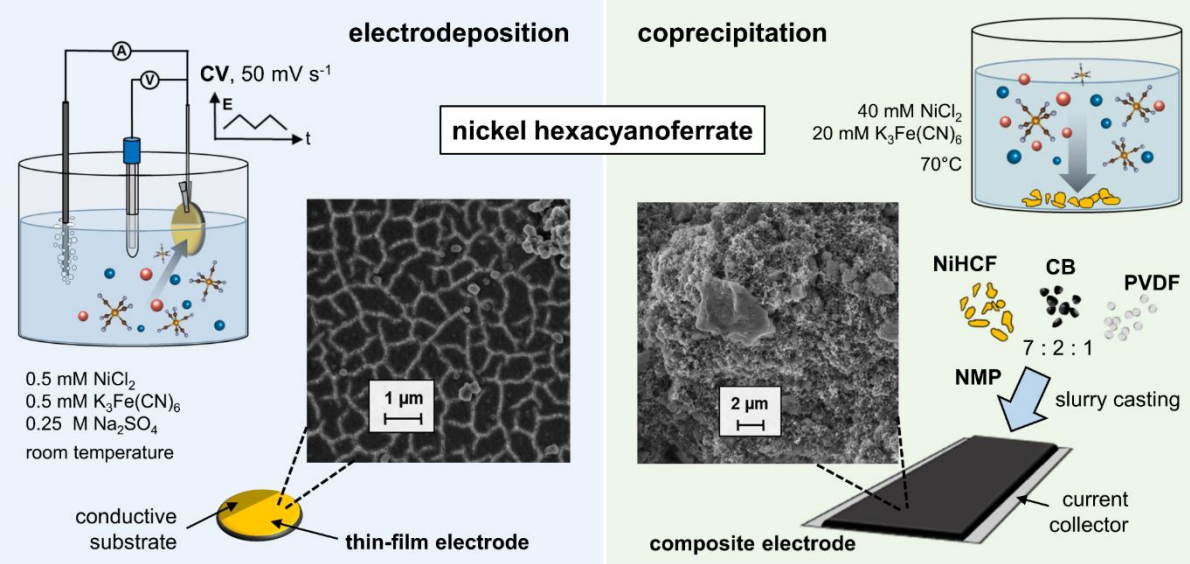

***Figure 18**. Comparison of the two PBA battery electrode preparation routines employed in this work: (**left**) electrochemical deposition of thin-film electrodes on conductive substrates and (**right**) traditional composite electrode fabrication via slurry-casting of active material powder. Reprinted with permission from ref. 225. Copyright © 2023, American Chemical Society.*

4.2.1 Electrochemically Deposited Thin-Film Electrodes

4.2.1.1 Cleaning Procedure for Metallic Substrates

Au-QCM substrates were used for experiments where the mass loading and dissolution of active material, as well as the exact electrode area were of interest. For characterizing the PBA thin films by other techniques, Au-arrandee™ chips were used. These involved AFM, XPS, XRD, SEM, profilometry and flow-cell coupled ICP-MS. However, these substrates did not allow a precise determination of the deposited mass loading or immersed electrode surface area. These quantities could, however, be obtained indirectly from the measured capacity.

As the Au substrates were re-used several times, they were cleaned from PBA residues previous to the electrodeposition of new material following a two-step process described

elsewhere.[198,226] In short, a PBA-coated substrate was immersed in 0.1 M NaOH, and CV cycles at 50 mV/s were performed until the shape of CV stabilized, as shown in **Figure 19A**. In fact, this process represents the transformation of NiHCF to nickel hydroxide/oxyhydroxide phases accompanied by the extraction of $Fe(CN)_6$-species, a common degradation pathway for PBAs in alkaline solutions.[227,228] This transition can be seen by comparing the CV during initial cycles, which is very similar to the response in pH-neutral Na^+ electrolyte (0.25 M Na_2SO_4, pure intercalation) to the entirely changed response after 50 cycles. A detailed discussion of the underlying mechanism will be given in **Section 6.3.2.1**. After flushing the cell with ultrapure water, the transformed electrode was cycled in 0.1 M H_2SO_4 at 50 mV/s. As NiO_x is unstable under acidic conditions,[128] the CV response of a plain gold surface emerges after a few cycles as visible from **Figure 19B**, indicating the successful cleaning of the substrate from PBA-residues. Finally, the cell and substate were extensively flushed with ultrapure water.

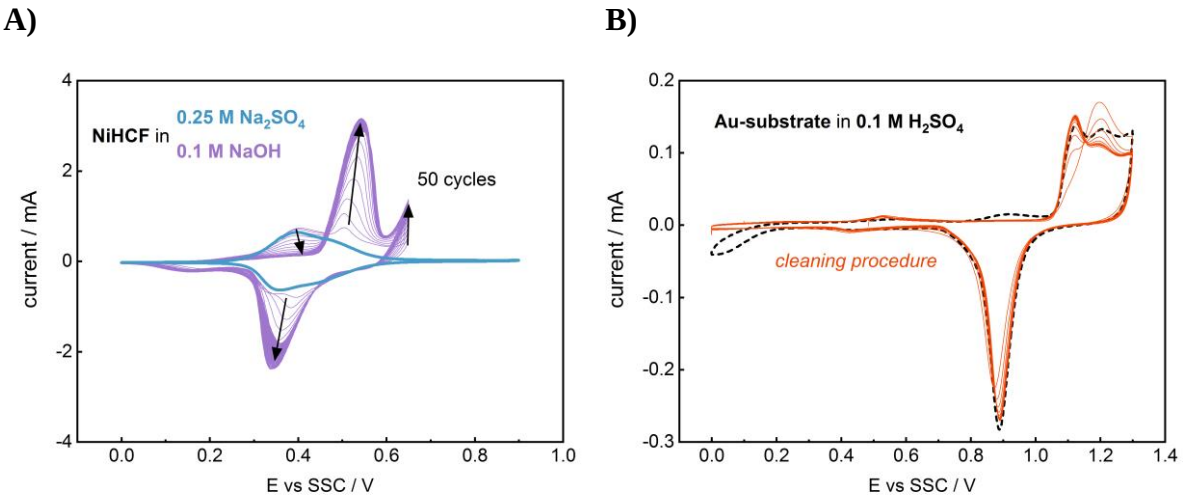

***Figure 19**. Cleaning procedure for Au-substrates from PBA residues via subsequent cycling in (**A**) 0.1 M NaOH and (**B**) 0.1 M H_2SO_4. The dashed line in **B** corresponds to the redox corresponds of plain gold in 0.1 M H_2SO_4.*

4.2.1.2 Electrodeposition Process

If not stated otherwise, the standard preparation of PBA thin films was carried out *via* electrochemical deposition following the method described in refs. 197,198,199,200 and 205. For this work, NiHCF, CoHCF, MnHCM and InHCF, as representatives from the PBA material class, were synthesized as described below and investigated as thin-film model systems. The electrodes were prepared by immersing the substrate (Au-QCM, Au-arrandee™ chips or carbon cloth) in the respective precursor solution and cycled by means of CV as indicated in

Table 2 with a scan rate of 50 mV/s. In general, the precursor solution includes the respective transition metal cations, hexacyanoferrate/hexacyanomanganate anions and Na_2SO_4 as a supporting electrolyte.

Table 2. Precursor solutions and potential ranges for the electrodeposition of the PBAs employed in this work.

PBA	**Precursor solution**	**Potential range**
NiHCF	0.5 mM $NiCl_2$ + 0.5 mM $K_3Fe(CN)_6$ + 0.25 M Na_2SO_4	0 ↔ 0.9 V *vs.* SSC
CoHCF	0.5/1 mM $CoCl_2$ + 0.5/1 mM $K_3Fe(CN)_6$ + 0.25 M Na_2SO_4	-0.2 ↔ 1.1 V *vs.* SSC
MnHCM	2 mM $MnSO_4$ + 2 mM $K_3Mn(CN)_6$ + 0.25 M Na_2SO_4	-0.6 ↔ -1.2 V *vs.* SSC
InHCF	2 mM $InCl_3$ + 2 mM $K_3Fe(CN)_6$ + 0.25 M Na_2SO_4	0.4 ↔ 1.05/1.15 V *vs.* SSC

Figure 20 shows examples of the deposition of NiHCF (**A**), CoHCF (**B**), MnHCM (**C**) and InHCF (**D**). The film growth is indicated by an advancing mass loading as measured *via in-operando* EQCM, as well as an increasing redox response in the CV. Correspondingly, the capacity (ΔQ) and the associated mass variation (Δm) due to the (de)intercalation of Na^+ from/into the deposited material increase as well. It should be noted that the deposition of InHCF proceeds in two steps, which include an initially smaller potential window for CV cycling to avoid side reactions of the electrolyte on the Au surface. After a few cycles, the film entirely covers the substrate and the potential window can be increased, which leads to a higher obtainable capacity by utilizing the full electrochemically active potential region of InHCF.[205]

Empirically, the obtainable mass loadings on flat metallic substrates were below ≈ 100 µg/cm^2. Depositions with higher loadings yielded low mechanical stability and even led to a (partial) detachment of the film. After reaching a desired mass loading or capacity, the deposition was terminated at the lower potential vertex, *i.e.,* in the reduced (intercalated) electrode state. After disposing of the deposition solution, the sample was washed thoroughly with argon-purged, ultrapure water and dried within the glass setup under an argon atmosphere.

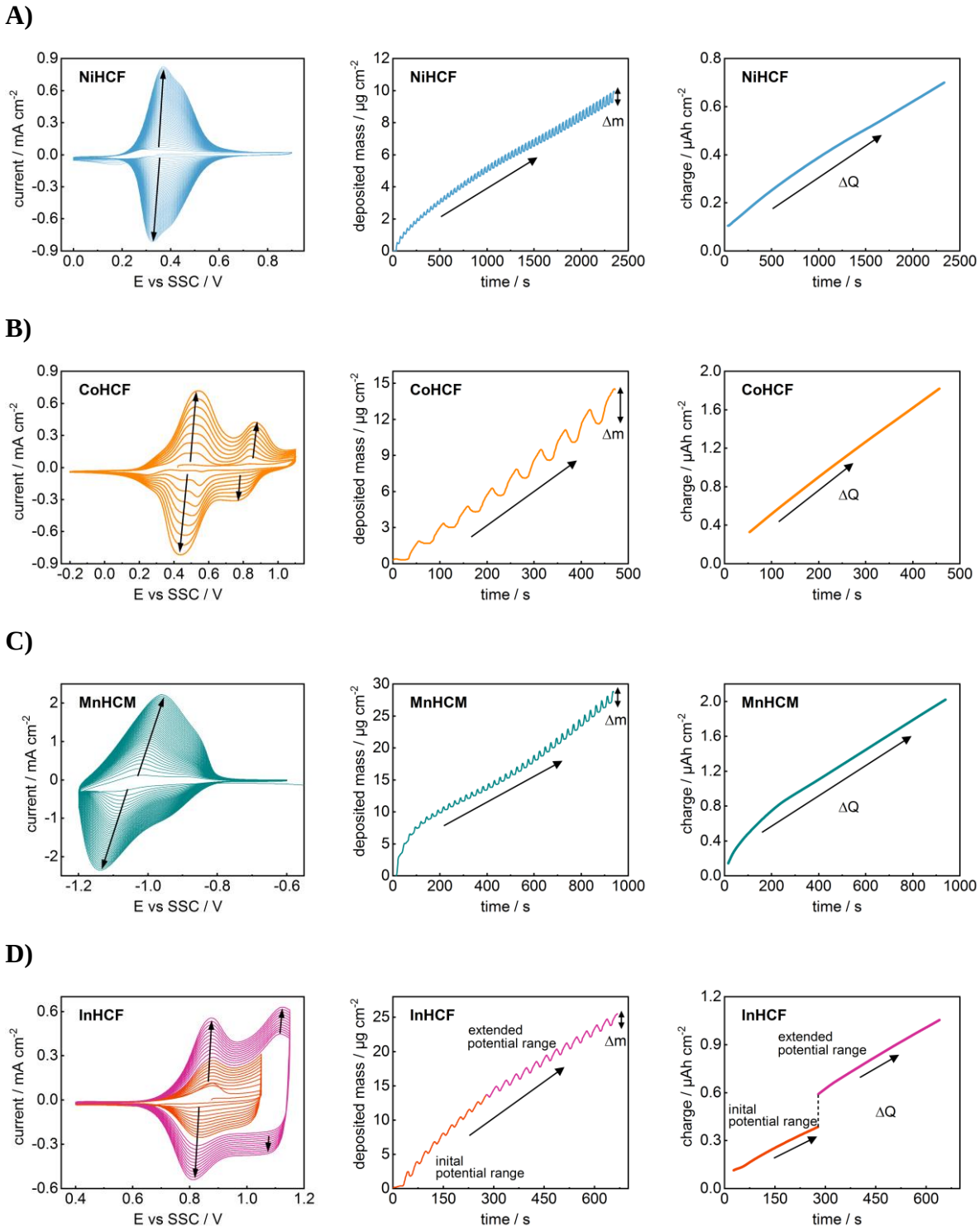

***Figure 20**. CV, mass variation and available electrode charge during the electrodeposition of (**A**) NiHCF, (**B**) CoHCF, (**C**) MnHCM and (**D**) InHCF on Au-QCM substrates. The electrode charge is shown from the first completed CV cycle onwards.*

4.2.2 Composite Electrodes

Composite PBA-based battery electrodes with active material mass loadings in the range of mg/cm^2 were produced following the routine described by Wessells *et al.*[84] The most important steps of electrode production are exemplarily shown in **Figure 21**. NiHCF active material powder was synthesized by dropwise adding the aqueous precursor solutions of 40 mM $NiCl_2$ and 20 mM $K_3Fe(CN)_6$ (co-precipitation, see **Figure 21A**). The reaction bath was heated to 70°C and allowed to rest for at least 10 minutes under continuous stirring. The resulting orange precipitate was centrifuged and washed with ultrapure water several times before drying it at 70°C under ambient conditions. The process was monitored by a nearby HCN detector for safety reasons.

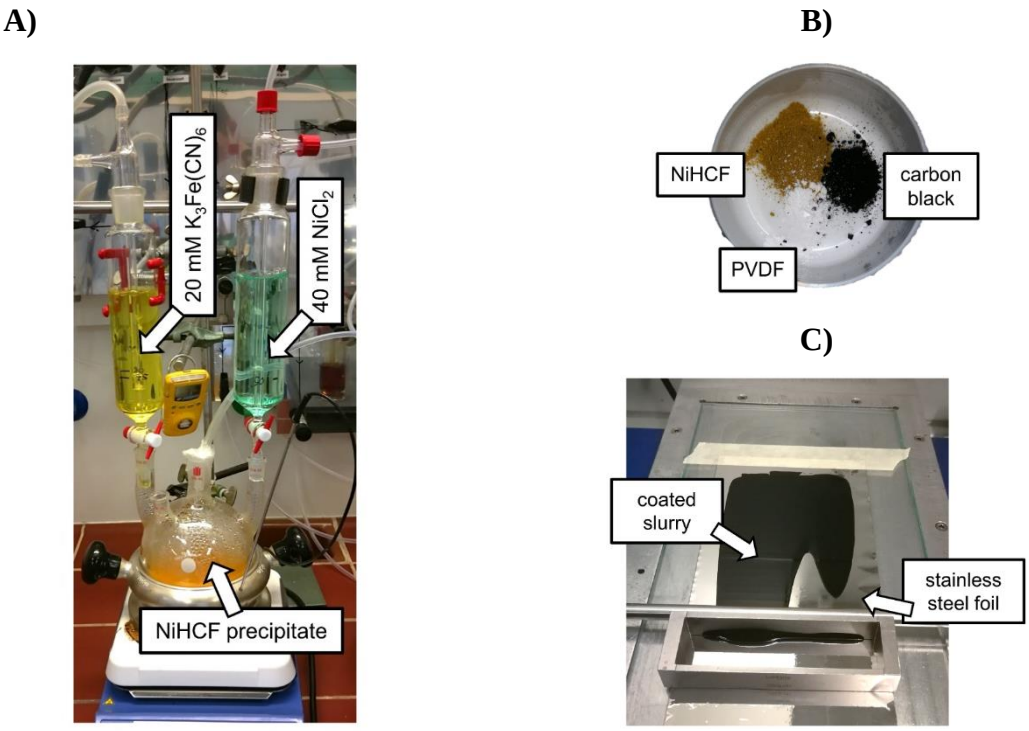

***Figure 21**. (**A**) Synthesis of NiHCF via co-precipitation from aqueous precursor solutions containing Ni^{2+} and $Fe(CN)_6^{3-}$ ions. (**B**) Mixing of the active material powder with carbon black as a conductive additive and PVDF as a binder. (**C**) Slurry-casting of the mixture dissolved in NMP on stainless-steel foil.*

NiHCF powder was mixed with carbon black and polyvinylidene difluoride (PVDF) in a 7:2:1 weight-ratio (see **Figure 21B**). N-methyl-2-pyrrolidone (NMP) was used as a solvent until a honey-like viscosity was obtained. The resulting slurry was casted on stainless-steel foil (see **Figure 21C**), which had previously been ground with sandpaper for better adhesion and wiped with isopropanol. The coated sheets were dried in an oven at 50 – 60°C to let the solvent

evaporate. The electrode fabrication process was performed in a fume hood due to the hazardous nature of NMP.[229] NiHCF electrodes were cut from the coated foil for characterization.

4.3 Electrochemical Characterization

4.3.1 Counter Electrode Considerations

The electrochemical characterization of PBA battery electrodes was performed in the setup described in **Section 4.1**. Usually, a Pt-wire serves as the counter electrode, especially for the characterization of thin-film electrodes. As the latter only involved small capacities in the order of 0.1 – 5 µAh, local pH variations due to OER/HER on the CE can be neglected, as shown in the following "worst-case" estimation.[230]

Under the assumption that a charge of 5 µAh must be provided by OER on the Pt counter electrode to completely reduce a PBA thin-film electrode, an additional amount $n_{H^+,add}$ of protons will be produced:

$$2H_2O \rightarrow O_2 + 4H^+ + 4e^-$$

$$n_{H^+,add} = \frac{5 \cdot 10^{-6}\ \text{Ah} \cdot 3600 \frac{\text{As}}{\text{Ah}}}{1.602 \cdot 10^{-19}\ \text{As} \cdot 6.022 \cdot 10^{23}\ \text{mol}^{-1}} = 1.866 \cdot 10^{-7}\ \text{mol}$$

Taking an initial pH of 5.5 for an experiment involving 8 M $NaClO_4$ as the electrolyte:

$$pH_{initial} = 5.5 = -\log_{10}\left(\frac{c(H^+)}{1\ \frac{\text{mol}}{\text{l}}}\right) \quad \rightarrow \quad 10^{-5.5} \cdot 1 \frac{\text{mol}}{\text{l}} = c(H^+) = \frac{n_{H^+}}{V_{H_2O}}$$

The original amount of n_{H^+} is obtained by taking the electrolyte volume of 120 ml with a volume ratio V_{H2O}/V_{total} = 62% for the highly concentrated 8 M $NaClO_4$ "water-in-salt" solution.

$$n_{H^+} = 10^{-5.5}\ \frac{\text{mol}}{\text{l}} \cdot 74.4\ \text{ml} = 2.353 \cdot 10^{-7}\ \text{mol}$$

Now considering the additional amount of H^+ produced from the OER on the Pt counter electrode and a uniform migration of these species towards the entire electrolyte volume, the pH will shift from initially pH = 5.5 to

$$pH_{new} = -\log_{10}\left(\frac{\frac{n_{H^+} + n_{H^+,add}}{V_{H_2O}}}{1\ \frac{\text{mol}}{\text{l}}}\right) = 5.2$$

during one half-cycle (reduction of the WE). The described effect will be smaller for less concentrated electrolytes, as a higher amount of H_2O is available. The following oxidation cycle will require charge compensation *via* HER on the Pt counter electrode, which in turn consumes H^+/adds OH^-. Accordingly, the pH shifts to the other direction towards slightly

higher pH, again, and therefore the bulk pH should remain constant during long-term measurements. As the thin-film electrode capacities involved in this work were mostly around only 1 µAh (10 – 20 µg/cm^2), the effect is almost negligible (pH variation of 0.1 for the example shown above). Therefore, the stability or performance of PBA electrodes should not be affected by (local) pH variations related to the OER/HER processes on the Pt counter electrode.

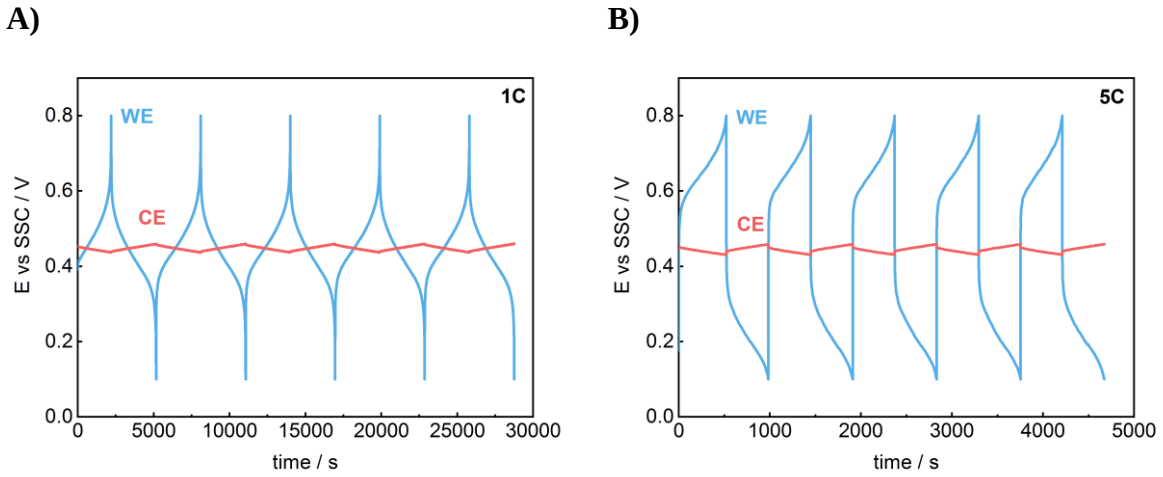

***Figure 22**. Working- and counter electrode potential for a symmetric configuration of NiHCF composite electrodes with a largely oversized counter electrode during galvanostatic cycling at a rate of (**A**) 1C and (**B**) 5C in 8 M $NaClO_4$. The capacity of the WE was 30 µAh in the depicted case. The counter electrode was brought to SOC = 50% before the experiment.*

Nevertheless, for high mass-loading composite electrodes with absolute capacities of 10 – 100 µAh in the experiment, local pH changes and/or counter electrode overload cannot be excluded. Therefore, a symmetric electrode configuration was set up for these experiments using. In such case, a largely oversized (ca. 10 x higher absolute electrode mass) PBA composite electrode identical to the WE was used as the counter electrode. To maximize its range for both charging and discharging during subsequent experiments, it was first connected as WE and brought to SOC ≈ 50% using a Pt counter electrode. Therefore, a constant-potential hold at $E_{SOC=50\%}$ was applied until the system was equilibrated. After this, the oversized electrode was connected as a counter electrode while removing the Pt-wire, whereas the actual electrode to be investigated was installed in the system as WE. As it is visible from **Figure 22** for the exemplary case of a 30 µAh NiHCF WE, this configuration allows to cycle high-capacity composite electrodes at reasonably high rates. While the oversized NiHCF counter electrode is capable of providing and sinking the required current by reversible Na^+ (de)intercalation reactions, its potential remains almost constant throughout cycling.

4.3.2 Applied Techniques and Settings

This work involves the electrochemical characterization of PBA battery electrodes by means of CV, GC and (S)PEIS. CVs were performed at different scan rates between 0.05 – 2000 mV/s. GC was performed at different C-rates between 0.1 – 3000C. The fastest applied rate of 3000C implies a (dis)charging time of 1.2 seconds, whereas the real time will depend on the capacity retention at the specific rate and could therefore be shorter. The C-rates given in this work were calculated by taking the imposed absolute current of a specific experimental sequence and the maximum achieved capacity of the electrode during cycling at a low rate. To avoid potential overshoot, the working electrode potential was limited for constant current techniques. The potential ranges for both CV and GC were selected according to the redox-active potential region of the respective material. For experiments involving high absolute currents, the ohmic drop can significantly impact the working electrode potential. In such cases, the measured WE potential was corrected afterward for the respective uncompensated resistance, which was determined *via* EIS.

(S)PEIS measurements were performed using an AC probing signal with a 10 mV amplitude. The applied frequency range was usually between 100 kHz and 100 mHz with 10 points per decade in logarithmic spacing. System stationarity was guaranteed by an appropriate waiting period before the measurement until the system equilibrated as indicated by vanishing current transients. The data validity within the analysis interval was verified by the Kramers-Kronig check. The respectively analyzed range depended on the individual experiment taking into account the validity of the data.

4.4 List of Chemicals

The chemicals used in this work are listed in **Table 3**. Ultrapure water was used for preparing aqueous salt solutions.

Table 3. Chemicals used for the synthesis, preparation, and characterization of PBA battery electrodes with their respective suppliers and grades.

Chemicals	**Formula/trade name**	**Supplier & grade**
Sulfuric acid	H_2SO_4	Carl Roth, 96%
Potassium ferricyanide(III)	$K_3Fe(CN)_6$	Sigma-Aldrich, 99%
Potassium hexacyanomanganate (III)	$K_3Mn(CN)_6$	synthesized in-house [ref. 200]
Nickel(II) chloride	$NiCl_2$ hexahyd.	Alfa Aesar, 99.3%
Cobalt(II) chloride	$CoCl_2$ hexahyd.	Sigma-Aldrich, 98%
Manganese(II) sulfate	$MnSO_4$ monohyd.	Amresco, >99%
Indium(III) chloride	$InCl_3$	Carl Roth, ≥99.9%
Sodium sulfate	Na_2SO_4	Sigma-Aldrich, >99%
Sodium perchlorate	$NaClO_4$ monohyd.	Sigma-Aldrich, >98%
Sodium chloride	NaCl	Sigma-Aldrich, ≥99%
Sodium nitrate	$NaNO_3$	Merck, ACS reagent
Sodium acetate	$NaCH_3COO$	Sigma-Aldrich, >99%
Sodium hydroxide	NaOH	Grüssing, 99%
Carbon black	Super C65	MTI
Polyvinylidene difluoride (PVDF)	$[C_2H_2F_2]_n$	MTI, >99.5%
N-methyl-2-pyrrolidone (NMP)	C_5H_9NO	Merck, >99.5% (anhydr.)

4.5 List of Materials

The materials used in this work are listed in **Table 4**.

Table 4. List of materials with their respective suppliers.

Material	**Specification**	**Supplier**
Au-QCM substrates	AT-cut quartz crystal wafer, Au on Ti adhesive layer, 5 MHz, 1.37 cm^2 circular electrode area, c_f = 56.6 Hz μg^{-1} cm^2	*Stanford Research Systems*, USA
Au-arrandee™ substrates	11x11 cm, gold on glass	*Arrandee Metal*, Germany
Carbon cloth	AvCarb 1071 HCB plain carbon cloth fabric	*Fuel Cell Store*, USA
Pt-wire	99.9 % platinum	*GoodFellow*, Germany
Argon gas	Ar 5.0	*Westfalen*, Germany

4.6 List of Equipment

The equipment used in this work is listed in **Table 5**. Experimental and instrumentation details on SEM, XRD and other techniques can be found in the respective original publications discussed in **Chapters 5**, **6** and **7**.

Table 5. List of equipment with respective specifications and suppliers.

Instrument/device	**Specification**	**Supplier**
Potentiostat	VSP-300	*Bio-Logic*, France
Reference electrode	SSC, B3420+	*SI Analytics*, Germany
QCM controller and analyzer	QCM200	*Stanford Research Systems*, USA
Profilometer	DekTak	*Bruker*, Germany
XPS	X-ray source: XR50 Al anode	*Specs*, Germany
	Photoelectron detector: hemispherical energy analyzer PHOIBOS 150 2D	*Specs*, Germany
Water purification systems	Ultra Clear 10 TWF 30 UV	*Evoqua*, Germany
	Elix® Essential 3, Milli-Q® EQ 7000	*Merck Millipore*, Germany
HCN detector	GasAlertExtreme HCN	*Honeywell*, USA

4.7 List of Software

The software for instrumentation control and data analysis used in this work is listed in **Table 6**.

Table 6. List of software and respective suppliers.

Application	**Software**	**Supplier/source**
EIS data analysis	EIS Data Analysis 1.3-1.6[192,231]	*Prof. A. S. Bandarenka*
Potentiostat control and data acquisition	EC-Lab®, version 11.43 and earlier versions	*Bio-Logic*, France
QCM control and data acquisition	QCM200 software	*Stanford Research Systems*, USA
XPS control and data acquisition	SpecsLab Prodigy	*Specs*, Germany
General data analysis and plotting	OriginPro 2019	*OriginLab*, USA
Crystal structure visualization and XRD pattern simulation	Vesta 3.0[232]	*K. Momma* and *F. Izumi*
Anion drawings	https://molview.org/	Open-source web app
Preparation of schemes and customization of figures	PowerPoint	*Microsoft*, USA

5 Prussian Blue Analogs as Battery Materials

5.1 General Properties and Charge Storage Mechanism

Since the renowned work of C. D. Wessells (2011)[84] and M. Pasta (2014)[233] from Y. Cui's group at Stanford and J. B. Goodenough's group in Austin (2012),[88] Prussian blue analogs have gained increasing interest over the last decade as active materials for intercalation-type battery electrodes in both organic and aqueous electrolytes (see **Figure 23**).[56,62] In this work, their application will only be discussed for water-based applications.

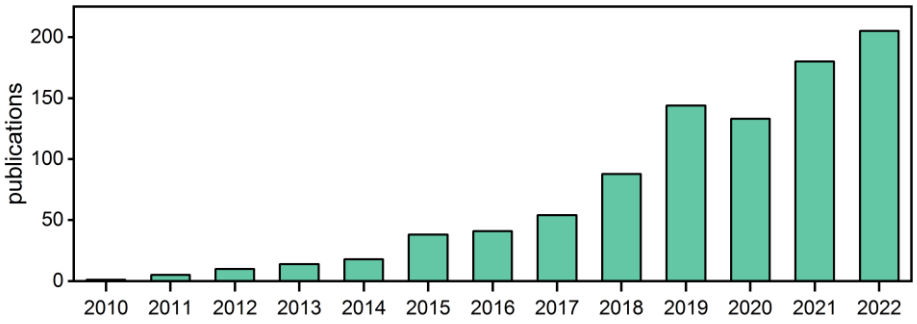

***Figure 23**. Publication report from Web of Science using the search terms "Prussian Blue Analogs" and "Battery". Data included herein are derived from Clarivate Web of Science. Copyright © Clarivate 2023. All rights reserved.*

Their general composition is described by **Equation 58**, where A represents an intercalated cation, $TM^{(1)}$ is a transition metal, such as, for example, Fe, Ni, Co, Zn, In, Mn or Cu, which is coordinated to a hexacyanometallate-species $[TM^{(2)}(CN)_6]$.[62,63]

$$A_x TM^{(1)}[TM^{(2)}(CN)_6] \qquad \textbf{Equation 58}$$

As coordination compounds with C≡N-ligands interconnecting the transition metal atoms in the structure, PBAs can be considered as derivatives of the well-known material class of metal-organic frameworks (MOFs).[234] PBAs are typically associated with the face-centered cubic (fcc) lattice structure with a size of ≈ 10 Å (see **Figure 24A**). However, monoclinic or rhombohedral structures are also frequently observed along with redox-associated phase transitions or incorporated symmetry distortions such as octahedral tilts, Jahn-Teller distortions, hexacyanometallate vacancies or framework hydration.[62,63,69,235,236] In general, two different types of hydration can be differentiated in PBAs:[237] Hexacyanometallate vacancies

are compensated by rather strongly bound H_2O molecules, which is also called coordination or ligand water in this case and plays an important role in structural stabilization. Furthermore, so-called zeolitic or interstitial water exists, which can block ion-intercalation by occupying the A-sites and is therefore unwanted in general.[62,235] PBA electrodes are reported to have high thermal stability. HCN-release was only observed at temperatures well above the application-relevant temperature range, which is ultimately limited in the upper direction to the evaporation of water from the electrolyte.[233]

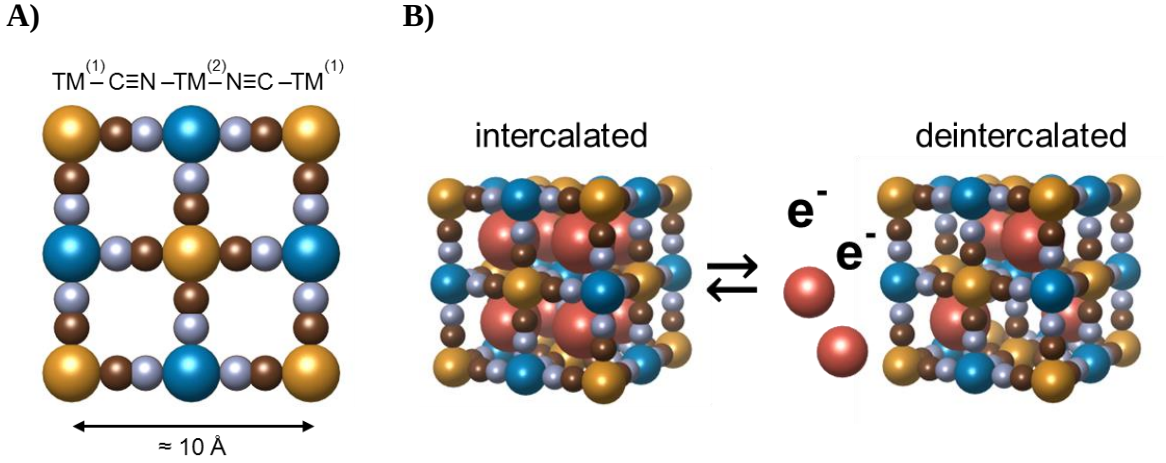

***Figure 24**. (**A**) Representative fcc PBA crystal structure with empty nanopores. (**B**) Reaction scheme of redox-active PBAs and metal cations (red) with fully occupied and 50% occupied interstitial sites.*

As seen in **Figure 24A**, the PBA framework comprises large nanopores (A-sites, ≈ 5 Å), which can accommodate a variety of cations, motivating the usage as intercalation compound for, *e.g.*, Na^+, Li^+, K^+ or even Mg^{2+} or Zn^{2+} batteries. The nanoporous network provides wide channels allowing the transport of the inserted cations throughout the crystal *via* solid-state diffusion. The reversible intercalation and deintercalation of these ions is associated with the redox activity of the transition metals.[62,63,69] For nickel hexacyanoferrate, a well-studied PBA representative, the transition of the C-coordinated $Fe^{II/III}$-center is responsible for the reversible (de)intercalation of sodium ions as shown in **Equation 59**:[84]

$$Na_2Ni^{II}[Fe^{II}(CN)_6] \rightleftarrows Na^+ + e^- + NaNi^{II}[Fe^{III}(CN)_6] \qquad \textbf{Equation 59}$$

The theoretical specific capacity of this reaction is calculated in **Equation 60**:

$$q_{NiHCF} = \frac{N_A \cdot e^-}{M(Na_2NiFe(CN)_6)} = 84.5\ \frac{mAh}{g} \qquad \textbf{Equation 60}$$

N_A is the Avogadro number, and $M(Na_2NiFe(CN)_6) = 316.6$ g/mol is the molar mass of NiHCF. The resulting theoretical specific capacity is higher than the usually observed 60 – 70 mAh/g, from which it can be concluded that the crystal must be hydrated to a certain degree (*ca.* 25%)[233] and/or contain some inactive $[Fe(CN)_6]$ vacancies.[62]

5.2 Tunability of the Intercalation Potential

The nature of the employed transition metals strongly determines the physical and chemical properties of the resulting compound, such as electronic, ionic and structural properties, color and redox activity.[63,68,69,70,71,72] **Figure 25A** shows the CVs of the PBAs investigated in this thesis with the RHE potential scale for orientation. Nickel hexacyanoferrate (NiHCF), cobalt hexacyanoferrate (CoHCF) and indium hexacyanoferrate (InHCF) are on the edge of the stability window towards the OER and are therefore potential candidates to be used as cathodes. Manganese hexacyanomanganate (MnHCM) features two redox peaks, the lower of which could be employed for a potential application as anode material[95] if the HER can be sufficiently suppressed. This will be further discussed in **Section 7.4**.

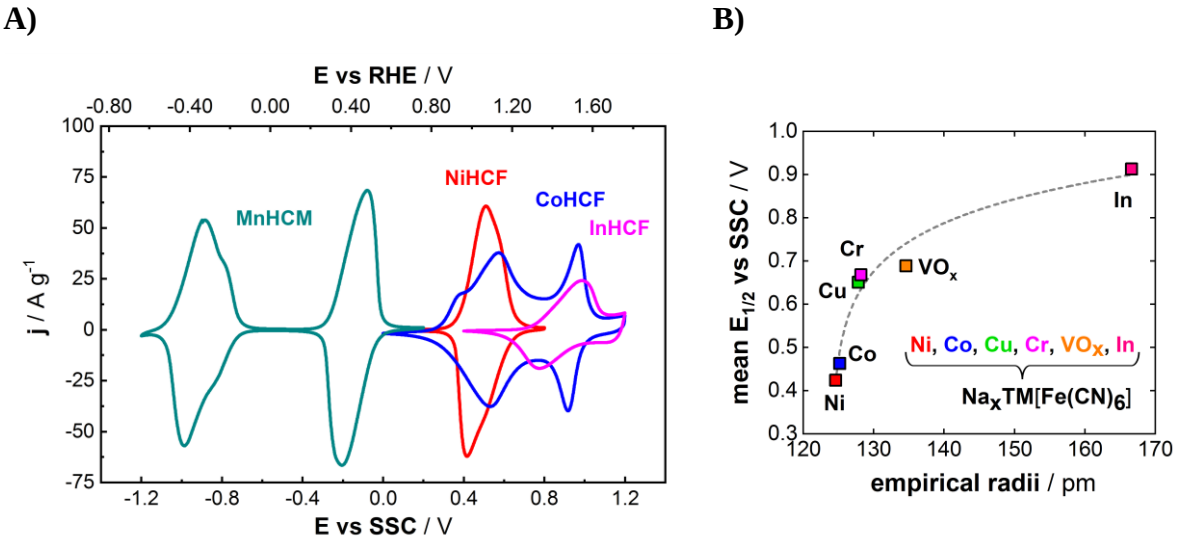

***Figure 25**. (**A**) CVs of the PBAs investigated in this thesis with an RHE potential scale as a reference for the theoretical stability window of the electrolyte. All CVs were measured in 8 M $NaClO_4$, pH ≈ 5.6. (**B**) Tunability of the intercalation potential for Fe-based PBAs in 0.25 M Na^+ electrolytes by varying the N-coordinated transition metal. **B** reproduced from ref. 205 with permission from the Royal Society of Chemistry. Open access, CC BY 3.0.*

Nevertheless, it is apparent that the redox response of PBAs can be tuned by employing different combinations of transition metals.[68] By fixing Fe as the C-coordinated transition metal and redox-active center ($Fe^{II/III}$) and varying the N-coordinated (redox inactive) component, a strong impact of the latter on the formal potential of Na^+ (de)intercalation can be seen (see **Figure 25B** for 0.25 M $NaClO_4$). It was found that $E_{1/2}$ phenomenologically correlates with the empirical radii of the N-coordinated transition metals.[68,197,198,204,205] With $E_{1/2}$ = 1.57 V *vs.* RHE in 8 M $NaClO_4$ at pH = 5.8 (1.0 V *vs.* SSC), InHCF appears as a very promising candidate as cathode material for high-voltage ASIBs compared to other PBAs

based on Ni, Co, Cu or Cr. The performance and properties of InHCF, as well as open challenges, are discussed in the published article "X. Lamprecht, P. Marzak, A. Wieczorek, N. Thomsen, J. Kim, B. Garlyyev, Y. Liang, A. S. Bandarenka, J. Yun. **High voltage and superior cyclability of indium hexacyanoferrate cathodes for aqueous Na-ion batteries enabled by superconcentrated $NaClO_4$ electrolytes**. *Energy Advances* **2022**, *1*, 623-631", but will not be further elaborated in this thesis.

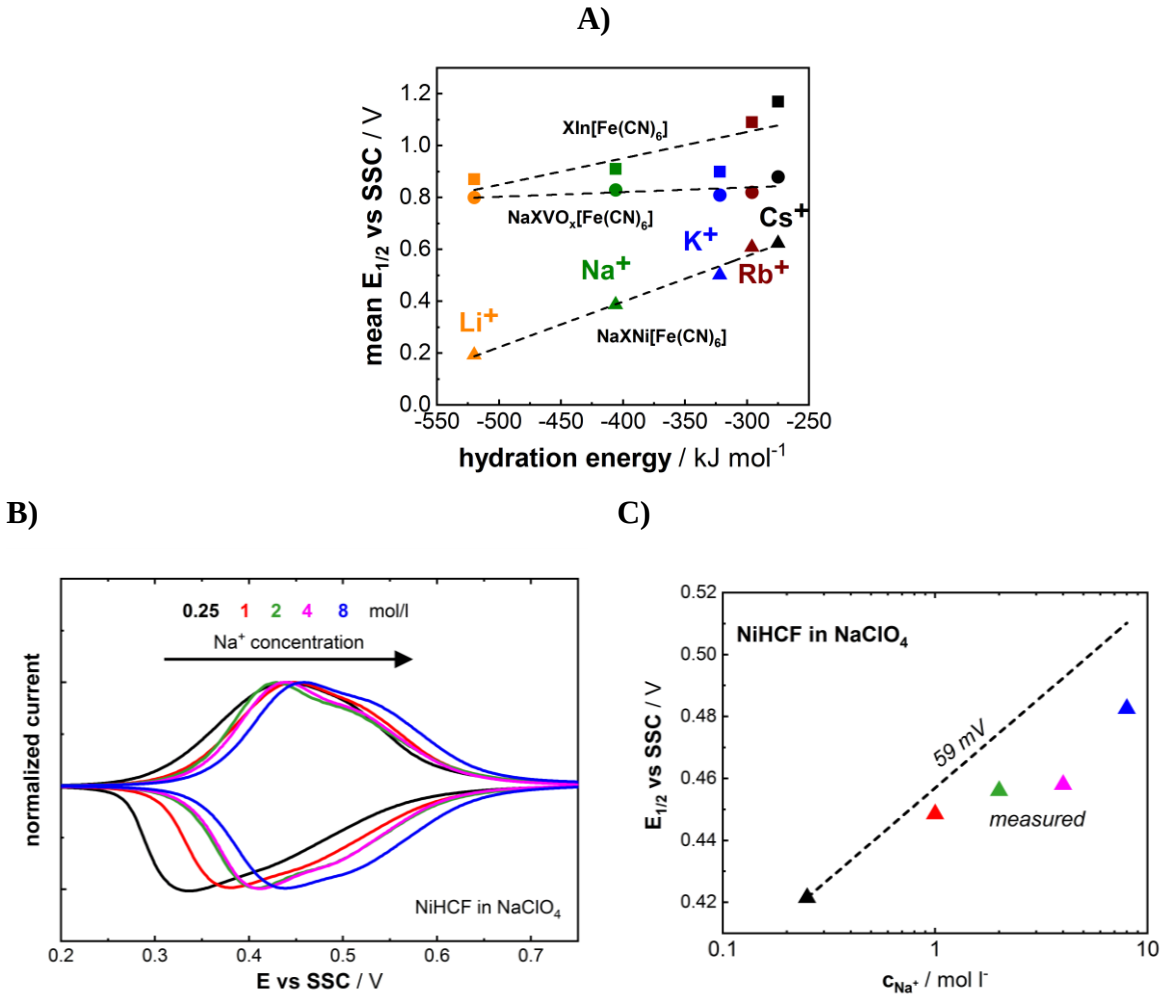

***Figure 26**. (**A**) Tunability of the intercalation potential of NiHCF, VO_xHCF and InHCF by varying the alkali metal cation A in the electrolyte (0.25 M A_2SO_4). Reproduced from ref. 205 with permission from the Royal Society of Chemistry. Open access, CC BY 3.0. (**B**) The CV of NiHCF in $NaClO_4$ shifts towards more positive potentials when increasing the electrolyte concentration. (**C**) Plot of the resulting formal intercalation potentials versus the electrolyte concentration. The dashed line shows an extrapolation of **Equation 61** based on the datapoint for 0.25 M und replacing the activity by concentration.*

Apart from the N-coordinated transition metal, also the nature of the intercalating alkali metal cation offers great tunability for the intercalation potential. It has been found that $E_{1/2}$ correlates with the hydration enthalpy of the intercalate in certain PBAs.[68,198,204,205] As shown in **Figure**

26A, this effect is especially significant for NiHCF, where $E_{1/2}$ shifts more than 0.4 V when going from Li^+ over Na^+, K^+ and Rb^+ to Cs^+. From a thermodynamic point of view, the intercalation potential is directly linked to the Gibbs free energy of ion solvation. As less energy is needed to remove the solvation shell from large ions like Cs^+, their intercalation proceeds at a higher potential than small ions like Li^+ or Na^+. As a result, the intercalation of large ions is thermodynamically more favorable.[68,238,239,240] This trend is less pronounced for InHCF, while the $E_{1/2}$ of VO_xHCF is almost constant regardless of the alkali metal.[204,205]

Lastly, the intercalation potential can be tuned by varying the concentration of the alkali metal cation in the solution. Hereby, higher concentrations lead to higher intercalation potentials.[241] As shown in **Figure 26B** for NiHCF in $NaClO_4$ electrolytes, the $E_{1/2}$ value of respective cyclic voltammograms shifts from 0.42 V *vs.* SSC in 0.25 M to 0.48 V *vs.* SSC in 8 M. This behavior is well-expected from the Nernst equation as shown by Scholz *et al*.[68,237,242] (see **Equation 61**):

$$E_0' = E_{A,0} + \frac{RT}{F} \ln \frac{a_{A,s}}{a_{A,0}} = E_{A,0} + 59\ \text{mV} \cdot \log \frac{a_{A,s}}{a_{A,0}} \qquad \textbf{Equation 61}$$

Here, $a_{A,s}$ is the activity of the alkali metal cations in the solution, and $E_{A,0}$ is the equilibrium intercalation potential at a reference activity $a_{A,0}$. This relation allows to include the cation concentration effect into the formal potential E'_0, which is identical to the equilibrium potential at SOC = 50% in the intercalation isotherm in **Equation 17**. **Figure 26C** shows $E_{1/2}$ in relation to the logarithmically plotted concentration. The dashed line represents an extrapolation of **Equation 61** from $E_{A,0}$ at 0.25 M, replacing the activity by concentration. This, however, leads to an overestimation of E'_0 since $c \approx a$ is not valid at such high concentrations.[242]

5.3 Establishing a Model System

In the following chapters, the focus is set on discussing the degradation mechanisms (**Chapter 6**) as well as the fast-charging capability (**Chapter 7**) of PBA electrodes in aqueous electrolytes. For these studies, NiHCF thin-film electrodes are used as a model system.

As described in **Section 4.2.1.2**, NiHCF and other PBA thin-films can be immobilized on conductive substrates *via* electrochemical deposition from an aqueous solution containing Na^+, Ni^{2+} and $[Fe(CN)_6]^{3-}$ ions. In fact, this preparation technique has been known for over forty years.[243,244,245,246] The electrodeposition likely involves the pathways shown in **Equation 62**, including a preceding reduction of the $[Fe(CN)_6]^{3-}$ ion:[247,248,249]

$$[Fe(CN)_6]^{3-} + e^- \rightarrow [Fe(CN)_6]^{4-}$$
$$[Fe(CN)_6]^{4-} + Ni^{2+} + 2Na^+ \rightarrow Na_2Ni[Fe(CN)_6]$$
and
$$2[Fe(CN)_6]^{4-} + 3Ni^{2+} + 2Na^+ \rightarrow 2NaNi_{1.5}[Fe(CN)_6]$$
or
$$2[Fe(CN)_6]^{3-} + 3Ni^{2+} \rightarrow 2Ni_{1.5}[Fe(CN)_6]$$

Equation 62

Figure 27A shows the voltammetric response of a NiHCF thin-film electrode in 0.25 M $NaClO_4$. The CV entails a superposition of two peaks centered at ≈ 0.38 V and ≈ 0.46 V *vs*. SSC, representing the two possible stoichiometries formed during the synthesis procedure. This will be further discussed in the following section. In either case, $Fe^{II/III}$ remains the redox-active center in NiHCF, triggering the (de)insertion of Na^+ for charge compensation (**Equation 63**):[247,248,249]

A) $$NaNi^{II}[Fe^{III}(CN)_6] + Na^+ + e^- \rightleftarrows Na_2Ni^{II}[Fe^{II}(CN)_6]$$

and

B) $$Ni^{II}_{1.5}[Fe^{III}(CN)_6] + Na^+ + e^- \rightleftarrows NaNi^{II}_{1.5}[Fe^{II}(CN)_6]$$

Equation 63

For simplicity, this work will mainly refer to $Na_2Ni[Fe(CN)_6]$ without restriction of generality. The redox activity of $Fe^{II/III}$ is further reflected in the XPS spectra shown in **Figure 27B**. In the fully reduced (intercalated) state (0.1 V *vs*. SSC), one sharp peak associated with the Fe(II) oxidation state is visible in both sections of the spin-orbit doublet of the Fe 2p region. Upon electrode oxidation (0.8 V *vs*. SSC, deintercalation of Na^+); an additional peak associated with Fe(III) appears at higher binding energies.[250] In contrast, the Ni 2p region remains unchanged

within the investigated potential window proving the electrochemical inertness of Ni species (see **Figure 27C**).

The electrode mass Δm, as measured *via* EQCM, varies in strict accordance with the transferred charge ΔQ (see **Figure 27D**). By using **Equation 13**, an apparent molar mass of the intercalating species of 22.6 g/mol is obtained, confirming the charge compensation of the electrode's redox activity *via* the reversible transport of Na^+ ions (M = 22.9 g/mol) across the electrode-electrolyte interface (see **Figure 27E**). The galvanostatic charge-discharge curve of NiHCF in 8 M $NaClO_4$ is shown in **Figure 27F**. The specific capacity was determined as ≈ 68 mAh/g over a range of mass loadings from 10 – 20 µg/cm^2 (see **Figure 27G**), which is in good accordance with usually reported values.[62] As discussed in **Section 5.1**, this is around 20% below the theoretical value, which can be explained by redox-center vacancies and lattice hydration.

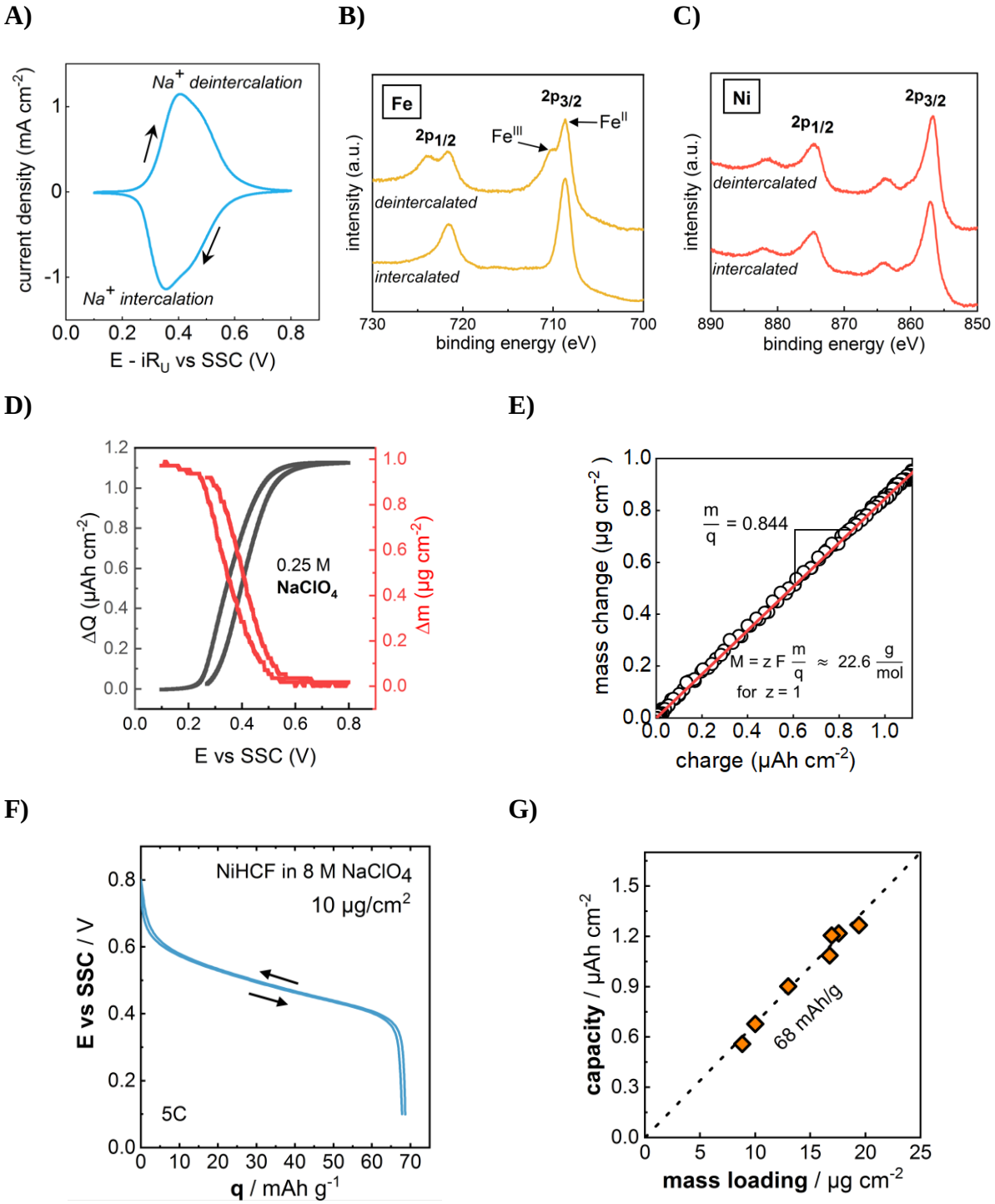

Figure 27. *(**A**) Representative CV of NiHCF in 0.25 M $NaClO_4$. The redox activity of $Fe^{II/III}$ centers is confirmed by the XPS spectra of the Fe 2p region (**B**), while the Ni 2p region remains unchanged (**C**). The transferred charge during (de)intercalation is correlated to the electrode's mass variation (**D**), indicating the reversible (de)insertion of sodium (**E**). The red line represents a fit of the data according to Faraday's law. (**F**) Representative galvanostatic charge-discharge curve of NiHCF in 8 M $NaClO_4$. (**G**) Correlation of the areal capacity and mass loading to obtain the specific capacity (see fitting line). **A**-**E** reprinted with permission from ref. 251. Copyright © 2023, American Chemical Society. Data in **F**-**G** reproduced with permission from ref. 225. Copyright © 2023, American Chemical Society.*

As seen in **Figure 28A**, the XRD pattern of the electrodeposited NiHCF thin-film corresponds well with a calculated *Fm-3m* reference structure for $Na_2NiFe(CN)_6$ (see **Figure 24**). The lattice constant can be calculated from the strong (200) peak using **Equation 55** and **Equation 56**, which yields 10.28 Å in good accordance with the literature.[84] This result matches well with the value obtained from DFT-optimization (10.32 Å). Further details can be found in ref. 251. The deposited thin-film is characterized by a rigid and homogenous coating on top of the Au-substrate, as visible from the SEM image in **Figure 28B**. As supported by the AFM image in **Figure 28C**, the film probably consists of polycrystalline vertical grains with an approximate horizontal size of around 100 nm and has, in general, a low surface roughness between 5 – 10 nm. Whereas the roughness remains low and independent of the mass loading, the film thickness scales linearly with the latter with a slope of 6.6 nm/(cm^2/µg) as determined for loadings below 20 µg/cm^2 (**Figure 28D**). Experimentally, thin films with a maximum mass loading of ≈ 100 µg/cm^2 could be achieved on Au substrates for the case of NiHCF (around 660 nm thickness). Beyond this, no further growth or even mass decay was observed, which is likely caused by the mechanical instability of the coating and partial detachment. This threshold might vary for other PBAs or substrates, but the order of magnitude is expected to be in the range of < 1 µm.

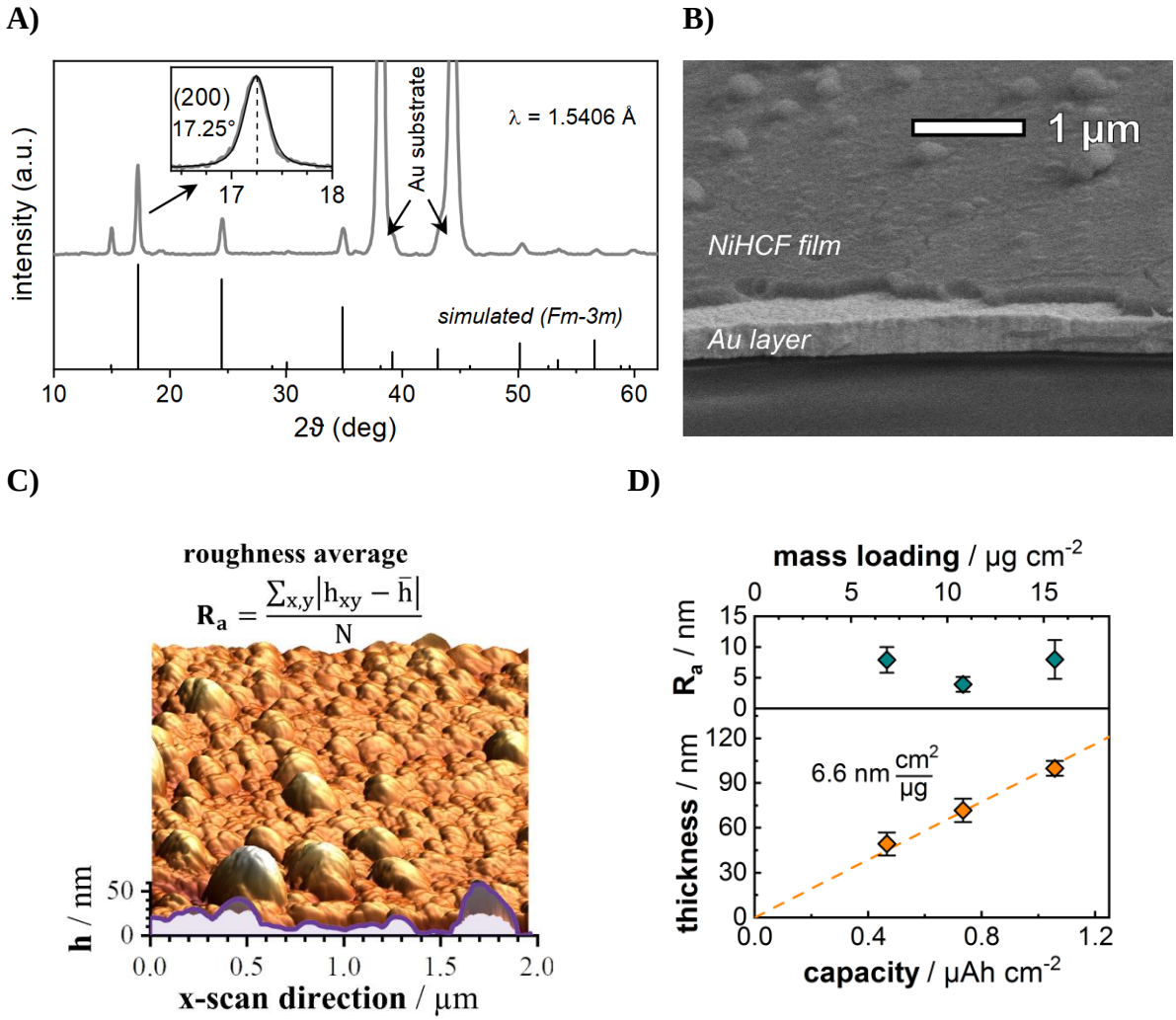

***Figure 28**. (**A**) Measured and simulated XRD pattern of $Na_2NiFe(CN)_6$. (**B**) SEM and (**C**) AFM images of a NiHCF thin-film electrodeposited on an Au-substrate. (**D**) Thickness and roughness of the coatings correlated to the areal capacity and mass loading. **A** reprinted with permission from ref. 251. Copyright © 2023, American Chemical Society. **B-D** adapted and reprinted with permission from ref. 225. Copyright © 2023, American Chemical Society.*

Lastly, the electrodeposited thin-film electrodes should be compared to a composite electrode prepared from co-precipitated NiHCF particles, as described in **Section 4.2.2**. **Figure 29A** shows the CVs of such electrodes in 8 M $NaClO_4$ at respectively slow scan rates of 1 mV/s (thin-film) and 0.05 mV/s (composite electrode). The redox response of the thin-film comprises the double-peak structure already described above. The peaks are centered around ≈ 0.44 V and ≈ 0.52 V *vs.* SSC, originating from the two possible stoichiometries obtained from the electrodeposition. The peak at the higher potential corresponds to **Equation 63A**, while the peak at the lower potential corresponds to **Equation 63B**.[247] In contrast, the composite electrode only consists of a single peak centered around ≈ 0.45 V *vs.* SSC.

The chemical synthesis of NiHCF from an aqueous solution, as described in **Section 4.2.2,** was reported to result in an approximate stoichiometry as presented in **Equation 64**:[252]

$$2[Fe(CN)_6]^{3-} + 3Ni^{2+} \rightarrow 2Ni_{1.5}[Fe(CN)_6] \qquad \textbf{Equation 64}$$

Accordingly, its redox activity is entirely described by **Equation 63B**, and the peak from the precipitated NiHCF particles appears in good agreement with the one at lower potential obtained for the thin-film electrode in line with the respective stoichiometries. As shown in **Figure 29B**, the XRD pattern of the chemically synthesized NiHCF powder is in good agreement with the thin film, and the absence of deviating diffraction peaks confirms that no undesired side products were formed. Furthermore, the lattice constant obtained for the powder sample agrees well with the thin-film (10.21 Å) and matches with values usually reported in the literature.[84,238,252]

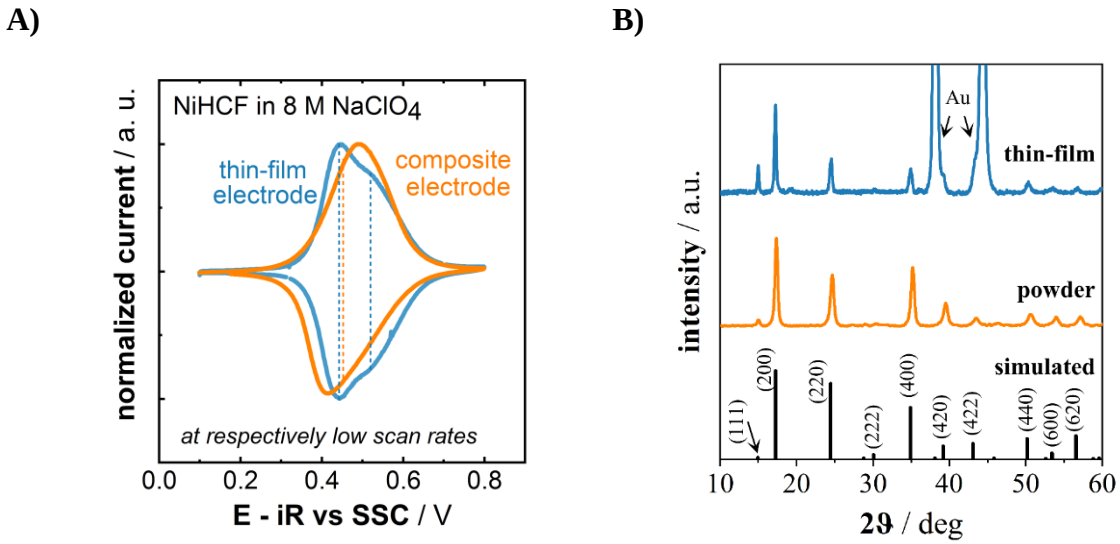

***Figure 29**. (**A**) CVs of a NiHCF thin-film and composite electrode in 8 M $NaClO_4$. The dashed lines indicate the center of the respective peak potentials. (**B**) Comparison of the XRD patterns of NiHCF thin-film and powder samples together with a simulated pattern for an Fm-3m reference structure ($Na_2NiFe(CN)_6$, a = 10.28 Å). Data in **B** reproduced with permission from ref. 225. Copyright © 2023, American Chemical Society.*

5.4 Excursion: Modelling of Charge-Discharge Characteristics in Quasi-Equilibrium

In this position, a brief perspective on a modelling-based approach to the charge-discharge characteristic based on the theoretical background provided in **Section 2.2.3** will be given. Such endeavor helps to build a solid understanding of a model system introduced for NiHCF in the previous section and verify underlying assumptions on the electrochemical properties and behavior of the material under operation. The aim of the simulation is to obtain the current (*i*), potential (*E*), and state-of-discharge (*X*) or specific charge (*q*) interdependencies for the two experimentally relevant cases of galvanostatic and potentiodynamic (dis)charging and compare it with the measured curves to verify the model. Here, *q* is related to the absolute charge *Q* as shown in **Equation 31**, and *Q* is obtained as the integral of *i* over the time *t* (see **Equation 28**). Furthermore, it should be remembered that *Q* and SOD/ *X* are related quantities according to **Equation 32**. This treatise has been presented by the author in ref. 225.

For the case of a constant-current discharge profile and a current low enough so that the system remains in quasi-equilibrium, the $E(q)$ characteristics are readily available as the intercalation isotherm (see **Equation 17**). **Figure 30A** shows the simulated discharge curve of NiHCF along with the underlying model and the respective parameters under the assumption of a single-phase active material using the Langmuir isotherm. It can be easily seen that the simulation does not accurately describe the experimentally obtained curve. This results from the fact that the electrodeposition of the NiHCF thin-film electrode yields two different stoichiometries and therefore electrochemically active phases, as already discussed in **Section 5.3**. Accordingly, the $E(q)$ characteristics must be modelled for both phases, which will be arbitrarily called A and B. Here, the factors A and B account for their relative share of the total material (A + B = 1). Furthermore, the respective states of discharge $X_{A,B}$ of each phase are given by:

$$X_A = \frac{q}{\mathrm{A} \cdot q_{max}}, \quad 0 < X_A < 1$$

$$X_B = \frac{\frac{q}{q_{max}} - \mathrm{A}}{\mathrm{B}}, \quad 0 < X_B < 1$$

The two-phase model already results in a significantly improved approximation of the experimentally obtained curve (see **Figure 30B**). Whereas the response of phase B, which is centered at the lower formal potential, is in good accordance with the model, the simulation of phase A, which is centered at the higher formal potential, is too narrow compared to the

measured curve. This is likely caused by an oversimplification using the Langmuir isotherm, which neglects the interaction of intercalated ions with the host lattice. This is accounted for by using a Frumkin-type isotherm with the phenomenological parameter g (see **Equation 65**):

$$E_{eq} = E_0' + \frac{RT}{F}\ln\left(\frac{1-X}{X}\right) + \frac{RT}{F}\cdot g\cdot\left(\frac{1}{2}-X\right) \qquad \textbf{Equation 65}$$

Here, $g > 0$ represents repulsive interaction and $g < 0$ attractive interaction, leading to a broadening or narrowing of the $E(q)$ characteristics. A theoretical treatment and further description are provided in great detail in refs. 141 and 142. The correspondingly adapted simulation of phase A with $g = 2$ (see **Figure 30C**) results in almost perfect correspondence with the measurement.

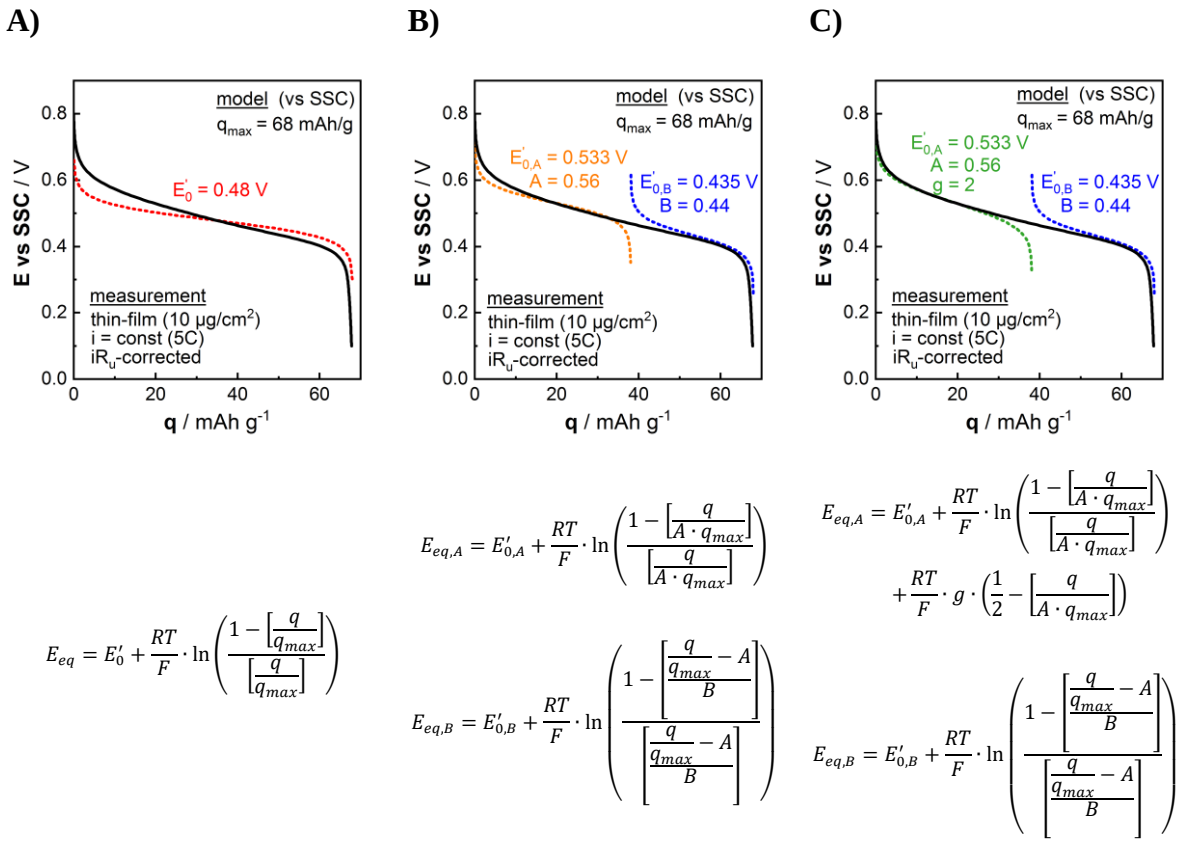

Figure 30*. Modelling approach for the galvanostatic discharge characteristics of NiHCF in 8 M $NaClO_4$ using (**A**) a single-phase Langmuir intercalation isotherm, (**B**) two-phase Langmuir intercalation isotherms and (**C**) two-phase Frumkin and Langmuir intercalation isotherms. For further details see the text. The parameters used for the indicated models are given in the respective graphs. Furthermore, 25°C was used as the temperature. Data reproduced with permission from ref. 225. Copyright © 2023, American Chemical Society.*

In conclusion, the response of a 10 µg/cm^2 NiHCF thin-film electrode in 8 M $NaClO_4$ to constant-current discharge is very well described by a model employing two phases identical to $Na_2NiFe^{II}(CN)_6$ / $NaNiFe^{III}(CN)_6$ (phase A, $E'_0 \approx 0.533$ V *vs.* SSC, 56% of total active

material, repulsive ion-host interaction with g = 2) and $NaNi_{1.5}Fe^{II}(CN)_6$ / $Ni_{1.5}Fe^{III}(CN)_6$ (phase B, E'_0 = 0.435 V *vs*. SSC, 44% of total active material, no ion-host interaction) and a total specific capacity of 68 mAh/g. It should be noted that the respective formal potentials are in great agreement with the values extracted from the CV curves in the previous section (see **Figure 29A**). The reason why only the model of one phase requires the involvement of the ion-host interaction is not clear at this point and will not be discussed further, as it is beyond the scope of this thesis.

For the case of potential control as in cyclic voltammetry ($E = E_{start} + \nu \cdot t$), the treatment is more complicated. In general, the current is defined as:

$$i = \frac{\mathrm{d}Q}{\mathrm{d}t}$$

In equilibrium, it holds that:

$$i = \frac{\mathrm{d}Q}{\mathrm{d}t} = \frac{\mathrm{d}Q}{\mathrm{d}E} \cdot \frac{\mathrm{d}E}{\mathrm{d}t} = \frac{\mathrm{d}Q}{\mathrm{d}E} \cdot \nu$$

The so-called differential capacity[ii] dQ/dE is obtained from the intercalation isotherm $E(X)$:

$$\frac{\mathrm{d}Q}{\mathrm{d}E} = Q_{max} \cdot \frac{\mathrm{d}X}{\mathrm{d}E}$$

For a reversible, single-phase system described by the Langmuir isotherm, dX/dE can be analytically calculated from **Equation 17**, and the equilibrium current-potential characteristics for a CV is given by **Equation 66**:[141]

$$i = \nu \cdot Q_{max} \cdot \frac{\mathrm{d}X}{\mathrm{d}E} = \nu \cdot Q_{max} \cdot \frac{F}{RT} \cdot \frac{\exp\left(\frac{F}{RT}(E - E'_0)\right)}{\left[1 + \exp\left(\frac{F}{RT}(E - E'_0)\right)\right]^2} \qquad \textbf{Equation 66}$$

Accordingly, the current response is symmetrically centered around the formal potential ($E = E'_0$) and is proportional to the scan rate, while it only depends on the overall capacity of the active material, the temperature and the momentary potential. The maximum of $i(E)$ is obtained at the formal potential and is given by

$$i_{peak} = \nu \cdot Q_{max} \cdot \frac{F}{4 \cdot RT}$$

Interestingly, these results are entirely identical to the characteristics of a thin-layer electrochemical cell (no mass transport limitations, cell thickness smaller than diffusion layer thickness) with solvated redox-active species, where Q_{max} is accordingly replaced by FVC^*

[ii] It is easily recognized from these relations why purely capacitive charge-storage processes (dQ/dE = const) result in a rectangular-shaped CV.

(*F* is the Faraday constant, *V* corresponds to the solution volume and C^* the concentration of redox species).[119]

For non-equilibrium conditions (sluggish kinetics and/or slow mass transport), the exact current-potential dependency becomes more complicated and will not be further discussed herein. The experimentally observable peak current i_{peak} and peak position E_{peak} as a function of the imposed scan rate can serve as straightforward diagnostic criteria to differentiate these cases as introduced in **Section 3.1.1**.

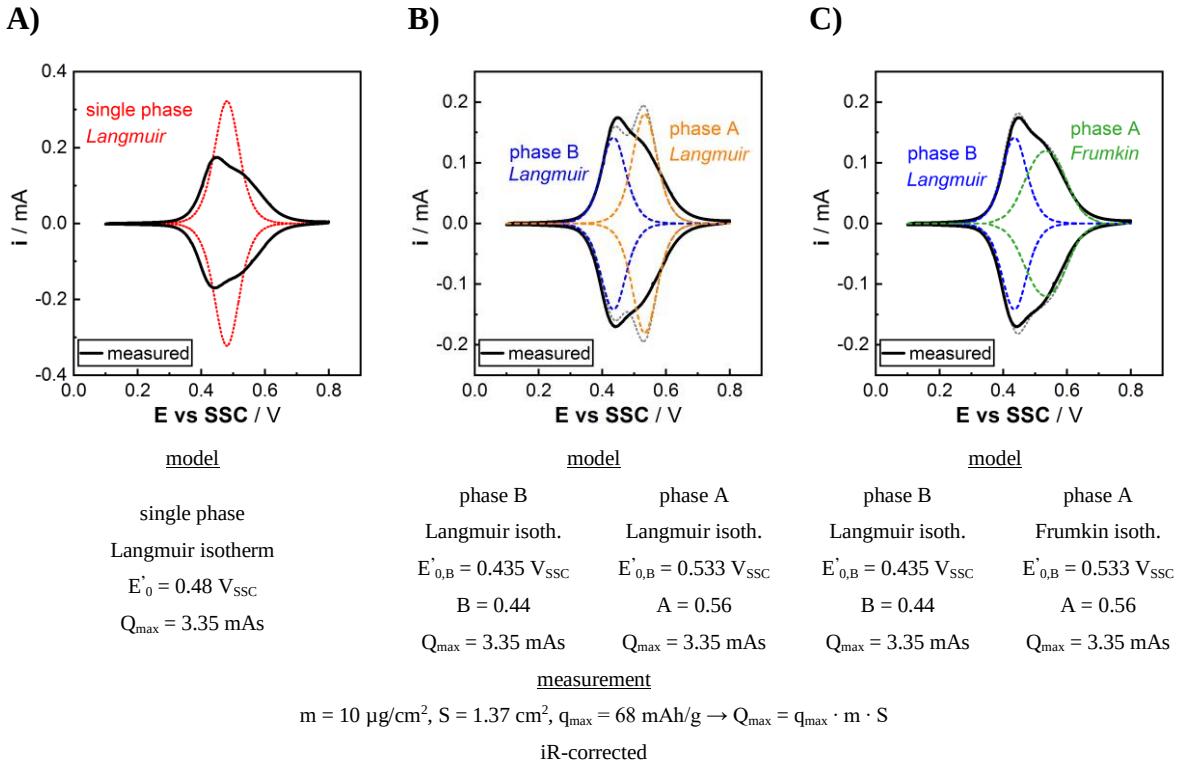

***Figure 31**. Modelling approach for the CV characteristics (at 10 mV/s) of NiHCF in 8 M $NaClO_4$ using (**A**) a single-phase Langmuir intercalation isotherm, (**B**) two-phase Langmuir intercalation isotherms and (**C**) two-phase Frumkin and Langmuir intercalation isotherms. For further details see the text. The employed parameters used for modelling are given below the respective graphs. Furthermore, 25°C was used as the temperature. Data reproduced with permission from ref. 225. Copyright © 2023, American Chemical Society.*

As for the galvanostatic case, a single-phase model using the Langmuir isotherm based on **Equation 66** cannot adequately describe the CV response of NiHCF (see **Figure 31A**). Similarly, a model based on two phases using the Langmuir isotherm fails to simulate the experimentally observed *i*(*E*) characteristics (see **Figure 31B**). To calculate the current stemming from each phase, Q_{max} must be multiplied with the respective stoichiometric factor A or B. As discussed above, a Frumkin isotherm accounting for ion-host interaction and leading to a peak-broadening must be used for the CV peak at higher potential ($Na_2NiFe^{II}(CN)_6$ /

$NaNiFe^{III}(CN)_6$, phase A). However, an analytical solution of dX/dE is not available for **Equation 65**. Therefore, dX/dE was graphically determined as the derivative of the $X(E)$ dependency used in the previous modelling of the galvanostatic discharge curve.[iii] The superposition of the resulting modelled curves for phases A and B perfectly matches the experimentally measured CV as shown in **Figure 31C**. The overall model of the electrode can be easily adapted for different mass loadings as expressed by:

$$\frac{i}{v} = Q_{max} \cdot \frac{\mathrm{d}X}{\mathrm{d}E_{total}} = q_{max} \cdot m \cdot \frac{\mathrm{d}X}{\mathrm{d}E_{total}}$$

The high accordance of the calculated $E(Q)$ and $i(E)$ responses with the experimental data in both the galvanostatic and potentiodynamic case by using the identical models and parameters, respectively, confirms the accuracy and self-consistency of the employed theoretical approach. It should be remembered that these models only apply to quasi-equilibrium conditions, and more complicated dependencies must be considered for non-negligible kinetic and mass transport limitations. This will be discussed in detail in **Chapter 7**.

[iii] From this perspective, it becomes clear why the dQ/dE *vs.* E plot, which is calculated from the galvanostatic cycling data and is commonly used in battery research whenever no CV was measured, is a good approximation to the i/v *vs.* E dependency obtained from CV.

6 Degradation Mechanisms of PBA Electrodes in Aqueous Media

6.1 Introduction and Background

As outlined in **Chapter 1,** the cycling stability of a battery is one of the most important properties to consider for stationary applications. For traditional LIBs, this topic has been thoroughly investigated over the last decades, resulting in various excellent discussions and reviews describing the effects limiting the lifetime of batteries.[253,254,255] Among others described therein, electrolyte decomposition and subsequent SEI formation, loss of lithium-inventory, and SEI instability have been identified as important drivers for capacity decay. Transition metal dissolution from the cathode and subsequent plating on the anode, particle cracking, phase transitions and structural disorder, or dendrite formation are furthermore considered as major degradation pathways. However, most of these processes cannot be transferred straightforwardly, or they are not applicable to aqueous systems.

For PBAs in aqueous media, many previous studies focused on the electrolyte pH as a crucial factor governing electrode stability with both strongly acidic (low pH)[256,257,258,259,260] and basic (high pH)[227,228,256,261,262] solutions initiating severe material deterioration. Apart from this, discussed degradation pathways include mechanical stress and phase transformations upon intercalate insertion, structural instability due to lattice distortions, vacancies and defects, as well as unspecified trace solubility of active material.[62,63,69,263,264] Effective stabilization measures for PBAs are, however, well known in the literature. These involve electrolyte optimization (such as using highly concentrated salt solutions, acidification, and additives or co-solvents),[84,95,161,233,241,263 265,266,267,268,269,270] protective core-shell structures or coatings of the active material,[62,63,263,271,272,273] as well as improved synthesis methods, transition-metal doping, and other treatments for higher structural stability.[62,63,269, 274,275,276,277,278,279]

Whereas most research efforts in the past focused on structural instability and general stabilization techniques for PBAs, the specific role of the electrolyte composition on capacity fading has been largely overlooked. Consequently, the underlying physico-chemical mechanisms driving active material dissolution in aqueous solutions as a function of pH, anions, and cation concentration remain mostly unclear. This chapter aims to build a systematic

and fundamental understanding of these processes to serve as a basis for refining the interpretation of experimental results and optimization of PBAs for ASIB applications. Furthermore, a subsequent second-order degradation mechanism will be discussed based on active material passivation and deteriorated rate capability due to faulty re-crystallization from dissolved active material constituents.

The ideas, findings, discussions, and analyses presented in this chapter are based on the following published articles and originated from close collaboration with the mentioned co-authors: "X. Lamprecht, F. Speck, P. Marzak, S. Cherevko, A.S. Bandarenka. **Electrolyte effects on the stabilization of Prussian blue analog electrodes in aqueous sodium-ion batteries**. *ACS Applied Materials and Interfaces* **2022**, *14*, 3515-3525" and "X. Lamprecht, I. Evazzade, I. Ungerer, L. Hromadko, J. M. Macak, A. S. Bandarenka, V. Alexandrov. **Mechanisms of degradation of $Na_2Ni[Fe(CN)_6]$ functional electrodes in aqueous media: a combined theoretical and experimental study**. *The Journal of Physical Chemistry C* **2023**, *127*, 2204–2214". Both articles are reprinted in the appendix. Furthermore, some aspects and findings herein (especially in **Sections 6.2** and **6.3.1**, as well as in parts of **Sections 6.4** and **6.5**) have been initially presented in the author's Master's thesis (see ref. 280) and served as a starting point for the systematic study elaborated in the following.

6.2 Manifestation of Electrode Degradation

As a zero-strain material with negligible lattice volume change during intercalate insertion,[62] NiHCF is an ideal model system to study the influence of the electrolyte composition on the deterioration of active material. Furthermore, using thin-film electrodes with pure active material circumvents other effects usually observed in composite electrodes with conductive additives and binders, like structural degradation, active-material contact loss, binder deterioration, or porosity effects.[253] An extensive characterization of NiHCF thin-film model electrodes is provided in **Section 5.3**. In the following, it will be initially elucidated how the electrode degradation manifests itself during battery operation before discussing the underlying mechanism in the following sections.

Figure 32A shows the evolution of the available electrode capacity of NiHCF during continuous cycling in 0.25 M Na_2SO_4, an electrolyte typically used for ASIB studies. Furthermore, the electrode mass was monitored *via* EQCM. An advancing loss of capacity is observed, which constitutes a fatal deterioration of the electrode's cycling capability. It should be noted that the time per cycle significantly decreases (see upper axis) due to the application of a constant current. Hence less and less charge is stored with advancing time. Furthermore, the electrode mass decreases linearly over time. However, the relative extent is much less pronounced than the capacity decay: after 1700 cycles around 25% of the electrode mass is lost, while the remaining material is uncapable of storing any charge indicating a 100% loss of available capacity. The coulombic efficiency remains very high over the entire experiment, evidencing the absence of side reactions, which therefore cannot explain the material fatigue. The constant rate of mass loss, however, strongly implies an ongoing dissolution process.

This was further investigated by employing voltammetric cycling with open-circuit periods, as shown in **Figure 32B**. Whereas the NiHCF electrode seems to be entirely stable in its fully reduced (intercalated) state, a significant loss of material and available capacity is observed in its fully oxidized (deintercalated) state. As in the galvanostatic case, both capacity decay and material dissolution proceed during the subsequent CV cycling period. After this sequence, around 5.5 µg of active material is lost, corresponding to a theoretical capacity of ≈ 0.4 µAh using the specific capacity of NiHCF (68 mAh/g). This is, however, well below the actual capacity decline of around 1.0 µAh.

A)

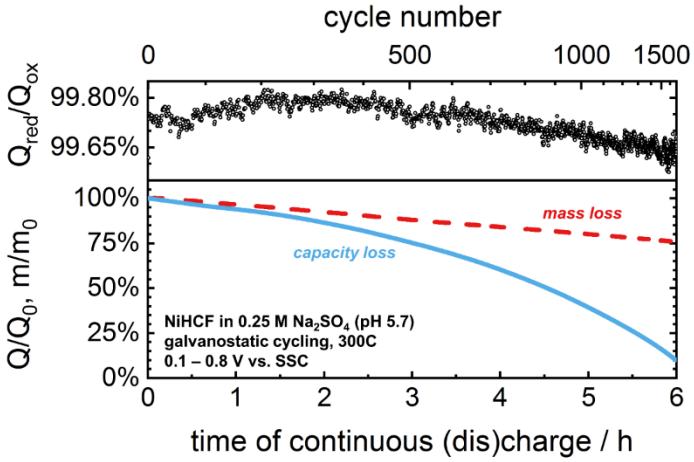

B)

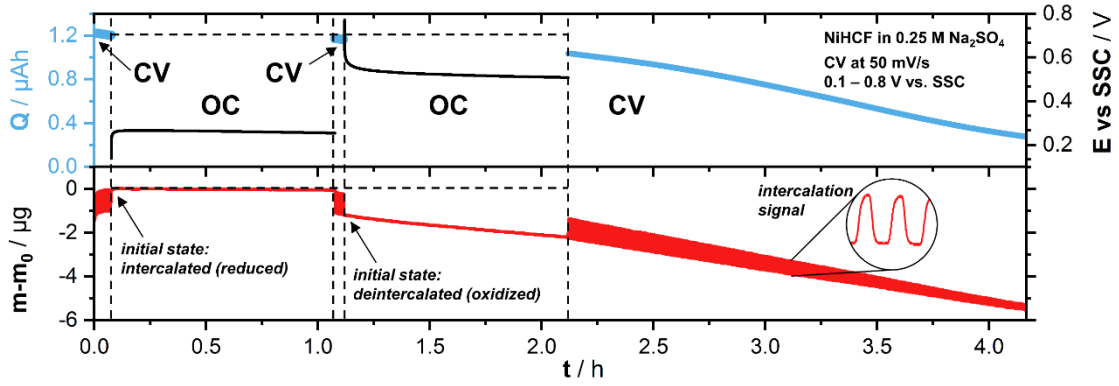

***Figure 32**. Capacity and mass loss of NiHCF electrodes in 0.25 M Na_2SO_4 during (**A**) consecutive galvanostatic cycling and (**B**) voltammetric cycling interrupted by open circuit periods in charged and discharged states, respectively. Reprinted with permission from ref.* 281. *Copyright © 2022, American Chemical Society.*

These disproportionate relations of mass and capacity loss indicate that the electrode degradation proceeds *via* a two-fold mechanism: an ongoing active material dissolution and a passivation of the remaining electrode inhibiting its ability to store charge by Na^+ (de)intercalation. These processes will be successively discussed in detail in the following.

6.3 Active Material Dissolution

Dissolution processes of materials in electrochemical applications, such as batteries or electrocatalysts, are generally very complex and can be strongly coupled to the electrode potential and current, as well as the electrolyte composition.[282] Most state-of-the-art methods are based on *post-mortem* analyses, which can only give limited insights into specific transient degradation phenomena.[283] The following sections will present an innovative technique for investigating the real-time elemental electrode constituent leaching rates during battery operation, along with the results obtained for NiHCF and CoHCF model electrodes. Afterward, the impact of the electrolyte composition on the active material stability will be systematically studied by a combined experimental and computational approach.

6.3.1 In-Operando Quantification with Elemental Sensitivity

As presented above, the EQCM technique gives an approximate insight into the overall material loss. However, it lacks elemental sensitivity, *i.e.*, disclosing individual leaching rates of the electrode constituents. Furthermore, its poor resolution and overlay with the (de)intercalation signal (see magnified view in **Figure 32B**) does not allow any correlation to the ongoing potential- and current-dependent dissolution processes. Taking the values presented in **Figure 32**, a mean dissolution rate in the order of < 1 ng cm^{-2} s^{-1} is obtained.

The most straightforward and common battery research approach involves an *ex-situ* electrolyte analysis after cycling to identify leached electrode constituents quantitatively. A few examples of the transition metal dissolution from active battery materials can be found for Li-transition-metal-oxides in refs. 284, 285, 286 and for PBAs in refs. 269, 270, 273, 287, 288, 289, 290, 291, 292. Whereas this resolves the problem of elemental sensitivity, again, no real-time correlation to the electrochemical processes during cycling is achieved in this way. More advanced and hyphenated techniques are highly needed in electrochemical research to gain meaningful and valuable insights into the degradation mechanisms of functional electrodes.[282,293]

New approaches in this direction involve the real-time analysis of evolving gas, such as C_2H_4, H_2, or CO_2, which originates from side reactions inside the cell. These involve electrolyte and SEI decomposition, yielding indirect insights into the ongoing degradation processes.[294,295,296] Another *operando* approach is based on x-ray absorption analysis of dissolved transition-metal ions, which enables the direct correlation between applied electrochemistry and detrimental

side reaction intermediates, but its applicability is limited by low time resolution in the range of several minutes.[297,298] A further discussion of appropriate techniques can be found in refs. 282, 293, 299 and 300. Overall, methods for directly examining the dynamics of electrode constituent dissolution are still scarce, and only a few reports have provided insights into real-time or *in situ* detection of elemental leaching rates during battery operation.[281,293,301,302,303,304,305]

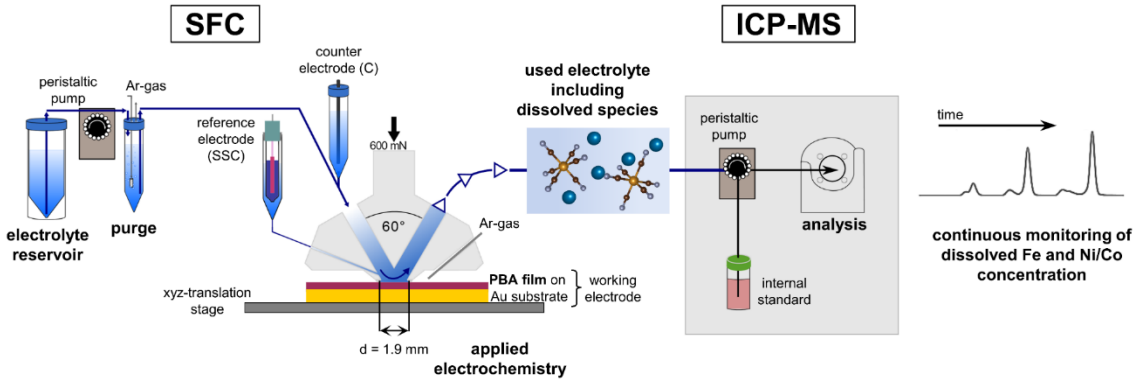

***Figure 33**. Scheme of the in-operando setup used for online dissolution monitoring. It includes a flow cell that continuously pumps the electrolyte from a battery thin-film electrode surface towards an ICP-MS for the detection of dissolved electrode constituents during electrochemical cycling. Reprinted with permission from ref. 281. Copyright © 2022, American Chemical Society.*

Online dissolution monitoring by coupling an inductively coupled plasma mass spectrometer (ICP-MS) to an electrochemical cell enables the *in-operando* correlation of dynamic leaching rates of electrode constituents to the applied electrochemistry with high elemental sensitivity and gravimetric resolution.[306,307,308] Whereas this approach has already been successfully employed to investigate the dissolution of electrocatalysts in various studies,[307,309,310,311,312,313,314] only very few have so far adopted this technique in the field of battery research.[302,304] The results presented herein from ref. 281 are among the first of such reports. **Figure 33** shows a schematic representation of the setup, which involves a scanning flow cell (SFC) that constantly pumps electrolyte from the electrode surface towards the ICP-MS for continuous tracing of dissolved species. The flow cell contains a counter and reference electrode, which allows to perform electrochemical experiments with the investigated sample as the working electrode. A more detailed description of the technique and setup can be found in ref. 307. Dr. S. Cherevko and Dr. F. Speck are gratefully acknowledged for performing the flow-cell ICP-MS experiments. The reader is referred to the original publication for details regarding the operation of the flow cell and ICP-MS in the study presented herein.[281] It should

be noted that only diluted electrolytes could be used in compliance with the ICP-MS analyzing unit. Furthermore, the detection of elemental iron by the ICP-MS very likely corresponds to an extraction of the entire $[Fe(CN)_6]$-complex, as it is highly stable by itself.[256,262,315]

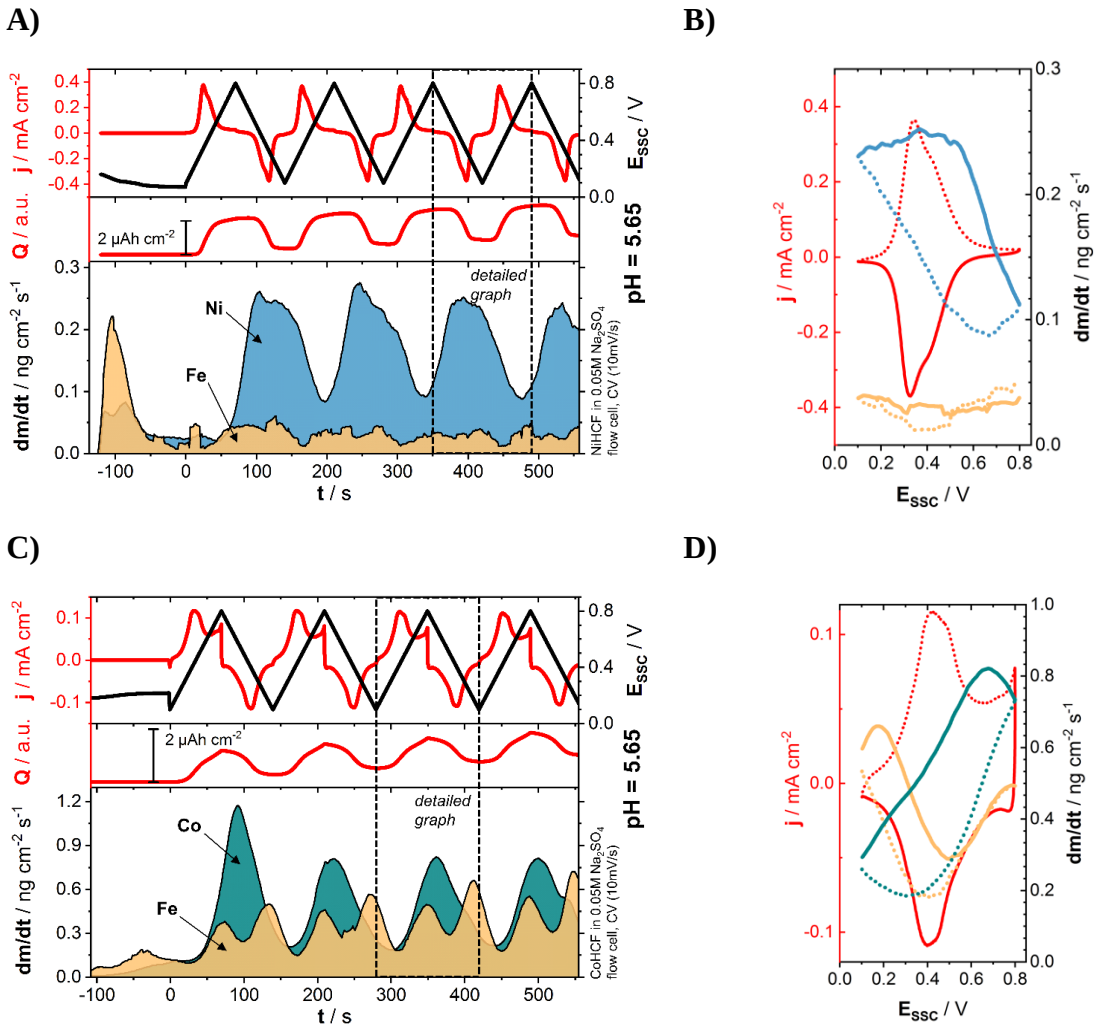

***Figure 34**. In-operando dissolution profiles detected by the online flow-cell ICP-MS technique of (**A**) Ni and Fe from NiHCF and (**C**) Co and Fe from CoHCF during an initial open-circuit period, followed by four CV cycles in 0.05 M Na_2SO_4 at neutral pH. The elemental dissolution rates are correlated to the potential together with the current in a detailed, CV-like representation for one exemplary cycle in (**B**) for NiHCF and (**D**) for CoHCF. The dotted lines correspond to the oxidation, and the solid lines to the reduction direction. Reprinted with permission from ref. 281. Copyright © 2022, American Chemical Society.*

Figure 34A shows the elemental dissolution rate of iron and nickel from NiHCF in 0.05 M Na_2SO_4 at neutral pH during an initial open-circuit period, followed by four CV cycles. The transient dissolution peak upon contact of the electrode with the electrolyte in the beginning probably results from an initial wash-away of surface defects. It is visible that the dissolution of nickel is much more pronounced than that of iron. During each CV cycle, roughly 23 ng/cm^2

of Ni are lost, which is five times more than Fe. Furthermore, the dissolution rate of nickel strikingly correlates with the electrode current (see **Figure 34B**), in contrast to that of iron. The extraction is minimum in the fully oxidized state, but immediately rises upon the onset of reductive currents ($Fe^{III} + e^- \rightarrow Fe^{II}$ and intercalation of Na^+ into NiHCF). A maximum is reached at the peak current and stays at a high level until the electrode is fully reduced. Once the potential scan direction is reversed and oxidative currents set in ($Fe^{II} \rightarrow Fe^{III} + e^-$ and deintercalation of Na^+ from NiHCF), the leaching rate decreases continuously until reaching its minimum in the fully oxidized state. In the meantime, the extraction of iron remains at a low, rather constant level, regardless of the electrochemical processes.

As another example of a PBA material, **Figure 34C** shows the dissolution of cobalt and iron from CoHCF under similar conditions as for NiHCF. As for the latter, a very distinct pattern can be seen for both Co and Fe. However, the absolute extraction is much higher, with ≈ 68 ng/cm^2 per cycle for cobalt, which is on average only 20% more than that of iron. It should be noted that in contrast to NiHCF, where Ni is electrochemically inert, CoHCF has, in general, two redox transitions, as shown in **Equation 67**: [275]

$$\begin{aligned} &Na_2Co^{II}[Fe^{II}(CN)_6]_{\text{rhombohedral}} \\ &\quad \rightleftarrows Na^+ + e^- + NaCo^{III}[Fe^{II}(CN)_6]_{\text{cubic}} \\ &\quad \rightleftarrows Na^+ + e^- + Co^{III}[Fe^{III}(CN)_6]_{\text{cubic}} \end{aligned} \qquad \textbf{Equation 67}$$

The $Co^{II/III}$ transition occurs at lower potentials and corresponds to the full peak seen in **Figure 34D**, while the $Fe^{II/III}$ transition occurs at higher potentials and is only slightly visible in the presented data. This double peak structure is reflected in the dissolution pattern of Fe in **Figure 34C** and **Figure 34D**. The redox activity of cobalt is associated with a phase transition of the CoHCF lattice,[316] which likely causes the increased dissolution of Fe towards lower potentials due to the associated phase and volume change of the lattice. The dissolution of cobalt increases in the vicinity of the $Fe^{II/III}$ transition, while it is in general higher during electrode reduction than oxidation. This behavior is in good accordance with the dissolution of Ni from NiHCF.

Apart from the data presented herein, similar experiments were also conducted in alkaline and acidic Na^+-electrolytes, and the reader is referred to the original publication for a detailed discussion.[281] Overall, the employed online dissolution monitoring technique has demonstrated the ability to access the individual electrode constituent extraction pattern directly and has proven to be a valuable tool in battery materials research. Although the dissolution study conducted in this case is limited in its knowledge of long-term trends, the technique can be

easily adapted in future experiments. Apart from other battery materials and electrolytes, the elemental dissolution profiles could also be investigated during more realistic battery operation scenarios, such as galvanostatic and potentiostatic (dis)charging at varying rates and extended resting periods.

It can be concluded from these experiments that the degradation of PBAs at neutral pH and phase-preserving redox transitions is strongly driven by selective extraction of the N-coordinated transition metal (see **Figure 35A**). This is generically expressed by **Equation 68**:

$$A_xTM^{(1)}\left[TM^{(2)}(CN)_6\right] \rightarrow A_xTM^{(1)}_{1-\square}\left[TM^{(2)}(CN)_6\right] + \square \cdot TM^{(1)}_{solvated} \qquad \textbf{Equation 68}$$

Accordingly, it can be easily understood why the addition of a small amount of N-coordinated $TM^{(1)}$ ions into the electrolyte can reduce the driving force of this process and thereby significantly decrease the dissolution of the material during cycling, as reported by Wang *et al.*[265] and Wessels *et al.*[264] As shown in **Figure 35B**, the stability of NiHCF in 0.25 M Na_2SO_4 is strongly enhanced by adding 1 mM Ni^{2+} into the electrolyte.

A) **B)**

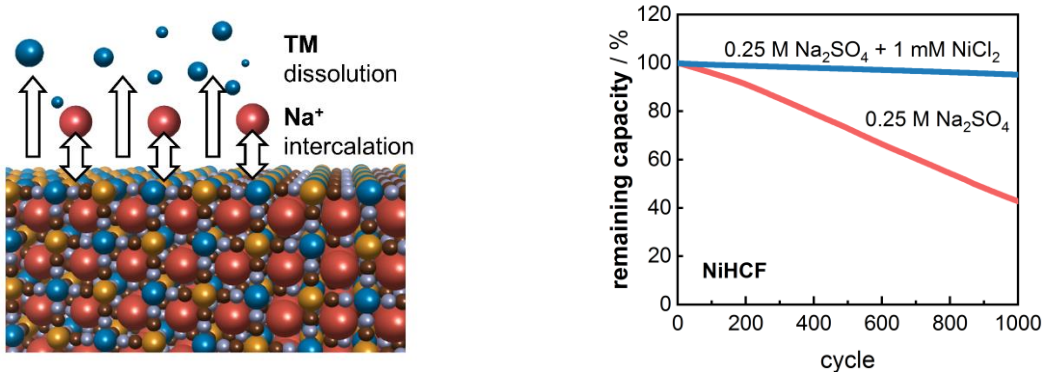

***Figure 35**. **(A)** Schematic illustration of the dissolution of the N-coordinated transition metal from a PBA electrode during cycling. **(B)** Stability of NiHCF in 0.25 M Na_2SO_4 with and without the addition of 1 mM $NiCl_2$ during galvanostatic cycling at 300C.*

6.3.2 A Combined Experimental and Computational Approach

As discussed in the previous chapter, the rate of transition metal extraction was found to be explicitly coupled to the electrochemical processes of the electrode, with a distinct prevalence of dissolution associated with reductive currents. However, the underlying mechanisms driving it on an atomistic level remained unclear, which motivated to expand the methodology to

investigate the degradation phenomena. The combination of experimental and computational/theoretical approaches has proven to be a highly effective strategy for gaining fundamental understanding of electrochemical processes and the design of optimized functional materials.[317,318,319,320,321,322,323,324,325] In this chapter, density functional theory (DFT) calculations are used to support the experimental findings with the goal of elucidating the interfacial properties and identifying the processes driving the mechanisms of dissolution of NiHCF model electrodes as a function of the electrolyte composition. An introduction of these computational methods is far beyond the scope of this thesis and the interested reader is referred to the dedicated literature referenced above. Prof. Dr. V. Alexandrov and Dr. I. Evazzade are gratefully acknowledged for performing the theoretical calculations presented in the following. The computational details of this study are reported in the original publication.[251] The electrochemical experiments were performed in close collaboration with I. Ungerer, whose Bachelor's thesis was advised as part of this project.[326]

6.3.2.1 Effect of pH

In this section, the degradation mechanisms towards the edges of the pH-scale will be analyzed successively.

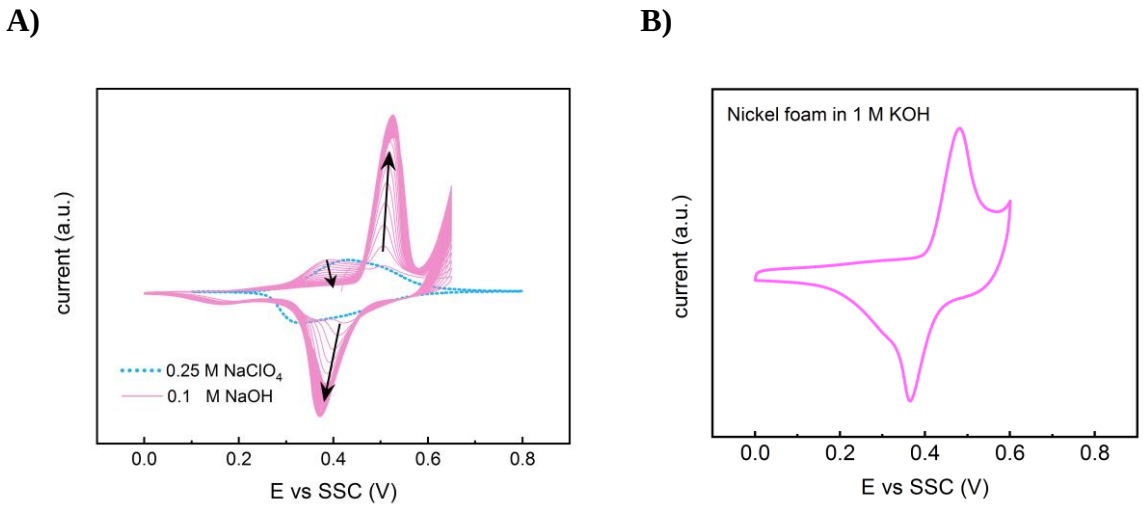

***Figure 36**. (**A**) Transformation of NiHCF in 0.1 M NaOH during CV cycling toward nickel hydroxide/oxyhydroxide. The response of NiHCF in 0.25 M $NaClO_4$ is depicted for comparison. Reprinted with permission from ref. 251. Copyright © 2023, American Chemical Society. (**B**) CV of pure nickel foam in 1 M KOH for comparison.*

It has been shown by previous studies that the degradation of NiHCF in basic solutions with abundant OH^- is characterized by an entire loss of $[Fe(CN)_6]$-species, while the electrode is

gradually transformed toward surface-confined nickel hydroxide/oxyhydroxide.[227,228,262,281] A possible pathway of this process is reflected by **Equation 69**:

$$\mathrm{Na_xNi^{II}[Fe^{II/III}(CN)_6]} + 2\mathrm{OH^-} \rightarrow \mathrm{x \cdot Na^+} + \mathrm{Ni^{II}(OH)_2} + \mathrm{[Fe^{II/III}(CN)_6]^{4/3-}} \qquad \textbf{Equation 69}$$

As seen in **Figure 36A**, the typical CV response of a NiHCF electrode almost immediately disappears during cycling in 0.1 M NaOH with pH = 13. In fact, the CV becomes very similar to that of pure nickel foam in an alkaline solution (see **Figure 36B**). The emergence of the characteristic $Ni(OH)_2$/NiOOH redox couple (see **Equation 70**), as well as the catalytically enhanced OER at the anodic vertex in the CV confirm the formation of the new phase.[76,227]

$$\mathrm{Ni^{II}(OH)_2} \rightleftarrows \mathrm{Ni^{III}OOH} + \mathrm{H^+} + \mathrm{e^-} \qquad \textbf{Equation 70}$$

Based on this long-known instability of PBAs in basic solutions, the reduction of OH^- concentration in the electrolyte by intentional acidification has been introduced by Wessells *et al*. as a stabilization measure for electrodes.[84,268] Indeed, as seen in **Figure 37A**, decreasing the pH of 0.25 M $NaClO_4$ from 5.7 to 3.1 *via* the addition of $HClO_4$ undoubtedly enhances the stability of NiHCF during cycling. However, a too strong acidification towards pH = 0.6 in a 1:1 solution of 0.25 M $NaClO_4$ and 0. 25 M $HClO_4$ has the opposite effect: the electrode degradation is significantly accelerated, which will be discussed later.

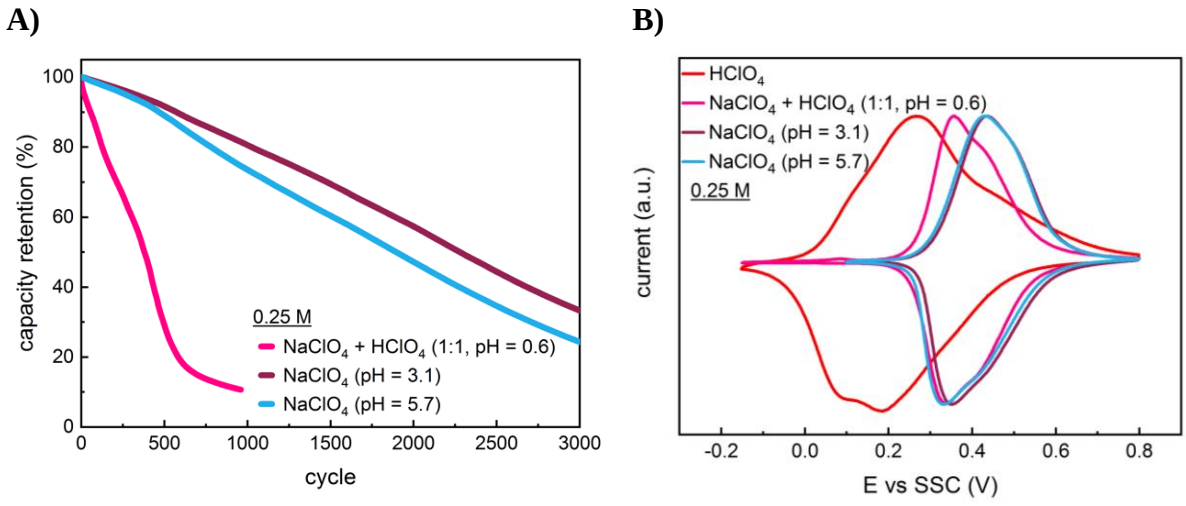

***Figure 37**. (**A**) Cycling stability of NiHCF for different H^+/Na^+ availabilities in the electrolyte and (**B**) corresponding CVs. Reprinted with permission from ref. 251. Copyright © 2023, American Chemical Society.*

A closer look at the respective CVs (see **Figure 37B**) in these equally concentrated solutions reveals that for the 1:1 H/$NaClO_4$ mixture the CV is shifted to the left. At the same time, for the acidified $NaClO_4$ electrolyte the CV is identical to the unmodified one. For comparison, the CV of NiHCF in pure 0.25 M $HClO_4$ is also shown, with the redox peak being located at significantly lower potentials compared to the ones with Na^+ present in the solution. As explained in **Section 5.2**, the position of the formal potential is determined by both the concentration and the nature of the intercalating species. Since the formal potential for an intercalation reaction is directly linked to Gibb's free energy of ion solvation, it appears reasonable that the insertion of the small, hydrated proton would be thermodynamically less favorable compared to the larger sodium ion. Correspondingly, the CV peak of NiHCF in pure $HClO_4$ appears at lower potentials compared to $NaClO_4$ for equally concentrated solutions. According to **Equation 61** and by reasonably approximating $a \approx c$ at the employed concentrations, the CV of the 1:1 H/$NaClO_4$ solution should be shifted by ≈ 18 mV towards lower potentials compared to the 0.25 M $NaClO_4$ reference since the concentration of Na^+ is only 0.125 M. However, the experimentally obtained shift is ≈ 30 mV. This hints towards a partial co-insertion of H_3O^+ next to Na^+. It has been reported that the coincident insertion of two cationic species A and B from a solution results in a single CV peak with its formal potential being between the two individual formal potentials $E'_{0,A}$ and $E'_{0,B}$.[240] Thus, the resulting E'_0 for the mixed insertion indicates the dominating intercalate from A and B, which is clearly Na^+ in this case (see **Figure 37B**).

Another way to identify the intercalating species is to analyze its apparent molar mass using Faraday's law (**Equation 13**) and the EQCM data measured while cycling the electrodes. As discussed in **Section 5.3**, a value of M_{app} = 22.99 g/mol would be expected for the insertion of sodium ions. This presumption is fulfilled when cycling NiHCF in the acidified 0.25 M $NaClO_4$ (pH = 3.1) electrolyte (see **Figure 38A**). In turn, for the intercalation of H_3O^+, an apparent molar mass of 19 g/mol would be expected. However, it was found for NiHCF in 0.25 M $HClO_4$ that M_{app} strongly fluctuates between 8.2 g/mol and 19.4 g/mol over five CV cycles (see **Figure 38B**). A similar range was found for cycling in 0.25 M H_2SO_4 (data not shown here). This behavior can likely be explained by the overlaid severe mass loss, as well as the noisy EQCM data caused by that. For further details the reader is referred to the original publication.[251] Nevertheless, hydronium undoubtedly participates in the electrode charge compensation *via* (de)intercalation. For the 1:1 mixed solution of 0.25 M H/$NaClO_4$, $M_{app} \approx$ 21.2 g/mol was

found as shown in **Figure 38C**, indicating a co-insertion of H_3O^+, but also the prevalence of Na^+ in analogy to the conclusion from the CV peak positions.

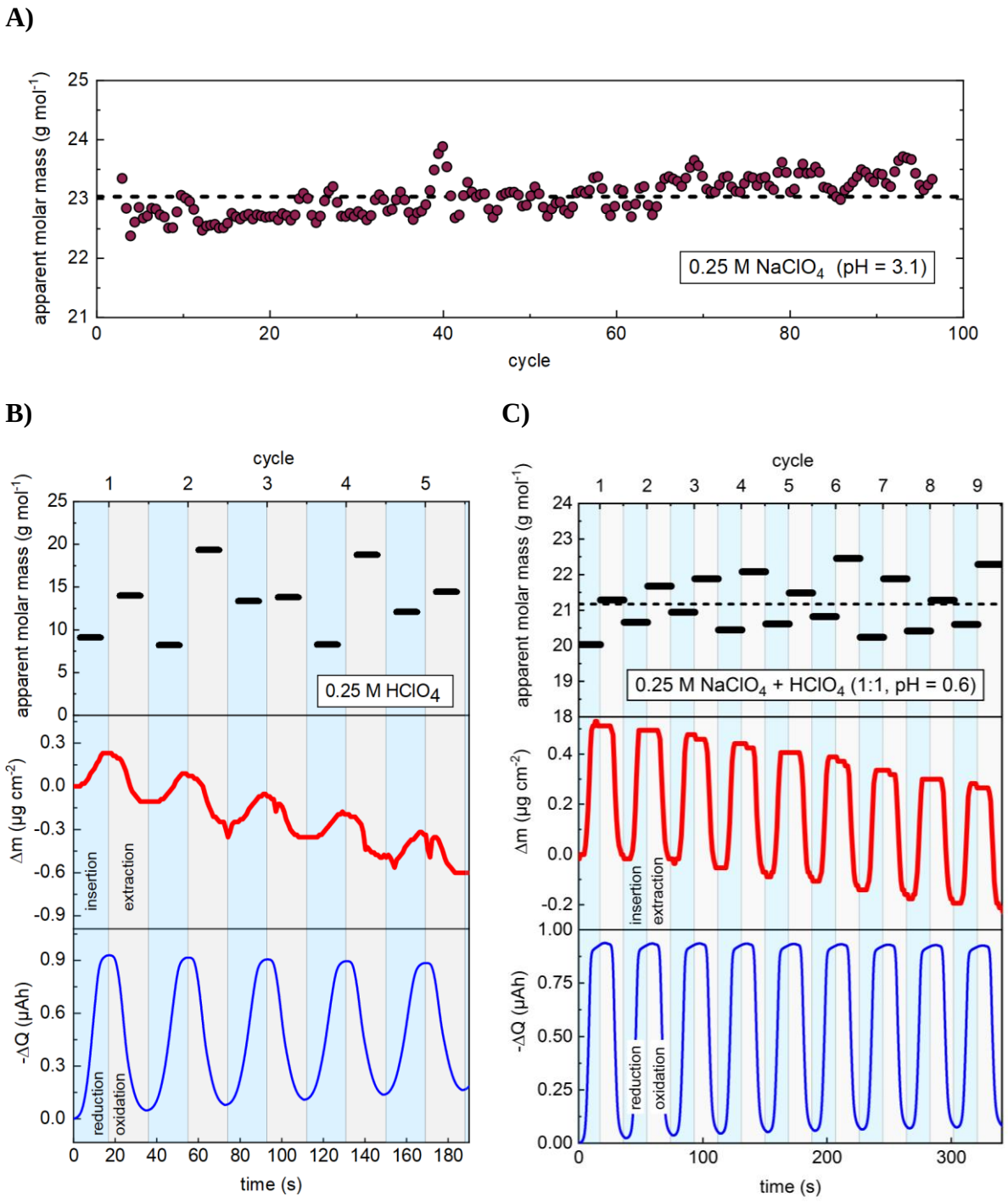

***Figure 38**. Apparent molar mass of the intercalating species for NiHCF in (**A**) 0.25 M $NaClO_4$, (**B**) 0.25 M $HClO_4$ and (**C**) 1:1 mixed 0.25 M H/$NaClO_4$. Adapted and reprinted with permission from ref. 251. Copyright © 2023, American Chemical Society.*

As mentioned above, a too high concentration of H_3O^+ in the mixed H/$NaClO_4$ electrolyte outweighs the stabilizing effect of OH^- reduction and leads to an increased degradation rate of

NiHCF during cycling. This is further reflected by the clearly visible dissolution of electrode material in that solution (see Δ*m* in **Figure 38C**). Apparently, the co-insertion of hydronium somehow destabilizes the PBA framework. To analyze the stability of NiHCF in the absence of Na^+ with H_3O^+ as the only available intercalate, the electrode was extendedly cycled in pure 0.25 M $HClO_4$. As shown in **Figure 39A**, the CV diminishes within 30 cycles, demonstrating an extremely fast degradation of the electrode material. This goes along with its continuous mass loss observed during cycling (see **Figure 38B**). Again, a similar behavior was found in 0.25 M H_2SO_4, which is shown in detail in ref. 251.

Due to the poor cycling stability of NiHCF in the Na^+-free acidic solutions compared to pH-neutral Na^+-electrolytes, it is suspected that the intercalation of H_3O^+ plays a considerable role in the rapid degradation of the material. To gain insight into the dissolution mechanism in acidic electrolytes, *ab initio* molecular dynamics (AIMD) simulations were conducted by replacing Na^+ ions in the NiHCF structure with H_3O^+. Within just 1-2 picoseconds of AIMD equilibration, spontaneous protonation of the N-sites is observed, leading to the formation of $Fe(CN\text{-}H)_6$ moieties (see **Figure 39B**). This suggests that the N-sites are particularly vulnerable to attack in acidic environments, initiating the disintegration of the PBA framework by the cleavage of the [Fe–C≡N]–Ni bond and subsequent dissolution of its constituents. Based on these findings, it could be concluded the electrode stability is significantly enhanced when Na^+ is available as an intercalate. This results from a reduced co-insertion of hydronium due to the higher affinity for inserting Na^+ compared to H_3O^+. This concept reasonably explains why slight acidification of the electrolyte (pH ≈ 3) was found in the past as an effective strategy for improved stability of PBAs. This is caused by impeding the OH^--related degradation pathway due to its practical absence while still providing a sufficiently high Na^+/H_3O^+ ratio.

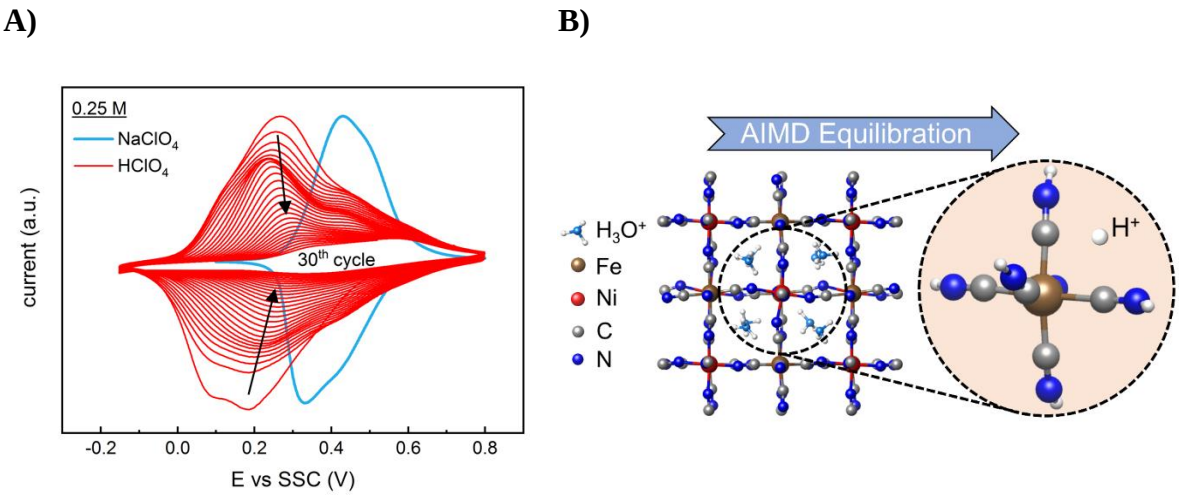

***Figure 39**. (**A**) Stability of NiHCF during CV cycling in 0.25 M $HClO_4$ compared to $NaClO_4$. (**B**) Ab initio molecular dynamics simulations show the protonation of N-sites of the [Fe–C≡N]–Ni bond if Na^+ is replaced by H_3O^+ in the framework structure. Reprinted with permission from ref. 251. Copyright © 2023, American Chemical Society.*

Next to the stabilizing effect of acidification of $NaClO_4$ presented herein, a similar result was obtained by acidifying $NaNO_3$, whereas the opposite effect was observed for acidified Na_2SO_4. For a more detailed discussion of this peculiar inconsistence, the reader is referred to the original publication.[281] Furthermore, another study has reported that defect-rich CuHCF, a Turnbull's blue analog with a significant share of $[Fe(CN)_6]$-vacancies, can be used as a stable and reversible proton insertion electrode in 2 M H_2SO_4, whereas the replacement of Cu by Ni, Co, or Mn significantly impaired the stability.[327] Similar to NiHCF, our AIMD simulations also predict the protonation of N-sites for the case of CuHCF, which is in contrast to the stability of the reported system. Speculatively, the presence of coordination water in that highly defective CuHCF lattice may protect the N-sites from rapid protonation, implying that a high degree of crystal hydration could facilitate more stable proton insertion into PBAs. As exemplified in the case of CuHCF and Na_2SO_4 acidification, it is important to be cautious when inferring the stability of materials in different environments from a single model system. Nevertheless, the general trends presented above for pH-related effects should be widely recognized for the class of PBAs.

6.3.2.2 Effect of Anions

A series of sodium salts typically considered for electrochemical applications was investigated to elucidate the role of the employed anion on the stability of NiHCF electrodes. **Figure 40A** shows the CVs of the very same NiHCF electrode consecutively cycled in 0.25 M $NaClO_4$,

$NaNO_3$, NaCl, $NaCH_3COO$ and Na_2SO_4. Apparently, neither the peak shape, position nor reversibility are significantly influenced by the respective anion. The declining peak currents reflect the degradation of the electrode in accordance with the order of the measurements. The determined apparent molar masses of the intercalating species are reasonably close to the expected value for sodium (see **Figure 40B**), confirming that only the cation participates in the interfacial mass transfer. Nevertheless, the cycling stability of the electrode strongly deviates among the different employed anions, as seen in **Figure 40C**. To avoid OH^-/H_3O^+ effects on the degradation (see discussion above), the pH of all solutions was adjusted to a comparable, neutral value (5.7 – 6.2). While ≈ 67% of the capacity remained after 2000 cycles in the presence of perchlorate, the electrode was almost entirely degraded in the case of sulfate. The stability was found to decrease with the order $ClO_4^- > NO_3^- > Cl^- > CH_3COO^- > SO_4^{2-}$. Similar results were found for InHCF (see **Figure 40D**),[205] while a comparable anion trend was also previously reported for chromium hexacyanoferrate in K^+-electrolytes.[328]

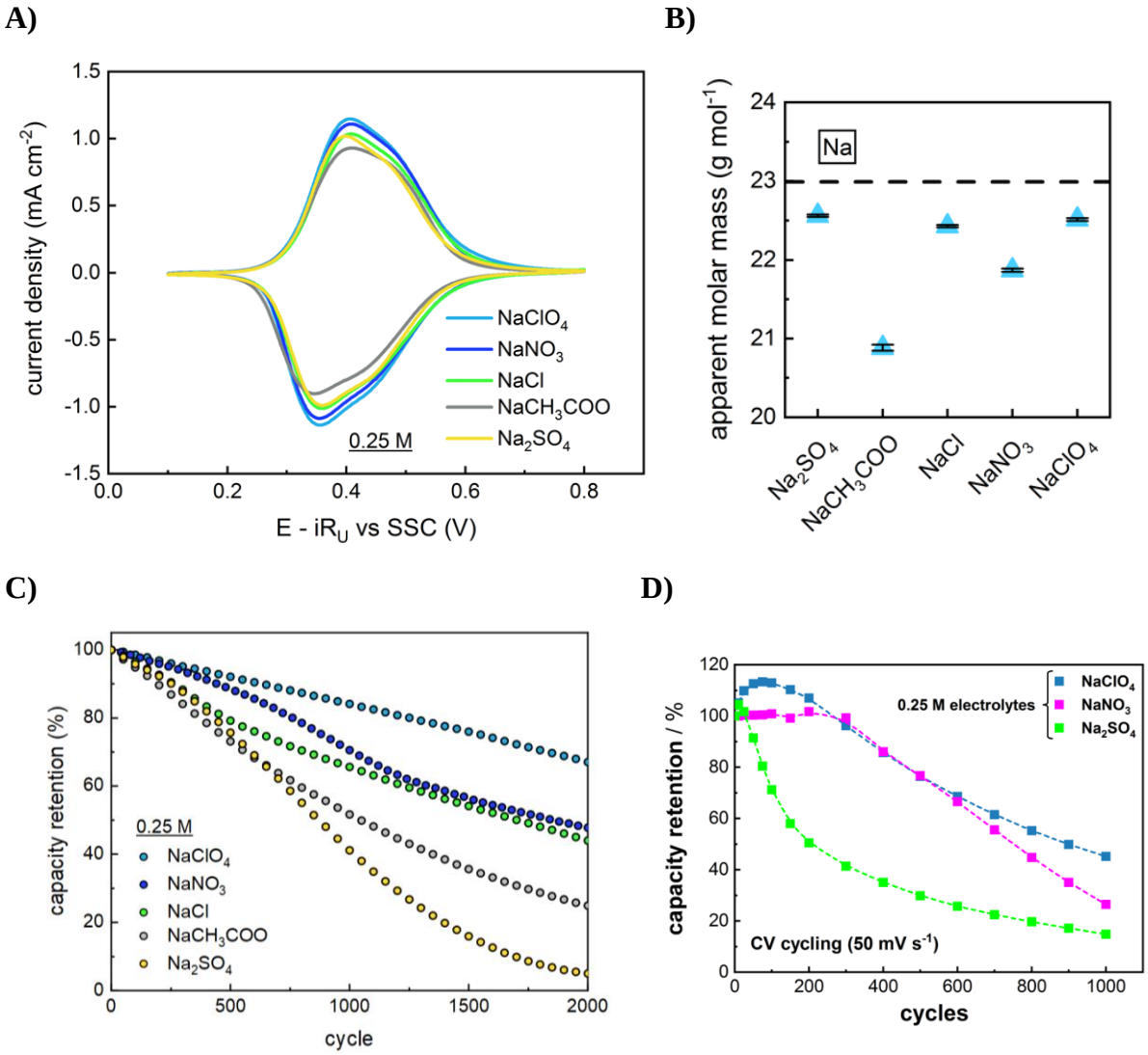

***Figure 40**. (**A**) CVs of NiHCF in different Na^+ electrolytes with varying anionic species and (**B**) correspondingly determined apparent molar masses of the intercalate for all solutions. (**C**) Stability of NiHCF during galvanostatic cycling at 300C and (**D**) stability of InHCF during CV cycling in these electrolytees. **A-C** reprinted with permission from ref. 251. Copyright © 2023, American Chemical Society. **D** reprinted from ref. 205 with permission from the Royal Society of Chemistry. Open access, CC BY 3.0.*

In conclusion, some anionic species undoubtedly play a notable role in the degradation mechanism of PBAs. However, anions are apparently neither intercalated nor impact the electrochemical reversibility of the charge transfer, as shown by the CV and EQCM results presented above. Therefore, the question arises of how they can influence the electrode stability despite their allegedly inactive role during intercalation. In fact, it was reported before that anions are indeed no passive spectators in the interfacial charge and mass transfer mechanism of PBAs and other intercalation materials, but play an important role by compensating temporary surface charges during the cation (de)intercalation process *via* intermediate

adsorption on the electrode surface.[197,199] This so-called three-step-mechanism of intercalation is reviewed in very detail in **Section 3.1.3.3** and can be well probed by electrochemical impedance spectroscopy as described therein. As seen from **Figure 41A**, characteristic "loop"-shaped spectra were obtained for all investigated sodium electrolytes, which could be unanimously fitted with the proposed EEC model representing the anion ad/desorption intermediate steps. As shown in **Figure 41B**, the charge transfer resistance and the corresponding rate constant of the redox reaction are not significantly affected by the nature of the anions, which is in line with expectations. However, the anion adsorption model elements, G_1 and X_1, exhibit pronounced differences among the various anions (**Figure 41C**), indicating that the complex interfacial mechanism of cation intercalation is strongly influenced by the adsorption affinity of the involved anionic species. Remarkably, the order of G_1 and X_1 variation exactly resembles the stability trend in **Figure 40C**. The uncompensated resistance values in **Figure 41D** reflect the different ionic conductivities of the salt solutions, which are found to be within a comparable range.

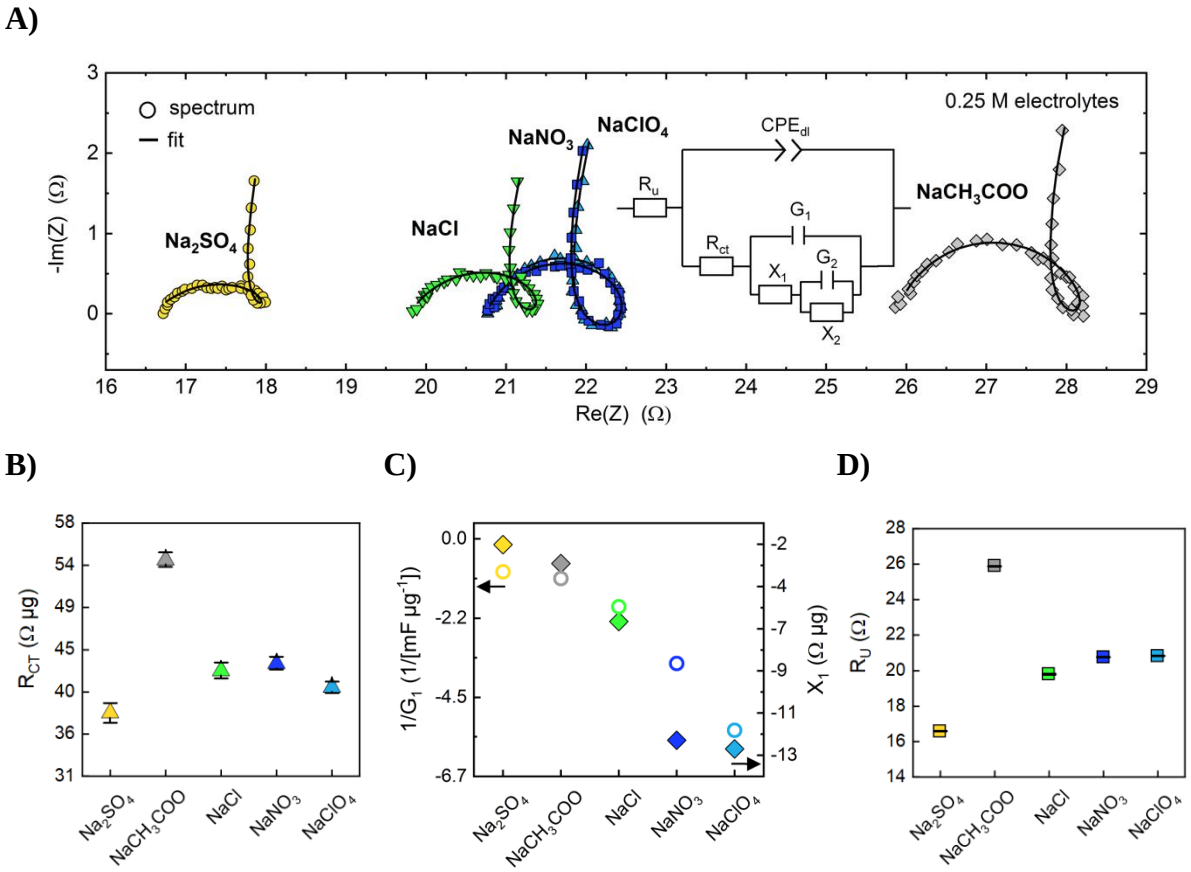

***Figure 41**. (**A**) Impedance spectra of NiHCF in different Na^+-electrolytes with varying anionic species at a degree of sodiation of ≈ 60%. The shown EEC model (see **Section 3.1.3.3**) was used for fitting the data, yielding the plotted parameters for (**B**) R_{CT}, (**C**) $1/G_1$ (hollow symbols) and X_1 (filled symbols) and (**D**) R_u. Reprinted with permission from ref. 251. Copyright © 2023, American Chemical Society.*

By combining these findings with the determined impact of the anion on the PBA stability, the hypothesis can be developed that the dissolution process might be initiated by the adsorption of anionic species from the electrolyte over metal sites on the PBA surface. As also seen from the EIS results for the anion adsorption model elements, the respective adsorption strength and corresponding impact on the stability should differ based on their individually distinct geometry, size, charge density and polarity. To further quantify this behavior, the adsorption energetics for ClO_4^-, NO_3^-, Cl^-, CH_3COO^-, SO_4^{2-} and OH^- over Fe and Ni surface sites in NiHCF were determined using DFT calculations. The respective binding energies are given in **Table 7** for both oxidized and reduced NiHCF configurations. The obtained values emphasize a considerable affinity of the surface for anionic species, indicating specific adsorption with E_{ads} in the range of a few eV. Iron centers appear to be preferred binding sites for both Fe^{II} and Fe^{III} states.

Table 7. DFT computed adsorption energies for different anionic species adsorbed over Fe and Ni surface sites of reduced and oxidized NiHCF. Data reproduced with permission from ref. 251. Copyright © 2023, American Chemical Society.

adsorbate	$Na_2NiFe^{II}(CN)_6$		$NaNiFe^{III}(CN)_6$	
	$E_{ads\text{-}Fe}$ (eV)	$E_{ads\text{-}Ni}$ (eV)	$E_{ads\text{-}Fe}$ (eV)	$E_{ads\text{-}Ni}$ (eV)
ClO_4^-	−2.65	−2.35	−2.47	−2.25
NO_3^-	−1.29	−1.35	−1.57	−1.23
Cl^-	−2.73	−2.04	−2.52	−1.74
CH_3COO^-	−1.89	−1.26	−1.57	−1.28
SO_4^{2-}	−3.54	−1.84	−3.55	−2.49
OH^-	−2.87	−1.41	−2.91	−1.58

The atomic configurations of the anions adsorbed on the Fe-sites of the NiHCF surface are shown in **Figure 42**. The anions with higher adsorption energies, such as SO_4^{2-} and OH^-, exhibit shorter interatomic distances than those with weaker adsorption. The distances are reduced upon deintercalation, which agrees with the computationally determined increase of the positive Bader charge on the host Fe-sites after Na^+ removal (see ref. 251 for further details). This behavior might give rise to the potential- and current-dependent dissolution rate of the transition metals from PBAs discussed in **Section 6.3.1**. However, further dynamic simulations would be necessary to elucidate the exact process entirely. Nevertheless, these computational results support the previously proposed mechanism in which anions control the overall kinetics of interfacial charge and mass transfer *via* surface adsorption on the transition metal centers during the (de)intercalation of cations in PBAs in accordance with the experimental findings.

Importantly, the adsorption affinity of the individual anions also seems to correlate with the electrode stability in the respective electrolytes. The anions characterized by a weak binding to the NiHCF surface metal sites also come with higher stability and *vice versa*. Especially sulfate, which leads to the fastest degradation of NiHCF, shows significant adsorption to Fe, while the weakly adsorbing nitrate enabled a longer electrode lifetime. Remarkably strong adsorption is also found for OH^-, reflecting the fast deterioration of PBAs in basic solutions, as discussed in **Section 6.3.2.1**. In contrast to the other anions, the electrode is in that case transformed to a transition metal oxide rather than being entirely dissolved. This can be understood from the Pourbaix diagrams (see ref. 128) and should therefore be considered as a secondary degradation

effect. Whereas these results do not entirely represent the prevailing stability in perchlorate, an overall qualitative trend can be recognized.

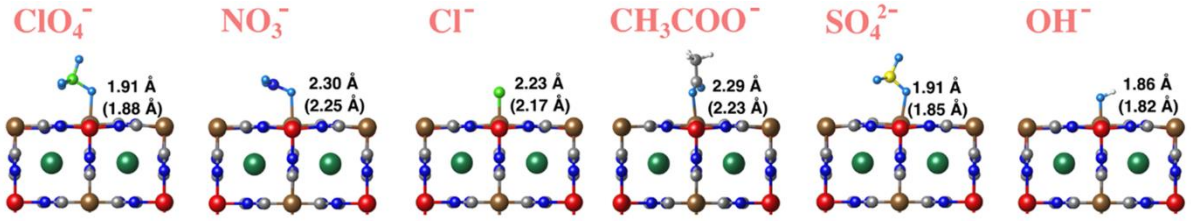

***Figure 42**. DFT optimized structures for various anionic species adsorbed over Fe on a NiHCF crystal surface. The Fe–O and Fe–Cl distances are given for $Na_2NiFe^{II}(CN)_6$, while the values for the $NaNiFe^{III}(CN)_6$ case are given in parentheses. Reprinted with permission from ref. 251. Copyright © 2023, American Chemical Society.*

Furthermore, higher stability would be expected for NiHCF in $NaCH_3COO$ based on the comparably low adsorption energy of the acetate anion. This deviating behavior likely results from its considerably higher basic strength compared to the other anions, with its $pK_b = 9.2$[329] compared to ≈ 29[330] for ClO_4^-. As a result, local deprotonation of H_2O with subsequent CH_3COOH formation and OH^- appearance could occur on a molecular level. This cannot be ruled out, even though the overall pH was adjusted to neutral before the experiment, which is however a purely statistical quantity. If hydrolysis happens close to the electrode surface, it will effectively turn a beneficial anion (acetate) into an especially detrimental one (hydroxide), thereby clarifying the impaired stability. An analogous concept can probably also explain the initial dissolution of PBAs in the presence of divalent intercalation cations, such as Mg^{2+}, Ca^{2+} and Sr^{2+}.[202,265] In these cases, the local appearance of H_3O^+ by cation-induced hydrolysis might cause fatal hydronium (co-)intercalation and promote PBA degradation. This is elaborated in further detail in the original publication.[251]

Nevertheless, the presented approach strongly implies a generalized mechanism initiated by the adsorption of anionic species over surface metal sites at the electrode-electrolyte interface. This holistic description allows an understanding of the dissolution of PBAs in medium to high pH media. To elucidate the exact dissolution pathways, further dynamic simulations are necessary in the future. Considering the strong binding energies of the adsorbates in the order of 2 – 3.5 eV, ligand exchange at hexacyanoferrate complexes causing subsequent dissolution of the N-coordinated transition metal seems to be a likely intermediate step.

6.3.2.3 Effect of Concentration

According to the results presented in the previous sections, $NaClO_4$ is the best choice amongst the investigated anions to ensure high stability of PBAs during cycling. Furthermore, as reviewed in **Section 2.2.4**, this salt can be highly concentrated in aqueous solutions towards forming a "water-in-salt" system, enabling an increased operational voltage window for aqueous batteries.[162] At such high concentrations, the dissolution process was found to be effectively suppressed, making this one of the most successful stabilization strategies for PBAs (see the introduction to **Chapter 6**).[233] Altogether, $NaClO_4$, therefore, appears as the "perfect" salt for optimized aqueous PBA-based batteries in practical applications.

The stabilizing effect of raising the electrolyte concentration is shown in **Figure 43A** for NiHCF in $NaClO_4$. While there is a slight decrease in stability when the concentration is increased from 0.25 M to 1 M, a considerable enhancement is noticeable at concentrations exceeding 2 M. Eventually, the material displays hardly any degradation in an 8 M solution. In solutions of low-to-medium concentrations, a slight decrease in stability can likely be attributed to the increasing activity of the ClO_4^- anion. Although the adsorption of this species on the electrode surface is rather weak, its increased activity at higher concentrations could lead to stronger material degradation (see section before). Concentrations exceeding 2 M exhibit a prevailing stabilizing effect. This extremely beneficial behavior is maintained at both low and high cycling rates (see **Figure 43B**).

In such superconcentrated electrolytes, the suppression of active material dissolution is achieved through the scarcity of free water molecules, which are excessively incorporated into the ions' solvation shells due to strong salt hydration. In fact, there exist only about two H_2O molecules for each sodium ion in the 8 M solution. This can be easily understood from the following calculation: First, the volume ratio of solvent:solute for 8 M $NaClO_4$ is reduced to $\approx$ 62% as experimentally determined, including water from the initially mono-hydrated salt. This is caused by the high quantity of added solute. As a result, one liter of the solution now only contains 620 g H_2O, which is equal to 34 moles using its molar mass of 18 g/mol, compared to pure concentration of water in water (55.6 M). The solution also contains 8 mol of Na^+ and 8 mol of ClO_4^-, and therefore the average ratio of solvent:solute-ion is 34:16. Based on these considerations, a schematic illustration of the electrode-electrolyte interface for NiHCF in 0.25 M and 8 M $NaClO_4$ is presented in **Figure 43C**, giving a visual impression of the high amount of Na^+ and ClO_4^- ions in the concentrated electrolyte. It should be noted that

the above calculation just reflects the overall ion and solvent quantities, while the real nature of the solvation sheath composition and electrolyte structure are exceedingly intricate in such "water-in-salt" systems.[159,164] Nevertheless, this approach leads to a limited uptake capacity for dissolved electrode constituents, resulting in the effective prevention of material hydrolysis. Furthermore, the sluggish diffusion dynamics of dissolved constituents toward the bulk electrolyte significantly inhibits the dissolution process.[270]

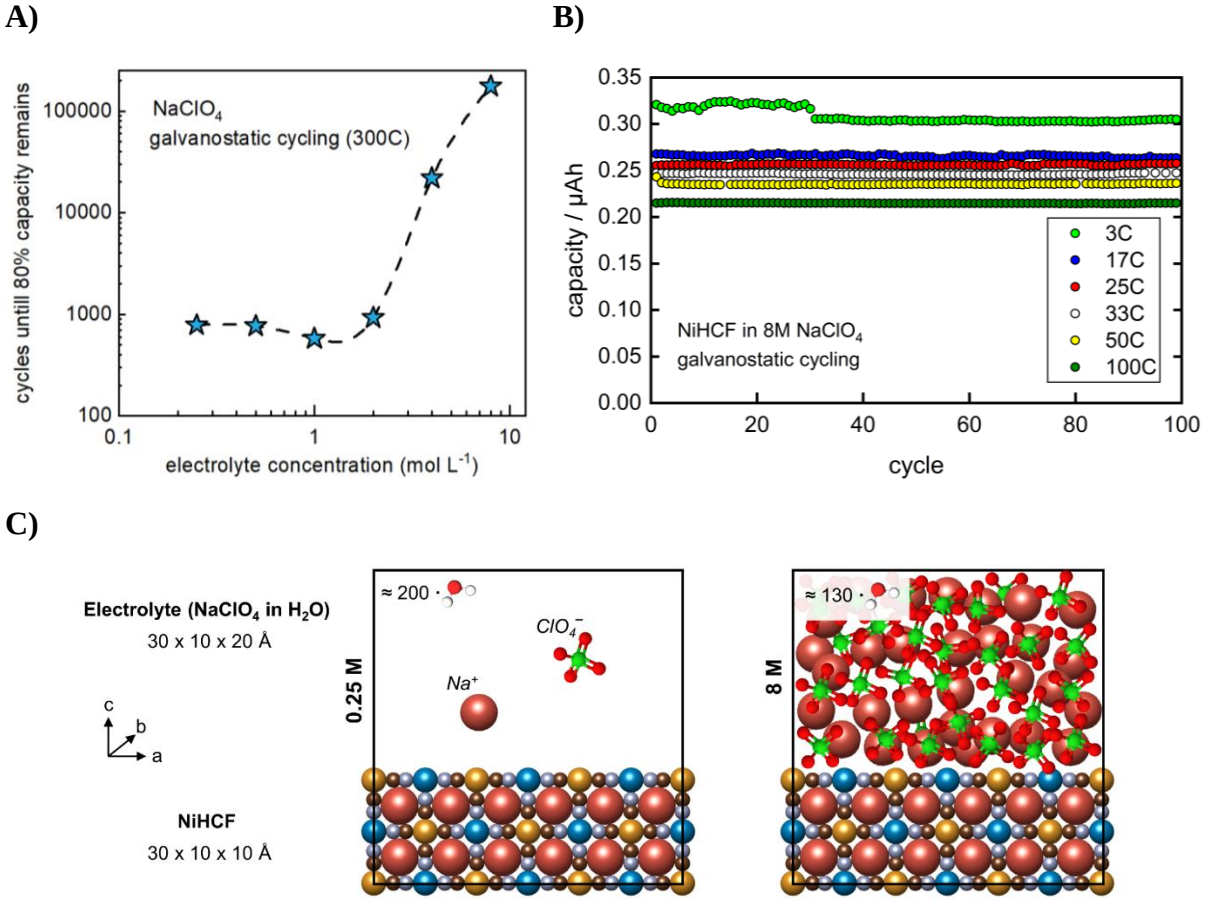

***Figure 43**. (**A**) Cycling stability of NiHCF in different concentrations of $NaClO_4$. For the 4 M and 8 M solutions, the presented data points were extrapolated based on the determined capacity losses of 2.6% after 2840 cycles and 1.2% after 10,500 cycles.[281] The dashed line serves as a guide to the eye. Reprinted with permission from ref. 251. Copyright © 2023, American Chemical Society. (**B**) Stability of NiHCF in 8 M $NaClO_4$ during galvanostatic cycling at various rates. Reprinted with permission from ref. 281. Copyright © 2022, American Chemical Society. (**C**) Schematic illustration of the electrode-electrolyte interface for NiHCF in 0.25 M and 8 M $NaClO_4$, which represents a 32x increase of the amount of Na^+ and ClO_4^-. The number of ions in the indicated cell (black frame, 30 x 10 x 30 Å) represents the real volumetric concentration. Water molecules are omitted for clarity, but their amounts in the cells are indicated in the upper left corner. Visualized atom sizes are true to scale. Ion-solvent, ion-ion, ion-surface, and solvent-surface interactions are neglected in this simplified image.*

6.4 Passivation of the Electrode Material

The findings presented in this section have not yet been published. Therefore, specific instrumental details not covered in **Chapter 4** will be provided in the respective instances. For the sake of transparency, it should be mentioned again that a few aspects and ideas of this chapter have already been elaborated in the author's Master's thesis.[280] These are nevertheless included in the following to provide the groundwork for interpreting the new results discussed herein and elaborate a comprehensive understanding of the degradation process.

Even though highly concentrated solutions can significantly extend the cycling stability of PBAs, such electrolytes are not entirely undisputed, as they come with specific disadvantages, such as increased weight, cost, and high viscosity, impairing the wetting properties.[331] Therefore, the overall degradation mechanisms in rather diluted electrolytes will be further investigated in the following. As indicated in **Section 6.2**, the active material dissolution process treated in **Section 6.3** is insufficient to entirely explain the quantitative capacity fade observed during cycling. To ensure that this is not an electrolyte anion- or concentration-specific effect, **Figure 44** shows the remaining relative capacity and mass (measured *via* EQCM) of NiHCF thin-film model electrodes in 0.25 M $NaClO_4$ (**A**), $Na2SO_4$ (**B**) and $NaNO_3$ (**C**), as well as different $NaClO_4$ concentrations of 0.5 M (**D**), 1 M (**E**) and 8 M (**F**). To avoid pH-related degradation effects, all solutions were tested at pH ≈ 6. In contrast to 8 M $NaClO_4$, where the electrode is entirely stable (see **Section 6.3.2.3**), a distinct two-fold degradation mechanism is discernable in all other solutions. Apart from the irreversibly lost capacity due to active material dissolution (red-shaded), an increasing share of non-active material emerges with an advancing degradation state (blue/yellow/green-shaded). This capacity loss will be termed "passivation" in the following since it constitutes a process inhibiting the capability of remaining electrode material to convert charge and thereby diminishes its capacity beyond the share of dissolved active material. This section aims at analyzing and clarifying this passivation effect.

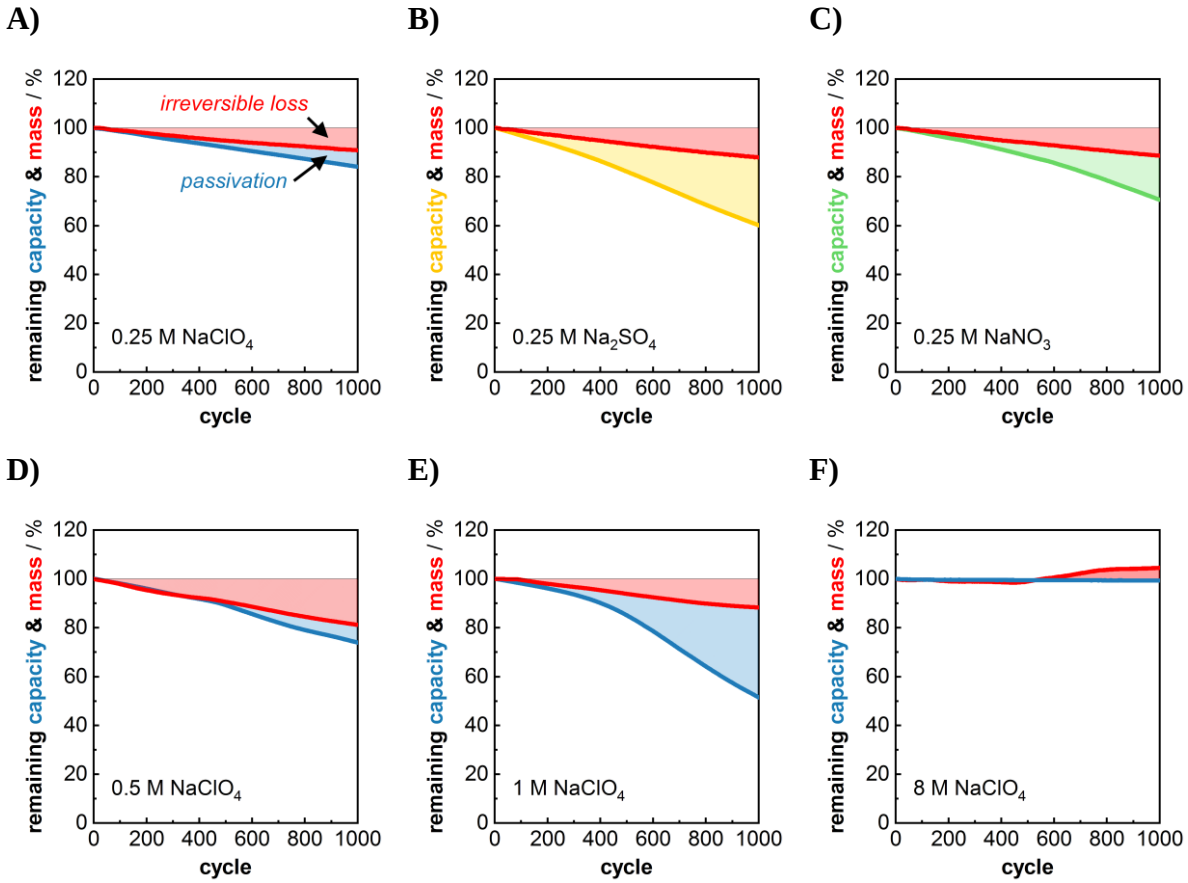

***Figure 44**. Electrode stability represented by the remaining relative capacity and mass of NiHCF thin-film model electrodes in different Na^+-electrolytes (pH ≈ 6) with varying anions and concentrations during galvanostatic cycling at 300C.*

6.4.1 Is the Active Material (Electro)chemically Transformed During Degradation?

To first exclude that the electrochemical inactivity of the remaining electrode material stems from a transformation of NiHCF towards another compound, the chemical bonding environment and elemental oxidation states were probed by XPS. **Figure 45A** and **Figure 45B** show the spectra of a pristine and degraded sample for the Ni 2p and Fe 2p regions (spin-orbit doublets $2p_{3/2}$ and $2p_{1/2}$). Both samples were measured in the fully reduced state, meaning the electrodes were immediately removed from the solution after the cycling was stopped at 0.1 V *vs.* SSC. The reader is referred to **Section 5.3** for a detailed characterization of as-synthesized NiHCF. For nickel, both the peak structure and positions are found to be entirely unaffected by degradation. For iron, the overall spectrum also remains unchanged upon degradation, showing a main signal coming from the Fe(II) oxidation state. However, a small

peak at higher binding energies associated with the Fe(III) oxidation state appeared, indicating that the degraded electrode is not entirely electrochemically reduced. This could be strongly related to the passivation effect, since apparently not all Fe redox centers are accessible for charge storage during cycling and consequently constitute non-active material. Nevertheless, an (electro)chemical transformation of the NiHCF electrode upon degradation can be excluded from these findings, as a significant change of peak positions and structure would be expected for a deviating compound due to altered chemical oxidation states and bonding environments. Strictly, these findings only apply to the surface, but a transformed bulk material with an unaltered surface seems unlikely since any conceivable transformation process triggered by continuous cycling would naturally have to proceed from the electrode-electrolyte interface.

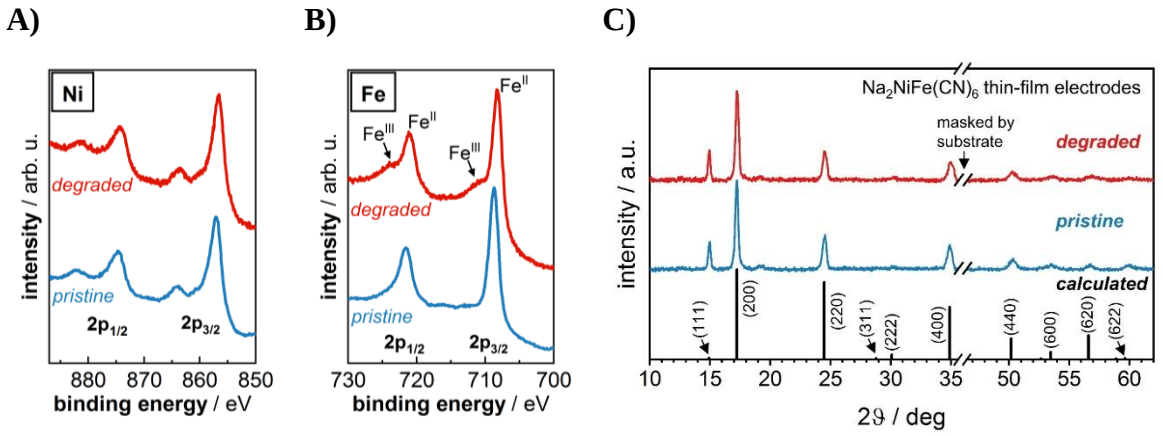

***Figure 45**. XPS spectra for (**A**) Ni and (**B**) Fe 2p regions in pristine and degraded NiHCF. The degraded sample was galvanostatically cycled at 300C in 0.25 M Na_2SO_4 until 25% capacity remained. Both samples were measured in the electrochemically reduced state (cycling stopped at 0.1 V vs. SSC). (**C**) XRD pattern of a pristine and degraded NiHCF electrode along with a calculated pattern for a $Na_2NiFe(CN)_6$ reference structure (Fm-3m, a = 10.28 Å). The degraded sample was galvanostatically cycled at 300C in 0.25 M Na_2SO_4 until 15% capacity remained. The instrumental details for both XPS and XRD are identical to the ones reported in ref. 251. Data adapted from ref. 280.*

The effect of electrode degradation was further probed by XRD (see **Figure 45C**). The diffraction pattern of the pristine and degraded electrodes are very similar regarding the occurring peaks and relative intensities and correspond well with a calculated *Fm-3m* $Na_2NiFe(CN)_6$ reference structure. The lattice constant calculated from the (200) peak yields 10.26 Å for the degraded sample, compared to 10.28 Å for the pristine one (see **Section 5.3**). It can therefore be concluded that the overall crystal structure is preserved upon degradation. Furthermore, no unassigned peaks can be discerned, confirming that no other material phase apart from NiHCF is present. The findings from XPS and XRD analysis give unambiguous

evidence for the unaltered chemical composition and integrity of the electrode in the degraded state. Furthermore, the formation of a SEI-like interphase on the electrode surface, as in LIBs, can be excluded from these findings.

6.4.2 Impact of the Degradation Process on the Morphology

To find how the degradation process affects the morphology, NiHCF thin-film electrodes were examined using SEM and AFM (see **Figure 46**). The pristine sample revealed a very uniform and smooth thin-layer coating (**Figure 46A** and **Figure 46C**), with repetitive crack-like structures appearing at distances of a few micrometers. The origin of these structures is unknown, but they could likely emerge upon drying after the electrodeposition synthesis.[248] Although grains or grain boundaries, which are typical for polycrystalline electrodes, are not discernible from the top-view SEM image of the pristine electrode (**Figure 46A**), the structures are assumed to be < 100 nm in horizontal size, as apparent from AFM (**Figure 46C**). This is further confirmed by the cross-section SEM image of the pristine sample (**Figure 46B**), which reveals the NiHCF film as a very uniform rigid layer with a reasonable thickness of approximately 150 nm on top of the Au/borosilicate substrate. It is composited of sticks-like longish grains, reaching from the bottom to the top and demonstrating a horizontal thickness of < 100 nm, similar to the estimated value from the AFM image (**Figure 46C**). The surface roughness (≈ 7 nm) is very low compared to the film thickness.

Remarkably, the degradation process results in a severe transformation of the previously homogeneous surface into a porous patchwork of segments and cavities, which is distinguishable from the pristine layer (**Figure 46A**). The stick-like grains are transformed into aggregations consisting of smaller pebbles/nanoparticles stacked across each other as evident from **Figure 46B**. This significantly increases the number of grains and corresponding interfaces, resulting in a rise in the surface roughness by approximately 70% (**Figure 46D**). The formation of large "canyons" on the degraded film surface indicates the disintegration of the coating along the previously described crack edges. Nevertheless, the comparison of the degraded film and the Au substrate (see inset in **Figure 46A**) confirms that the latter is still completely covered with material. Hence, SEM and AFM images substantiate that a significantly high share of the initial film mass remains even after severe degradation, which, however, has an entirely changed morphology and structural composition.

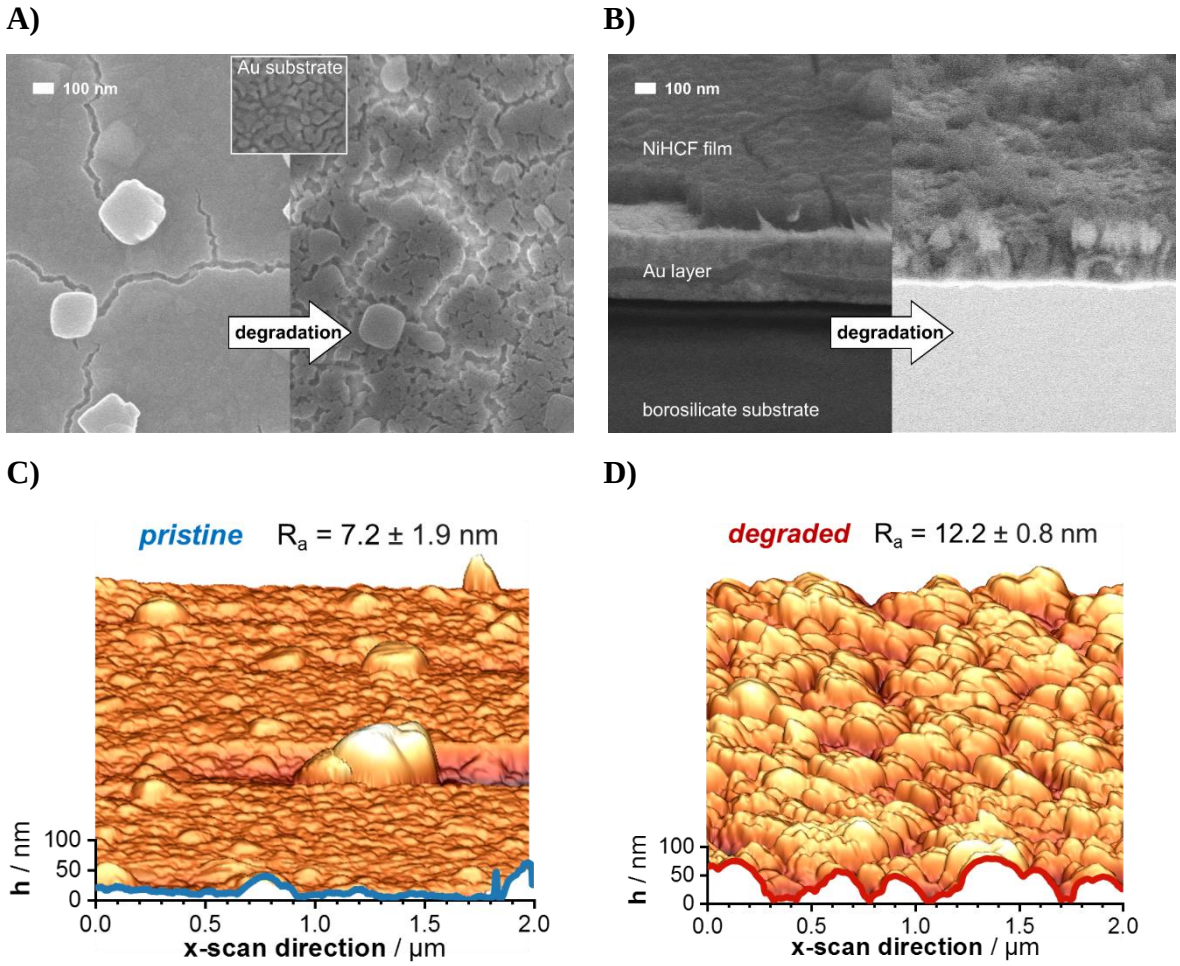

***Figure 46**. Top-view (**A**) and cross-section (**B**) SEM images of a pristine (left) and degraded (right) NiHCF thin-film model electrode. The degraded sample was galvanostatically cycled (300C) in 0.25 M Na_2SO_4 until 15% capacity remained. AFM images of a pristine (**C**) and degraded (**D**) NiHCF electrode. It should be noted that the indicated height (y-axis of the line profile) is identically scaled for better comparison. The degraded sample was galvanostatically cycled (300C) in 0.25 M Na_2SO_4 until 25% capacity remained. The instrumental details for both techniques are identical to the ones reported in ref. 225. **A** and **B** are adapted from ref. 280.*

6.4.3 Effect of the Degradation Process on the Electrochemical Properties

Apparently, the passivated electrode material is still identical to the initial NiHCF, which, however, increasingly loses its ability to participate in intercalation processes with ongoing degradation. The underlying reason will be investigated in the following. Electrochemical impedance spectroscopy is a very powerful technique to assess the state-of-health of a battery and systematically identify possible degradation mechanisms for capacity and power fade in a non-destructive way.[147,253,332,333]

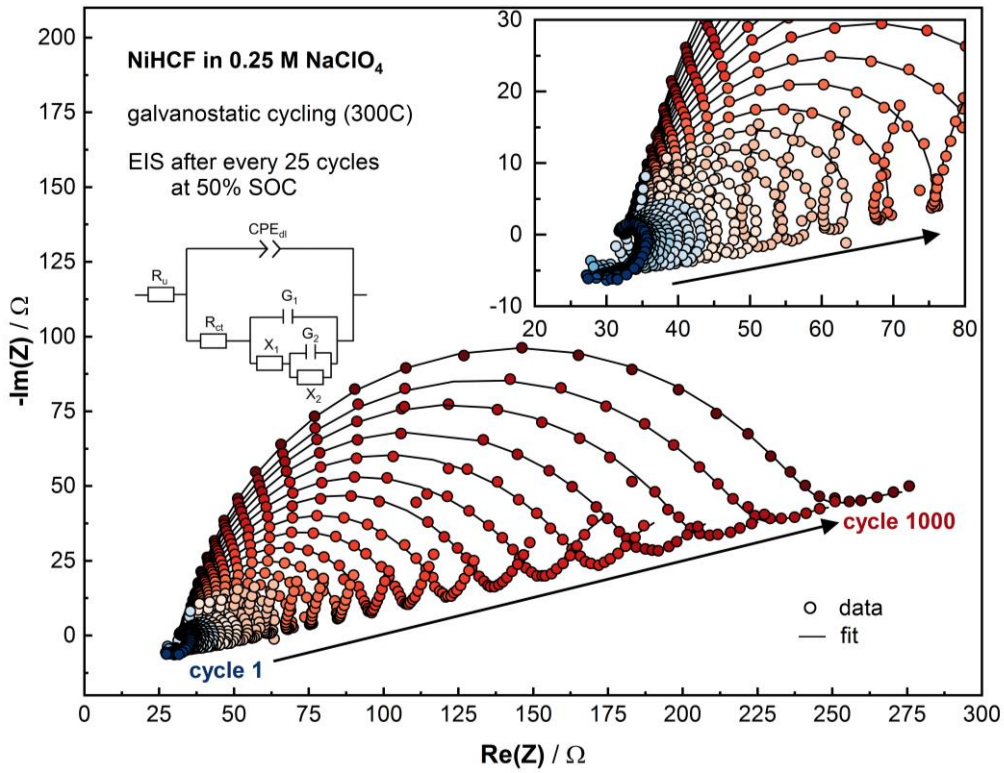

***Figure 47**. Impedance spectra of a NiHCF thin-film model electrode acquired during galvanostatic cycling (300C) in 0.25 M $NaClO_4$. EIS was performed every 25 cycles at 50% SOC. The spectra were fitted (solid lines) using the shown EEC, which is introduced in **Section 3.1.3.3**.*

To elucidate the effect of the passivation process on the charge and mass transfer properties, impedance spectroscopy was performed every 25 cycles during galvanostatic cycling (300C) of a NiHCF electrode in 0.25 M $NaClO_4$. The acquired spectra are shown in **Figure 47**. It can be clearly seen that the overall impedance significantly increases with the degradation state (blue to red coloring). All spectra could be unambiguously fitted with the indicated EEC model representing the three-step-mechanism of intercalation-type electrodes, which is extensively introduced in **Section 3.1.3.3**. In the pristine state (initial cycles), the spectra show the characteristic “loop”- shape in the mid-to-low frequency region (see inset), indicating a strong impact of the intermediate anion adsorption process. With ongoing cycling, the impedance response is increasingly dominated by the immensely growing first semi-circle, which is associated with the charge transfer resistance R_{ct}.

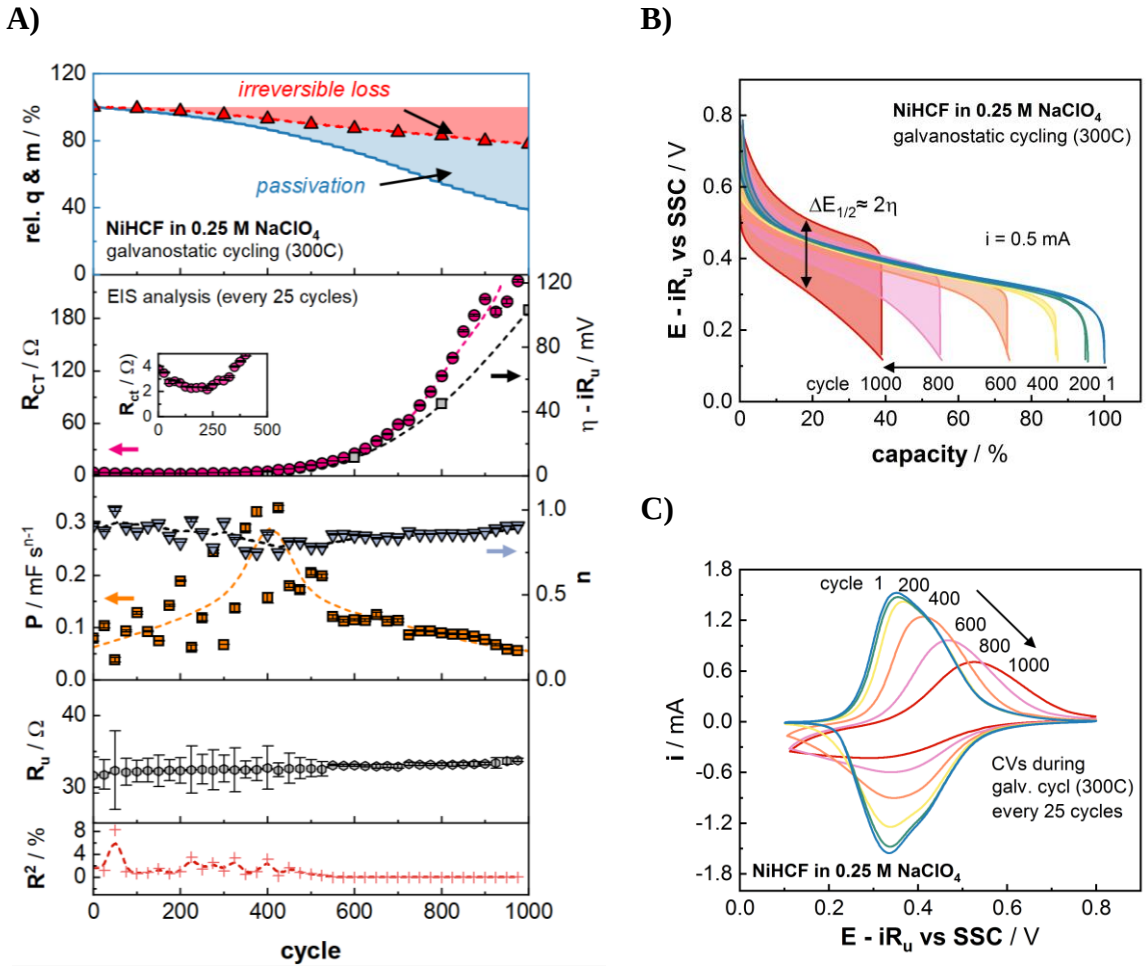

***Figure 48**. (**A**) Evaluation of the EEC model parameters obtained from fitting the impedance spectra in **Figure 47** together with the evolution of relative mass and capacity, as well as overpotential during long-term galvanostatic cycling. Dashed lines serve as a guide to the eye, while solid lines represent continuous data points. R_{ct}, R_u and P are intentionally not normalized to mass or area because both latter quantities evidently change with the ongoing degradation. (**B**) Galvanostatic charge-discharge curves and (**C**) CVs of the same electrode with an ongoing state of degradation. CVs were recorded along with EIS every 25 galvanostatic cycles.*

The EEC fitting parameters are quantitatively correlated to the electrode degradation over cycles in **Figure 48A**. In general, the fitting parameters show very small individual errors, and the overall fitting error (R^2 value, amplitude weighting) always remains in an acceptable range apart from one datapoint (cycle 50). As previously described, the degradation is represented by a continuous mass loss and disparately higher capacity decay, which constitutes a passivation of the remaining electrode material (see top graph). It should be noted that the extent of the relative mass and capacity loss cannot be quantitively compared to the values presented for NiHCF in 0.25 M $NaClO_4$ at the beginning of **Section 6.4** due to the dissimilar cycling protocol, since CV and EIS measurements were performed every 25 cycles in this case. The appearance

of a substantial share of passivated electrode material strikingly coincidences with a significant and continuous increase of the charge transfer resistance R_{ct} (around cycle 400). While its value is initially only 2 – 4 Ω with a slightly decreasing trend in the beginning (see inset), values above 200 Ω were obtained after 1000 cycles. At the same time, the uncompensated resistance R_u only slightly increases by ≈ 5%. The values obtained for the *n*-exponent of the CPE element ($n \approx 0.8$ – 1) indicate that the behavior of the double layer is mostly capacitive. The corresponding *P* parameter, which is related to its capacitance, largely fluctuates initially, while it is relatively stable towards higher cycles. Nevertheless, an overall trend can be discerned as indicated by the dashed line, which depicts the moving average of *P*. Since the double layer capacitance is proportional to the area of the electrically conducting material present at the electrode (see **Equation 3**), the variation of *P* with advancing cycles indicates an initial increase of the overall surface area, which, however, decreases again coincidentally with the rise of R_{ct}. In the case of the herein investigated thin-film electrode, this corresponds to the surface area of NiHCF since no conductive additive is present.

Remarkably, the increasing charge transfer resistance is represented by the electrode polarization during cycling. With ongoing electrode degradation, the initially hysteresis-free charge-discharge curves exhibit a significant hysteresis (see **Figure 48B**), and the iR_u-corrected overpotential increases to ≈ 100 mV (at 0.5 mA, see **Figure 48A**). This is further reflected by the evolution of the CVs (**Figure 48C**), which show, next to the overall decreasing current, an increasing voltammetric irreversibility and vanishing symmetry with ongoing degradation. Such behavior is a typical capacity fade mechanism observed for batteries since the increasing electrode polarization (see **Section 2.2.3**) causes the potential to hit its limiting boundaries prematurely and thereby reduces the available capacity with ongoing degradation.[207,254,255,299,334,335,336] Usually the underlying reason is mainly ascribed to the formation and growth of the insulating SEI layer which poses a growing barrier to be overcome for interfacial charge transfer to happen.[337,338] For the case investigated herein, the formation of a SEI can be excluded as such surface interphase should manifest itself as a second semi-circle towards higher frequencies in the impedance spectra,[339] which is not discernable in the spectra presented in **Figure 47**. Furthermore, an SEI layer is not expected for the employed salt-solvent system (see **Section 2.2.4**), nor is it supported by the XPS and XRD measurements discussed in **Section 6.4.1**.

Evidently, the charge transfer resistance is solely responsible for the increasing electrode polarization and thereby diminishing available capacity in the present case. Recalling

Equation 18 and **Equation 42**, it can be excluded that the observed change of R_{ct} is caused by an altering exchange current density (rate constant) or activation barrier symmetry of the reaction as supported by the findings in **Section 6.4.1**, nor variation of the state-of-charge, which was constant (X = 50%) in all measurements. Therefore, the variation of the absolute charge transfer resistance and the induced kinetic limitations can only be caused by the surface area available for an interfacial charge and mass transfer. This goes in hand with the behavior of the double layer capacitance described above, indicating an initial slight increase of the surface area (cycle 1 to approximately 400), followed by a tremendous decrease of the apparent surface area as evident from the decay of P and the 100x rise of R_{ct}. The slight increase of the surface area in the beginning might be related to the dissolution process, which is expected to proceed randomly across the surface and might thereby introduce some micro/nanoporosity.

In fact, the SEM and AFM findings discussed in **Section 6.4.2** would actually lead to the expectation of a higher surface area available, especially for interfacial ion transfer in the degraded state due to the increased roughness and structural disorder with small pebble-like grains stacked on each other rather than the initial longish sticks reaching from the bottom to the top of the thin-film. However, it is very likely that many of these aggregations of irregular structures and particles in the degraded case are only badly connected (small solid-solid contact area), posing an enormous hindrance for electronic charge transfer to the active Fe-redox centers across solid/solid interfaces. Furthermore, deeper electrode material might be partially or fully blocked by upper particles, thereby exposing no or only a small contact area with the electrolyte for ionic charge transfer, effectively making it a "dead" mass. As a result, the kinetic properties of the electrode material will become increasingly sluggish with the ongoing degradation, excluding a growing share of the remaining active material from participating in the redox reactions due to the strong polarization at higher rates.

Next to the impaired charge-transfer kinetics causing substantial polarization, the rate-dependent charge-discharge characteristics of a degraded electrode appear to be additionally indicative for diffusion-limited behavior. The corresponding features for differentiating rate control mechanisms are discussed in **Section 2.2.3** and **Section 3.1**. **Figure 49A** shows the CVs of a degraded NiHCF electrode at different scan rates. Whereas a linear proportionality for the peak current to the scan rate is a typical characteristic for the thin-film electrodes investigated herein (no diffusion or kinetic limitation, this will be discussed in very detail in **Chapter 7**), the obtained exponent of $a \approx 0.77$ points towards a substantial contribution of diffusion-limited processes to the overall faradaic current. The origin of this mass transport

limitation remains unknown, especially since it could not be seen at the investigated frequencies in the EIS measurements or could not be resolved therein due to decreasing time constant associated with the charge transfer resistance. As there is no such limitation in the pristine state, its evolution must result from morphological degradation. Whereas both the properties of planar diffusion in the bulk electrolyte, as well as the solid-state diffusion within the active material itself should remain unchanged, it could be hypothesized that the inter-particle transport of Na^+-ions across the newly created grain boundaries towards deeper electrode material layers not in contact with the electrolyte by their own is substantially impaired or entirely interrupted. Furthermore, a possibly decreased long-range lattice periodicity of NiHCF in the degraded structure could introduce disrupted migration channels for sodium.[340] Another possible reason could be the depletion of Na^+ in the confined electrolyte volume within the newly created nanopores upon intercalation, similar to the phenomena observed in porous composite electrodes.[341]

It follows that it should be possible to regenerate a significant share of capacity by reducing the current during galvanostatic cycling to allow enough time for diffusive mass transport and prevent prematurely hitting the potential boundaries by reducing the current-dependent kinetic polarization. Indeed, a successive reduction of the initial current I_0 down to $I_0/60$ returns almost two times the capacity obtained at I_0 in the degraded state, while also the potential hysteresis is incrementally reduced (see **Figure 49B** and **Figure 49C**). By this, around 75% of the previously "passivated" material can be "re-activated" to participate again in the charge storage reactions. However, next to the irreversibly lost share of capacity due to dissolved active material, 25% of passivated material remains that could not be regenerated. As hypothesized above, this is likely related to electrically unconnected particles or blocked grains in the deeper electrode layer not in contact with the electrolyte.

In conclusion, the "passivation" is caused by impaired kinetics and mass transport properties of the degraded electrode and, in fact, represents a power fade rather than a capacity fade,[253,254,255,336] consequently restricting its operation to lower currents. Such successive current reduction based on the cell impedance or state of health to maintain an as-high-as-possible capacity even after extended cycling is known in practice as "derating".[342]

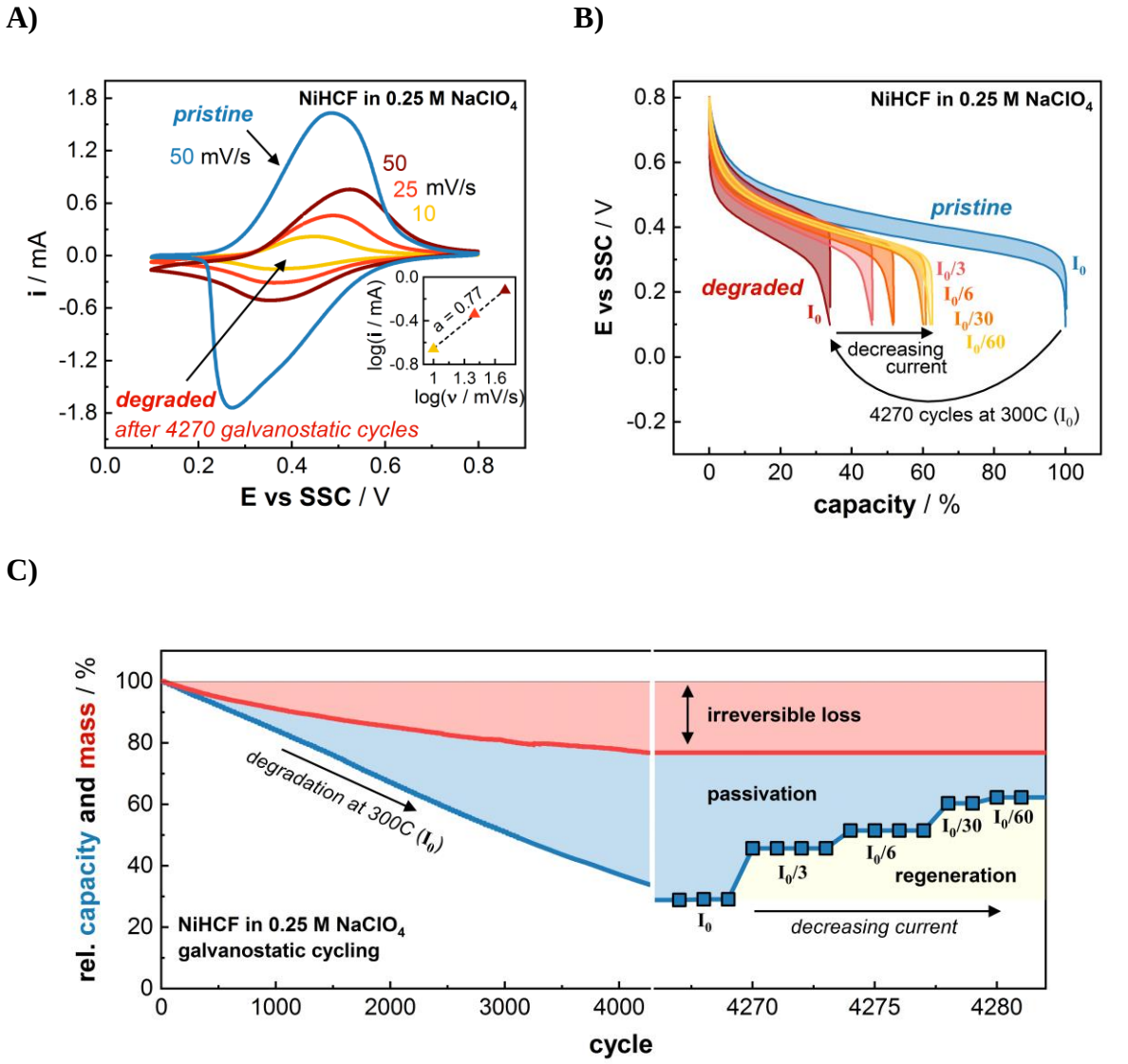

***Figure 49**. (**A**) CV of a degraded (galvanostatic cycling at 300C until 30% capacity remained) NiHCF electrode in 0.25 M $NaClO_4$ at different scan rates. For comparison, the CV at 50 mV/s of the same electrode before degradation is also provided. The inset shows a linear fit of log(i_p) with log(v). (**B**) Galvanostatic charge-discharge curve of the same electrode before and after degradation with successive reduction of the imposed current in the degraded state (see arrows). (**C**) Relative remaining capacity and mass of the same electrode during galvanostatic cycling at 300C for 4270 cycles (degradation period), followed by the regeneration of passivated capacity by the current reduction protocol shown in (**B**). Data partially adapted from ref. 280.*

6.5 Proposal of an Overall Dissolution and Re-Deposition Mechanism

As discussed in the previous two sections, the degradation of NiHCF model electrodes was found to proceed along two pathways. First, the extraction of transition metal cations leads to an overall dissolution of active material, causing irreversible capacity loss as fewer redox centers are present with ongoing degradation (**Section 6.3**). Second, the morphological breakdown of the initially well-crystallized thin film causes increasing passivation of the remaining active material. The rising impedance and impaired mass transport properties necessitate a reduction of the (dis)charging current to maintain an as-high-as-possible capacity in the degraded state (**Section 6.4**). Nevertheless, it appears likely that both pathways are linked to each other, which is also indicated by the fact that no passivation is observed in the absence of dissolution (see **Figure 44F**). A possible common mechanism will be elaborated in the following.

For the well-studied LIB-cathode material class of transition metal oxides operated in organic lithium electrolytes, it is well-known that dissolved transition metal (TM) cations can re-deposit on the cathode together with electrolyte constituents as insoluble, insulating and electrochemically inactive species, *e.g.*, TM-O, TM-F or TM-CO_3 and other compounds. Such processes, which strongly resemble the well-known SEI formation on graphite, were found to have strongly detrimental effects on the kinetics and mass transport properties of the battery electrodes and thereby represent a major degradation pathway for LIB-cathodes.[147,253,286,343,344] A similar dissolution and re-deposition mechanism could possibly be responsible for the herein discussed degradation of PBAs. This hypothesis integrates both the observed active material dissolution, as well as the detrimental morphological transformation. In contrast to organic electrolyte systems, however, the dissolved transition metals would, in this case, not be re-deposited as deviating species, but as the same as the original material. This results from the absence of available reactants stemming from electrolyte decomposition, as the aqueous $NaClO_4$ solution is expected to be entirely stable. The compositional integrity of the surface was furthermore confirmed by the findings from **Section 6.4.1**.

Re-precipitation and familiar phenomena are, in fact, not unknown for PBAs. In previous studies, intentional dissolution and subsequent re-crystallization, complexation or transition metal ion exchange have been used as advanced synthesis routes to engineer PBAs and

derivatives with special crystal shapes, geometries and structural properties.[288,345,346,347] Further, it was shown that electrode-electrolyte species crossover is, in general, also possible under *operando* conditions. By cycling CuHCF in the presence of Zn^{2+} ions in the electrolyte, partial cation exchange ($Cu^{2+} \leftrightarrow Zn^{2+}$) and subsequent nucleation of ZnHCF phases was observed during extended cycling.[289] Similar findings were reported for FeHCF cycled in the presence of Cd^{2+},[348] and for MnHCF cycled in the presence of Fe^{3+}.[349] Interestingly, under controlled and specifically tailored conditions, electrochemically driven dissolution and re-crystallization can even have a self-healing "rejuvenation" effect on PBA particles during cycling, as recently shown by Xie *et al*. (for a composite-electrode) and thereby mitigate morphological degradation.[350] They found that conventional thermodynamics does not control the dissolution and re-crystallization process, as it cannot respond quickly enough under fast, dynamic electrochemical charge-discharge conditions. Rather, a more complex mechanism governed by the local electric field was proposed. In reverse analogy, an uncontrolled and random re-deposition of NiHCF phases is likely to result in the heavily distorted structure and inhomogeneous morphology of the degraded electrode as revealed in **Section 6.4.2**.

This can be further understood by drawing a parallel to the common electrodeposition process as described in **Section 5.3**, where Na^{+}, Ni^{2+} and $Fe(CN)_6^{3-}$ are provided as precursors in equal and uniform concentrations in the deposition solution. By performing CV, ordered nucleation of NiHCF is achieved on the Au-substrate, while the developing grains serve as continuous anchoring points for the advancing deposition. This process leads to a homogenous film formation with longish, stick-like grains. In contrast, the morphological degradation during battery-electrode operation results in the random aggregation of re-deposited small, irregular pebble-like grains. This might be caused by non-uniform reactant availability depending on the transient dissolution of electrode constituents (see **Section 6.3.1**) and/or inhomogeneous current- and electric field distribution across the surface under fast, dynamic charge-discharge conditions. Similarly, it is well known for the PBA co-precipitation synthesis routine that uncontrolled conditions allowing "too-fast" precipitation result in particles of very inhomogeneous and irregular morphology with a high $[Fe(CN)_6]$-defect density and detrimental electrochemical properties.[275,277,351,352,353] From this point of view, redox-center vacancies in the herein discussed re-deposited NiHCF particles could also play a substantial role in lowering the capacity of the remaining material. Nevertheless, further studies will be needed in the future to explain the ongoing processes on the nano- and microscale.

In conclusion, the initial stage of material degradation is driven by the dissolution of active material. At the same time, the observed passivation effect of NiHCF electrodes cycled in rather dilute Na^+-electrolytes can be considered as a second-order mechanism. It results from the re-deposition of entirely new phases of NiHCF from the dissolved species instead of just a surface film formation, as discussed above. The accompanying morphological transformation to inhomogeneous aggregates of nanoparticles instead of regular grains as in the pristine state reflects the continuous power fade during cycling. This process is schematically depicted in **Figure 50**. It is strongly supposed that the combined dissolution and re-deposition degradation mechanism can be extrapolated to other PBAs and electrolytes involving different alkali metal cations. However, it is not clear how these findings based on pure active-material thin-film electrodes translate to composite-type ones. This question arises as the latter intrinsically come with a strongly deviating structural composition due to the incorporation of conductive, high surface area carbon and a polymeric binder. Distinct studies will be necessary for the future, but similar degradation pathways appear plausible.

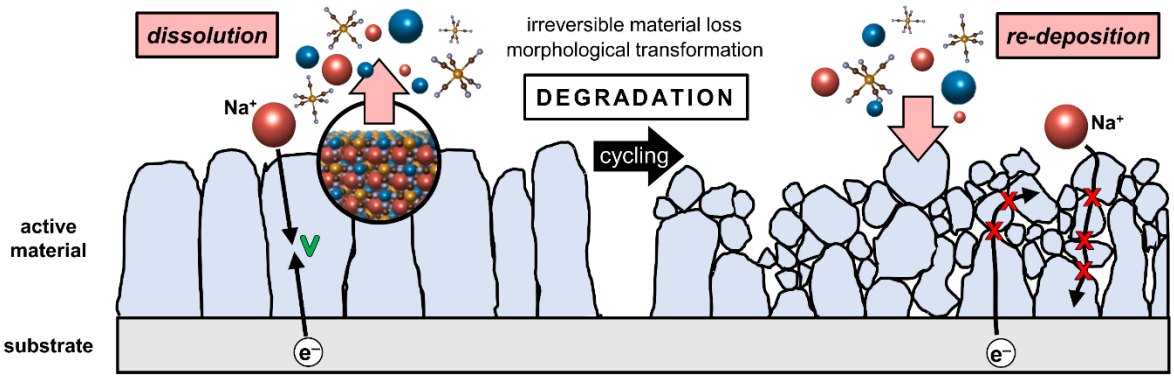

***Figure 50**. Schematic illustration of the proposed two-fold degradation mechanism for NiHCF during cycling based on the dissolution and subsequent re-deposition of electrode constituents. The morphologically reconstructed representation of the degraded electrode is based on the findings from SEM and AFM. Visualized atom sizes are not true to scale. For further details see the text.*

7 Fast-Charging Capabilities of Thin-Film Electrodes

7.1 Introduction and Background

Despite having several advantages over "traditional" LIBs, as outlined in **Chapter 1**, aqueous battery systems remain intrinsically limited in their achievable energy density. The stability window of the electrolyte usually only allows cell voltages of approximately 1.5 V and below to avoid parasitic side reactions associated with water splitting. Promising advances from the "water-in-salt"-strategy could result in raising the possible cell voltage above 2.0 V in the future (see **Section 2.2.4**). Unfortunately, the attainable potential range excludes the high-gravimetric-capacity carbon-based anode materials used for "traditional" intercalation-type batteries, *e.g.*, graphite with q = 372 mAh/g and E'_0 < – 2.8 V *vs*. SHE.[354] In contrast, the materials usually considered for ASIB-electrodes, such as PBAs, oxide- and phosphate-compounds, reach specific capacities in the range of ≈ 100 mAh/g or even less.[58,150] As a result, the energy density of aqueous batteries remains significantly below ≈ 2 V · 100 mAh/g · ½ = 100 Wh/kg based on the active materials for cathode and anode, which makes them uncompetitive to organic-electrolyte-based lithium- or sodium-ion batteries for long-range mobile applications.[41] Therefore, aqueous sodium- and potassium-ion batteries are expected to be adopted mainly for stationary use-cases.[53,55] However, raising their power rating and thereby the fast charging capability could significantly increase the attractiveness of ASIBs. So-called hybrid battery-supercapacitor systems combine a sufficient energy density with a high power density.[108,109] Supposing that a desirable recharging time of, *e.g.*, less than a minute (60C) can be enabled, new use-cases and opportunities could potentially involve not only fast-response power grid stabilization, but also urban short-distance electric mobility, *e.g.*, for public transportation as outlined in **Chapter 1**.

Inherited from the traditional fabrication procedure of LIBs,[355] PBA cathodes and anodes are usually prepared as composite electrodes using active material particles obtained from the co-precipitation synthesis routine.[64] This procedure follows mixing the active material powder, conductive carbon and a polymeric binder with an appropriate solvent and casting the slurry on a current collector, such as metal foil. Despite being the prevailing up-to-date method, it bears certain drawbacks, including a substantial presence of inactive material (carbon and

binder), as well as specific degradation pathways for composite electrodes as mentioned in **Section 6.2**. Importantly, the preparation of composite-type electrodes is very prone to cause performance deterioration if not implemented properly.[355] For example, the presence of binders can severely impact the electrode properties.[177,356,357] Contribution to hindered electron transport can stem from high active-material to current-collector contact resistance.[358] Furthermore, the diffusive transport of ions through the electrolyte-filled porous network of such composite structures can limit the power capability, especially for thick coatings.[341] In addition, if the synthesis conditions are not properly optimized and controlled, the PBA co-precipitation method often yields primary and secondary particles that exhibit inhomogeneous, detrimental crystallinity and morphology with long pathways for solid-state diffusion and unfavorable kinetic properties.[252,275,351,353,359] These effects have the potential to reduce the available capacity significantly and may cause severe hysteresis when operating the electrodes at high rates.[144]

In contrast, advanced binder-free and pure-active-material battery electrodes promise great potential to circumvent these problems.[177,183,356,357,360] Therefrom deduced strategies involve three-dimensional nano- and microstructured active material designs with beneficial conductivity and mass transport properties exposing a high surface area to the electrolyte for interfacial mass and charge transfer. Correspondingly, downscaling of active material dimensions and structures has evolved as an intriguing strategy to enable high rate capability and thereby evoke supercapacitor-like properties for batteries.[108,361,362,363,364,365] In recent years, this approach has as well been employed to create PBA-based and PBA-derived systems with high power rating.[346,366,367,368,369] In 2019, Marzak *et al*. reported an entirely PBA-based ASIB with promising fast-charging capability.[224] By synthesizing the active material electrodes as thin films *via* electrochemical deposition, the resulting full cell could be charged at 360C (10 seconds) while maintaining a 24 Wh/kg energy density. The electrodeposition technique is potentially well-suited to synthesize tailored nano- and microstructured battery electrodes under highly controlled conditions with the goal of achieving the abovementioned beneficial properties of binder-free systems.[370] Next to using appropriate conductive substrates intrinsically providing a structured template for conformal active material coating,[177] such endeavors could even involve entirely new battery designs based on, for example, 3D-printed matrixes.[371,372]

Despite not being commonly used to prepare battery electrodes in today's practice, the electrodeposition method is well known for PBAs, as it was very common especially in the

initial period when research interest in this functional material class started more than forty years ago.[243,244,245] Despite these early studies, a practical guideline for optimized thin-film electrode designs for high-power applications remains elusive. Yet, a systematic investigation of the interfacial processes and subsequent intercalate transport during (dis)charging is indispensable to reasonably benchmark their performance against the usual composite electrode assembly with active-material particles.[208] This chapter aims to provide a mechanistic understanding of the fast-charging capabilities of thin-film PBA electrodes and derive a perspective on their design as hybrid battery-supercapacitor systems. First, the rate-limiting steps governing the interfacial mass and charge transport properties will be systematically investigated for NiHCF model electrodes by varying the thickness of the electrochemically active film. The role of parasitic side reactions in the context of low-mass-loading electrodes and flat cell geometries will be briefly discussed. The findings on the fast-charging capability will be extrapolated to entirely PBA-based full-cell ASIBs. Finally, a possible pathway to transferring the beneficial properties of such model systems towards practically relevant mass loadings will be elaborated.

The investigatory approach, findings and discussions in this chapter are in close accordance with the published article: "X. Lamprecht, P. Zellner, G. Yesilbas, L. Hromadko, P. Moser, P. Marzak, S. Hou, R. W. Haid, F. Steinberger, T. Steeger, J. M. Macak, A. S. Bandarenka. **Fast Charging Capability of Thin-Film Prussian Blue Analogue Electrodes for Aqueous Sodium-Ion Batteries**. *ACS Applied Materials and Interfaces* **2023**, *15*, 23951–23962" and originated from close collaboration with the mentioned co-authors. A reprint is available in the appendix.

7.2 Impact of Film Thickness on Charge-Discharge Characteristics

Thin-film model electrodes on planar Au-substrates, as presented and characterized in detail in **Section 5.3**, were used to study the impact of the film thickness of electrodeposited NiHCF on the fast-charging capability. The potentiodynamic deposition in combination with EQCM allows to determine the mass loading of the active material coating precisely. For mass loadings above 20 µg/cm^2, an increasing contribution from viscous coupling was observed with EQCM, which could possibly result in erroneous mass determination (see **Section 3.1.4**). Therefore, the loading was extrapolated coulometrically using the specific capacity of NiHCF (68 mAh/g, see **Figure 27G**) determined below the EQCM-deviation threshold. This is justified by considering that there is no apparent physical or chemical reason why higher loadings should have a deviating stoichiometry and corresponding intrinsic specific capacity. The thickness of the coating was estimated similarly for higher loadings using a specific thickness of 6.6 nm/(cm^2/µg) (see **Figure 28D**).

Figure 51 schematically illustrates the individual steps involved during the intercalation of sodium in NiHCF thin-film battery electrodes. The process is initiated by the electron transfer at Fe(II/III) centers, followed by the insertion of previously desolvated Na^+ across the electrode-electrolyte interface (coupled electron and ion transfer). As explained in **Section 3.1.3.3**, intermediate anion ad/desorption is involved to compensate transient surface charges ("three-step mechanism"). Subsequently, intercalated Na^+-ions propagate within the nanoporous framework of NiHCF *via* solid-state diffusion to entirely occupy all available intercalation sites of the active material. Replenishment of sodium ions at the electrode-electrolyte interface is achieved by diffusion from the bulk electrolyte. Overall, the achievable (dis)charging rate of the battery material depends on these individual steps and their complex interplay. In the following study, thin-film electrodes with mass loadings from 10 – 83 µg/cm^2 (approximated thickness of 66 – 548 nm) are investigated to identify the rate-limiting step. The theoretical background of non-equilibrium charge-discharge characteristics, including sluggish kinetics and slow mass transport, is introduced in **Section 2.2.3**. Experimentally accessible diagnostic criteria to differentiate these cases using galvanostatic and potentiodynamic cycling are introduced in **Section 3.1.1**. The electrochemical experiments were performed in close collaboration with P. Zellner, whose Bachelor's thesis and activity as a working student was advised as part of this project.[373]

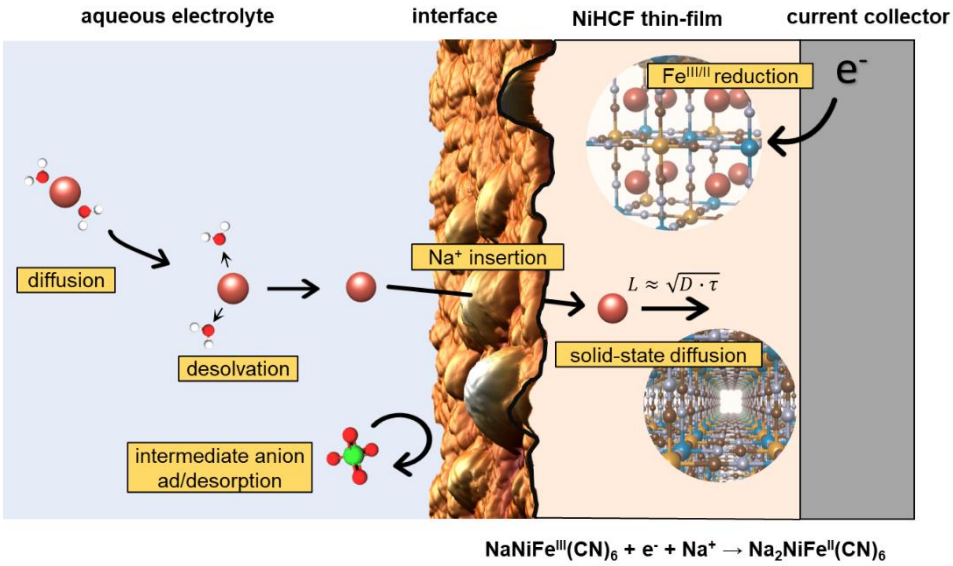

***Figure 51**. Scheme of the individual steps involved in the intercalation of sodium in NiHCF. See text for a detailed description. Note that the solvation shell of sodium only consists of a few water molecules, as discussed in **Section 6.3.2.3**. Reproduced with permission from ref. 225. Copyright © 2023, American Chemical Society.*

Exemplary galvanostatic discharge curves of NiHCF thin-film electrodes from low to remarkably high rates (3000C, 1.2 seconds) are shown in **Figure 52A-C** for thin, intermediate, and thick coatings. The iR_u-corrected (R_u is mainly caused by the ionic conductivity of the electrolyte) discharge curves exhibit almost no potential hysteresis regardless of the imposed rate, implying very fast, reversible charge transfer kinetics associated with a negligible driving force. Accordingly, the coupled electron and ion transfer step should not pose a limiting factor to the system during oxidation and reduction. For the lowest investigated mass loading (10 µg/cm^2), the discharge curve and attainable capacity are almost insensitive to the applied current. Correspondingly, the electrode remains in quasi-equilibrium and the $E(q)$-curve can be entirely described by the intercalation isotherm (see **Section 5.4**).[142] Nevertheless, higher loadings and therefore thicker films increasingly suffer from deteriorating capacity retention at higher C-rates, as shown in **Figure 52D**. In contrast to the 10 µg/cm^2-film, the available capacity of the 83 µg/cm^2-film drops below 95% at rates higher than ≈ 5C, while only 50% remain at a rate of 2600C. As the associated coulombic efficiency remains continuously high and unchanged, such behavior strongly implies that less and less active material participates in the charge-storage processes when increasing the rate.

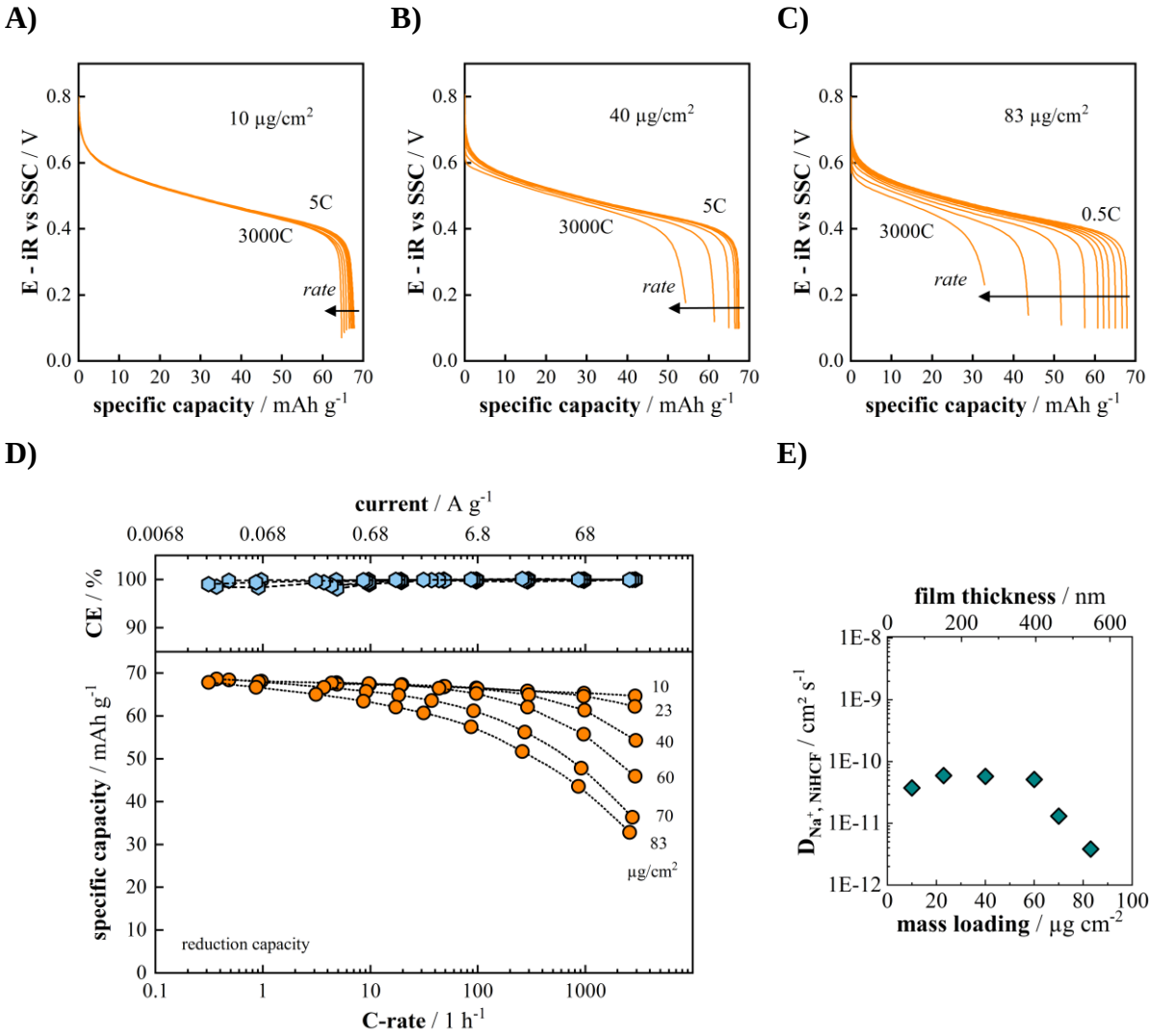

Figure 52. *(**A**-**C**) Galvanostatic discharge curves of NiHCF thin films with varying mass loadings cycled in 8 M $NaClO_4$ at low-to-high C-rates. The horizontal arrows indicate the decreasing available capacity. (**D**) Capacity retention of different mass loadings of NiHCF thin films for a large range of tested C-rates. The dashed lines serve as a guide to the eye. (**E**) Estimation of the apparent solid-state diffusion coefficient for Na^+ within the active material using a simplified approach according to* ***Equation 71****. See text for details. The data presented in these graphs are reproduced with permission from ref. 225. Copyright © 2023, American Chemical Society.*

Supposedly, beyond a characteristic rate limit, the solid-state diffusion of Na^+ is no longer fast enough to entirely penetrate the material, which leads to the buildup of a Na^+-concentration gradient within the thin film.[186,208,374,375] Therefore, the charge-discharge characteristics likely change from quasi-equilibrium to diffusional rate control.[142] As reflected in the experimental findings, where this transition is observed at lower C-rates for higher film thicknesses, the characteristic diffusion time τ is strongly coupled to the electrode dimension as described by **Equation 71**:[142,144]

$$\tau = \frac{l^2}{D_{Na^+,NiHCF}} \qquad \textbf{Equation 71}$$

Here, l is the diffusion length, which corresponds to the film thickness if τ is exactly long enough to entirely fill up the active material during electrode reduction. $D_{Na^+,NiHCF}$ is the apparent diffusion coefficient of Na^+ within the NiHCF lattice. As a plausibility check,

$$\tau \approx \frac{1}{C\text{-}rate_{max}}$$

should therefore scale with the squared film thickness and allow to estimate the apparent diffusion coefficient. A capacity retention of 95% was used as a threshold to determine the C-rate at which the system transitions to diffusional control ($C\text{-}rate_{max}$). As shown in **Figure 52E**, $D_{Na^+,NiHCF} \approx 10^{-12} - 10^{-10}$ cm^2/s is obtained throughout the investigated mass loadings, which possibly slightly overestimates D, but still is in reasonable agreement with reported values.[208] It should be noted that this approach reflects an extremely simplified approximation of the much more complex mass transport dynamics within the film, which are in general governed by **Equation 20** and **Equation 23** with the appropriate boundary conditions. Nevertheless, it should yield a reasonable approximation of the order of magnitude of the solid-state diffusion coefficient, also allowing to certainly exclude diffusion of Na^+ within the electrolyte ($D_{Na^+,8M\ NaClO_4} \approx 10^{-6} - 10^{-5}$ cm^2/s)[164] as a potential source for rate limitation.[376] In addition, an excess reservoir of Na^+ ions is available in the vicinity of the electrode surface within the highly concentrated electrolyte, preventing the buildup of a concentration gradient in the liquid phase during intercalation. In conclusion, the available reaction time during charge-discharge cycles must remain long enough to maintain a Na^+-concentration profile in the NiHCF thin film, which allows continuous current flow until every lattice site is filled with Na^+ during reduction. This equally applies *vice versa* for the oxidation direction (deintercalation). This condition is equal to the diffusion length at a certain C-rate remaining larger than the film thickness. Accordingly, **Equation 71** can serve as an easy and practical guideline to specifically design active material coatings for a desired power rating under the condition of fast charge-transfer kinetics.[144,183] For almost complete capacity usage at 60C (one minute), the thickness of a NiHCF thin-film electrode should therefore remain below ≈ 500 nm, which corresponds to a mass loading of ≈ 80 µg/cm^2 on a flat substrate geometry. Strategies to achieve higher mass loadings per substrate footprint will be discussed in **Section 7.6**.

A) **B)**

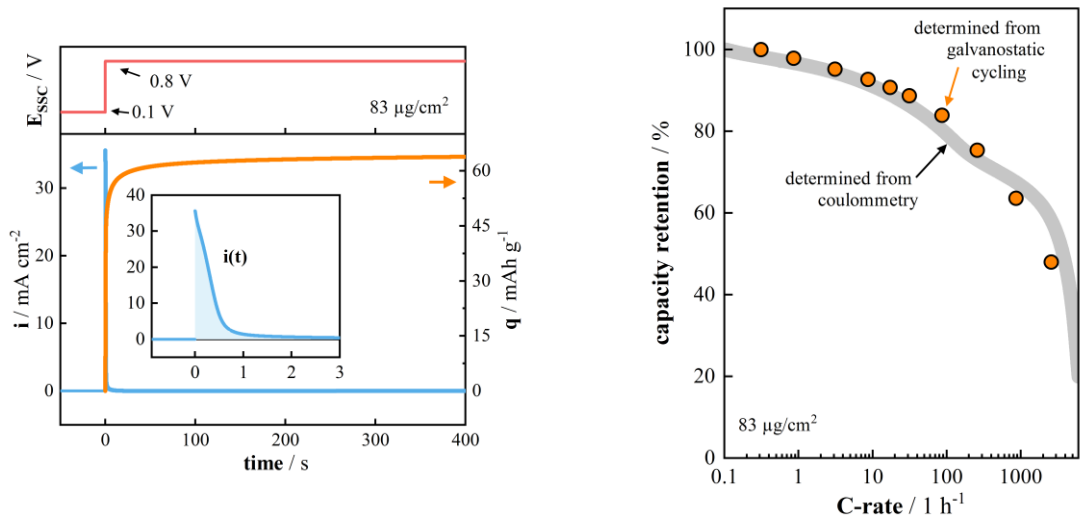

***Figure 53**. Exemplary presentation of the coulometric potential-step method as an accelerated alternative rate capability test according to ref. 377. (**A**) Transient response of an entirely reduced NiHCF thin-film electrode in 8 M $NaClO_4$ to a potential step causing full oxidation. (**B**) Therefrom obtained rate capability curve (grey) in comparison to the galvanostatically obtained data (orange circles).*

As an interesting side note, it should be mentioned that the usually quite time-consuming acquisition of rate capability data can be substantially accelerated. Especially when testing battery materials down to low charging speeds, such experiments can take several days to collect a set of different rates with a few cycles each. It has been proposed by Heubner *et al.*[377] that similar information can be obtained by employing the coulometric potential-step method, which only takes a few seconds to minutes. As shown in **Figure 53A** for the exemplary case of an 83 µg/cm² NiHCF thin-film electrode, the potential is stepped from a value where the active material is entirely reduced towards a value which stipulates full oxidation according to the intercalation isotherm. The recorded time-dependent current transient and therefrom obtained transferred charge can be used to calculate a capacity retention to C-rate dependency:

$$Q(t) = \int_0^t i(t) \cdot dt\,, \qquad Q(t \to \infty) = Q_{max}$$

$$\rightarrow \quad \frac{Q(t)}{Q_{max}} = \frac{\int_0^t i(t) \cdot dt}{\int_0^\infty i(t) \cdot dt} \quad \text{and} \quad C\text{-}rate(t) = \frac{i(t)}{\int_0^\infty i(t) \cdot dt} \cdot 3600\,\frac{\text{s}}{\text{h}}$$

Accordingly, for any time *t*, the measured ratio $Q(t)/Q_{max}$ can be assigned a corresponding C-rate and the current transient curve can be transformed into a rate-dependent capacity retention. For a more detailed discussion of the analysis, the reader is referred to ref. 377. As seen in **Figure 53B** this approach yields a remarkably good agreement with the

galvanostatically determined rate capability plot, while only a few minutes were needed to acquire the data. It should be noted that this method was originally reported for porous composite electrodes, while it is apparently equally applicable to thin-film electrodes.

In analogy to the galvanostatic experiments presented above, the charge-discharge characteristics of NiHCF thin-film electrodes were investigated by means of CV to determine the rate-limiting processes in dependence of the mass loading over a wide range of scan rates up to 2000 mV/s. Exemplary *iR*-corrected and scan-rate-normalized CVs (current divided by scan rate) are shown for thin, intermediate, and thick coatings in **Figure 54A-C**. For all loadings, highly reversible CV-shapes are obtained at low scan rates, which perfectly match with the modelled Nernstian response for a two-phase NiHCF electrode as introduced in **Section 5.4**. As exemplarily analyzed in detail for a 40 µg/cm^2 electrode (see **Figure 54D**), a linear $i_{peak}(v)$ dependency (a = 1, see **Equation 35**) is obtained from low to medium scan rates, showing negligible peak-to-peak separation. This confirms that the system exhibits fast charge transfer kinetics with a negligible driving force not affecting the shape of the CV.[142] Such characteristic is analogous to the capacitive response observed for the adsorption of surface-near ionic species in liquid electrolytes (double-layer capacitors) and 2D-confined faradaic reaction centers (pseudocapacitance, for example RuO_2) employed for supercapacitors. This analogy is related to the nature of the intercalation process as quasi-3D-adsorption (see **Section 2.2.3**).[378,379] Beyond a certain scan rate, the linear correlation is gradually lost ($d\log(i_p)/d\log(v) \rightarrow 0.5$), accompanied by an increase of ΔE_{pp} towards 50 – 60 mV. At the same time, a "tail-like" current decay after reaching the peak emerges in the CV shape. Such behavior is characteristic for the transition of the redox response from quasi-reversible to diffusional control, where mass transport limitations can no longer be neglected.[142,379,380] This transition proceeds at even slower scan rates for increasing mass loadings and thereby higher film thicknesses (see **Figure 54E**).[248,374] This strongly implies that the solid-state diffusion of Na^+ within NiHCF is the source of rate limitation in great similarity to the result from galvanostatic analysis. An arbitrary deviation of 10% of the absolute peak current from the fitted quasi-Nernstian linear dependency (a = 1) is set as an approximate threshold to determine the scan rate v_{max} at which the system transits to diffusional control. Accordingly, the duration of a half-cycle at this specific scran rate can be used to estimate the characteristic diffusion time:

$$\tau \approx \frac{E_{upper\ vertex} - E_{lower\ vertex}}{v_{max}}$$

Using **Equation 71**, apparent diffusion coefficients in the range of $D_{Na^+,NiHCF} \approx 10^{-11}$ – 10^{-10} cm^2/s are obtained (see **Figure 54F**), which is in good agreement with the results from the galvanostatic approach discussed above.

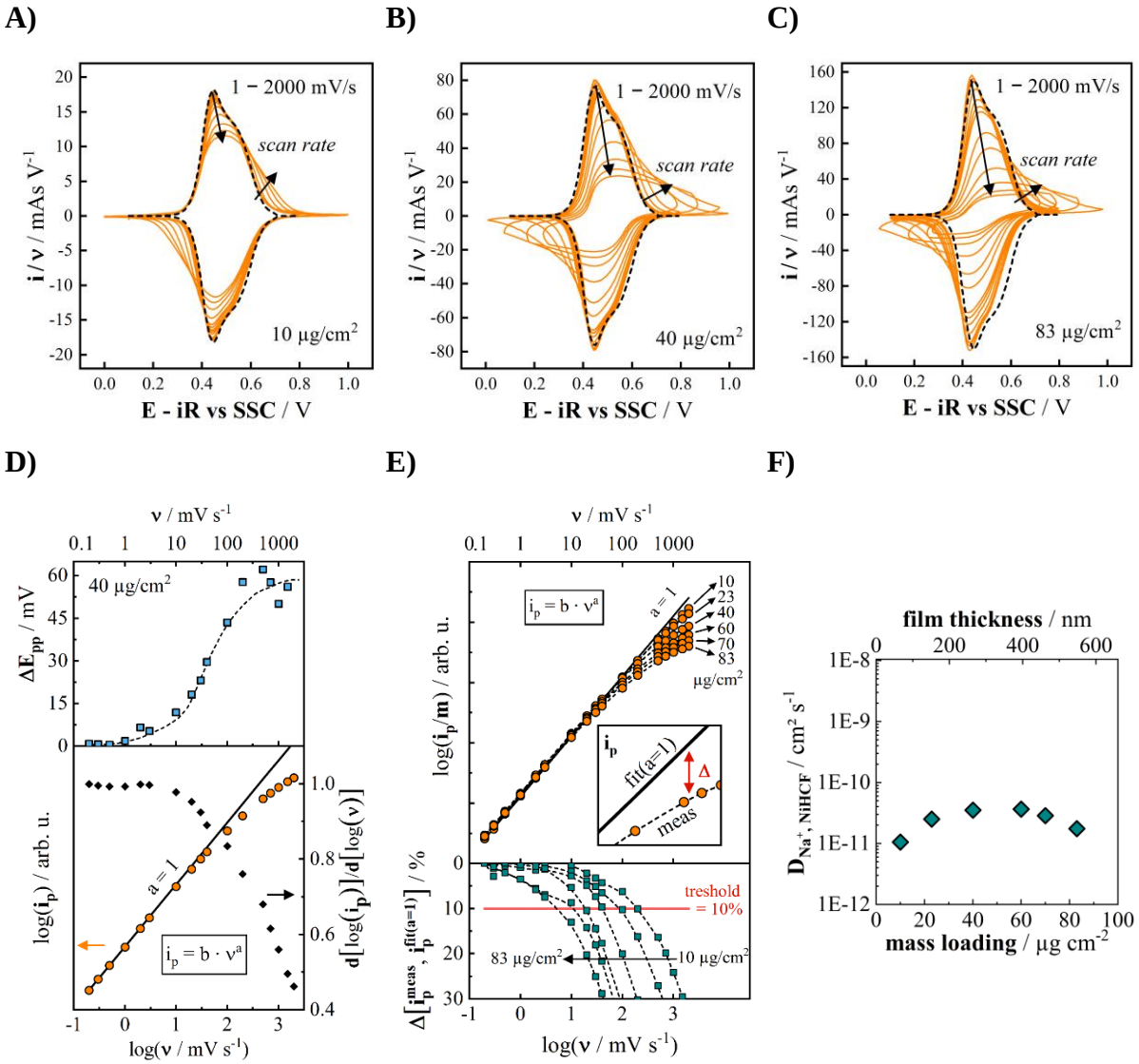

***Figure 54**. (**A**-**C**) CVs of NiHCF thin films with varying mass loadings cycled in 8 M $NaClO_4$ at low-to-high scan rates. The arrows indicate the development of the i(E) characteristics for increasing scan rates. The black dashed lines depict the modelled response of the active material in quasi-equilibrium according to **Section 5.4**. (**D**) Exemplary detailed analysis of the iR-corrected peak-to-peak separation and peak current to scan rate dependency. The solid black line shows a linear fit (a = 1) of log(i_{peak}) as a function of log(v), while the black diamonds show the local derivative. (**E**) Mass-normalized peak-current to scan rate dependency (upper graph) for various mass loadings and corresponding deviation (lower graph) of the absolute peak current from the linear fit (solid line). The dashed lines in **D** and **E** serve as a guide to the eye. (**F**) Estimation of the apparent solid-state diffusion coefficient for Na^+ within the active material using a simplified approach according to **Equation 71**. See text for details. The data presented in these graphs are reproduced with permission from ref. 225. Copyright © 2023, American Chemical Society.*

In summary, the (de)intercalation of Na^+ in NiHCF is associated with remarkably fast and reversible kinetics, allowing rapid cycling of the electrode without significant losses up to very high rates until mass transport limitations take over the rate control. It is, however, necessary to note that this fast-charging capability is not enabled by extraordinarily fast diffusional properties of the intercalate within the active material. Instead, it rather results from the short required diffusion length within the sub-micron-sized thin-film electrodes[208] next to the fast kinetic properties of the active material in the thin-film configuration. Nevertheless, their supercapacitor-like properties strongly support the opportunities associated with microstructured active materials for high-power batteries.

7.3 Comparison to Composite-type Electrodes

To provide a comparison and classification of the performance of the thin-film electrodes, results obtained for a NiHCF composite electrode under similar testing conditions should be briefly commented in the following. The latter were prepared and characterized as described in **Section 4.2.2** and **Section 5.3** with a probably more commercially-relevant mass loading of 1.49 mg/cm^2. It should be noted that the performance, especially the rate capability, of composite-type electrodes strongly depends on the loading or, more precisely, the thickness of the electrode coating.[180] The following analysis should therefore mostly be considered as a qualitative reference for practical battery electrodes.

A) **B)**

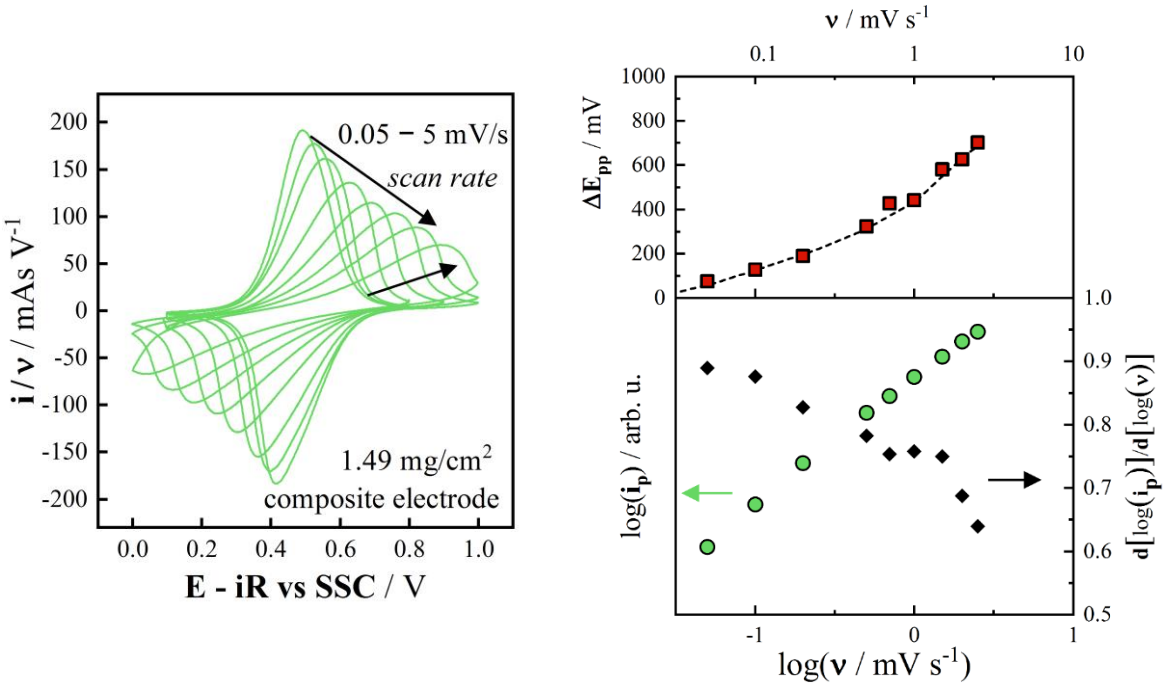

***Figure 55**. (**A**) CV at different scan rates of a NiHCF composite electrode in 8 M $NaClO_4$. The arrows indicate the development of the i(E) characteristics for increasing scan rates. (**B**) Analysis of the iR-corrected peak-to-peak separation and peak-current to scan rate dependency along with the derivative of $i_p(v)$. The dashed line serves as a guide to the eye. The data presented in these graphs are reproduced with permission from ref. 225. Copyright © 2023, American Chemical Society.*

The *iR*-corrected CVs at different scan rates expose a non-linearity of $i_{peak}(v)$ even at scan rates below 1 mV/s, while a strongly increasing peak-to-peak separation and irreversible $i(E)$-characteristic is observed for increasing rates (see **Figure 55A** and **Figure 55B**). Even at a scan rate of 5 mV/s, the oxidation and reduction half-waves already hit the allowed potential

boundaries, forbidding a further increase of the cycling rate. Overall, this behavior implies "mixed" rate control with both mass transport and charge-transfer kinetics, significantly limiting the intercalation dynamics already at a low cycling rate.[142]

In analogy to the CVs, the galvanostatic discharge curves of the NiHCF composite electrode are characterized by severe hysteresis for increasing rates (see **Figure 56A-B**). At a rate of 25C, the charge-discharge curves are separated by ≈ 500 mV and prematurely hit the potential limitations, possibly contributing to bad capacity retention. Impedance spectroscopy was performed to isolate and quantify the effect of the charge transfer on the overall polarization (**Figure 57A-B**). The spectra were fitted with the model described in **Section 3.1.3.3**. As seen in **Figure 57C**, the mass-normalized charge transfer resistance of the composite electrode is around two orders of magnitude larger than for the thin-film configuration, which consistently reflects its impaired kinetics compared to the hysteresis-free behavior of the thin films. The extracted charge transfer resistance R_{ct} = 1502 Ω at SOC = 50% and an assumed transfer coefficient of $\alpha = 0.5$ were used to construct a Butler-Volmer-like polarization curve according to **Equation 18** and **Equation 42**, as shown in **Figure 56C**. It should be noted that this semi-empirical treatment is based on a cumulative exchange current reflecting an overall response of the active material, which does not allow to extract system-specific properties due to the inhomogeneity of the NiHCF particles (see discussion below). For low currents, the *iR*-corrected polarization determined at SOC = 50% exhibits behavior as expected for a kinetically controlled process. However, for higher currents a significant deviation from the purely kinetic regime is observed with the slope of $\log(i)$ *vs.* $(\eta - iR)$ being smaller than $\alpha F/(2.303 \cdot RT)$ as predicted by the Tafel-equation, which indicates that mass-transport limitations become rate limiting.[194,375,381]

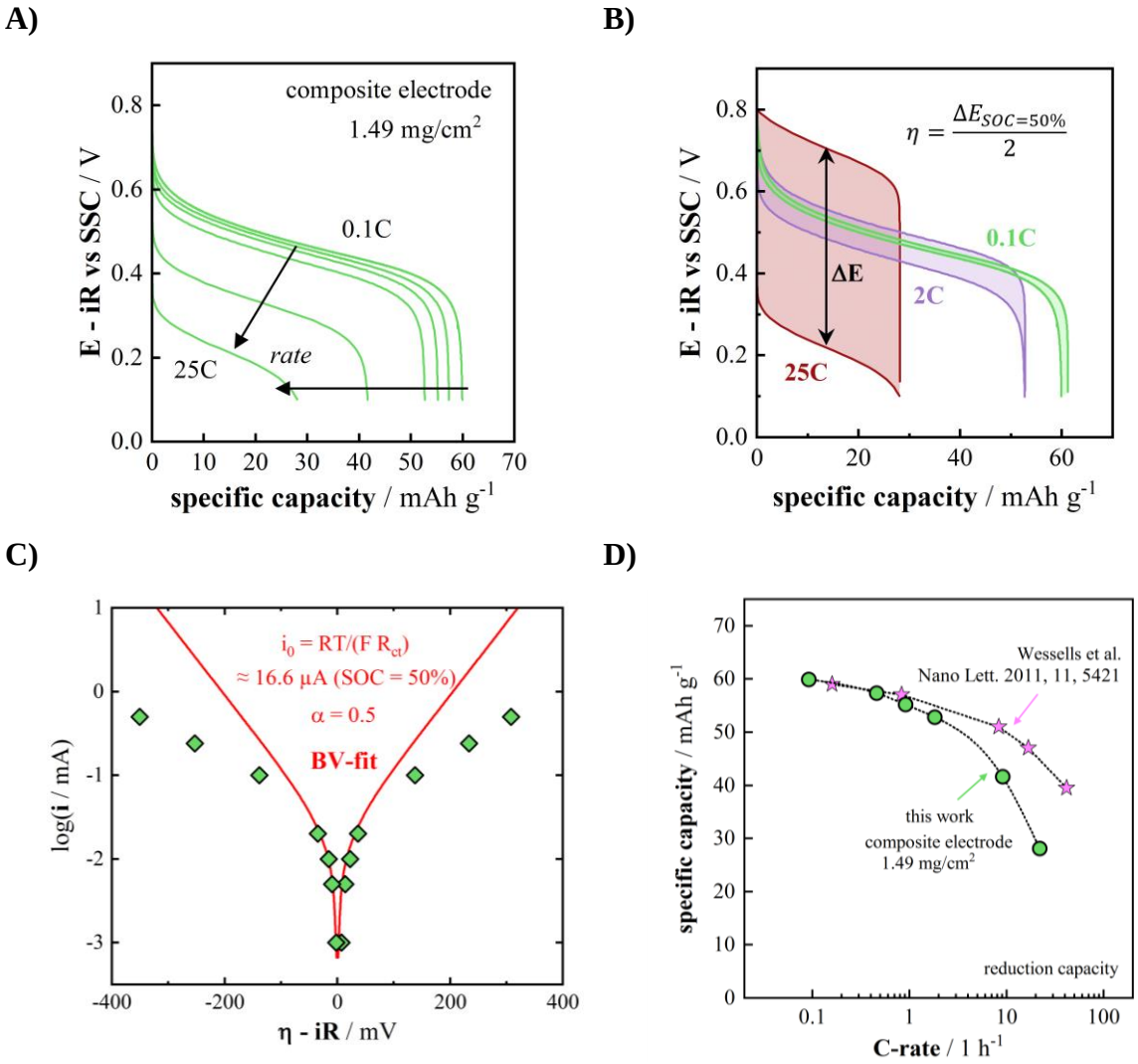

***Figure 56**. (**A**) Galvanostatic discharge curves at different C-rates of a NiHCF composite electrode in 8 M $NaClO_4$. The horizontal arrows indicate the decreasing available capacity, and the vertical arrows the growing hysteresis for increasing rates. (**B**) iR-corrected charge-discharge curves. The polarization can be approximated according to **Equation 36** at 50% SOC and is plotted in dependence of the imposed current in (**C**) along with a Butler-Volmer-like calculated polarization curve using R_{ct} to estimate i_0 at 50% SOC. (**D**) Capacity retention of the electrode in comparison to the performance of a literature-reported NiHCF composite-type electrode. The dotted lines serve as a guide to the eye. The data presented in these graphs are reproduced with permission from ref. 225. Copyright © 2023, American Chemical Society.*

Apart from the strong hysteresis, a detrimental capacity retention is obtained for the composite electrode as seen in **Figure 56D**, with a capacity reduction of 50% at 25C. Even though a slightly better performance was observed in other studies, as for example in ref. 84, it is undoubtedly inferior to the thin-film electrodes regarding mass-specific power. To understand this, the morphology of the active material was investigated using SEM. As shown in **Figure 57D**, the NiHCF powder obtained from the co-precipitation synthesis consists of very large

secondary particles with a size of several micrometers, while the arbitrarily shaped primary particles have a size of ≈ 50 nm as usually reported (see inset in **Figure 57D**).[84,238] These large active material agglomerates were maintained within the carbon-binder-matrix after slurry coating the composite electrode (see **Figure 57E**). The long solid-state diffusion pathway for sodium ions within these large secondary particles provides a reasonable explanation for the poor rate capability,[355] consistent with the mass-transport limitations concluded from the polarization analysis above. In addition, the agglomerates within the carbon-binder-matrix provide a significantly lower surface-area-to-mass ratio in comparison to the thin-film electrodes or other smaller, sub-micron-sized geometries, resulting in a higher mass-normalized charge transfer resistance and impaired kinetics.[252,382]

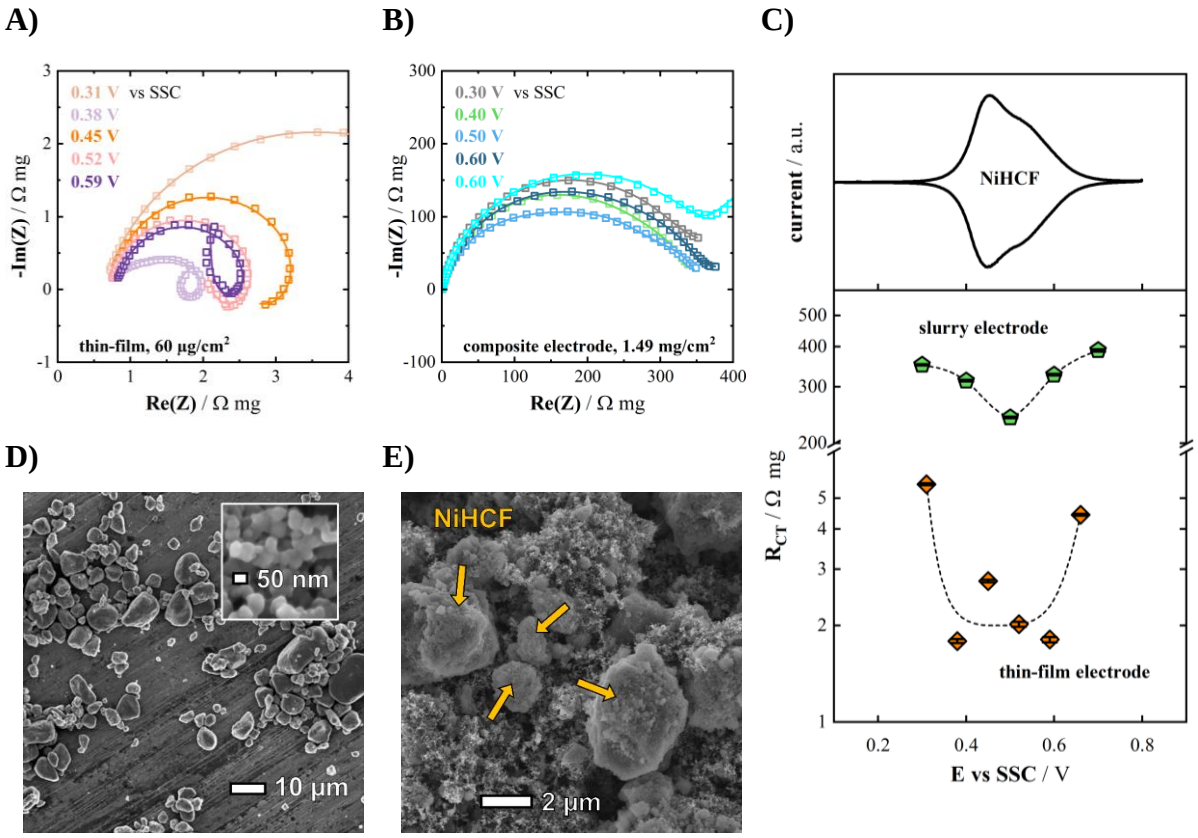

***Figure 57**. Impedance spectra of a NiHCF (**A**) thin-film and (**B**) composite electrode fitted using the EEC discussed in **Section 3.1.3.3**. The therefrom obtained mass-normalized charge transfer resistance within the electrochemically active potential range of NiHCF is shown in (**C**). The data presented **A**-**C** are reproduced with permission from ref. 225. Copyright © 2023, American Chemical Society. (**D**) SEM image of the NiHCF powder, which consists of large agglomerated secondary particles. The inset shows ≈ 50 nm-sized primary particles. (**E**) SEM image of the composite electrode, in which the structure of the large agglomerates is maintained (see exemplary arrows).*

In conclusion, the significant polarization and low rate capability of NiHCF in the composite electrode configuration can be consistently explained by the detrimental structure of the active material consisting of too large agglomerates with inhomogeneous morphology. The effect could be further enhanced by blocking active sites for interfacial ion transfer at NiHCF within the carbon-binder-matrix, poor contact with the current collector foil or detrimental transport properties of ions inside the electrolyte-filled porous network of the composite electrode (see introduction to this chapter). This highlights the necessity to precisely optimize the specific material synthesis and electrode preparation procedure in the case of slurry casting to ensure superior performance and reproducibility. In contrast, the thin-film electrodeposition technique employed herein allows to control and tune the active material composition and structure precisely and reproducibly, thereby enabling a high power capability.

7.4 Excursion: Role of Parasitic Side-Reactions Associated with Low-Mass-Loading Electrodes

As discussed in **Section 5.3**, the thin-film model electrodes investigated herein had mass loadings well below 1 mg/cm^2 and thicknesses in the range of 50 – 1000 nm. While this allows remarkably high current densities up to 100 A/g, it also comes with significant vulnerability for parasitic side reactions towards low currents. A brief discussion of this potential hazard will be provided in the following on the example of MnHCM. This PBA-derivative is considered a promising anode candidate for ASIBs due to the low redox potential of its $Na_xMn^{II}Mn^{I/II}(CN)_6$ transition (see **Figure 25A**).[68,95,200,233,383] The electrochemical experiments were performed in close collaboration with F. Steinberger and T. Steeger, whose Master's and Bachelor's theses were advised as part of this project.[384,385] The investigatory approach was in parts based on the previous work of P. Moser.[386]

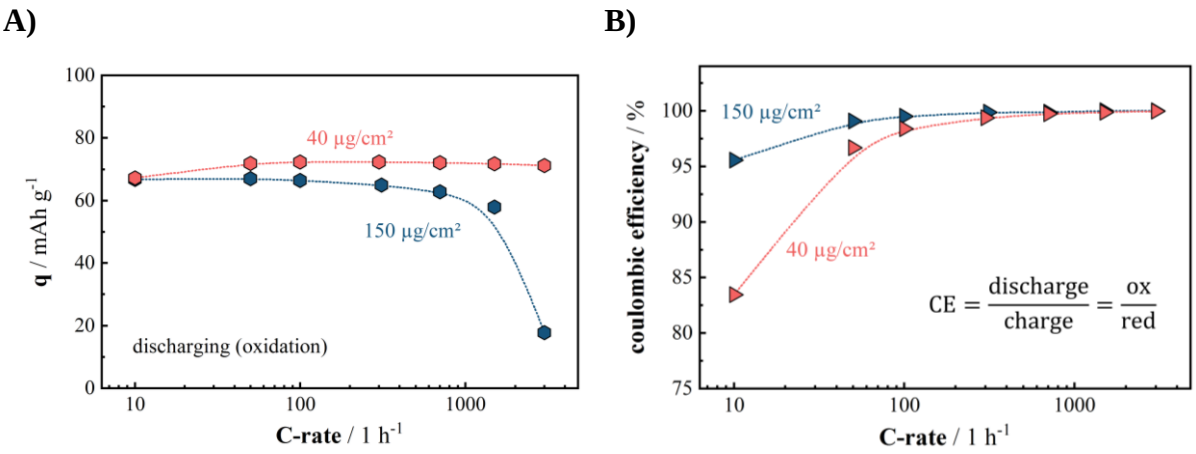

***Figure 58**. (**A**) Specific discharge capacity and (**B**) coulombic efficiency for two different mass-loadings of MnHCM thin-film electrodes during galvanostatic cycling in 8 M $NaClO_4$ (pH = 5.7) at various C-rates. The dotted lines serve as a guide to the eye. The data presented in these graphs are reproduced with permission from ref. 225. Copyright © 2023, American Chemical Society.*

In analogy to NiHCF, MnHCM thin-film electrodes on planar Au-substrates were obtained *via* electrochemical deposition, as described in **Section 4.2.1.2**. Whereas this enables a similarly beneficial loading-dependent capacity retention behavior up to very high rates, as shown in **Figure 58A**, a significant decrease of the coulombic efficiency is observed towards lower rates (see **Figure 58B**). For a 40 µg/cm^2 film, only 83% of the charge can be retained during oxidation compared to the reduction even at a moderate rate of 10C, while this value increases

to 95% for a loading of 150 µg/cm^2. Overall, the curves show a strongly decreasing trend of the coulombic efficiency towards longer (dis)charging times. As MnHCM is considered as an anode material, the oxidation direction corresponds to the electrode discharge. This means that such low CE represents a severely detrimental property of the material as much more charge is needed to recharge the electrode compared to one obtained during discharging. Apparently, the relative impact of this effect is stronger for lower mass loadings and therefore thinner films.

Whereas its low redox potential of ≈ – 0.9 V *vs.* SSC in 8 M $NaClO_4$ (– 0.35 V *vs.* RHE at pH = 5.7) makes MnHCM very attractive as an anode material for ASIBs, it also makes it an easy source of electrons for the reduction of a reaction partner as explained in **Section 2.1.3**. Such parasitic oxidation of a fully intercalated (reduced, $Na_3Mn^{II}[Mn^{I}(CN)_6]$) MnHCM anode effectively represents a self-discharge of the material. A possible oxidation pathway involves the reduction of trace amounts of atmospheric O_2 dissolved in the electrolyte. Such a process is enabled due to the standard reduction potential of O_2 (see **Table 1**) being well above the redox potential of MnHCM:[387]

$$4Na_3Mn^{II}[Mn^{I}(CN)_6] + 2H_2O + O_2 \rightarrow 4Na_2Mn^{II}[Mn^{II}(CN)_6] + 4Na^+ + 4OH^-$$

This hypothesis was assessed by intentionally purging the electrolyte with atmospheric air, which naturally contains ≈ 21% oxygen, and leaving a fully reduced MnHCM electrode in an open-circuit configuration. As seen in **Figure 59A**, the open-circuit potential of the electrode almost instantly reaches 0.3 V *vs.* RHE, reflecting a complete oxidation of the active material. At an equal mass loading, purging the electrolyte with argon leads to a ≈ 50 times reduction of the self-discharge speed. Concludingly, dissolved oxygen in the electrolyte can play an important role in the self-discharge of MnHCF. The amount of oxygen needed to entirely oxidize a 10 µg/cm^2 thin film of MnHCM can be estimated as done in the following. For pure water at 25°C, the solubility of oxygen from the air is ≈ 0.26 mmol/l, which should, however, be strongly reduced in the case of the herein-employed concentrated electrolyte.[170,388,389,390] The electrochemical cell was furthermore constantly purged with argon gas to avoid contamination of the electrolyte with undesired gases (see **Section 4.1**). The charge of the electrode available for parasitic conversion is

$$10\ \frac{\mu g}{cm^2} \cdot 1.37\ cm^2 \cdot 72\ \frac{mAh}{g} \approx 1\ \mu Ah = 3.6\ mAs.$$

Using the Faraday constant, it can be calculated that 3.6 mAs corresponds to a number of electrons of ≈ 0.037 µmol. According to the reaction equation above, one O_2 molecule can "steal" four electrons. Therefore, less than 0.01 µmol of dissolved oxygen would be needed to

fully discharge the electrode. Considering the electrolyte volume of 120 ml, it is found that this corresponds to a concentration of dissolved oxygen of 0.083 µmol/l, only ≈ 0.03% of the theoretical solubility in pure water under ambient conditions. Therefore, considering potential leakage of the electrochemical cell or other oxygen entry pathways, a hypothetical role of O_2 in the parasitic oxidation of MnHCM electrodes cannot be excluded. Such a detrimental impact of oxygen in the electrolyte has also been reported in previous studies on, *e.g.*, Li/$NaTi_2(PO_4)_3$, another material considered as anode for aqueous intercalation-type batteries.[170,387,389,390]

Naturally, the electrode operation at potentials below 0 V *vs*. RHE thermodynamically also allows the parasitic oxidation of the material by H_2O decomposition (H_2 evolution) at its surface.[387]

$$2Na_3Mn^{II}[Mn^{I}(CN)_6] + 2H_2O \rightarrow 2Na_2Mn^{II}[Mn^{II}(CN)_6] + 2Na^+ + 2OH^- + H_2$$

This process can theoretically proceed until the electrode potential reaches 0 V *vs*. RHE, corresponding to complete oxidation for the specific case of MnHCM in 8 M $NaClO_4$ (see **Figure 59B**). A pH-induced shift of the thermodynamic onset of water decomposition (see **Equation 10**) *via* electrolyte basification could strongly decrease the driving force for this parasitic oxidation pathway. In fact, it was even reported that an evolving local pH increase due to the continuous formation of OH^- (see equations above) could have a self-limiting effect on the hydrogen evolution and thereby reduce the vulnerability of the active material to parasitic oxidation.[151,391] It must however be ensured that the stability of the material is not negatively affected by such a pH-related approach. Unfortunately, PBAs are rather susceptible to alkaline solutions (see **Section 6.3.2.1**).

Both processes discussed above, namely parasitic oxidation of MnHCM by dissolved trace amounts of oxygen, as well as water decomposition at the active material surface can serve as a possible explanation for the self-discharge of the material. Apart from these, a possible pathway involving the parasitic reduction of ClO_4^- might be worth investigating.[392] Such an approach, however, appears challenging as highly concentrated $NaClO_4$ appears to be one of the only effective ways to prevent the degradation of MnHCM in purely aqueous solutions.[200,233,384,385]

Nevertheless, apart from self-discharge under resting/open-circuit conditions, such processes also proceed in parallel to the battery operation during intentional discharging (oxidation). This causes the retained usable capacity to be smaller than the intrinsic capacity of the material ($Q_{intrinsic}$) as shown in **Figure 59C**. However, it is also visible that the charging (reduction)

direction is affected as well by parasitic processes causing much higher charge consumption compared to $Q_{intrinsic}$. Similar to the processes discussed above, this might be caused by irreversible side reactions due to "bypassing" electrons intended for the reduction of the active material to the electrochemical ORR and HER at the electrode surface:

$$O_2 + 2H_2O + 4e^- \rightarrow 4OH^- \qquad \text{and} \qquad 2H_2O + 2e^- \rightarrow H_2 + 2OH^-$$

Therefore, these potentially occurring processes might be virtually identical to the self-discharge phenomenon, with the only difference being that, in this case, the potentiostat serves as the source of electrons instead of the intercalated MnHCM anode.

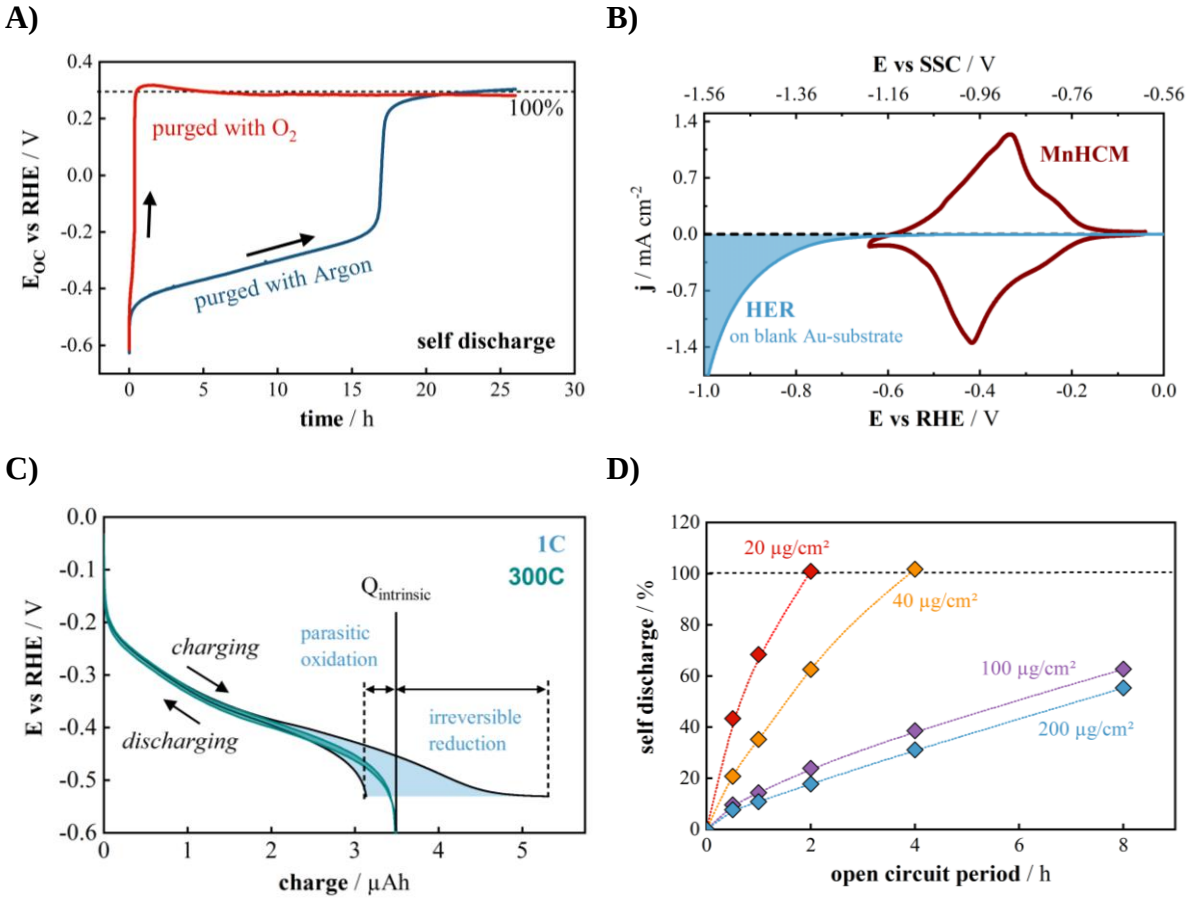

***Figure 59**. (**A**) Evolution of the open-circuit potential of a MnHCM thin-film electrode under the impact of oxygen in the electrolyte compared to inert argon gas. (**B**) CV of MnHCM in relation to the hydrogen evolution reaction on blank Au-substrate. (**C**) Impact of the (dis)charging rate of MnHCM on the parasitic oxidation and irreversible reduction processes. (**D**) Influence of the MnHCM mass-loading on the relative impact of the side reactions expressed by the self-discharge rate. All measurements were performed in 8 M $NaClO_4$ (pH = 5.7). The dotted lines serve as a guide to the eye. The data presented in these graphs are reproduced with permission from ref. 225. Copyright © 2023, American Chemical Society.*

In summary, parasitic reduction processes of electrolyte species and contaminations can serve as a sufficient explanation for the self-discharge and low coulombic efficiency of the material. Considering these processes as a non-vanishing leakage with certain current-potential characteristics[152,153] allows to explain the strong rate dependency of the CE, which is low at low rates and close to 100% at high rates (see **Figure 58B** and **Figure 59C**). As long as the imposed charging and discharging current is way above the leakage current (high C-rate), the impact of the latter can be neglected due to sluggish kinetics and transport properties of the reactants and products of the side reactions. If the current is sufficiently small (low C-rate) and at the same order of magnitude as the leakage, the parasitic processes strongly influence the charge balance during cycling. As the underlying parasitic processes are strongly surface related, it should follow that the relative impact of the side reactions is especially strong for low-mass loading electrodes (very thin films), but should decrease for thicker films (supposing unaltered surface area), thus higher mass loadings. This is confirmed by the trend shown in **Figure 59D**. Assuming that the leakage has a constant surface-normalized current density at a given potential, its ratio to the imposed (dis)charging current becomes even smaller for thicker films. This results from the fact that a given C-rate corresponds to a given mass-normalized current, while the corresponding surface-normalized current drastically increases for thicker films. An explanatory analogy for this geometric relation would be entirely filling up a cylinder with water in a given time. If now a twice-as-high cylinder with the same diameter (corresponds to doubled volume) should be filled up within the same time, the water flow per area must also double, while the water flow per volume remains constant. In the case of a solid-state intercalation host, volume equally translates to mass *via* its density.

Apart from a higher film thickness, which is not infinitely scalable as discussed in **Section 5.3** and **Section 7.2**, a further increase of the electrolyte concentration should also mitigate the impact of side reactions due to lower oxygen solubility,[170,389] as well as impeded HER and thereby an extended stability window (see **Section 2.2.4**). Furthermore, more realistic electrode geometries (microstructured instead of planar surface as employed for the herein presented model system) should also reduce the impact due to transport limitations of the products and reactants of the side reactions, as well as local pH effects (see discussion above). Of course, also the large electrolyte volume (120 ml) compared to the planar electrode surface area (1.37 cm^2) and the order of magnitude of the employed absolute capacities (< 10 µAh, < 100 µg active material) plays an important role: While transport and replenishment of side-reaction-reactants are facilitated, the electrolyte volume also offers high uptake capability for

corresponding products, as well as electrolyte contaminants. Whereas the employed electrochemical cell was optimized for experimental purposes,[224] the resulting ratio of electrolyte volume to electrode material (≈ 1200 ml/mg) is incomparably higher than in more realistic battery geometries such as pouch- or coin-cells (< 1 ml/g)[95,393] by several orders of magnitude. Therefore, the data presented above likely reflects an overestimation of the impact of side reactions at low C-rates and low mass loadings, and better results should be obtained in, *e.g.*, a coin-cell configuration. Lastly, the impact of electrolyte contaminants, such as oxygen, can be alleviated by the fabrication of sealed cell geometries in an inert atmosphere as provided by a glovebox.

7.5 Model Full Cells: NiHCF – MnHCM and NiHCF – CoHCF

This section aims to extrapolate the findings on the fast-charging capability presented above for NiHCF thin-film electrodes in half-cell configuration to other PBA materials (see **Section 5.2**) in a full-cell setup. Therefore, two prototypical entirely PBA-thin-film-based model batteries were set up and characterized. Similar to NiHCF, CoHCF, and MnHCM electrodes were prepared *via* electrochemical deposition on Au-QCM substrates as explained in **Section 4.2.1.2**. 8 M $NaClO_4$ was used as the electrolyte to allow a degradation-free operation of the cell as discussed in **Chapter 6** and enable an extended stability window (see **Section 2.2.4**). The employed electrochemical setup for the dedicated investigation of thin-film model electrodes and full-cell assemblies reported by Marzak *et al.*[224] is described in **Section 4.1**. The individual electrode potentials were corrected by the *iR*-drop to compensate for the large ohmic resistance of the electrolyte volume between the electrodes associated with the cell geometry. Data of the full cells have been previously reported in parts by Marzak *et al.*[224] and P. Moser.[386] The discussion herein will be presented to showcase the prototypical implementation of fast-charging thin-film electrodes in the context of the findings elaborated in this chapter. P. Marzak and P. Moser are gratefully acknowledged for the close collaboration on the presented results.

Figure 60 shows the characterization of a model battery with NiHCF as the cathode and MnHCM as the anode. The corresponding reaction during operation can be expressed as:

$$Na_2Ni^{II}Fe^{II}(CN)_6 + Na_2Mn^{II}Mn^{II}(CN)_6 \underset{\text{discharging}}{\overset{\text{charging}}{\rightleftarrows}} NaNi^{II}Fe^{III}(CN)_6 + Na_3Mn^{II}Mn^{I}(CN)_6$$

As seen in **Figure 60A** and **Figure 60B**, the cell delivers a voltage of 1.47 V with a specific capacity of up to ≈ 17 mAh/g and a corresponding energy density of 25.5 Wh/kg based on the active material mass of both anode and cathode. Both the capacity and energy exhibit an extremely high rate capability with full capacity retention up to 360C, which corresponds to a (dis)charging time of only 10 seconds (**Figure 60C**). Accordingly, the fast-charging properties of the individual thin-film electrodes are maintained in the full-cell model assembly. Its hysteresis-free charge-discharge characteristics and capacity retention translate into a high energy efficiency approaching 97% even at high rates. Despite this loss-free operation at moderate and high rates, the coulombic efficiency and the energy efficiency significantly drop

when reducing the cycling speed. This is also reflected by the decreasing discharge capacity and energy. Such detrimental behavior can be attributed to the increasing role of parasitic side reactions observed for low mass-loading thin-film electrodes, as discussed in **Section 7.4**. These additionally cause an increasing imbalance of the individual electrode potential with advancing cycles, further decreasing the attainable capacity. As reasoned from the discussion in the previous section, a significantly improved performance of the battery is expected for more realistic electrode and cell geometries and properties.

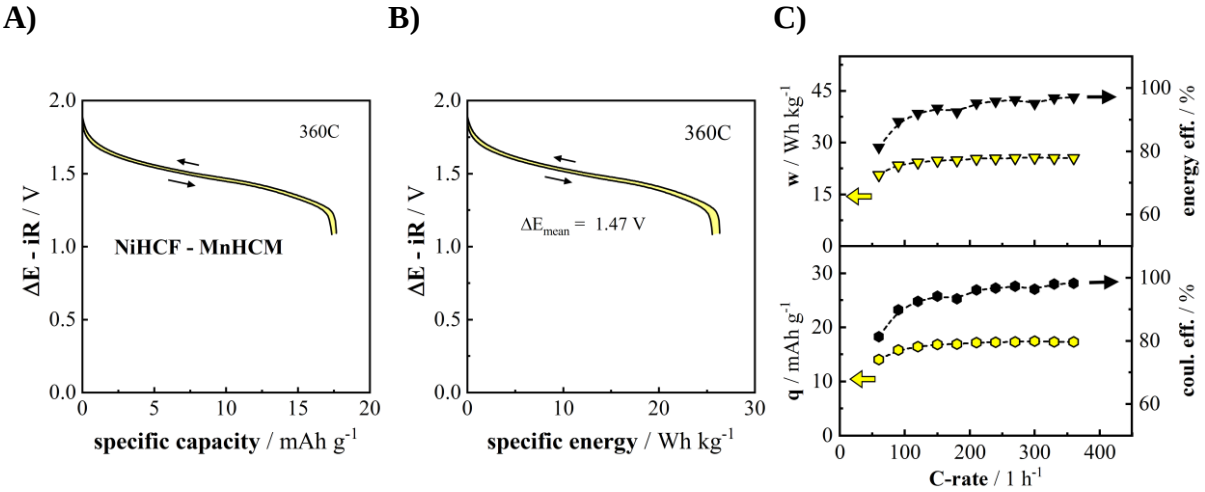

***Figure 60**. NiHCF–MnHCM model battery using thin-film electrodes and 8 M $NaClO_4$ as electrolyte. Exemplary galvanostatic charge-discharge curves at a rate of 360C showing the iR-corrected cell voltage versus (**A**) specific capacity and (**B**) specific energy. (**C**) Rate capability of the capacity and energy with the corresponding coulombic- and energy efficiencies. The dashed lines serve as a guide to the eye. The gravimetric figures are based on the total mass of active materials. The data presented in these graphs are reproduced with permission from ref. 225. Copyright © 2023, American Chemical Society.*

As another example, a full cell based on CoHCF as cathode and NiHCF as anode is shown in **Figure 61**. As previously discussed in **Section 6.3.1** and shown in **Figure 25**, CoHCF exhibits two redox transitions based on the activity of $Co^{II/III}$ (at lower potential) and $Fe^{II/III}$ (at higher potential).[275] In this case, only the latter was allowed by restricting the potential boundaries of the cathode to maintain a positive driving force for the cell. The corresponding reaction during operation can be expressed as:

$$NaCo^{III}Fe^{II}(CN)_6 + NaNi^{II}Fe^{III}(CN)_6 \underset{\text{discharging}}{\overset{\text{charging}}{\rightleftarrows}} Co^{III}Fe^{III}(CN)_6 + Na_2Ni^{II}Fe^{II}(CN)_6$$

The cell only delivers a voltage of 0.42 V due to the energetic proximity of the two individual intercalation reactions, while a maximum specific capacity based on the active materials of

26 mAh/g is obtained (see **Figure 61A**). As shown in **Figure 61B**, the resulting energy density of 10 Wh/kg is lower compared to the NiHCF–MnHCM model battery due to the significantly lower cell voltage. Nevertheless, an equally beneficial fast charging capability is observed with a loss-free and stable capacity and energy retention up to 180C (see **Figure 61C**). The coulombic efficiency is close to 99% at high rates, while it decreases towards lower rates. In turn, the energy efficiency of the cell only reaches 94% at the highest investigated rate, which is reflected in the more pronounced irreversibility of the charge-discharge curve shown in **Figure 61B**. This can be explained by irreversible chemical reactions, potentially OER, towards the higher potential vertex (fully charged state) as seen from the CV shown in **Figure 25A**. Similar to the NiHCF–MnHCM system, this effect becomes stronger towards lower rates.

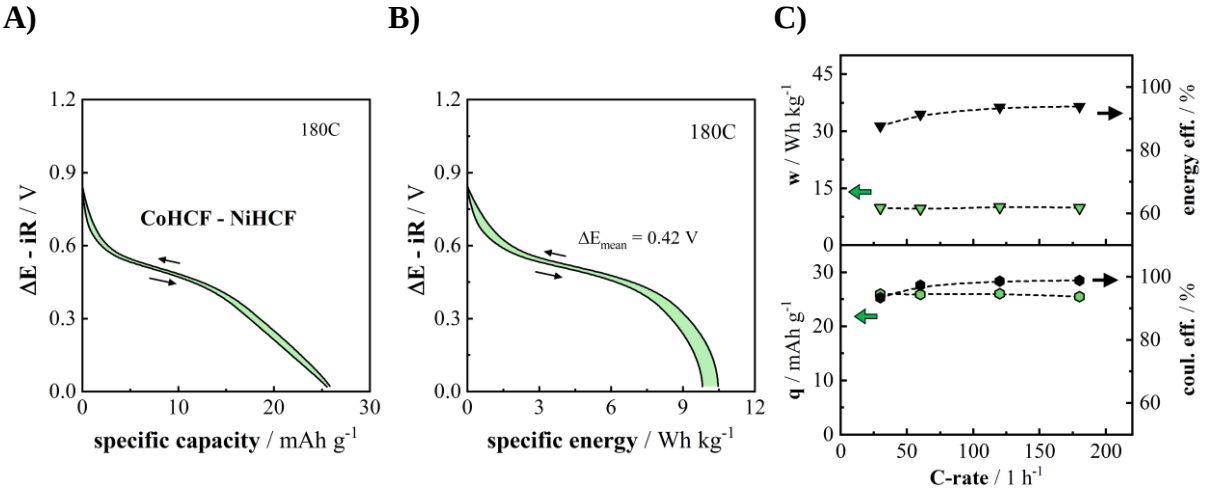

***Figure 61**. CoHCF–NiHCF model battery using thin-film electrodes and 8 M $NaClO_4$ as electrolyte. Exemplary galvanostatic charge-discharge curves at a rate of 180C showing the iR-corrected cell voltage versus (**A**) specific capacity and (**B**) specific energy. (**C**) Rate capability of the capacity and energy with the corresponding coulombic- and energy efficiencies. The dashed lines serve as a guide to the eye. The gravimetric figures are based on the total mass of active materials. The data presented in these graphs are reproduced with permission from ref. 225. Copyright © 2023, American Chemical Society.*

In previous research, full-cell ASIBs entirely based on PBAs as active materials in composite electrode configurations were shown to deliver energy densities of ≈ 27 Wh/kg at 1C (cathode: CuHCF, anode: MnHCM, ≈ 74% energy retention at 50C)[233] and ≈ 27 Wh/kg likely[iv] at 1C (cathode: CuHCF, anode: FeHCF, ≈ 78% capacity retention at 10C).[394] Whereas the intrinsic energy density is similar to the results presented herein, the high rate capability and corresponding power density of 1 – 10 kW/kg achieved by the thin-film electrodes, as presented

[iv] Unfortunately, the cited article is ambiguous at this incident.

herein, is unrivalled. The Ragone plot shown in **Figure 62** allows to classify the performance of the model batteries presented herein in relation to the usual properties of electrochemical energy storage systems on a gravimetric scale.[108,109,361,395] Accordingly, their properties qualify binder-free and therefore pure-active-material thin-film PBA electrodes for application as hybrid battery-supercapacitor devices combining the desirable advantages from both classes: a decent energy density with a stable operating voltage over the entire SOD on one side, and an extremely high power density and ultimate rate capability on the other side allowing almost loss-free (dis)charging within seconds. However, this superior performance of the model cells comes for the price of a significantly lower, commercially not viable footprint mass loading. A critical discussion of this drawback and pathways to resolve it will be further elaborated in **Section 7.6**.

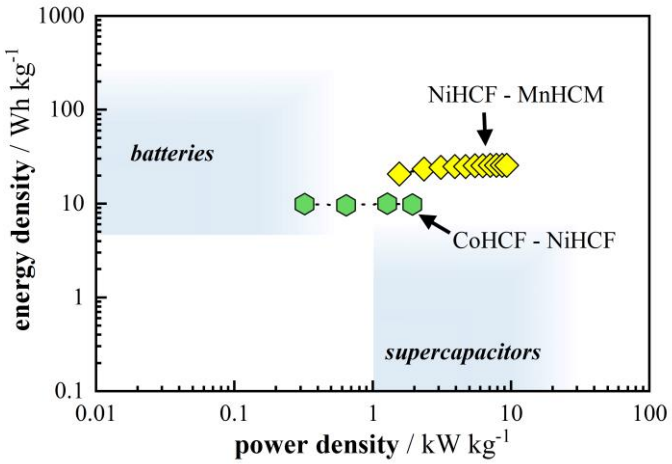

***Figure 62**. Schematic Ragone-plot showing the performance of the herein presented PBA thin-film model batteries in comparison to the usual properties of batteries and supercapacitors. Refs. 108 and 137 were used as data sources for the schematic battery and supercapacitor regions. The data presented in this graph is reproduced with permission from ref. 225. Copyright © 2023, American Chemical Society.*

7.6 Outlook on the Potential Realization for Practical Applications

The thin-film electrode configurations discussed in the previous sections should be regarded as model systems to investigate and showcase their beneficial kinetics and mass transport properties. Yet, the achievable areal mass loadings (< 100 µg/cm^2) obtained from the electrodeposition technique are too low and therefore not competitive for practical batteries. For these, usual loadings in the order of 10 mg/cm^2 (even up to 50 mg/cm^2) are easily realized using the slurry-casting method.[180,396,397,398] However, it should be remembered that the electrodeposited electrodes were prepared using planar gold substrates. Apart from the fact that gold is, of course, not a reasonable choice for a real-world current collector, using a macroscopic planar metal foil (as in the case of composite electrodes) to hold a sub-micron thick active material layer naturally leads to a low active-material to current-collector ratio. Much more suitable templates for the binder-free decoration with functional materials on the sub-micron-scale would be lightweight, low-cost, and conductive substrates with an intrinsically microporous or microstructured shape. Naturally, such templates provide a real surface area largely exceeding its geometric footprint. A conformal coating *via* electrodeposition following the three-dimensional large-area surface contour should therefore significantly enhance the achievable mass loadings for thin-film battery electrodes while maintaining the beneficial high-power capability.[108,177,356,360,370,399,400,401,402]

To specify the requirements on the surface and weight relations of a potential substrate one can use the following parameters and considerations. An important aspect is the real surface-area (SA) to geometric-footprint-area (GFA) ratio (SFR = SA/GFA). The gain-factor SFR reflects how much surface area is really provided by a sample with a given geometric footprint, while its specific surface area (SSA) quantifies the real surface area per substrate mass. Setting a rate of 60C, which corresponds to a (dis)charging time of one minute, as the goal for loss-free performance of the PBA material, the thickness of the thin film should not exceed ≈ 500 nm (see **Section 7.2**). This is equal to a mass loading (ML) of ≈ 75 µg/cm^2 on the real surface area (assuming a homogenous coating, see **Figure 28D**). Accordingly, an SFR > 130 would be needed to achieve a footprint-mass-loading $ML_{\square}$ ($ML_{\square} = ML \cdot SFR$) of 10 mg/cm^2 on the GFA. Accepting a substrate weight of 50% of the active material per geometric footprint, which is equal to 5 mg/cm^2, the template must at least have an SSA of $\frac{SRF}{50\% \cdot ML_{\square}} \approx 2.6$ m^2/g. Whereas this

order of magnitude is easily reached for powders and nanoparticles, an appropriate substrate for the electrodeposition must have a cohesive 2D structure and needs to be sufficiently robust to hold a sub-micron-sized thin film.

Potential templates involve, for example, metal/metal-oxide meshes, foams, nanotubes and nanowires.[177,356,401,403] Apart from other carbonaceous options, such as graphene or carbon-nano-tubes, carbon cloth (CC) has been introduced as a promising material fulfilling the above-discussed requirements. In contrast to metal-based alternatives, it is also chemically stable in aqueous environments under various conditions. Carbon cloth is a woven fabric consisting of carbon-fiber yarn (diameter 5 – 10 µm), and is therefore highly conductive, flexible, mechanically stable, and low-cost while offering an increased surface area due to its microstructured scaffold. It has found application as a template for functional material decoration in various energy conversion and storage research directions, such as batteries, supercapacitors or electrocatalysis, furthermore bearing potential especially for wearable devices and electronics.[177,178,356,357,404,405]

In a few recent studies, carbon cloth has accordingly been introduced as a template for the preparation of binder-free PBA and PBA-composite electrodes for batteries, supercapacitors and de-ionization devices, or PBA-derived electrocatalysts (see **Table 8** for selected examples with corresponding references). The employed PBA-on-CC synthesis schemes can, in principle, be grouped into three categories: the (chemical) conversion of pre-deposited transition metal coatings in a solution containing hexacyanoferrate ions, precipitation on CC by immersion in respective precursor solutions, or direct electrodeposition. While a few of these studies reported mass loadings > 10 mg/cm^2 obtained from the conversion method, the loading was often in the order of 1 mg/cm^2 or not reported at all. Furthermore, some of the presented papers on PBA-on-CC for battery and supercapacitor applications reported very promising rate capability results. The morphology of the PBA-functionalization varied strongly from conformal or thick non-conformal coatings to attached nano-cubes/sheets/needles.

Table 8. Selected examples of PBAs, PBA-composite and PBA-derivative functional electrodes directly fabricated on CC or carbon paper.

functional material	PBA synthesis method	reported loading	application	ref.
FeHCF-MnO_2	electrodeposition	1-2 mg/cm^2	supercapacitor	406
CoHCF on polyaniline	precipitation	1.42 mg/cm^2	battery	407
ZnHCF	conversion	15 mg/cm^2 (estimated)	battery	408
FeHCF	precipitation	not found	battery	409
CoHCF	conversion	not found	battery	410
CoHCF	precipitation	1.2 mg/cm^2	supercapacitor	411
NiHCF	conversion	26.4 mg/cm^2	supercapacitor	412
CuHCF	conversion	9.4 mg/cm^2	supercapacitor	413
MnHCF	precipitation	3 mg/cm^2	deionization	414
FeHCF-derived $FeNi(OH)_x$	electrodeposition	Not found	OER electrocatalyst	415

This section aims at exploring the usage of carbon cloth to extrapolate the fast-charging properties discussed for low-mass-loading model electrodes to more application-relevant battery mass-loadings and electrode geometries. It is based on the (not published/preliminary) findings that resulted from the close collaboration with N. Thomsen and R. List, whose Master's and Bachelor's theses were advised as part of this project,[416,417] as well as the activity of T. Steeger as a working student. Z. Hussain is gratefully acknowledged for his scientific advice and experimental help in pretreating CC substrates. The brief following treatise should serve as a conceptual introduction to illustrate a potential direction for future research and highlight some open challenges on the example of some initial experiments.

A)

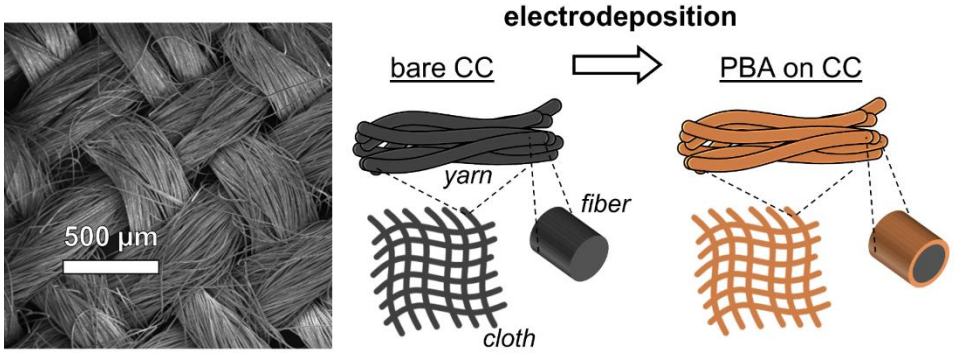

B)

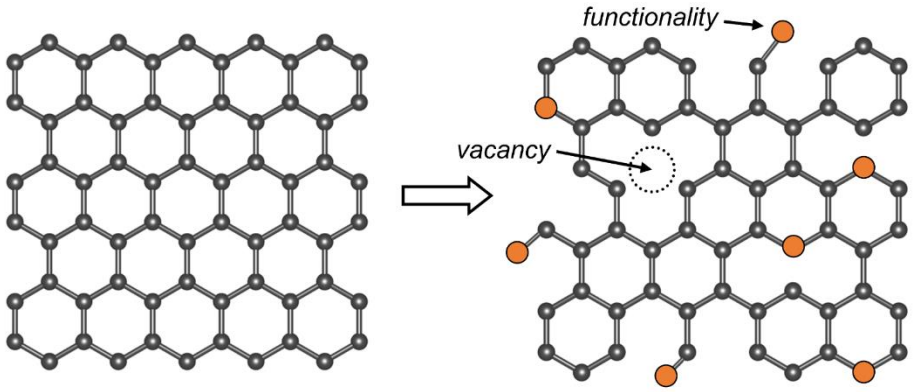

***Figure 63**. (**A**) SEM image of bare carbon cloth and schematic illustration of its microscopic structure. The cloth is woven from yarns, which consist of several hundred carbon fibers. By electrodepositing a thin PBA film on the conductive fibers, a homogenous functional coating of the cloth should be achieved. (**B**) Schematic illustration of the chemical structure of a bare and defective carbon surface obtained by pretreatment methods, as explained in the text.*

The decoration of carbon cloth with a conformal coating of the fibers with PBA thin films *via* electrodeposition is schematically depicted in **Figure 63A**. From an experimental point of view, such an approach is initially hindered by the strong hydrophobicity of bare carbon surfaces.[418] However, a high wettability of the fibers with the electrolyte is particularly important for successful electrodeposition and operation of the functional coating. A variety of pretreatment methods to increase the hydrophilicity of carbon cloth have been proposed in the literature, including wet chemical- and electrochemical oxidation, calcination in the presence of oxygen, as well as plasma- and ozone activation.[404,419,420,421,422,423] In a simplified approximation, a carbonaceous surface can be represented by a graphene-like scaffold as shown in **Figure 63B**. Whereas the non-polar chemical structure of bare carbon has a low affinity for H_2O, the local introduction of surface defects and polar functionalities can

significantly increase the wettability by providing anchoring points for water molecules *via* H-bonding and other short-range interactions. Oxygen functional groups are especially beneficial for improved hydrophilicity and can include C−OH (hydroxyl), C=O (carbonyl), O=C−OH (carboxyl), or O=C−O (ester).[418,420] Several pretreatment methods and their impact on the deposition of PBAs have been investigated in detail by R. List in his Bachelor's research project,[417] but will not be further discussed herein.

To first illustrate the principle and practicability of metallic coatings on hydrophilic carbon cloth, pure nickel was electrochemically deposited from an aqueous solution consisting of 0.25 M $NiSO_4$, 0.1 M H_2SO_4 and 0.25 M Na_2SO_4 under potentiostatic control at -0.6 V *vs.* SSC (-0.11 V *vs.* Ni/Ni^{2+}). This way, metallic nickel loadings in the order of 10 mg/cm^2 could be easily accomplished within a few hours. As seen in **Figure 64**, the carbon fibers are homogeneously decorated with a metallic coating. It consists of sub-micron-sized nickel nuclei, which have conglomerated to form a film-like structure covering the fibers.

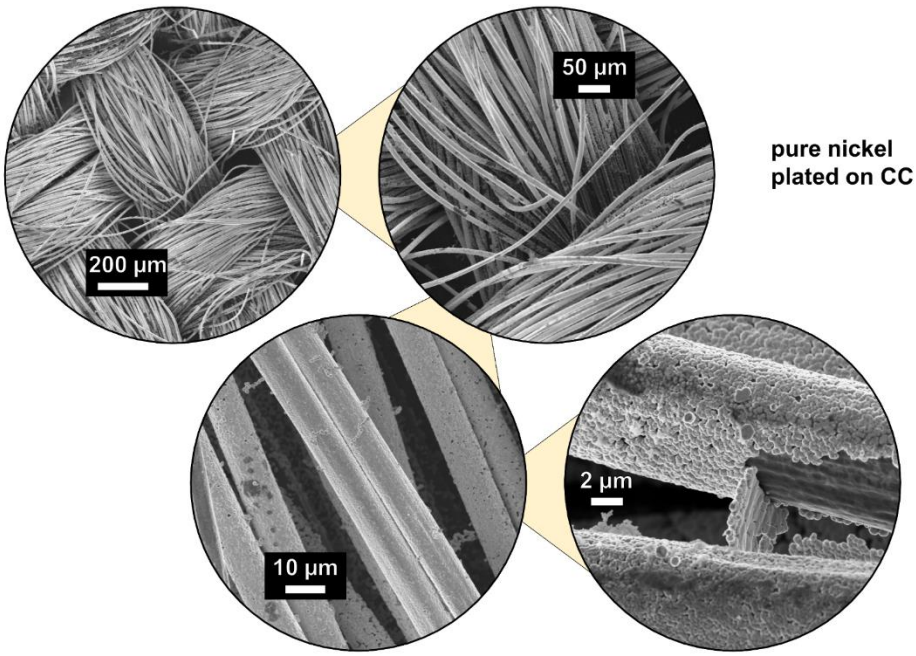

***Figure 64**. SEM images at increasing magnifications of metallic nickel electrodeposited on carbon cloth. Overall, a homogenous coating of the individual fibers with a film-like structure is visible.*

In contrast, the direct electrodeposition of PBA functional electrodes turned out to be much more challenging. **Figure 65** exemplarily shows the obtained coatings for NiHCF (**A**) and InHCF (**B**). Especially for NiHCF, the carbon fibers are only irregularly covered with the electrode material, and it can be seen that the coating is very unstable and readily detaches from

the template on many spots. While the coverage is slightly better overall for InHCF, the film itself appears to be very rough and brittle. It should be noted that the displayed examples should not be seen as representative, as a low degree of reproducibility was, in general, observed for the electrodeposition of PBA functional electrodes on carbon substrates (in comparison to Au-QCM).

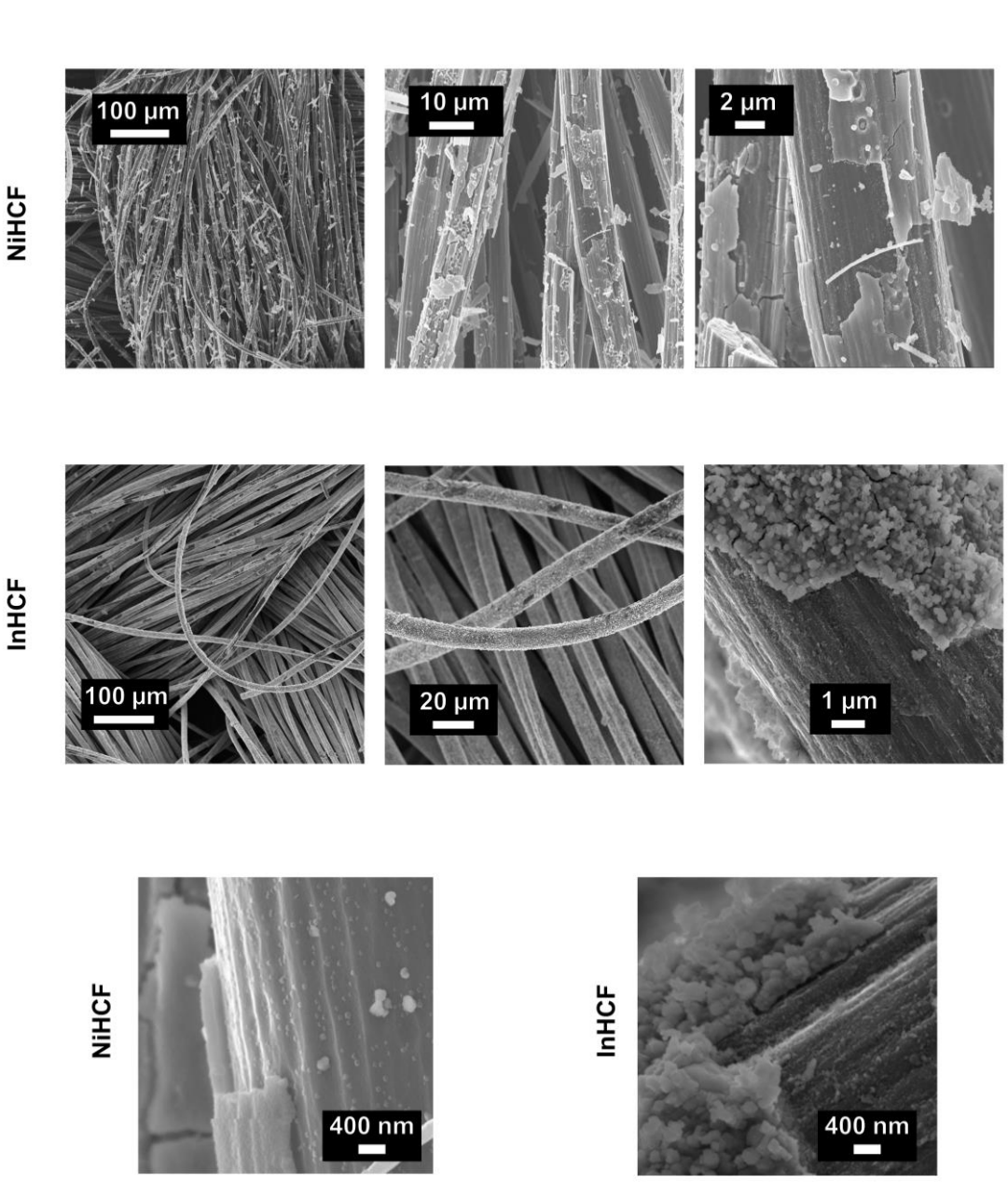

***Figure 65**. SEM images at increasing magnifications of (**A**) NiHCF and (**B**) InHCF electrodeposited on carbon cloth. Closeup-views to estimate the film thickness are provided in (**C**). The images of InHCF on CC are reprinted with permission from ref. 417.*

Unfortunately, relatively low mass loading improvements up to only ≈ 500 µg/cm² were achieved. A possible explanation will be outlined in the following: According to the manufacturer, the fibers of the employed CC have a diameter of 7.5 µm with a density of 1.76 g/cm³ and a carbon content of 99.5%.[424] The surface S_f and mass M_f of one fiber with a length of 1 cm is then calculated as

$$S_f = 7.5\ \mu\text{m} \cdot \pi \cdot 1\ \text{cm} = 0.0024\ \text{cm}^2$$

$$M_f = \left(\frac{7.5\ \mu\text{m}}{2}\right)^2 \cdot \pi \cdot 1\ \text{cm} \cdot 1.76 \frac{\text{g}}{\text{cm}^3} = 7.8 \cdot 10^{-4}\ \text{mg}$$

The specific mass of the substrate was weighed as 12.29 mg/cm². For comparison, 10 µm-thick copper foil, usually used as the current collector for graphite electrodes in LIBs, has a specific mass of ≈ 9 mg/cm². Accordingly, carbon cloth with a footprint of 1 cm² comprises of ≈ 15,800 fibers. The resulting SFR and SSA are obtained as

$$\text{SFR} = \frac{15{,}800 \cdot 0.0024\ \text{cm}^2}{1\ \text{cm}^2} \approx 38 \quad \text{and} \quad \text{SSA} = \frac{38}{12.29 \frac{\text{mg}}{\text{cm}^2}} = 0.31 \frac{\text{m}^2}{\text{g}}.$$

This approximation might overestimate the available SRF and SSA, as it neglects potential masking of individual fibers from neighboring or crossing ones. Nevertheless, both quantities are significantly smaller than the target values (SFR > 130 and SSA > 2.6 m²/g) introduced at the beginning of this section. In conclusion, the SFR and SSA of the specific CC substrate are too small to achieve reasonable loadings for PBA functional coatings, while its high specific mass further aggravates its applicability.

Apart from the detrimental properties of the employed carbon cloth, the quality of the obtained PBA coatings was inferior to the model system introduced in **Section 5.3**. Overall, the targeted thickness of the PBA films of 500 nm could not be achieved. As visible from **Figure 65C**, its value approximately ranged around 200 nm, which corresponds to an areal mass loading of ML ≈ 30 µg/cm² using the specific thickness of 6.6 nm/(cm²/µg) (see **Figure 28D**). Using the SFR calculated above, the theoretical total mass loading on the footprint area of the CC substrate would accordingly be $ML_{\square} \approx 1140$ µg/cm². This value is more than two times higher than the really obtained loading, which was determined using the accessible electrode charge and the specific capacity. As a result, either the really obtained film thickness is on average significantly smaller, a portion of the deposited film is not active (*e.g.*, because of deficient attachment to the fiber) or the coverage of the CC fibers is on average significantly smaller than 100%. Whereas a detailed root-cause analysis is beyond the scope of this high-level introductory discussion, likely an interplay of all the mentioned effects causes the low observed mass loadings.

Even though the goal of reaching commercially viable mass loadings in the range of 1 – 10 mg/cm^2 could not yet be reached, these initial results and literature overview show that the overall approach of electrodepositing PBA thin-film electrodes on high surface area templates might represent a promising direction for further research. While other, better suited carbon-based substrates might offer more beneficial SFR and SSA specifications, also the coating needs to be significantly optimized. Most importantly, an extension of the film thickness, as well as improved adhesion of the film on the substrate are crucial to increase the overall mass loading. For example, an interesting strategy has been presented by Quan *et al*. who used an interlayer of polyaniline on carbon cloth to provide anchoring points for the transition metal centers in CoHCF *via* its nitrogen functionality. In this way, the interlayer acts like "double-sided tape" allowing the fixation of PBA on CC.[407]

8 Conclusion and Outlook

This work focused on aqueous sodium ion batteries based on the material class of Prussian blue analogs as potential candidates for stationary energy storage applications. In particular, different PBA representatives considered as active materials for both cathode and anode in combination with suitable water-based electrolyte compositions were investigated as model systems with the goal of optimizing the battery performance. The focus of this work is centered around cycling stability and fast-charging capability.

In the beginning, a model system based on $Na_2NiFe(CN)_6$ thin-film electrodes immobilized on Au-QCM substrates was introduced. The preparation of the active material is based on the electrodeposition method from an aqueous precursor solution, which allows to tune the composition and thickness of the functional coating precisely. By this approach, electrodes with mass loadings of < 100 µg/cm^2 can be fabricated. The electrodeposited active material was shown to adequately resemble the usually prepared particle-based NiHCF precipitate while avoiding the carbon- and binder-additives needed to prepare electrodes therefrom. The obtained films were highly reproducible and exhibited a smooth and regular surface, which ideally qualifies such model systems as the basis for further investigation of specific material aspects. In this way, disturbing effects, as in the case of using the traditional composite-type electrodes, can be avoided. Using a modelling approach, it was shown that the intercalation of sodium can be described by common quasi-equilibrium kinetics, further emphasizing the suitability of such a simplified model electrode as the basis for the intended studies.

The first research topic presented in this thesis was the cycling stability of PBA active material. In the beginning, it was shown that the overall degradation of thin-film model electrodes proceeds *via* a twofold mechanism involving their dissolution and subsequent passivation, leaving electrode material without electrochemical activity. The treatise first focused on investigating the dissolution processes. As an alternative to traditional *post-mortem* or *ex-situ* investigation methods, an innovative *in-operando* technique was employed in this work, involving a flow cell with online ICP-MS. This technique allows to investigate dissolution processes with elemental sensitivity down to the sub ng cm^{-2} s^{-1} range and correlate them with the electrode potential and current. Whereas it had been readily adopted in electrocatalysis research in the past, the results discussed herein have been one of the first such reports on battery materials. Thereby, it could be shown on the example of NiHCF and CoHCF that the

dissolution of transition metal centers from the PBA-complex drives the decomposition of the compound under pH-neutral conditions. Specifically, the N-coordinated Ni/Co ions appeared to be the center of the attack. This process was found to be highly coupled to the redox activity of the $Fe^{II/III}$ transition, being reflected in increased leaching rates during electrode reduction. For CoHCF, an additional increased leaching rate was found at the $Co^{II/III}$ activity, which is likely associated to the ongoing phase transition of the complex in contrast to the phase-preserving oxidation and reduction of Fe-centers.

To further resolve the underlying reasons for the dissolution of constituents from PBA complexes on an atomistic level, DFT calculations were included in combination with dedicated experiments on NiHCF model electrodes. One of the most important factors influencing the degradation of active material is the electrolyte composition. In aqueous Na^+-electrolytes, the main options for modifications include the pH, the employed anion of the salt and the concentration. Regarding pH-effects, it was shown that the presence of both H_3O^+ and OH^- can be harmful to the active material: *via* co-insertion followed by protonation of N-sites within the compound in the too-acidic case or transformation of the PBA-complex to nickel hydroxide/oxyhydroxide in the too-alkaline case. As an important finding, a significant effect of the electrolyte anion on the cycling stability was found. The degradation rate of NiHCF increased with the order $ClO_4^- < NO_3^- < Cl^- < CH_3COO^- < SO_4^{2-}$ in 0.25 M Na^+ solutions. The combined computational and experimental approach strongly indicated a correlation between the degradation rate with the adsorption affinity of the respective anions on the electrified electrode surface. Lastly, the significant stabilizing effect of increasing the electrolyte concentration was showcased. This improvement is mostly achieved *via* the scarcity of free water molecules, diminishing the uptake capability of dissolved active material constituents. Even though the PBA stabilization measures of slight acidification, usage of "water-in-salt" electrolytes or N-coordinated transition metal additives were known before, the work presented in this thesis provides an understanding of these remedies on a mechanistic level based on the underlying physico-chemical processes. This work provides a "common picture" of dissolution mechanisms and conclusively allows to derive and understand the benignancy of highly concentrated $NaClO_4$, which has been adopted by the community as a "perfect" electrolyte for PBAs with respect to longevity.

Apart from active material dissolution, a second-order degradation mechanism based on the passivation of remaining electrode material during extended cycling of NiHCF model electrodes in rather dilute Na^+-electrolytes was presented in this thesis. This process is

expressed *via* a disparate reduction of the available capacity compared to the dissolved mass, which was found to go hand in hand with an increasing electrode polarization. By performing EIS during long-term cycling, this could be correlated to a significant and continuous rise in the charge transfer resistance. Apart from impaired kinetics, analysis of the electrode performance also indicated deteriorated mass transport properties. Interestingly, a significant share of available capacity could be regenerated by sequentially reducing the (dis)charging current. It was followed that the "passivation" process represents a power fade rather than a capacity loss.

Further analysis was performed to shed light on the underlying processes causing such degradation behavior. While an (electro)chemical conversion of the initially active material or the formation of passive interphases could be excluded *via* XPS and XRD measurements, a severe morphological collapse of the pristine thin-film structure was identified using SEM and AFM. It was hypothesized that the structural reassembly of the material is caused by a common dissolution and re-position mechanism, yielding irregular nanoparticle aggregates due to uncontrolled re-crystallization conditions. Nevertheless, further studies will be needed in the future to entirely resolve the underlying processes on the nano- and microscale and allow conclusions on the deteriorated electrode performance. Even though such behavior was very reproducible for the thin-film electrodes investigated herein, its effect on "traditional" electrode geometries would be an interesting topic for further research.

The second research topic presented in this work was centered on the fast-charging properties of PBA thin-films to enable high-power applications. Using NiHCF model electrodes with precisely adjustable mass loading and, thus, film thickness, the impact of the latter on the performance and the achievable (dis)charging rates was investigated in detail. It was found that the charge storage mechanism is governed by quasi-equilibrium kinetics with negligible driving force and correspondingly hysteresis-free cycling behavior. Such characteristics lay the foundation of high rate capability, theoretically allowing a loss-free increase of the (dis)charging rate. However, the electrode performance is ultimately limited by the mass transport of intercalated ions within the host structure *via* solid-state diffusion. Once the latter can no longer keep up with the imposed rate, the system behavior transits from quasi-equilibrium to diffusional control. Hereby, knowing the diffusion coefficient of Na^+ in PBAs (or at least its order of magnitude), the film thickness can be used to predict the limits for fast charging. This relation is especially useful when designing electrodes with a desired rate capability. It was found for the investigated system that a maximum thickness of ≈ 500 nm can

be allowed to retain an achievable (dis)charging time of one minute (60C), accepting only negligible losses. This performance was experimentally compared to "traditional" composite electrode configurations using NiHCF powder synthesized *via* precipitation, showing the potential superiority of thin film electrodes. Herein discussed ASIB model full cells based on two configurations of thin-film electrodes using NiHCF, CoHCF and MnHCM yielded 10 – 25 Wh/kg at up to 10 kW/kg, motivating the design of such systems as hybrid battery-supercapacitor devices.

Overall, the results and discussion presented in this thesis yielded valuable insights and provided approaches toward optimized ASIBs based on PBA materials for real-world application. Nevertheless, certain open questions and specific problems remain to be solved in the future: It should be remembered that most of the results herein are based on NiHCF thin-film model electrodes. Even though general trends regarding the degradation mechanism and its drivers can likely be extrapolated to a wide range of other PBAs, caution must be taken when inferring specific properties to other material class representatives, electrolyte compositions or electrode designs. Additional experiments tied to the systematics introduced herein would certainly be beneficial to complement the picture of relevant degradation processes and determine common characteristics for the entire material class. Furthermore, the significant affinity of thin-film electrodes towards parasitic processes and the correspondingly strong impact at low rates remain to be solved for optimized performance. This is especially important for the anode material MnHCM with its redox potential being well below the theoretical HER onset. It will be necessary for the future to also search for alternative anode materials due to the significant challenges of MnHCM regarding stability and self-discharge. Organic active materials stand out as promising options for aqueous batteries. Research into this material class has been commenced by R. Streng, whose Master's thesis[425] has been advised with the goal of exploring new active materials. Even though the promising fast-charging properties of PBA thin-film model electrodes stand out on mass-normalized metrics, it remains indispensable to raise the overall footprint mass loading by two orders of magnitude to enable a commercial uptake. A possible pathway using microstructured templates with a large intrinsic surface area for the electrodeposition was briefly outlined in this thesis based on existing literature and initial results. The underlying rationale is still to coat a conductive substrate with a thin film, but with its real surface largely exceeding its geometric footprint. However, it needs to be shown in the future whether such scaling efforts will be successful and, if so, whether the fast-charging capabilities can be maintained.

Appendix

List of Abbreviations

AIMD	Ab initio molecular dynamics
AFM	Atomic force microscopy
ASIB	Aqueous sodium-ion battery
CC	Carbon cloth
CE	Coulombic efficiency
CoHCF	Cobalt hexacyanoferrate
CPE	Constant phase element
CV	Cyclic voltammetry
DFT	Density functional theory
EDL	Electrical double layer
EEC	Electrical equivalent circuit
EIS	Electrochemical impedance spectroscopy
EQCM	Electrochemical quartz crystal microbalance
FCC	Face-centered cubic
GC	Galvanostatic cycling
HCF	Hexacyanoferrate
HER	Hydrogen evolution reaction
InHCF	Indium hexacyanoferrate
KK	Kramers-Kronig
LIB	Lithium-ion battery
LFP	Lithium-iron phosphate
MnHCM	Manganese hexacyanomanganate
NCA	Lithium-nickel-cobalt-aluminum oxide
NiHCF	Nickel hexacyanoferrate
NMC	Lithium-nickel-manganese-cobalt oxide
NMP	N-methyl-2-pyrrolidone
OER	Oxygen evolution reaction
OHP	Outer Helmholtz plane
PBA	Prussian blue analog

PVDF	Polyvinylidene difluoride
RE	Reference electrode
RHE	Reversible hydrogen electrode
SEM	Scanning electron microscopy
SHE	Standard hydrogen electrode
SOC	State of charge
SOD	State of discharge
SSC	Silver-silver chloride
TM	Transition metal
XPS	X-ray photoelectron spectroscopy
XRD	X-ray diffraction
WE	Working electrode

Related Publications

Review on physical impedance models in modern battery research.

Physical Chemistry Chemical Physics **2021**, *23*(23), 12926-12944.

PCCP

ROYAL SOCIETY OF CHEMISTRY

PERSPECTIVE

View Article Online
View Journal | View Issue

Check for updates

Cite this: *Phys. Chem. Chem. Phys.*, 2021, **23**, 12926

Review on physical impedance models in modern battery research

Rohit Ranganathan Gaddam, *† Leon Katzenmeier,† Xaver Lamprecht† and Aliaksandr S. Bandarenka *

Electrochemical impedance spectroscopy (EIS) is a versatile tool to understand complex processes in batteries. This technique can investigate the effects of battery components like the electrode and electrolyte, electrochemical reactions, interfaces, and interphases forming in the electrochemical systems. The interpretation of the EIS data is typically made using models expressed in terms of the so-called electrical equivalent circuits (EECs) to fit the impedance spectra. Therefore, the EECs must unambiguously represent the electrochemistry of the system. EEC models with a physical significance are more relevant than the empirical ones with their inherent imperfect description of the ongoing processes. This review aims to present the readers with the importance of physical EEC modeling within the context of battery research. A general introduction to EIS and EEC models along with a brief description of the mathematical formalism is provided, followed by showcasing the importance of physical EEC models for EIS on selected examples from the research on traditional, aqueous, and newer all-solid-state battery systems.

Received 12th February 2021,
Accepted 4th May 2021

DOI: 10.1039/d1cp00673h

rsc.li/pccp

1. Introduction

Rechargeable batteries play a significant role in mitigating climate change and realizing a decarbonized global economy.[1] Their pollution-free operation and lower dependence on fossil fuel resources make them a promising alternative for "clean electricity".[2] The chemistry and architecture of batteries play an essential role in determining their performance indicators. In particular, lithium-ion batteries (LIBs) have captured the market for battery electric vehicles, plug-in hybrid electric vehicles, and portable electronics given their high energy-to-weight ratio and low self-discharge.[3–5] "Traditional" LIBs are based on the mechanism of intercalating a Li-ion into host structures and

Physik-Department ECS, Technische Universität München, James-Franck-Str. 1, D-85748, Garching, Germany. E-mail: rohit.gaddam@tum.de, bandarenka@ph.tum.de
† The authors have contributed equally.

Rohit Ranganathan Gaddam

Rohit Gaddam is presently a Humboldt Research Fellow in the Energy Conversion and Storage group at the Technical University of Munich. He was awarded IPRS and UQ Centennial Scholarships for his PhD study on alkali-ion batteries at the University of Queensland, which he completed in 2019. He carried out his research works at Washington University in St Louis, USA, as a visiting scholar and at the Indian Institute of Chemical Technology as a researcher, where he also completed his dissertation as a part of his master's degree. Rohit's research focuses on material synthesis and characterization for electrochemical energy storage applications.

Leon Katzenmeier

Leon Katzenmeier is a PhD candidate in the Department of Physics at TUM and the TUM int. Energy Research GmbH. He has been a researcher in the group of Physics of Energy Conversion and Storage in TUM since 2018. His current research is concerned with the physical processes at the lithium-metal/solid electrolyte interface.

operating *via* ion shuttling between the anode and cathode with an interposed separator soaked with the electrolyte. It is worth noting that the pioneering work in rechargeable LIBs received the Nobel Prize in the year 2019, reinstating the importance of battery research.[6] Nevertheless, researchers and industries worldwide persistently work towards improving energy storage capability and reducing the cost associated with batteries.

Improvement in the performance of battery systems is based on understanding the underlying operation mechanism and ongoing processes.[7] Crucial cell components like the anode and cathode interact with the electrolyte and form the so-called electrode–electrolyte interphase that is detrimental towards storage capabilities. Furthermore, the internal resistance increasing over time could be problematic in batteries.[8] As several incidents over the last few years have exemplified, safety is a serious concern for traditional LIBs. The degradation of the electrolyte can lead to the formation of volatile organic compounds within the cells, posing a severe fire risk when a short circuit occurs.[9] Motivated by these concerns, batteries based on aqueous and solid-state electrolytes (SSEs) have been developed. The use of such alternative electrolytes has the potential to make batteries cheaper and more environmentally benign.[10] In particular, aqueous electrolytes provide better ionic conductivity and act as a better heat sink than aromatic and aliphatic carbonates used in organic electrolytes. Hence fluctuation-free battery performance and cost reduction could be expected. Solid-state electrolytes mitigate safety issues and could be promising for high energy density batteries by enabling lithium-metal anodes.[11]

Nevertheless, performance optimization and implementation of these alternative technologies are hindered by a lack of fundamental understanding of the inherent physical electrochemistry of the devices. In general, this involves the electrochemical redox processes, phase changes that occur during operation, side reactions, interphases formed on the electrodes, degradation mechanisms, transport properties, and battery stability at varying temperatures.[12] *Ex situ* and/or *in operando* techniques involving X-ray, neutron, electron, and optical methods have been frequently used in studying these influencing factors and processes. However, a non-invasive, cost-effective approach to study the battery operation still remains elusive. Furthermore, finding a common characterization technique for different length scales ranging from the atomic to system level is difficult. An atomic scale involves understanding diffusion and charge transport within the electrode and the electrolyte.[13] At a micro-scale, mechanical degradation, electrode–electrolyte interphase formation, and dendrite growth are the phenomena of interest.[14] An individual battery cell needs to be evaluated for ageing, internal resistance, temperature, and current variations. At the system and pack levels, the overall performance is defined by safety, efficiency, environmental changes, and charging methods. Understanding the battery behavior at all these levels using a non-destructive approach has been made feasible by electrochemical impedance spectroscopy (EIS).

In the past fifty years, EIS has evolved as a very powerful method to study and characterize the electrochemistry of battery systems and materials with complex processes and has gained much attention in the field of battery research (Fig. 1). It is not only capable of observing different phenomena on different length and time scales simultaneously, but also capable of differentiating and identifying the related mechanisms. In most cases, an electrical equivalent circuit is employed to fit the response of a system with unknown properties ("black box") to an external probing signal in order to both qualitatively and quantitatively characterize the interfacial processes (Fig. 2).[16]

The basic experimental principle of EIS relies on the perturbation of an equilibrated electrochemical system by an electrical probing signal and the analysis of its linear response. Two kinds of EIS approaches can be differentiated: potential or current perturbation, leading to potentiodynamic EIS (PEIS) or galvanodynamic EIS (GEIS). The system's tendency to oppose a potential perturbation is measured by its alternating-current (ac)

Xaver Lamprecht

Xaver Lamprecht received his MSc in Applied and Engineering Physics in 2019 from the Technical University Munich and is since then a PhD candidate in the group of Energy Conversion and Storage at TUM. His research efforts involve thin-film electrodes for aqueous sodium-ion batteries, with focus on the corresponding degradation mechanism and fast-charging capabilities.

Aliaksandr S. Bandarenka

Aliaksandr S. Bandarenka received his PhD from Belarusian State University in 2005. After a postdoc at the University of Twente, Netherlands and Technical University of Denmark, he joined the Center for Electrochemical Sciences (CES) at Ruhr University Bochum (Germany) as a group leader (2010–2014). Currently, he is an Associate Professor at the Department of Physics, Technical University of Munich, Germany. His research interests focus on the development of electrocatalysts, battery systems, methodologies for characterization and modification of electrified solid/liquid interfaces, and interfacial charge transfer.

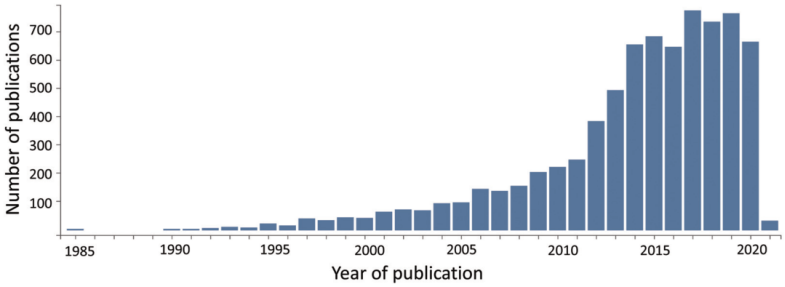

Fig. 1 Yearly publication count metrics obtained from the *Web of Science* with the search term 'Electrochemical Impedance Spectroscopy and Battery'.[15]

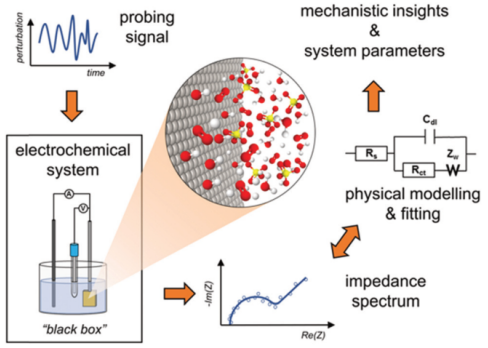

Fig. 2 EIS as an experimental approach to solving the inverse problem. An external signal is applied to perturbate an equilibrated electrochemical system and impedance data can be extracted from its response. The underlying interfacial charge and mass transfer processes are modeled employing an EEC, which, after thorough and iterative fitting to the obtained data, allows for a deep understanding of the investigated system.

impedance, which is a function of the signal's frequency and converges to the ohmic resistance in the stationary direct-current (dc) case. D.D. Macdonald summarizes the following advantages of the technique: (1) its linearity, allowing the treatment of the system in terms of Linear Systems Theory; (2) an infinite frequency impedance spectrum would deliver the same information on the system as acquired from linear electrical perturbation/response techniques; (3) EIS easily generates a high amount of information compared to the acquired data; and (4) the data validity can be determined by mathematical techniques (discussed in the section below) irrespective of the involved processes in the experiment.[17]

As different kinetic steps within a battery have different time scales, EIS allows differentiating the associated electrochemical processes. The transport processes of electrons through wires, the current collector, and from there towards and through the electrochemically active material, as well as that of ions within the bulk electrolyte and – for most cases – throughout the porous electrode structure can be separated from physicochemical changes in the system.[18] The (re)arrangement of the double layer, the charge transfer across the electronic–ionic conduction boundary, and possibly the solid-state diffusion of ions within the crystalline host structure are processes that can be observed with careful EIS analysis. In many cases, the change of the crystalline structure of individual components constitutes a further, rather slow, process involved during the battery operation.[19] Being capable of acquiring impedance spectra from MHz to mHz frequencies within a relatively short time and thereby creating extensive and meaningful datasets, modern potentiostats allow measuring all the above-mentioned time scales in a single measurement. In general, a qualitative assessment of the investigated system is possible by evaluating the acquired impedance spectrum, the Nyquist plot in most cases, for characteristic features, representing the respective limiting processes for different frequencies, thus time scale regions. However, an appropriate interpretation requires *a priori* knowledge. A physico-chemical model is employed for fitting the impedance spectra, allowing the extraction of quantitative information on the material and interface properties. Such a model is called an electrical equivalent circuit (EEC), representing the occurring processes within the investigated system as a combination of elements known from electrical network theory, such as resistors and capacitors. Commonly, software for building and fitting the EEC to the EIS data is employed.[20]

As an example, a commonly accepted model reflecting the parametrization of the contributions from the double layer, faradaic reactions, and the electrolyte pathway is shown in Fig. 2. This generic configuration involves a capacitor to represent the double layer and a parallel pathway for faradaic reactions, which is represented by a resistor to account for the charge transfer and a Warburg impedance for the diffusion of charge carriers. A series resistor represents the conductivity of the electrolyte and further electronic resistivities of the setup. This simple EEC is also known as Randles circuit, which is in most cases insufficient to account for the measured impedance of more complex systems, however. In general, finding a model compliantly fitting the measured spectra in a mathematical sense is not a big issue at first glance. This is especially true

when (several) non-ideal elements, introducing additional degrees of freedom, are being incorporated. Furthermore, models can degenerate, delivering the same output for different arrangements of their elements, and finally, their physical interpretability is lost.[21] Hence, one must always bear in mind that such a model can be nothing but a representation of the relevant equations describing the electrochemical system and must always be questioned regarding its exactness. However, if appropriately analyzed, EIS establishes the direct link between mathematical equations and the real world. The informative power of this technique can be further increased by combining it with simultaneous (non-) electrochemical techniques to complement each other, such as quartz-crystal microbalance (QCM) or cyclic voltammetry (CV).[16]

The present review highlights the importance of modeling impedance spectra with equivalent circuits having a physical significance to understand the electrochemistry of batteries. Starting with general intercalation-type battery systems, the underlying guest-ion insertion and extraction mechanism is discussed based on a model employing intermediate anion adsorption. Furthermore, several prominent examples of detrimental processes in traditional organic-electrolyte systems studied by EIS are showcased, such as the formation of the solid electrolyte interphase, solid-state diffusion of intercalated guest-ions, as well as structural phase changes of the host electrode due to ion insertion. The physico-electrochemistry of more recently developed systems based on a solid-state electrolyte is analyzed for a deeper, profound understanding of the inherent charge transport mechanisms.

2. Understanding EIS & general models

The measurement principle of EIS is as easy as applying sinusoidal potentials or currents of different frequencies to an electrochemical system and measuring the associated current or potential response. This can either be done in a two-electrode setup, where the reference and counter electrodes of the investigated cell are in electrical contact or a three-electrode configuration, allowing the separation of impedances from the counter and working electrodes, respectively. A two-electrode system is useful to analyze properties where differentiation of the separate electrode processes is not needed, such as symmetric half cells. However, a three-electrode configuration is more suitable for batteries as it allows precise separation of the interface properties associated with either the cathode or anode. The mathematical basis of EIS, the models for electrochemical systems, and measures for validating the EIS data are discussed in the forthcoming section.

2.1. Mathematical formalism for impedance data

An equivalent circuit of physical significance is essential to understand an electrochemical system *via* impedance spectra. However, the foundation of such understanding is built upon mathematical formulism. The reader is referred to the book of Lasia[22] for further details and an in-depth review of the literature. As introduced above, EIS is based on the frequency-dependent potential or current response of any electrochemical system. A potential-controlled excitation (PEIS) can be represented in the form:

$$E(t) = E_0 \sin(\omega t) \quad (1)$$

The corresponding current response will then take the form:

$$I(t) = I_0 \sin(\omega t + \phi) \quad (2)$$

where I_0 and ϕ represent the current amplitude and the phase shift. However, this response requires a set of conditions to be held: linearity and stationarity, as sketched in Fig. 3. A (pseudo) linear response means that the current follows the potential while (locally) adhering to Ohm's law. Linearity can be easily achieved by choosing a sufficiently small excitation amplitude (U_0 for PEIS), typically set to U_0 = 5–20 mV for battery applications. However, stationarity is a problem that must be carefully considered when measuring EIS as it cannot be obtained by simply setting experimental parameters. For a non-stationary system, the current response will have an additional term as

$$I(t) = I_0 \sin(\omega t + \phi) + I_{\text{non-stationary}}(t). \quad (3)$$

This additional term cannot be accounted for in typical impedance analysis and will make qualitative and quantitative results hard to come by. However, the Kramers–Kronig analysis (KK check) can help to reveal non-stationary measurement conditions. A constant non-stationary current can be compensated with a drift correction by dedicated software. More complicated cases can be investigated using potentiodynamic electrochemical impedance spectroscopy (PDEIS), as it can be found in an article on EIS in the presence of non-linear distortions[23] and non-stationary cases.[24]

Once linearity and stationarity are assured, the impedance data can be analyzed. As both the potential excitation and the current response are sine waves with a common frequency, the (complex) impedance can be defined as:

$$Z(\omega) = \frac{U(t)}{I(t)} = \frac{U_0 \sin(\omega t)}{I_0 \sin(\omega t + \phi)} = Z_0(\cos\phi + j\sin(\phi)) = Z_0 \exp(j\phi) \quad (4)$$

The complex impedance can be represented by its amplitude and phase ($|Z|$,ϕ) or real and imaginary parts (Re(Z),Im(Z)), and

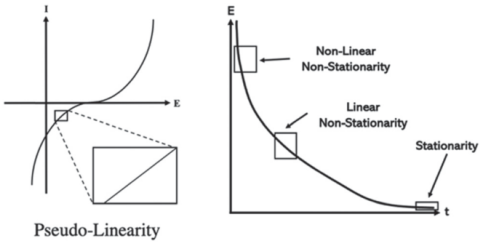

Fig. 3 Graphical depiction of the two requirements for data acquisition in PEIS: linearity and stationarity. A linear non-stationarity can be accounted for by software, whereas algorithms cannot correct a non-linear disturbance.

is defined for every frequency in the spectroscopic range. The resulting data are a three-dimensional array with the frequency as a discrete variable. Typical representations of these data include Nyquist ($-\mathrm{Im}(Z)$ *vs.* $\mathrm{Re}(Z)$) or Bode ($|Z|$ *vs.* ω) plots which are projections along with one of the three axes. However, all projections of the 3D data will hide some of the information, which becomes important when a model is fitted to the data.

2.2. General EEC modelling of electrochemical systems

The notion of an EEC to model the impedance response of electrochemical systems is used throughout a wide field of applications, such as piezoelectrics,[25] ferroelectrics,[26] and of course, LIBs.[27] EECs comprise a number of single electrical network elements connected in series or parallel, with the most obvious ones being a resistor, a capacitor, and an inductor. The impedance function of the relevant elements can be found in Table 1.

An interested reader is referred to a more generalized view describing resistance, capacitance, and inductance as only the boundary cases of a unified energy efficiency conserving quantity.[28] More advanced components, like the constant phase element (CPE), are used to model the imperfect behavior of capacitances or resistances, always describing a mathematical relation of (complex) impedance and frequency. The CPE is of special importance for the description of double-layer capacitances and is described by

$$Z = Q(j\omega)^{-\alpha} \tag{5}$$

and while for $\alpha = 0$ the element represents a resistor, for $\alpha = 1$ a perfect capacitor, and therefore, this reflects the degree of non-ideality. There are several possible explanations for the physical origin of the constant phase element: surface roughness,[29,30] several reaction rates,[31] and non-uniform current distributions.[32,33]

As a real electrochemical system contains an unknown number of impedance constituents in an unknown arrangement, it is important to build an EEC model which both represents the system's physics and fits the experimental data. The graphical representation in the form of an EEC is a visualization for combining the single element equations based on Kirchhoff's laws. For example, a simple charge transfer process at an electrified interface can be represented by a single parallel connection of R and C (RC-element), with an interface charge transfer resistance and the capacitance across this interface. This RC-element reveals itself as a semi-circle in the Nyquist plot and is one of the most easily distinguishable features of impedance spectra. However, even a simple sample such as a solid ionic conductor in between two electrodes already involves a number of effects:[34] bulk resistance (R_{bulk}), polarization contribution (C_{geom}), and two interfacial charge transfers (R_{int} and C_{int}), which are – in a symmetric setup – not distinguishable from each other. Therefore, the EEC already contains four elements that remain to be arranged. Importantly, even simple EECs can degenerate, meaning that the same fitting can be achieved by multiple configurations of the same elements leading to different parameter sets.[35] As the application of EIS ranges over a wide field of systems, there are a few standard models describing the impedance response of various physical phenomena which will be introduced in the following: an electrified interface in its simplest form, with a charge accumulation (C) and resistance (R), is described by a Voigt element.[36] Multiple RC-elements in series are called a Voigt circuit, potentially describing the impedance response of multiple interfaces in series. However, these simple models cannot describe the more intricate nature of complicated systems, such as the charge transfer behavior of, for example, porous electrodes, for which the transmission line model has been developed.[37–39]

Table 1 Impedances of different simple elements, which are commonly used in electrical equivalent circuits

Element	Resistor	Capacitor	Constant phase	Inductor	Warburg
EEC parameter	R	C	CPE	L	W
Impedance	R	$\frac{1}{j\omega C}$	$\frac{1}{Q(\omega C)^{\alpha}}$	$j\omega L$	$\frac{A_{\mathrm{w}}}{\sqrt{\omega}} + \frac{A_{\mathrm{w}}}{j\sqrt{\omega}}$

2.3. Developing a physical model

The complexity of assigning elements for an EEC increases with the difficulty of evaluating the number of time constants for a particular dataset.[40] Furthermore, the decoding of the physical features might also be quite challenging to obtain from the EIS spectra. Here, the distribution of relaxation times (DRT) could be a handy technique to transform the EIS data to a time instead of frequency space, revealing characteristic time constants.[40,41] However, DRT analysis is heavily prone to statistical deviations limiting the quantitative use.

It is also understood that there is no single model that fits all, which leaves the question of ranking the best model that can be used. One criterion for ranking the models is the Akaike information criterion, which estimates the quality of a statistical model.

It is important to note that there are two distinct ways to determine a suitable equivalent circuit for a given EIS spectrum. The straightforward approach is to use an adhoc model available and apply it to the system. However, many of these EECs are empirical and, while more or less accurate fitting of the impedance spectra can be obtained, are hard to verify using secondary techniques or simulations. In the case of batteries, one can easily think of some physical origin for impedances: resistances of electrodes, the electrolyte, and their respective interfaces, as well as capacitive effects on such interfaces. The elements of an empirical EEC can therefore be assigned a physical meaning *a posteriori*. With all elements of the equivalent circuit assigned to a physical origin and arranged in a logical order, the empirical EEC becomes a physical EEC. This physical model then provides information on the underlying electrochemistry and charge transfer mechanisms and is by its nature also verifiable by other techniques or can be tested in simulations. A prominent example of this is the confirmation of the EEC involving the double layer capacitance in electrical double layer capacitors based on other electrochemical tests.[39] From a quantitative point of view, parameters obtained from a physical

model should be in an acceptable agreement with those determined from other electrochemical techniques to ensure the model's correctness. One must keep in mind that any fitting problem is inherently prone to the error of "overfitting". Any simple semi-circle in impedance spectra can be fitted by an arbitrary amount of RC-elements, although a single RC-element would already fit the spectra well. Any additional fitting parameter, in the case of EIS an additional equivalent circuit element, giving a small improvement in fit quality must therefore be carefully considered. As with other fitting problems, an indicator of this is the errors for each fitting parameter.

3. Physical EIS modelling for selected battery systems

In order to provide an accurate picture of battery electrochemistry, it is important to understand the inherent components and their behavior.[42] Many factors, including the current collector, separator, electrode, electrolyte, *etc.*, need to be considered for interpretation. A generic EEC can be built to represent all these properties in one entire model, as seen in Fig. 4. However, for practicality, some of the insignificant components can be neglected in the interpretation. For instance, the contribution of the separator, which allows ions to pass through its pores and is designated with a RC-element, is negligible compared to other components, making it convenient to build the EEC without further consideration of this element.[43,44] Similarly, the resistances that stem from the current collector and electrolyte can be consolidated as a bulk resistance.

It is worth noting that EEC modeling for batteries is applied to the measured impedance spectrum in such a way that the obtained data and the model have a minimal difference in parameters.[45] In general, EIS is far from the ideal, which leads to imperfect features in the Nyquist plot with indistinguishable time constants for various processes.[40] Therefore, modeling EIS using an EEC needs to be performed with better scrutiny by understanding the electrochemical processes governing the battery system of interest. For an initial analysis, one could fit the EIS spectra with an EEC using a non-linear least squares fit usually done by using available software. Such a fitting leads to an empirical model with parameters that might (not) be helpful. One could also introduce additional RC-elements to lower the error margin. However, such an approach can be misleading as it might not represent the exact physical processes associated with the electrochemical reaction. Having said this, a generic model for all the systems is also very complex and clear differences can be observed with modifications in battery components (electrodes, electrolyte, separators, *etc.*). For instance, in a ceramic SSE one would need to consider a brick-layer model where the current can pass through grains and also across grain boundaries.[46] Considerations for EEC, in this case, depend on whether additional elements are required to represent the grain boundary. Furthermore, computationally simulated electrode materials have provided some insights into modeling that can be taken into consideration. However, in real-time, the behavior is much more complex. Therefore, physical impedance models that take into account the physical processes associated with the system of interest (based on experimental observations) would be a more reliable approach for building an EEC.

3.1. The mechanism behind intercalation in liquid electrolyte batteries

3.1.1 Early models for ion intercalation into host electrodes. Intercalation is a remarkable redox reaction where charged species in the electrolyte form a nonstoichiometric intercalate with the host molecule *via* reversible insertion into the host lattice.[47] A typical example would be graphite intercalation compounds with a configuration of LiC_6 formed during lithiation. Apart from charge transfer, other mechanisms occur during the intercalation process and battery operation. EIS is a powerful tool to optimize the system performance by understanding these various processes in intercalation-type battery materials, including the formation of a solid–electrolyte interphase (SEI), other physical and chemical reactions, and irreversible ion storage sites. Despite EIS being versatile in

Fig. 4 Representation of a battery with an empirical EEC considering all its components. Reproduced with permission from ref. 42. Copyright©2016, John Wiley and Sons.

explaining such interplays, it would be ambitious to fit all spectra with a single model. Many electrochemistry research groups have invested in developing a reliable physical model to understand the behavior of such a battery system, which are discussed in the following.

One of the initial models by Bruce and Saidi describes the lithium-ion intercalation in amorphous and cubic TiS_2 using an adsorbed atom model.[48] Building on this work, several researchers have developed a similar model to understand intercalation-type materials in batteries.[49,50] This model considers that solvated ions near the electrode surface undergoes partial desolvation, thus getting adsorbed, followed by the transfer of electrons from the external circuit into the solid host. The ion now diffuses through the electrode surface until it reaches a point where it completely loses its solvation layer and can intercalate into the host lattice (Fig. 5A). Kobayashi analyzed $LiMnO_2$ based intercalation electrodes using EIS.[50] The EEC is presented in Fig. 5B and was used to fit the obtained impedance spectrum consisting of two semi-circles in the high and medium frequency regions followed by a straight line. The model consists of an RC-element connected in series with the bulk electrolyte resistance, R_s (Fig. 5B). An additional R/CPE-element represents the impedance determining the mid- and low-frequency regions of the spectrum, respectively. Semi-circle 1 represents the partial removal of the solvation layer during the Li-ion interaction followed by another semi-circle in the mid-frequency region representing the adsorption and intercalation of the lithium-ion into the host material. Though such a model discusses some interesting aspects of cation intercalation, the model does not account for the SEI formation or other simultaneous reactions occurring during reversible lithiation. This topic will be discussed in section 3.2.1.

Despite the myriad of models considered for these processes, there still exists a need for explaining the EIS spectra with physics, when models considering partial solvation of ions or later models involving the SEI only partially represent the overall process. Advanced understanding of multi-stage processes considering various aspects of the electrode–electrolyte interface is indispensable for future battery optimization efforts. These processes sometimes manifest as loops in the mid-frequency range of the impedance spectra. In earlier battery research, these uncommon features have been considered measurement artifacts with no physical meaning, whereas their appearance is widely accepted in other electrochemical research fields, such as corrosion systems.[51] EIS spectra of a Li^+/graphite system studied by Iconatti's group suggested that the loop was formed due to the superimposition of an electromotive force during lithium intercalation.[52] A more convincing reason was provided in recent studies associating the observed loops in the transition region between the mid- and low-frequency regions to a multi-stage reaction accompanying the (de)intercalation process.[58,59] A detailed review of this proposed mechanism will be discussed in the following section with the example of a sodium ion intercalation material. The *a posteriori* formulated EEC is validated by both theoretical considerations and experiments and, therefore, can be considered to have physico-electrochemical meaning.

3.1.2 Three-step mechanism of Na^+ intercalation into NiHCF in aqueous systems. The material class of Prussian Blue Analogues (PBAs) has continuously gained interest over the last few years as a promising candidate for stationary aqueous sodium-ion battery systems. Similar to the LIB technology, the capability of PBAs to store and provide electrical energy relies on the process of intercalation. Despite its lower energy density, the inherent environmental benignancy, low cost, scalability, and safety might resolve some of the increasingly discussed drawbacks of the "conventional" Li-ion technology.[53] Despite its penetration into modern technology and society over the last 30 years – peaking in the 2019 Nobel Prize – the exact underlying process of storing charge by intercalating a guest ion into a host structure remains a topic of discussion in today's literature. In general, the fully reversible (de)intercalation process is described by a simple chemical equation. For example, the insertion of sodium into nickel hexacyanoferrate ($Na_2Ni[Fe(CN)_6]$ = NiHCF), a well-known PBA representative, is described by:

Fig. 5 (A) Typical representation of the adatom model. (B) EEC used to analyze the obtained impedance spectra for $LiMnO_2$. Reprinted with permission from ref. 50. Copyright©2005, American Chemical Society.

$$NaNi[Fe^{III}(CN)_6] + e^- + Na^+ \leftrightarrow Na_2Ni[Fe^{II}(CN)_6]$$

This representation implies that the electrochemical reduction of the active material is immediately followed by the intercalation of the alkali metal cation.[54–57]

However, Yun *et al.* argued that this representation might oversimplify the complex processes associated with the electrochemical insertion of guest ions into the host structure. SPEIS measurements at different potentials within the faradaic active region of the discussed reaction, shown in a CV in Fig. 6A, revealed the appearance of loop-shaped impedance spectra in the Nyquist plot (Fig. 6G and H). Quasi-stationarity of the investigated system and validity of the data were guaranteed by simultaneous QCM measurements and KK check.[58] However, these obtained spectra can only be analyzed and interpreted properly incorporating a physical model. It was reasoned that the interfacial charge and mass transfer proceeds through an (at least) three-stage interfacial mechanism, which is unfolded in the following.

First, a host metal cation from the active material will change its oxidation state, in this case of deintercalation of Na^+ from NiHCF (Fig. 6B):

$$Na_2Ni[Fe^{II}(CN)_6] - e^- \rightarrow Na_2Ni[Fe^{III}(CN)_6]^+ \text{ (step 1)}$$

Due to the high electronic conductivity of the film, this electroactive step proceeds very fast. However, as schematically illustrated in Fig. 6C, this leads to the appearance of an intermediary excess positive surface charge, which cannot immediately be balanced by releasing the guest cation due to the associated slow solid-state diffusion. Due to the faster mass transport of ions in liquids, electrolyte anions quickly approach the surface to specifically adsorb within the inner Helmholtz layer in order to temporarily compensate this charge (Fig. 6D):

$$2Na_2Ni[Fe^{III}(CN)_6]^+ + SO_4^{2-} \rightarrow (Na_2Ni[Fe^{III}(CN)_6])_2SO_4 \text{ (step 2)}$$

Finally, the adsorbed electrolyte anions and guest cations leave the surface in the last step, which involves no net interfacial charge transfer (Fig. 6E):

$$(Na_2Ni[Fe^{III}(CN)_6])_2SO_4 \rightarrow 2Na^+ + SO_4^{2-} + 2NaNi[Fe^{III}(CN)_6] \text{ (step 3)}$$

It should be mentioned that all of these three interconnected steps are quasi-reversible, and therefore, the proposed mechanism also applies to the direction of intercalation.[58,59] From a mathematical point of view, the oxidation of the host active material (1), electrolyte anion adsorption (2), and its following desorption, including the release of the guest ion (3) are represented by chemical rate equations, which are further evolved to calculate the impedance of such a system. An interested reader is referred to Lasia's book on electrochemical impedance spectroscopy, where this derivation is demonstrated in great detail.[22] The resulting EEC for the described system is shown in Fig. 6F. It includes the classical elements like the uncompensated

Fig. 6 Cyclic voltammogram of NiHCF, exposing the potential region for the (de)intercalation of Na^+ into and from the hosting crystal structure (A). Adapted from ref. 58. Published by The Royal Society of Chemistry. Schematic representation of the intercalation process by a reversible 3-step mechanism involving the oxidation/reduction of the electrode material (1), ad/desorption of electrolyte anions (2) and (de)intercalation of alkali metal cations (3) (B–E). Reproduced with permission from ref. 59. Equivalent circuit of the physico-chemical model representing the 3-step mechanism (F). Corresponding impedance spectra measured within the (de)intercalation region, showing characteristic loop shapes, which are fitted by the introduced equivalent circuit (G and H). Reproduced with permission from ref. 58. Published by The Royal Society of Chemistry. Experimental detection of three different time constants appearing during intercalation for the same material and electrolyte as measured by LICT (I). Reproduced with permission from ref. 60. Copyright©2017, American Chemical Society.

resistance R_u, and two parallel pathways for the double layer impedance Z_{dl} and the charge transfer resistance R_{ct}, which are however extended by a further impedance representing the de/adsorption processes (dashed box), including the resistances $R_{a,i}$ and capacitances $C_{a,i}$. These parameters can formally have negative values, which results from the underlying equations employed in this model. The introduced EEC is capable of fitting the obtained "loop" spectra, finally reconciling both the empirical and the physical argumentation to explain the process of intercalation. It should be noted that the commonly employed Warburg element is not present in the proposed EEC (nor indicated by a straight 45° line in the low-frequency region of the Nyquist plot), as the associated electrolyte ion diffusion process appears not to be a limiting factor for the investigated intercalation mechanism at the employed electrolyte concentration of 0.25 M Na_2SO_4. Each of the above-mentioned steps takes place with a distinct time constant, allocating the electroactive step in the high-frequency region and the subsequent steps involving ad/desorption in the mid- and low-frequency regions of the EIS spectrum. The appearance of three distinguishable time constants accompanying the intercalation process was further investigated employing the laser-induced current transient (LICT) technique. The sudden disturbance of the electrochemical double layer by the temperature jump of the electrode surface due to laser irradiation and its subsequent reorientation allows deducing the temporal and persisting excessive surface charge at the investigated electrode potential from the sign of the observed current transients. Strikingly, these current transients changed their direction two times when investigating the potential region of sodium and potassium intercalation for NiHCF in an aqueous electrolyte (Fig. 6I). This observation indicates the presence of three distinguishable time constants associated with interfacial mass and charge transport. Thereby it qualitatively supports the theory that the intercalation mechanism cannot occur on the basis of a single-step reaction. This correlation further promotes the combination of EIS with auxiliary techniques to both challenge a proposed EEC and gain additional insights.[60]

Interestingly, the LICT method predicts an overall positive excess surface charge across the entire intercalation potential region of NiHCF at quasi-steady-state, further highlighting the distinctive influence of chemisorbed anions on the interfacial processes.[60] A previous discussion on the role of electrolyte anions mainly emerged from observing deviating QCM waves, as well as differing shapes of the respective CV curves, the kinetic behavior, and the corresponding voltammetric reversibility of the associated redox reaction in the case of PBA intercalation materials.[58,61–65,68] The presented findings might contribute to a better understanding of these effects, by proposing a (de)intercalation mechanism that involves the efficient intermediary compensation of excess electrode surface charge by electrolyte constituents.

3.1.3 Generalization of the three-step mechanism towards the wide class of intercalation-type battery systems. While the three-step mechanism of interfacial mass and charge transport was introduced for a model NiHCF system in an aqueous sodium electrolyte, further EIS studies revealed its generic validity for a wide subset of intercalation-type battery systems. The characteristic loop spectra were reproduced and successfully fitted with the proposed model within the (de)intercalation potential region for several PBA materials. These studies include cobalt hexacyanoferrate ($Na_2Co[Fe(CN)_6]$ = CoHCF),[59,65,67] vanadium hexacyanoferrate ($Na_2VO_x[Fe(CN)_6]$ = VHCF),[66,67] indium hexacyanoferrate ($NaIn[Fe(CN)_6]$ = InHCF)[67] and copper hexacyanoferrate ($Na_2Cu[Fe(CN)_6]$ = CuHCF),[59] which are commonly considered as promising cathode materials for aqueous alkali metal-ion batteries. The investigation of the novel PBA anode material manganese hexacyanomanganate ($Na_3Mn[Mn(CN)_6]$ = MnHCM) yielded similar results within its very low (de)intercalation potential region (<-0.7 V *vs.* SSC).[59,68] While the employed electrolytes were mainly aqueous Na^+, K^+, Li^+ and even Mg^{2+} salts with varying pH value, concentration and respective anions, such as SO_4^{2-}, ClO_4^-, NO_3^-, and Cl^-, the EIS results and corresponding model for the (de)intercalation mechanism remained unchanged even in co-solvent H_2O:CH_3CN and fully organic propylene and butylene carbonate electrolytes.

The mechanism was further confirmed for a selection of "traditional" LIB systems. Fig. 7A–C shows the obtained characteristic loop features in the Nyquist plot for the anode materials $Li_4Ti_5O_{12}$ and anatase TiO_2, as well as for the common cathode material $LiFePO_4$, which were fitted with the three-step model for (de)intercalation.[59] The employed organic electrolyte was the standard $LiPF_6$ (EC:DEC) solution. This list is further continued by the rather exotic MoS_2 nanosheet-modified $TiNb_2O_7$ nanofiber electrode, another promising LIB anode material.[69] Similar results were obtained at various states of charge (SOC) for the classic Li^+/graphite anode in a $LiPF_6$ EC:EMC + 2 wt% vinyl carbonate electrolyte (Fig. 7D).[70] The EEC model representing the multistep mechanism of (de)intercalation was modified by a series RC-element in order to account for the SEI formation commonly associated with this type of anode material (see section 3.2.1). Fig. 7E deconvolutes the obtained EIS spectrum into the schematically indicated respective contributions from the EEC. As commonly accepted, the uncompensated resistance R_u is represented by a Re(Z) shift on the x-axis of the Nyquist plot, while the RC_{SEI} element introduces a small-radius semi-circle in the high frequency region (red dashed line). This is followed by another large-radius semi-circle in the high- to mid-frequency region associated with the time constant for the rather quick electron charge transfer of the involved redox reaction ($R_{ct}Z_{dl}$, step one, green dashed line). After this, the characteristic loop arises in the mid- to low-frequency part of the spectrum, which is associated with intermediate electrolyte anion ad/desorption and the slower cation (de)intercalation (steps 2 and 3, blue dashed line). This is accounted for by a combination of two more $R_{a,i}C_{a,i}$ elements with formally negative parameters. As a comparison, the traditionally employed SEI-modified Randles circuit was used to fit the loop-featuring spectrum obtained for the Li^+/graphite system (Fig. 7F). However, this single-step mechanism model fails to fit the full frequency range of the spectrum, only coinciding when being applied to the partial high- to mid-frequency range.

Fig. 7 Characteristic loop shapes of the impedance spectra for $Li_4Ti_5O_{12}$, TiO_2 and $LiFePO_4$ in the standard battery electrolyte 1 M $LiPF_6$ (EC:DEC), which are fitted by the proposed equivalent circuit for a 3-step mechanism for the intercalation process (A–C). Reproduced with permission from ref. 59. Loop-featuring impedance spectra for various SOC of Li^+ intercalation into a graphite anode (D). Extension of the physico-chemical model towards the Li^+/graphite system by adding an RC-element into the EEC representing the SEI layer. Its respective impedance contributions are schematically highlighted in an exemplary spectrum, with the intermediate anion adsorption segment being able to fit the loop in the mid to low frequency part (E). As a comparison, the obtained loop spectrum is fitted with a SEI-modified Randles circuit, considering a Warburg element to account for ion diffusion instead of intermediate adsorption. While being in good agreement in the high- to mid-frequency part of the spectrum, the EEC fails to fit the loop in the mid to low frequency part (F). Reproduced with permission from ref. 70. Copyright©2018, American Chemical Society.

This corresponds to the SEI-penetration process and fast electron transfer associated with the oxidation and reduction of graphite. However, the supposed diffusion limitation of the system established by the Warburg element does not represent the actual processes being reflected in the low-frequency range of the spectrum, making this EEC a non-physical, insufficient model for this respective system.

In general, the predominant rate-limiting process of a battery has a great impact on the rational choice of a physical model to fit the obtained spectra. It has been shown for simulated $LiMnO_2$ that limitations from the solid-state diffusion of intercalated Li^+ within the host structure are negligible for $D > 10^{-12}$ cm^2 s^{-1}, even for a 1 μm sized particle.[71] The diffusion coefficients for alkali metal cations in non-dilute electrolytes are normally several magnitudes higher, excluding their contribution to rate limitations inherently. The applicability of an EIS model involving diffusional control as rate-determining processes could be assessed beforehand by CV studies, investigating the proportionality of the peak current to the scan rate$^{1/2}$, peak-to-peak separation and symmetry, as well as a decreasing accessible capacity with increasing galvanostatic (dis)charging rates.[71] However, if properly justified, a Warburg element in series to R_{ct} in the EIS model can account for the solid-state diffusion limited intercalation type battery systems.[72,94] On the other side, the diffusionless behavior of Na^+ intercalation into NiHCF further emphasizes the applicability of the previously discussed three-step mechanism, involving intermediary anion ad/desorption as the limiting process.[73]

Concludingly, the characteristic loop-featured EIS spectra were obtained for differing cathode and anode chemistries at multiple SOCs, as well as differing electrolyte compositions, ranging from pure aqueous at multiple pH values, and mixed and pure organic solvents with varying salt concentrations with different cations and anions. It should be noted that all the mentioned PBA materials were produced as thin-film electrodes, while the investigated "traditional" LIB materials were made by the commonly employed slurry casting method. The proposed three-step mechanism and corresponding EEC were shown to be

an entirely valid model to describe the interfacial processes for a wide subset of intercalation-type batteries, independently of the mentioned system variations. However, this model has not yet been widely accepted, and many researchers stick with the traditionally employed Randles circuit and multiple modifications, yielding purely empirical EIS models with the Warburg element being placed at completely arbitrary positions in the circuit. While such modelling might be able to fit the obtained spectra up to an acceptable degree, it possibly ignores the exact underlying interfacial charge and mass transfer processes.

3.2. Characterization of detrimental processes for ion transport *via* EIS

3.2.1 Effect of the solid electrolyte interphase on charge transport. The electrochemical stability of electrodes against redox reactions with an electrolyte is an important aspect of battery chemistry. In particular, the high reactivity of non-aqueous, organic electrolytes causes disturbances in thermodynamic stability, which leads to passivation of the electrode due to electrolyte decomposition. This passivation layer or interphase formed on the electrode surface affects the physico-chemistry, stability, and charge transport across its interface towards and from the electrolyte, making it a very important aspect to consider in battery chemistry.[74] Such passivation layers form on both the cathode and, more prominently, on the anode side and are commonly denoted as SEI.

Goodenough *et al.*[75] conceived the concept of such an interphase being present on the cathode ($LiCoO_2$) side. The complex underlying electrochemistry was difficult to explain by a simple intra-compound charge diffusion. Therefore, the inclusion of the formation of a surface layer on the electrode due to local oxidation of the electrolyte was necessary (Fig. 8A). The so-called surface layer model considers that this layer has a smaller ion conductivity than the electrolyte itself. R_{sl} represents the resistance along this layer offered to the insertion of guest ions from the electrolyte, along with a capacitance C_{sl} in parallel caused by the polarisation of the additional surface layer (Fig. 8B). Furthermore, the model considers that this surface layer (now widely known as the solid electrolyte interphase) can be described by a set of physical properties: a resistivity ρ, a relative dielectric constant ε, and its thickness L. The resistance and capacitance associated with this surface layer are described by

$$R_{sl} = \rho\frac{L}{A} \tag{6}$$

and

$$C_{sl} = \varepsilon\frac{A}{L}. \tag{7}$$

The formed surface layer can also be visualized by transmission electron microscopy as an amorphous region around the crystalline lattice structure of the active material (Fig. 8C). The presented model was later widely adopted to treat passivation layers on both the anode and cathode.

Building upon the above model, incorporation of SEI-related parameters becomes essential to battery electrochemistry, as can be observed from the model developed by Aurbach and co-workers.[76–79]

Fig. 8 A surface layer of thickness L formed on a battery electrode due to electrolyte decomposition (A). Adapted from ref. 75. EEC based on the formation of such an electrode surface passivation layer (top) and pictorial representation of the cathode–electrolyte interface (bottom) (B). Adapted from ref. 74. Copyright©2004, American Chemical Society. TEM image of a surface passivated $LiCoO_2$ electrode (C). Reproduced with permission from ref. 75. Copyright©2004 IOP Publishing, Ltd.

Graphite based electrodes of varying thickness were used against lithium in a half-cell configuration for their work.[78] The electrochemical processes associated with intercalation systems involve the transport of charged species through the electrolyte and passivation layer, charge transfer at the interface of the electrode and electrolyte, followed by diffusion of ions within the electrode. At potentials below 1.5 V *vs.* Li/Li^+ the electrolyte degrades and deposits as surface films (SEI). It was found from XPS analysis that this deposited layer had a varying composition as a function of distance. Therefore, several RC-elements in series representing the migration of lithium through these layers are employed to account for the high-frequency region of the Nyquist plot. At the mid- and low-frequency region, the charge transfer reaction and corresponding intercalation of lithium ions are followed by solid-state diffusion of ions into the graphite electrode. Furthermore, at low-frequency regions corresponding to diffusion, one can observe Z_w, followed by a C_{int} in series. This intercalation capacity represents lithium-ion storage in bulk graphite. The presence of C_{int} at the lowest frequency region was confirmed by the authors by the observation of a peak-shaped behavior in the Im(Z) part of the impedance at various peak potentials as observed in the cyclic voltammogram.

Based on the introduced model, Barsoukov considered lithium-ion transport *via* pores within the electrode along with the diffusion of ions through the passivation layer (Fig. 9A).[19,80] In Fig. 9B, phase change during lithiation, charge transfer, and lithium-ion diffusion inside the solid electrode are assigned to their respective regions in the Nyquist plot. In another work, Jow and co-workers[81] studied the formation of the SEI during the first cycle and analyzed the formation potential and resistance offered by it using an EIS *via* an EEC model (with the SEI formation being represented by an RC element). The R_{SEI} value was ~450–510 Ω above 0.25 V (before lithiation) and continued to increase even when the voltage was approaching 0.25 V. This trend could possibly be due to the decomposition of electrolyte and formation of a resistive SEI film. In the voltage domain between 0.25 and 0.04 V a sharp decrease in the resistance value to 200 Ω is indicative of the formation of a conductive SEI layer. Furthermore, the cycling data showed that 11% of loss in the capacity occurred above 0.25 V, indicating a thicker SEI layer and suggesting the formation of a thinner and more protecting and conductive SEI below 0.25 V. This change of the resistance value near 0 V could be due to the rearrangement of the physical structures owing to the change in the *d*-spacing of graphite during deintercalation. Such observations related to the change in *d*-spacing during lithium insertion/de-insertion in graphite were made by Dahn[82] and Chao *et al.*[83] using XRD studies.

A further contribution that must be kept in mind is the microstructure of the electrode, which has a significant effect on EIS measurements. Initial developments of EIS models were focussed on the active material,[84,85] which was further combined with the porous structure of the electrode.[86] However, most of these models were assuming the homogeneity of the electrode

Fig. 9 Representation of lithium-ion transport into an intercalation type material as proposed by Barsoukov and co-workers[19] (A). Components of the impedance spectra representing various processes during battery operation (B). Adapted from ref. 19. Copyright©2005, John Wiley and Sons.

View Article Online
PCCP Perspective

materials.[87] Surface heterogeneity offered by varying particle sizes, pore geometry and non-uniform deposition of the solid electrolyte interphase needed to be considered. Mukharjee *et al.*[88] carried out EIS analysis for such varying microstructures *via* computational modeling. It was found that the non-homogeneity has an impact on the active surface area, which in turn dominates the impedance response. The electrolyte-to-active material volume fraction and morphology of the active material were found to be responsible for both charge-transfer resistance and resistance caused by the SEI.[89] Larger R_{SEI} and smaller R_{ct} values were observed for electrodes with a smaller volume fraction of active material. This indicates that materials with larger surface areas will have more capacity loss due to larger R_{SEI}. The shape of the particles affected the EIS response, with spherical particles showing larger R_{SEI} and R_{ct} as compared to cylindrical or platelet forms. Apart from the active material, the binder was found to decrease the active area, which is detrimental to the electrochemical activity of the electrode.

3.2.2 Quantifying intercalated-ion diffusion *via* Warburg impedance. Charge carrier diffusion is an important parameter to optimize battery performance. For intercalation-type battery systems, guest-ion diffusion is directly related to charge storage capacity and rate tolerance. The corresponding ion transport is characterized by the diffusion coefficient (D), which can be calculated using various methods like the galvanostatic intermittent titration technique (GITT), CV, and EIS. However, EIS is the most widely used method to understand charge carrier diffusion.[90] For a typical intercalation system, the Nyquist plot contains a depressed semi-circle with an inclined straight line. Z_w (in the EEC) represents this straight line in the low-frequency region, which corresponds to the complex impedance arising from the diffusion of ions. Huggins *et al.*[91] were among the first to publish theoretical calculations correlating Z_w and D. The Warburg impedance associated with the diffusion of ions is given by[92]

$$Z_w = A_w \omega^{-1/2}(1 - j) \quad (8)$$

Here A_w and ω are the Warburg coefficient and angular frequency of the probing signal, respectively. A way to measure the Warburg coefficient is to obtain the slope from the linear plot of Re(Z) against $\omega^{-1/2}$, directly yielding A_w. The diffusion coefficient is related to A_w as follows:[93]

$$A_w = \frac{RT}{n^2F^2A\sqrt{2}}\left(\frac{1}{C^*\sqrt{D}}\right) \quad (9)$$

where R is the gas constant, T is the temperature, C^* is the electrolyte concentration, A is the electrode area, F represents Faraday's constant, and n is the number of electrons per half-reaction.

Solid-state diffusion (*i.e.* within the electrode material) becomes especially important when designing modern ultra-fast (dis)charging batteries. Particularly, at regions experiencing below zero temperature, the ion kinetics could be sluggish, and tailoring material properties for enhanced diffusion becomes inevitable. Goodenough and co-workers[94] studied a Prussian blue and carbon nanotube (PB/CNT) composite-based cathode to overcome such limitations and promote fast ionic and electronic transport at sub-zero temperatures. It should be noted that, since the Warburg impedance at low frequencies is hardly differentiable at −25 °C, the impedance spectrum collected at this low temperature cannot be directly used for D_{EIS} calculation. However, the activation energy of PB does not change with temperature. Therefore, the Nyquist plots obtained at 30 °C to 55 °C, as seen in Fig. 10A, were used to calculate the

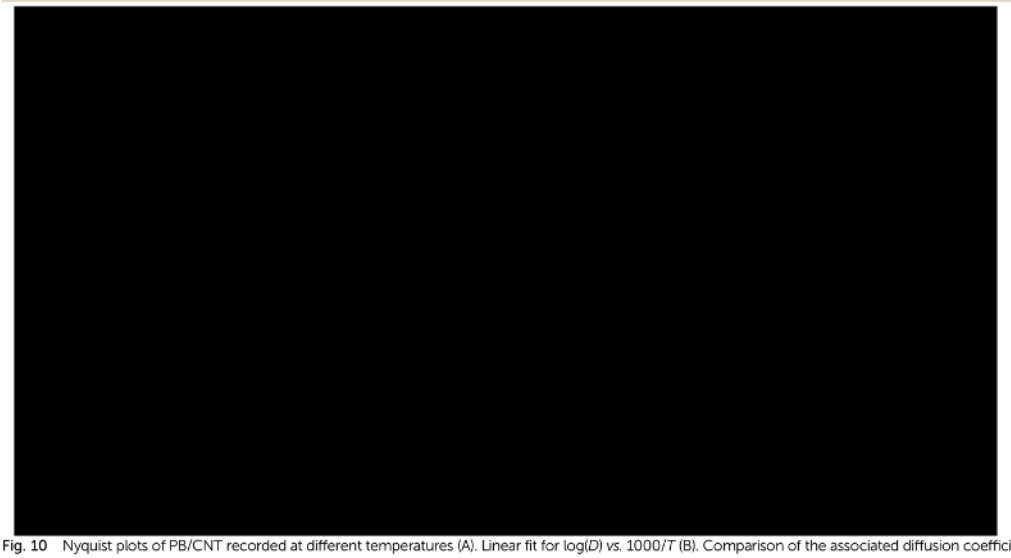

Fig. 10 Nyquist plots of PB/CNT recorded at different temperatures (A). Linear fit for log(D) *vs.* 1000/T (B). Comparison of the associated diffusion coefficient value as obtained from GITT, CV and EIS at 25 °C and at −25 °C (C). Reprinted with permission from ref. 94. Copyright©2016, John Wiley and Sons.

activation energy (E_a) at that lower temperature. The value of E_a was determined by plotting $\log(D)$ *vs.* $1000/T$ (Fig. 10B) and used to obtain the diffusion coefficient at −25 °C by extrapolation. A diffusion coefficient of $\sim 1.2 \times 10^{-12}$ cm^2 s^{-1} was calculated by this method for the PB/CNT cathode at −25 °C. The study is especially interesting in terms of understanding the performance of battery electrodes at sub-zero temperatures. A specific capacity of 142 mA h g^{-1} with cycling stability of more than 1000 cycles was observed. Furthermore, the diffusion coefficients obtained from various techniques like GITT, CV, and EIS are in good agreement at 25 °C and −25 °C within this work (Fig. 10C).

3.2.3 Correlating structural changes of the electrode with alkali-ion insertion/extraction. The electrochemistry of lithium-ion insertion into the active material itself is a complex process, which in some materials is accompanied by a phase change of the hosting crystal structure. For compounds that undergo volume changes during lithium insertion, the phase transformation can be observed from Nyquist plots. As an example, an electrodeposited Cu_6Sn_5 phase transformation was observed below 0.4 V *vs.* Li/Li$^+$ into $Li_xCu_6Sn_5$ ($0 < x < 13$) as a new arc was formed at a lower frequency.[95] This arc formation is reversible as it transforms into a straight line after reinstating the potential below 0.325 V. As a promising anode candidate for LIBs, Si involves the known problem associated with 400% volume expansion upon lithiation leading to a loss in capacity. Nevertheless, it holds an impressive stoichiometry of $Li_{22}Si_5$. Nanoscale Si could hold the key for buffering such volume change. In an interesting work, Haro and co-workers used Si/Ge double-layered nanotube electrodes (DLNT), which enhanced the electrochemical performance.[96] The higher electronic conductivity of Ge favors a reduction in charge transfer resistance associated with lithiation. The kinetic limitations in this system are represented in an EEC (Fig. 11A-C) with additional SEI components. R_{ll} and C_{ll} are the RC-components of the outer SEI layer formed on the anode. The electrode–electrolyte interface contains the R_{ct} and C_{dl} elements, respectively. The constant phase element S and C_μ are associated with alloying reactions. An arc in the mid-frequency region for Si nanotubes shows a behavior similar to an electrical double layer capacitor (Fig. 11D-E). A significant difference in the charge-transfer resistance between pristine and Ge-coated Si-nanotubes is observed. The R_{ct} value increases for the pristine sample below 0.5 V ($R_{ct} \approx 200$ Ωmg), while the Ge layer reduces this value significantly to ~3 Ωmg.

3.3. Impedance contribution in solid-state electrolytes

The investigation of solid electrolytes with EIS lays at hand with the discovery of a new material class within the thio-LISICONs by R. Kanno in 2001.[97] This material system was the first to reach ionic conductivities comparable to liquid electrolytes. The exceptional ionic conductivity of this material is accompanied by stability *vs.* Li(s), high-temperature stability, and negligible electronic conductivity. However, new problems arose when cycling a battery based on this material. While the original article does not show an impedance spectrum, a high-frequency semi-circle followed by a single arc is evaluated to determine the ionic conductivity based on the work of West *et al.*[98]

The polycrystalline nature of solid electrolytes with so-called grains as the crystallites introduces a myriad of additional interfaces between the grains. Additionally, the interface of an SSE towards an electrode with a large deviation of specific conductivities will lead to the formation of space charge layers. The impedance contribution of these phenomena will be discussed, and a physical EEC for space-charge layers is presented.

3.3.1 Observing grain boundary effects. A typical SEM image of an SSE is shown in Fig. 12A with the corresponding equivalent circuit used to fit the EIS data in Fig. 12B. While the majority of the conduction is *via* a hopping mechanism within the crystal structure of the grains,[99] the interfaces between grains, *i.e.*, the grain-boundaries (GBs),[100] pose additional resistances and pathways. EIS can be used to differentiate the effects and contributions to the overall conductivity under certain conditions. Typically, the grain size varies from a few hundred nanometres to a few microns at most, placing a

Fig. 11 Schematic representation of the EEC (A). Li-ion uptake in the Ge shell, which reduces the overall R_{ct} (B). Higher resistance to lithium transport in pristine Si-nanotubes (C). Nyquist plots obtained at 0.1 V of Si/Ge-nanotubes (D) and Si-nanotubes (E). Reprinted with permission from ref. 96. Copyright©2014, Royal Society of Chemistry.

Fig. 12 SEM image of an LLTO electrolyte with a high sintering temperature of 1450 °C. Multiple phases are clearly visible, and grain boundaries are ample and large (A). Simulated impedance spectra using the equivalent circuit shown in the plot. The central RC-element distinctly impacts the mid-frequency region (B). Reprinted with permission from ref. 102. Copyright©2017, Springer Nature.

hundred to a few thousand grains in lateral connection in a typical SSE film. As the bulk ion conductivity is a few orders higher than the grain-boundary contribution, a common way to make the GB impedance visible is to lower the temperature well below operating temperature. At 173 K, the semi-circle associated with the grain-boundary impedance becomes clearly visible in LiAlTiPO (LATP), a common Li-conducting oxidic glass ceramics similar to Ohara glass.[101] In another Li-conducting material, LiLaTiO (LLTO), the grain-boundary contribution was separated using the distribution of relaxation time analysis, showing that the grain conductivity is a few times higher than the grain-boundary conductivity.[102] The impedance data in both articles were fitted with purely empirical models (LLTO: RQ–RQ–RQ–Q, LATP: RQ–RQ). However, as stressed earlier, the use of constant phase elements should be carefully motivated as the only widely accepted physical origin of the imperfect capacitance is an electrochemical double layer.[103]

In addition to experimental data and empirical equivalent circuits, theoretical models developed to describe the Li-ion transfer within and between grains can be considered. A phenomenological model for Li-ion conductors suggests that the two processes occur on completely different time scales.[104] A geometrical consideration of the grains with grain-boundary effects can be found in the brick-layer model, initially developed for electrically conducting ceramics.[105] Adaptation of this model to an oxygen conducting material for fuel cells was assisted by a specific electrode design in yttria-stabilized zirconia.[106]

As suggested by Braun *et al.*[102] and Breuer *et al.*,[101] a simple RC- or RQ-element is sufficient to fit the isolated grain-boundary impedance without any additional elements. However, embedding this element into an equivalent circuit describing the other effects can be troublesome. To date, no physically motivated equivalent circuit has been found to describe the impedance of grain-boundary effects. While at low temperatures, mostly outside of the operating range, the various experimental findings show that the grain boundary impedance is clearly visible. The contribution at room temperature still remains hidden as an undescribed contribution to the overall electrolyte resistance. The parameters determined from grain-boundary contributions, such as the capacitance, are hard to validate with supplementary experiments. A physical or geometrical quantity, such as the size of the grain separation, has to be derived from the electrochemical parameters for validation.

3.3.2 Charge accumulation in solid-state electrolytes. While the SSE properties are ready to compete with their liquid counterparts, the focus of research now drifts more and more to the interface between solid electrolytes and electrodes. One issue that is still widely discussed today is the formation of charged layers when two materials of non-equal electrochemical potential come into contact. Analogous to liquids, the simultaneous formation of a compact double layer and a diffuse space charge layer and their impact on the interface resistance are widely discussed in modern literature.

For liquid electrolytes, the development of a model for charge accumulation at interfaces under electrochemical bias began with Hermann von Helmholtz in 1853.[109] In an iterative work over the course of over 100 years, the most recent work culminated in the description of pseudo-capacitances accurately describing the capacitance of so-called supercapacitors.[110] The theoretical work for the description of the double layer formation under electrochemical bias conditions started on oxidic solid electrolytes.[111] In the blocking electrode configuration, the capacitance of this layer was simulated for a variety of external conditions shown in Fig. 13. First indirect experimental evidence for a negatively charged layer was found in 2015 by Haruta *et al.* at the LiPON/$LiCoO_2$ interface.[112] However, the analysis of impedance data was performed without an electrical equivalent circuit and therefore should be carefully considered. While many supplementary techniques have been used and theories have been developed, no common understanding of the formation of the space charge layers has been published to date. In a prior work,[113] we showed that, indeed, the space charge layer formation is strongly dependent on the bias potential and can be clearly detected with EIS but only with a physical EEC. The development and argumentative chain for the equivalent circuit are based on interface *vs.* bulk influence on the impedance. The interface related parameters (R_{SCL}, C_{SCL}, and Z_{DL}) of the equivalent circuit should strongly correlate with the external conditions influencing the physical interface (such as electrode potential, electrode material, and temperature), whereas the parameters representing the bulk (C_{geom} and R_{bulk}) should only depend on the temperature in this case. Through careful observation and spectra fitting, the EEC was proven step-by-step, and each parameter was assigned to its physical origin. The influence of the space charge under blocking conditions reveals itself in a high contribution to the interface resistance at moderate potentials. From the physically motivated EEC, other properties such as the space charge thickness were determined to be up to a few tens of nanometres which in turn can be validated using other techniques.[114]

4. Suggestions, conclusion and outlook

Any electrochemical system involves various processes such as charge transfer mechanisms, adsorption, and diffusion of

Fig. 13 Theoretical potential distribution and charge carrier concentration in a solid-state electrolyte between a carbon cathode and lithium anode (A). Reprinted with permission from ref. 107. Copyright©2015, American Chemical Society. Surface capacitance under different potential bias conditions for different degrees of surface disorder (values next to curves) (B). Reprinted with permission from ref. 111. Copyright© 1984, Elsevier Ltd. EEC and geometric presentation of the electrochemical model developed for a model solid electrolyte under blocking conditions (C). Reprinted with permission from ref. 113. Copyright© 2021, American Chemical Society. Space-charge occurrence in ZnO (D). Reprinted with permission from ref. 108. Copyright©2019, American Chemical Society.

charged species. For typical battery systems, the intercalation of ions into electrode materials, which are themselves a mixture of an active material, a conductive additive, and a binder, further multiplies this complexity.

An impedance spectrum of a full cell battery will therefore contain a superposition of a wide range of processes, some of which can manifest in a similar frequency region. Without understanding the physical processes by considering various kinetic parameters, the interpretation of EIS data is not possible. The ion migration through the electrode, the growth of a solid electrolyte interphase, possibly occurring phase transformations, porosity, the non-homogeneity of the electrode, and various other parameters need to be taken into account. Therefore, the EEC model must be built based on the respective physical origins rather than on the empirical interpretation to yield useful insights into electrochemistry.

The significance of a physically motivated EEC is two-fold: in order to explore the physico-chemical origins of resistances and capacitances, any ambiguity must be ruled out by either auxiliary characterization techniques or a "clean" chain of arguments leading to the identification. The EEC elements are then not only assigned to a physical origin but the parameters can be quantitatively analyzed with high sensitivity. The exploration of changes in occurring capacitances, for example, can be linked to SEI growth. Therefore, the range of origins for impedances should be theoretically elucidated before EIS is conducted on an unknown electrochemical system. Once an impedance spectrum is recorded, cognitive bias will drive any researcher into assumptions about occurring processes by merely looking at the graph. A variation of additional external parameters can, in most cases, be used as the groundwork for an argumentative chain. Temperature, for example, will lead to a decrease of ionic resistances in almost all battery-relevant materials, but the temperature effect on interface-related impedances does not necessarily have to follow the same trend. External bias potentials can be used to (artificially) electrify interfaces and thereby explore interface impedances without direct observation by other methods, which is usually difficult to do *in situ* or even *in operando*. As the non-stationarity of the electrochemical system can lead to distortions of the impedance response, special

attention must be paid. As an example, when recording temperature-dependent impedances, one should not only measure a single impedance spectrum at a given temperature, but a few repetitions of stepwise temperature variations will elucidate any non-stationarity or even system degradation.

Intercalation-based systems have been thoroughly investigated in the past decades and extensive research has been dedicated towards understanding the SEI and charge-storage mechanism *via* EECs. Until recently, loops observed in the associated impedance spectra were commonly considered as measurement errors or artifacts by many researchers. It turned out that their occurrence is, in fact, an indispensable feature within the presented EIS spectra for intercalation-type battery systems that allowed accessing the actual physical mechanism accompanying the investigated process, as well as identifying the involved species. The presented multistage (de)intercalation mechanism, therefore, serves as a representative example for the superiority of such EECs with distinctive physical meaning over purely empirical models, as it allows an appropriate understanding and interpretation of the various influences determining the performance of the investigated battery system. In this special case, the important role of intermediary anion adsorption could be elucidated, which should be considered when interpreting the electrochemical behavior of existing systems, as well as when designing new types of electrode structures.

For solid-state electrolytes, the physical origin of the additional RC-element should be carefully considered for a given temperature, material composition, and especially grain-boundary size. The resistance contribution of this ambiguous process can be non-negligible for a given physical system and must be considered on a case-by-case basis. Fortunately, a bias-variation can be used to unambiguously assign the origin to either interface or bulk electrolyte.

As no two electrochemical systems are the same, no handbook for building an electrical equivalent circuit can be written. Approaches like machine learning for evaluating impedance spectra have been introduced in recent years but are limited to very narrow problems.[115]

It must therefore be concluded that proper analysis of impedance spectra is a very tedious task especially if no known EEC exists for the exact system. Processes and phenomena like intercalation, SEI formation, and space charge occurrence are on or beyond the cusp of scientific efforts for further understanding, and still, the impedance contribution is not well known. Further research should therefore be conducted on model systems, which might not lead to extraordinarily performing battery cells but instead to a physically motivated equivalent circuit that can be validated and later transferred to commercially viable battery systems.

List of abbreviations

AIC	Akaike information criterion
DRT	Distribution of relaxation times
EIS	Electrochemical impedance spectroscopy
EEC	Electrical equivalent circuit
LIB	Lithium-ion battery
SSE	Solid-state electrolyte
PEIS	Potentio-dynamic EIS
GEIS	Galvano-dynamic EIS
ac	Alternating current
dc	Direct current
QCM	Quartz-crystal microbalance
CV	Cyclic voltammetry
CPE	Constant phase element
KK check	Kramers–Kronig check
SEI	Solid–electrolyte interphase
PB/PBA	Prussian blue (analogues)
Ni/Co/V/In/CuHCF	Transition metal hexacyanoferrate
LICT	Laser-induced current transients
SOC	State of charge
GITT	Galvanostatic intermittent titration technique
CNT	Carbon nanotube
DLNT	Double-layered nanotube
GB	Grain boundary
LATP	LiAlTiPO
LLTO	LiLaTiO

Conflicts of interest

There are no conflicts to declare.

Acknowledgements

This work is part of the ASSB Bayern project funded by the Bavarian Ministry of Economic Affairs, Regional Development and Energy. Furthermore, the financial support from Germany's excellence cluster ''e-conversion'' is gratefully acknowledged.

References

1 A. Höltl, C. Macharis and K. De Brucker, *Energies*, 2018, **11**(1), 20.
2 N. Kittner, F. Lill and D. M. Kammen, *Nat. Energy*, 2017, **2**(9), 17125.
3 L. Lu, X. Han, J. Li, J. Hua and M. Ouyang, *J. Power Sources*, 2013, **226**, 272–288.
4 C. De las Casas and W. Li, *J. Power Sources*, 2012, **208**, 74–85.
5 A. Barré, B. Deguilhem, S. Grolleau, M. Gérard, F. Suard and D. Riu, *J. Power Sources*, 2013, **241**, 680–689.
6 P. V. Kamat, *ACS Energy Lett.*, 2019, **4**(11), 2757–2759.
7 G. L. Xu, R. Amine, A. Abouimrane, H. Che, M. Dahbi, Z. F. Ma and K. Amine, *Adv. Energy Mater.*, 2018, **8**(14), 1702403.
8 X. Yu and A. Manthiram, *Energy Environ. Sci.*, 2018, **11**(3), 527–543.
9 Q. Wang, B. Mao, S. I. Stoliarov and J. Sun, *Prog. Energy Combust. Sci.*, 2019, **73**, 95–131.

10 Y. Horowitz, C. Schmidt, D. H. Yoon, L. M. Riegger, L. Katzenmeier, G. M. Bosch and C. E. Diesendruck, *et al.*, *Energy Technol.*, 2020, **8**(11), 2000580.
11 W. Zhang, J. Nie, F. Li, Z. L. Wang and C. Sun, *Nano Energy*, 2018, **45**, 413–419.
12 D. Liu, Z. Shadike, R. Lin, K. Qian, H. Li, K. Li and X. Qin, *et al.*, *Adv. Mater.*, 2019, **31**(28), 1806620.
13 M. S. Islam, D. J. Driscoll, C. A. Fisher and P. R. Slater, *Chem. Mater.*, 2005, **17**(20), 5085–5092.
14 G. Bieker, M. Winter and P. Bieker, *Phys. Chem. Chem. Phys.*, 2015, **17**(14), 8670–8679.
15 http://apps.webofknowledge.com/ (Search terms: ''Electrochemical Impedance Spectroscopy and Battery'', last accessed on the 27th Jan 2021).
16 A. S. Bandarenka, *Analyst*, 2013, **138**(19), 5540–5554.
17 D. D. Macdonald, *Electrochim. Acta*, 2006, **51**(8–9), 1376–1388.
18 T. Osaka, D. Mukoyama and H. Nara, *J. Electrochem. Soc.*, 2015, **162**(14), A2529–A2537.
19 E. Barsoukov and J. R. Macdonald, *Impedance Spectroscopy Theory, Experiment, and Applications*, John Wiley and Sons. Inc. Publication, USA, 2005, pp. 13–20.
20 A. S. Bondarenko, *Anal. Chim. Acta*, 2012, **743**, 41–50.
21 M. D. Murbach and D. T. Schwartz, *J. Electrochem. Soc.*, 2018, **165**(2), A297.
22 A. Lasia, *Modern aspects of electrochemistry*, Springer, 2002, pp. 143–248.
23 R. S. Smith and J. C. Doyle, *American Control Conference*, IEEE, 1989, pp. 1435–1440.
24 M. Huang, J. B. Henry, B. B. Berkes, A. Maljusch, W. Schuhmann and A. S. Bondarenko, *Analyst*, 2012, **137**(3), 631–640.
25 R. Krimholtz, D. A. Leedom and G. L. Matthaei, *Electron. Lett.*, 1970, **6**(13), 398–399.
26 A. R. West, D. C. Sinclair and N. Hirose, *J. Electroceram.*, 1997, **1**(1), 65–71.
27 T. Osaka, T. Momma, D. Mukoyama and H. Nara, *J. Power Sources*, 2012, **205**, 483–486.
28 J. Jean, *Curr. Top. Electrochem.*, 1997, **4**, 127–136.
29 W. H. Mulder, J. H. Sluyters, T. Pajkossy and L. Nyikos, *J. Electroanal. Chem. Interfacial Electrochem.*, 1990, **285**(1–2), 103–115.
30 P. Córdoba-Torres, T. J. Mesquita and R. P. Nogueira, *J. Phys. Chem. C*, 2015, **119**(8), 4136–4147.
31 C. H. Kim, S. I. Pyun and J. H. Kim, *Electrochim. Acta*, 2003, **48**(23), 3455–3463.
32 J. B. Jorcin, M. E. Orazem, N. Pébère and B. Tribollet, *Electrochim. Acta*, 2006, **51**(8–9), 1473–1479.
33 K. B. Oldham, *Electrochem. Commun.*, 2004, **6**(2), 210–214.
34 I. M. Hodge, M. D. Ingram and A. R. West, *J. Electroanal. Chem. Interfacial Electrochem.*, 1976, **74**(2), 125–143.
35 S. Fletcher, *J. Electrochem. Soc.*, 1994, **141**(7), 1823.
36 H. Witzenhausen, PhD thesis, RWTH Aachen University, 2017.
37 J. C. Wang and J. B. Bates, *Solid State Ionics*, 1986, **18**, 224–228.
38 Z. Siroma, T. Sato, T. Takeuchi and T. Ioroi, *et al.*, *J. Power Sources*, 2016, **316**, 215–223.
39 M. Adamič, S. Talian, A. Sinigoj, I. Humar, J. Moskon and M. Gaberscek, *J. Electrochem. Soc.*, 2019, **166**, A5045–A5053.
40 P. Vadhva, J. Hu, M. Johnson, R. Stocker, M. Braglia, D. Brett and A. Rettie, *ChemElectroChem*, 2021, **8**, 1–19, DOI: 10.1002/celc.202100108.
41 K. Kobayashi and T. S. Suzuki, *J. Phys. Soc. Jpn.*, 2018, **87**(9), 094002.
42 U. Westerhoff, K. Kurbach, F. Lienesch and M. Kurrat, *Energy Technol.*, 2016, **4**(12), 1620–1630.
43 W. Choi, H. C. Shin, J. M. Kim, J. Y. Choi and W. S. Yoon, *J. Electrochem. Sci. Technol.*, 2020, **11**(1), 1–13.
44 N. Meddings, M. Heinrich, F. Overney, J. S. Lee, V. Ruiz, E. Napolitano and J. Park, *et al.*, *J. Power Sources*, 2020, **480**, 228742.
45 A. Lewandowski, B. Kurc, I. Stepniak and A. Swiderska-Mocek, *Electrochim. Acta*, 2011, **56**(17), 5972–5978.
46 N. J. Kidner, N. H. Perry, T. O. Mason and E. J. Garboczi, *J. Am. Ceram. Soc.*, 2008, **91**, 1733–1746.
47 M. M. Thackeray, *Prog. Solid State Chem.*, 1997, **25**(1-2), 1–71.
48 P. G. Bruce and M. Y. Saidi, *J. Electroanal. Chem.*, 1992, **322**(1-2), 93–105.
49 T. Okumura, T. Fukutsuka, K. Matsumoto, Y. Orikasa, H. Arai, Z. Ogumi and Y. Uchimoto, *J. Phys. Chem. C*, 2011, **115**(26), 12990–12994.
50 S. Kobayashi and Y. Uchimoto, *J. Phys. Chem. B*, 2005, **109**(27), 13322–13326.
51 C. N. Cao, *Electrochim. acta*, 1990, **35**(5), 837–844.
52 J. S. Gnanaraj, R. W. Thompson, S. N. Iaconatti, J. F. DiCarlo and K. M. Abraham, *Electrochem. Solid-State Lett.*, 2005, **8**(2), A128.
53 B. Wang, Y. Han, X. Wang, N. Bahlawane, H. Pan, M. Yan and Y. Jiang, *iScience*, 2018, **3**, 110–133.
54 J. Bacskai, K. Martinusz, E. Czirok, G. Inzelt, P. J. Kulesza and M. A. Malik, *J. Electroanal. Chem.*, 1995, **385**(2), 241–248.
55 X. Liu, L. Gu, Q. Zhang, J. Wu, Y. Long and Z. Fan, *Nat. Commun.*, 2014, **5**(1), 1–9.
56 W. Li, F. Zhang, X. Xiang and X. Zhang, *ChemElectroChem*, 2017, **4**(11), 2870–2876.
57 H. Kim, J. Hong, K. Y. Park, H. Kim, S. W. Kim and K. Kang, *Chem. Rev.*, 2014, **114**(23), 11788–11827.
58 J. Yun, J. Pfisterer and A. S. Bandarenka, *Energy Environ. Sci.*, 2016, **9**(3), 955–961.
59 E. Ventosa, B. Paulitsch, P. Marzak, J. Yun, F. Schiegg, T. Quast and A. S. Bandarenka, *Adv. Sci.*, 2016, **3**(12), 1600211.
60 D. Scieszka, J. Yun and A. S. Bandarenka, *ACS Appl. Mater. Interfaces*, 2017, **9**(23), 20213–20222.
61 J. Bacskai, K. Martinusz, E. Czirok, G. Inzelt, P. J. Kulesza and M. A. Malik, *J. Electroanal. Chem.*, 1995, **385**(2), 241–248.
62 M. A. Malik, G. Horanyi, P. J. Kulesza, G. Inzelt, V. Kertesz, R. Schmidt and E. Czirok, *J. Electroanal. Chem.*, 1998, **452**(1), 57–62.
63 M. A. Malik, K. Miecznikowski and P. J. Kulesza, *Electrochim. Acta*, 2000, **45**(22–23), 3777–3784.
64 M. H. Pournaghi-Azar and H. Nahalparvari, *J. Solid State Electrochem.*, 2004, **8**(8), 550–557.

65 D. Scieszka, C. Sohr, P. Scheibenbogen, P. Marzak, J. Yun, Y. Liang and A. S. Bandarenka, *et al.*, *ACS Appl. Mater. Interfaces*, 2018, **10**(25), 21688–21695.
66 B. Paulitsch, J. Yun and A. S. Bandarenka, *ACS Appl. Mater. Interfaces*, 2017, **9**(9), 8107–8112.
67 P. Marzak, M. Kosiahn, J. Yun and A. S. Bandarenka, *Electrochim. Acta*, 2019, **307**, 157–163.
68 J. Yun, F. A. Schiegg, Y. Liang, D. Scieszka, B. Garlyyev, A. Kwiatkowski and A. S. Bandarenka, *et al.*, *ACS Appl. Energy Mater.*, 2017, **1**(1), 123–128.
69 D. Pham-Cong, J. H. Choi, J. Yun, A. S. Bandarenka, J. Kim, P. V. Braun and C. R. Cho, *et al.*, *ACS Nano*, 2017, **11**(1), 1026–1033.
70 F. Dinkelacker, P. Marzak, J. Yun, Y. Liang and A. S. Bandarenka, *ACS Appl. Mater. Interfaces*, 2018, **10**(16), 14063–14069.
71 V. A. Nikitina, S. Y. Vassiliev and K. J. Stevenson, *Adv. Energy Mater.*, 2020, **10**(22), 1903933.
72 Z. Gao, J. Bobacka and A. Ivaska, *Electrochim. Acta*, 1993, **38**(2-3), 379–385.
73 H. W. Lee, M. Pasta, R. Y. Wang, R. Ruffo and Y. Cui, *Faraday Discuss.*, 2015, **176**, 69–81.
74 K. Xu, *Chem. Rev.*, 2004, **104**(10), 4303–4418.
75 M. G. S. R. Thomas, P. G. Bruce and J. B. Goodenough, *J. Electrochem. Soc.*, 1985, **32**(7), 1521.
76 D. Aurbach, Y. Ein-Eli, B. Markovsky, A. Zaban, S. Luski, Y. Carmeli and H. Yamin, *J. Electrochem. Soc.*, 1995, **142**(9), 2882.
77 D. Aurbach, K. Gamolsky, B. Markovsky, G. Salitra, Y. Gofer, U. Heider and M. Schmidt, *et al.*, *J. Electrochem. Soc.*, 2000, **147**(4), 1322.
78 M. D. Levi and D. Aurbach, *J. Phys. Chem. B*, 1997, **101**(23), 4630–4640.
79 M. D. Levi and D. Aurbach, *J. Phys. Chem. B*, 1997, **101**(23), 4641–4647.
80 E. Barsoukov, J. H. Kim, J. H. Kim, C. O. Yoon and H. Lee, *Solid State Ionics*, 1999, **116**(3–4), 249–261.
81 S. Zhang, M. S. Ding, K. Xu, J. Allen and T. R. Jow, *Electrochem. Solid-State Lett.*, 2001, **4**(12), A206.
82 J. R. Dahn, *Phys. Rev. B: Condens. Matter Mater. Phys.*, 1991, **44**(17), 9170.
83 H. He, C. Huang, C. W. Luo, J. J. Liu and Z. S. Chao, *Electrochim. Acta*, 2013, **92**, 148–152.
84 R. W. J. M. Huang, F. Chung and E. M. Kelder, *J. Electrochem. Soc.*, 2006, **153**(8), A1459.
85 J. Newman and W. Tiedemann, *AIChE J.*, 1975, **21**(1), 25–41.
86 A. M. Johnson and J. Newman, *J. Electrochem. Soc.*, 1971, **118**(3), 510.
87 J. S. Newman and C. W. Tobias, *J. Electrochem. Soc.*, 1962, **109**(12), 1183.
88 C. F. Chen and P. P. Mukherjee, *Phys. Chem. Chem. Phys.*, 2015, **17**(15), 9812–9827.
89 P. Lu, C. Li, E. W. Schneider and S. J. Harris, *J. Phys. Chem. C*, 2014, **118**(2), 896–903.
90 I. O. Santos-Mendoza, J. Vázquez-Arenas, I. González, G. Ramos-Sánchez and C. Castillo-Araiza, *Int. J. Chem. React. Eng.*, 2016, **17**(6), 20180095.
91 C. Ho, I. D. Raistrick and R. A. Huggins, *J. Electrochem. Soc.*, 1980, **127**(2), 343.
92 R. P. Janek, W. R. Fawcett and A. Ulman, *Langmuir*, 1998, **14**(11), 3011–3018.
93 A. J. Bard and L. R. Faulkner, *Electrochem. Methods*, 2001, **2**(482), 580–632.
94 Y. You, H. R. Yao, S. Xin, Y. X. Yin, T. T. Zuo, C. P. Yang and J. B. Goodenough, *et al.*, *Adv. Mater.*, 2016, **28**(33), 7243–7248.
95 X. Y. Fan, Q. C. Zhuang, G. Z. Wei, L. Huang, Q. F. Dong and S. G. Sun, *J. Appl. Electrochem.*, 2009, **39**(8), 1323–1330.
96 M. Haro, T. Song, A. Guerrero, L. Bertoluzzi, J. Bisquert, U. Paik and G. Garcia-Belmonte, *Phys. Chem. Chem. Phys.*, 2014, **16**(33), 17930–17935.
97 R. Kanno and M. Murayama, *J. Electrochem. Soc.*, 2001, **148**(7), A742.
98 A. R. West, *Solid state chemistry and its applications*, John Wiley and Sons, 2014.
99 M. Uitz, V. Epp, P. Bottke and M. Wilkening, *J. Electroceram.*, 2017, **38**(2–4), 142–156.
100 S. Ganapathy, C. Yu, E. R. Van Eck and M. Wagemaker, *ACS Energy Lett.*, 2019, **4**(5), 1092–1097.
101 S. Breuer, D. Prutsch, Q. Ma, V. Epp, F. Preishuber-Pflügl, F. Tietz and M. Wilkening, *J. Mater. Chem. A*, 2015, **3**(42), 21343–21350.
102 P. Braun, C. Uhlmann, A. Weber, H. Störmer, D. Gerthsen and E. Ivers-Tiffée, *J. Electroceram.*, 2017, **38**(2-4), 157–167.
103 S. Kochowski and K. Nitsch, *Thin Solid Films*, 2002, **415**(1-2), 133–137.
104 N. Goswami and R. Kant, *J. Electroanal. Chem.*, 2019, **835**, 227–238.
105 N. J. Kidner, N. H. Perry, T. O. Mason and E. J. Garboczi, *J. Am. Ceram. Soc.*, 2008, **91**(6), 1733–1746.
106 M. Gerstl, E. Navickas, G. Friedbacher, F. Kubel, M. Ahrens and J. Fleig, *Solid State Ionics*, 2011, **185**(1), 32–41.
107 A. C. Luntz, J. Voss and K. Reuter, *J. Phys. Chem. Lett.*, 2015, **6**(22), 4599–4604.
108 T. Tsuchiya, Y. Itoh, Y. Yamaoka, S. Ueda, Y. Kaneko, T. Hirasawa and K. Terabe, *et al.*, *J. Phys. Chem. C*, 2019, **123**(16), 10487–10493.
109 H. V. Helmholtz, *Ann. Phys.*, 1879, **243**(7), 337–382.
110 R. A. Marcus, *J. Chem. Phys.*, 1956, **24**(5), 966–978.
111 V. N. Chebotin, I. D. Remez, L. M. Solovieva and S. V. Karpachev, *Electrochim. Acta*, 1984, **29**(10), 1380–1388.
112 M. Haruta, S. Shiraki, T. Suzuki, A. Kumatani, T. Ohsawa, Y. Takagi and T. Hitosugi, *et al.*, *Nano Lett.*, 2015, **15**(3), 1498–1502.
113 L. Katzenmeier, S. Helmer, S. Braxmeier, S. Knobbe and A. S. Bandarenka, *ACS Appl. Mater. Interfaces*, 2021, **13**(4), 5853–5860.
114 L. Katzenmeier, L. Carstensen, S. J. Schaper, P. Müller-Buschbaum and A. S. Bandarenka, *Adv. Mater.*, 2021, **33**, 2100585, DOI: 10.1002/adma.202100585.
115 Y. Zhang, Q. Tang, Y. Zhang, J. Wang, U. Stimming and A. A. Lee, *Nat. Commun.*, 2020, **11**(1), 1–6.

Electrolyte effects on the stabilization of Prussian blue analog electrodes in aqueous sodium-ion batteries.
ACS Applied Materials and Interfaces **2022**, *14*, 3515-3525.

ACS APPLIED MATERIALS & INTERFACES

www.acsami.org Research Article

Electrolyte Effects on the Stabilization of Prussian Blue Analogue Electrodes in Aqueous Sodium-Ion Batteries

Xaver Lamprecht, Florian Speck, Philipp Marzak, Serhiy Cherevko,* and Aliaksandr S. Bandarenka*

Cite This: *ACS Appl. Mater. Interfaces* 2022, 14, 3515−3525 Read Online

ACCESS | Metrics & More | Article Recommendations | Supporting Information

ABSTRACT: Aqueous sodium-ion batteries based on Prussian Blue Analogues (PBA) are considered as promising and scalable candidates for stationary energy storage systems, where longevity and cycling stability are assigned utmost importance to maintain economic viability. Although degradation due to active material dissolution is a common issue of battery electrodes, it is hardly observable directly due to a lack of *in operando* techniques, making it challenging to optimize the performance of electrodes. By operating $Na_2Ni[Fe(CN)_6]$ and $Na_2Co[Fe(CN)_6]$ model electrodes in a flow-cell setup connected to an inductively coupled plasma mass spectrometer, in this work, the dynamics of constituent transition-metal dissolution during the charge−discharge cycles was monitored in real time. At neutral pHs, the extraction of nickel and cobalt was found to drive the degradation process during charge−discharge cycles. It was also found that the nature of anions present in the electrolytes has a significant impact on the degradation rate, determining the order $ClO_4^- > NO_3^- > Cl^- > SO_4^{2-}$ with decreasing stability from the perchlorate to sulfate electrolytes. It is proposed that the dissolution process is initiated by detrimental specific adsorption of anions during the electrode oxidation, therefore scaling with their respective chemisorption affinity. This study involves an entire comparison of the effectiveness of common stabilization strategies for PBAs under very fast (dis)charging conditions at 300C, emphasizing the superiority of highly concentrated $NaClO_4$ with almost no capacity loss after 10 000 cycles for $Na_2Ni[Fe(CN)_6]$.

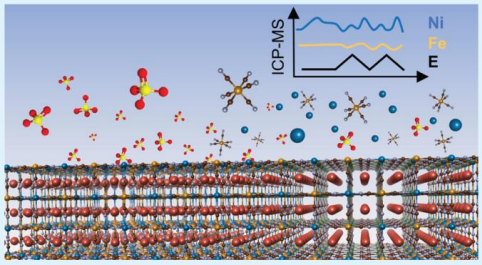

KEYWORDS: *Na-ion aqueous batteries, Prussian Blue Analogues, sodium nickel hexacyanoferrate, ICP-MS, active material dissolution, degradation*

INTRODUCTION

Over the last years, the emerging climate crisis due to the ever-increasing demand for energy and boundless CO_2 emissions has raised increasing awareness in society. Accordingly, the transition of the energy provision from fossil to renewable fuels is on the political agenda of almost any government around the globe.[1] However, the inherent mismatch of supply and demand within the centralized infrastructure of the existing power grids remains a crucial obstacle yet to be overcome.[2] Scalable battery technologies are expected to play a crucial role for the stationary energy sector to enable a sudden integration of, e.g., wind and solar power.[3] Although lithium-ion batteries (LIB) still dominate the energy storage market, the expected future competition of the stationary and mobility sector in the context of its resource-limited scalability will aggravate the pressure on this pioneering technology.[4−8] Furthermore, valid safety-related concerns might restrain a comprehensive adoption of LIBs for household-scale applications.[9] In contrast, aqueous sodium-ion batteries (ASIB) based on Prussian Blue analogue (PBA) materials are considered promising candidates for a scalable, cost-efficient, and ecologically friendly technology for stationary use cases.[10,11] This intercalation-type battery material class can be represented by the generic chemical formula $Na_xTM^1[TM^2(CN)_6]$, where $TM^{1,2}$ refers to the variety of transition metals that can be employed.[12] The implementation of water-based electrolytes compared to the flammable organic solvents in LIBs further provides reliable system safety. It might finally dispel doubts within the procurement decision, especially considering homeowners and large power infrastructure and storage facilities. Its considerably lower energy density of 20−30 Wh/kg (despite cheaper precursor materials) is expected to result in up to 5 times higher up-front capital costs of currently ca. 400 USD per kWh. This fact might naturally be evaluated as a severe drawback of PBA-based ASIBs compared to the state-of-the-art

Received: November 2, 2021
Accepted: December 28, 2021
Published: January 6, 2022

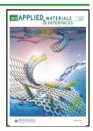

LIBs.[13,14] However, Marzak et al. have recently reported an aqueous thin-film PBA-based Na^+ battery prepared by a facile electrodeposition method, demonstrating a fast (dis)charging time of only 10 s (360C), opening new opportunities for hybrid battery-supercapacitor systems.[15] Thereby, this technology could pave the way for innovative use cases, such as grid stabilization.

Nevertheless, such high-power applications typically require very frequent (dis)charging patterns over several 1000 to 10 000 cycles.[16] This assigns utmost importance to cycling stability in high-power applications over several years to be economically viable and guarantee an outperforming cost per kWh per cycle ratio. Therefore, a comprehensive understanding of the inherent degradation mechanism proceeding during battery operation is indispensable to design optimized electrode and electrolyte compositions for a long-lasting battery system.

In general, active material dissolution is one of the driving forces for capacity fading and dissolved electrode constituents from the cathode are of great concern, especially in traditional LIB systems.[17] This process results in a loss of available capacity. It initiates plating of the corresponding transition-metal cations on the anode, leading to SEI formation, electrolyte decomposition, and other failure mechanisms.[18−21] A straightforward phenomenological approach to identify dissolved electrode constituents involves *ex situ* analysis of the electrolyte for transition-metal cations after battery operation.[22−24] More advanced *in operando* techniques were established over the last decades. These involve the real-time reaction gas analysis stemming from the decomposition of the electrolyte and SEI (such as C_2H_4, H_2, CO_2), thereby serving as an indirect tracer of ongoing electrode degradation processes.[21,25,26] Furthermore, X-ray absorption analysis of dissolved transition-metal ions allows the direct correlation between the applied electrochemistry and detrimental side reaction intermediates, but its low time resolution in the range of several minutes limits its applicability.[27,28] Nevertheless, methods for directly probing the dissolution process are still only scarcely available, and only a very few reports have provided insights into real-time or *in situ* detected elemental leaching rates during battery operation.[29−32]

However, strongly deviating degradation mechanisms might have to be considered for battery electrodes under aqueous conditions. In the case of PBA materials for ASIBs, research efforts related to their degradation mainly focused on finding and quantifying dissolved transition-metal cations and hexacyanometallate or cyanide anions in the electrolyte postmortem.[33−38] Several reasons for the observed instability have been discussed, attributing the loss of active material to the deterioration of the TM−N≡C−Fe bonds. Although the ligand bindings in $Fe(CN)_6^{3/4-}$ themselves are supposed to be stable up to moderately acidic conditions, the interaction of the N-coordinated TM atoms with hydroxide anions is believed to rupture the compound.[39−41] Naturally, some OH^- species will be present in any aqueous electrolytes and might even be specifically adsorbed at cathode materials with operating potentials close to the oxygen evolution reaction (OER), further promoting detrimental side reactions. Partial ligand exchange of CN^- or direct reaction of TM cations with the OH^- species has been discussed as drivers for the dissolution process. Such a degradation pathway in alkaline solutions can be proven by a complete transformation of nickel hexacyanoferrate (NiHCF) to insoluble NiO_x, indicating that iron is dissolved as the $Fe(CN)_6^{3/4-}$ complex.[41−44] Structural instability due to electrode swelling is probably of insignificant role in the case of PBAs since the lattice parameter was found to change only by less than 1% upon the insertion of guest ions into the hosting crystal structure.[42,45]

Regardless of the underlying mechanism and intermediate reaction steps, one can describe the dissolution of active material for the exemplary case of NiHCF, a well-studied PBA representative, by the following generic expressions

$$Na_2Ni[Fe(CN)_6] \rightleftarrows 2Na^+ + Ni^{2+} + [Fe(CN)_6]^{4-} \quad (1)$$

and

$$NaNi[Fe(CN)_6] \rightleftarrows Na^+ + Ni^{2+} + [Fe(CN)_6]^{3-} \quad (2)$$

It has been shown that the addition of transition-metal cations (such as Ni^{2+} in the case of NiHCF) into the electrolyte can shift the equilibrium toward the solid phase and extend the electrode lifetime.[46] Similarly, highly concentrated electrolytes, so-called "water-in-salt" systems, hugely impact the cycling stability of PBA electrodes.[13] In fact, the electrode material hydrolysis is suppressed through the absence of free water molecules due to its excessive incorporation in the salt ion solvation shells. Other stabilization approaches involve protective coatings, organic co-solvent electrolytes, and minimization of $Fe(CN)_6^{3/4-}$ crystal vacancies by optimized precipitation routines in the case of electrodes prepared from PBA nanoparticles.[47−53] Considering the previously discussed harmful role of OH^- on PBAs, acidification of the electrolyte toward pH ≈ 2 has furthermore proven to support the durability of such electrodes.[45,54]

Despite this variety of well-established stabilization measures, the underlying physicochemical mechanisms and governing electrolyte conditions driving the degradation of PBA electrodes remain unclear. Therefore, an innovative approach is employed in this study to investigate the dissolution of active material from PBA battery electrodes in detail. An electrochemical flow cell is coupled to a mass spectrometer, identifying and quantifying dissolved trace amounts of the examined material constituents and associating their respective leaching rates to the applied electrochemical conditions.[55−57] By applying this technique to an aqueous PBA system, this is one of the first experimental reports providing a direct *in operando*, time-resolved dissolution analysis of active material constituents in the context of battery research. NiHCF and cobalt hexacyanoferrate (CoHCF) are studied as model systems to gain relevant insights into PBAs' whole battery material class. Furthermore, several of the above-mentioned stabilization measures are screened for their effectiveness, with a particular focus on the role of the involved electrolyte anions. Finally, a tentative dissolution mechanism is proposed.

■ EXPERIMENTAL SECTION

Electrochemical Preparation and Characterization of Battery Electrodes. Electrochemical measurements were performed in a custom, argon-purged (5.0, Westfalen AG) glass setup with a three-electrode configuration. A Pt wire served as a counter electrode, and a Ag/AgCl (SSC, B3420+, SI Analytics) reference electrode was used.[15] A 1.37 cm^2 gold quartz crystal (in a QCM200 microbalance, AT-cut, Au on Ti adhesive layer, Stanford Research Systems) served as the substrate for electrodeposition of PBA films. A VSP-300 potentiostat with the associated software EC-Lab (Bio-Logic) was used to control and measure the electrode potentials and current.

Prior to the preparation of PBA electrodes, the Au substrates were rinsed with ultrapure water, cleaned using cyclic voltammetric (CV)

https://doi.org/10.1021/acsami.1c21219
ACS Appl. Mater. Interfaces 2022, 14, 3515−3525

ACS Applied Materials & Interfaces www.acsami.org Research Article

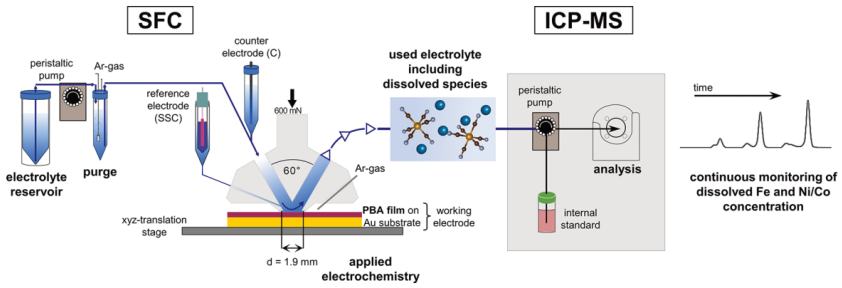

Figure 1. Schematic of the SFC ICP-MS setup. The electrolyte is pumped across the surface of the investigated PBA battery electrodes and is constantly analyzed for dissolved active material constituents. The respective leaching rates can be associated with the applied electrode potentials.

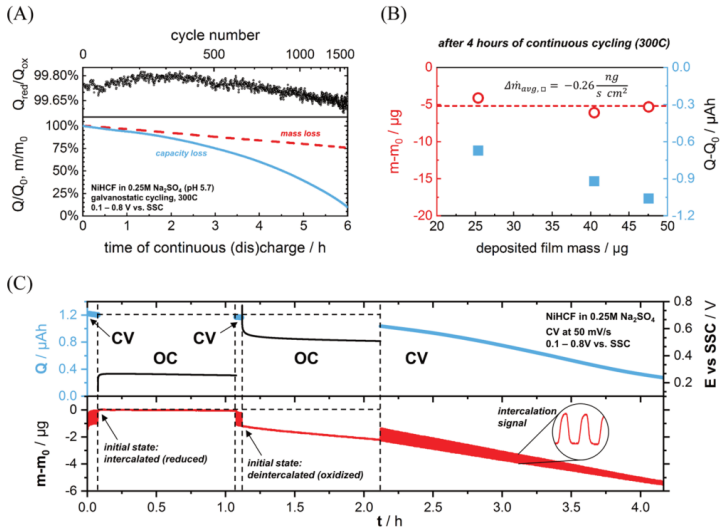

Figure 2. (A) Complete loss of capacity of NiHCF in 0.25 M Na_2SO_4 can be observed within less than 2000 consecutive galvanostatic cycles at 300C, whereas the film mass only drops by 25% at a constant rate with time. The elapsing time per cycle diminishes with decaying capacity due to the constant current technique, as represented in the upper *x*-axis. (B) Absolute mass loss after 4 h of continuous galvanostatic cycling at 300C does not correlate with the deposited NiHCF film mass, as indicated by the dashed horizontal line and corresponding average rate. However, the lost capacity increases for thicker films. (C) Active material dissolution and corresponding capacity loss happen mainly from oxidized NiHCF, whereas its reduced form remains stable during extended open-circuit periods. Electrochemical cycling (CV) accelerates the degradation process. The mass loss was determined by EQCM.

scans performed between 0 and 1.3 V vs SSC at 50 mV/s in 0.1 M H_2SO_4, and rinsed with ultrapure water again. PBA thin films were then electrodeposited following a similar routine adopted from refs 58, 59, cycling the working electrode (CV, 50 mV/s) in an aqueous precursor solution, consisting of 0.5 mM TM^{2+} ions (from $TMCl_2$ salts), 0.5 mM $K_3Fe(CN)_6$, and 0.25 M Na_2SO_4. TM^{2+} refers to Ni^{2+} in the case of NiHCF (potential boundaries for CV: 0–0.9 V vs SSC) and Co^{2+} in the case of CoHCF (potential boundaries for CV: −0.2 to 1.1 V vs SSC). After reaching the desired number of cycles, the process was stopped at the lower potential vertex, leaving the film in a fully intercalated (i.e., reduced) state. After disposing of the solution, the sample was washed with purged ultrapure water and dried under a continuous argon stream for at least 1 h.

Electrolytes and precursor solutions were prepared using ultrapure water (18.2 MΩ, Evoqua) and purged with argon gas for at least 10 min before being poured into the main cell of the described setup. If not stated otherwise, electrolytes were utilized without pH modification. A list of all chemicals and their suppliers can be found in Table S1.

Active Material Dissolution Study. Dissolution of PBA was studied in a custom-made electrochemical scanning flow cell (SFC) and tracked using an online inductively coupled plasma mass spectrometer (ICP-MS). A simplified scheme of the setup is shown in Figure 1. The involved electrolytes were purged with argon (5.0, Air Liquide) and pumped through the SFC across the PBA working electrode. A reference electrode (Ag/AgCl, Metrohm) was connected with a 0.4 mm channel close to the PBA surface, while a graphite rod (99.99, Sigma-Aldrich) acted as the counter electrode in the SFC electrolyte inlet. The electrolyte outlet was mixed in a 1:1 ratio with an internal standard and pumped to the ICP-MS (NexION 350X, PerkinElmer). To detect dissolved ^{56}Fe, the ICP-MS was operated in dynamic reaction cell mode using methane (5.0, Air Liquide), thus

https://doi.org/10.1021/acsami.1c21219
ACS Appl. Mater. Interfaces 2022, 14, 3515−3525

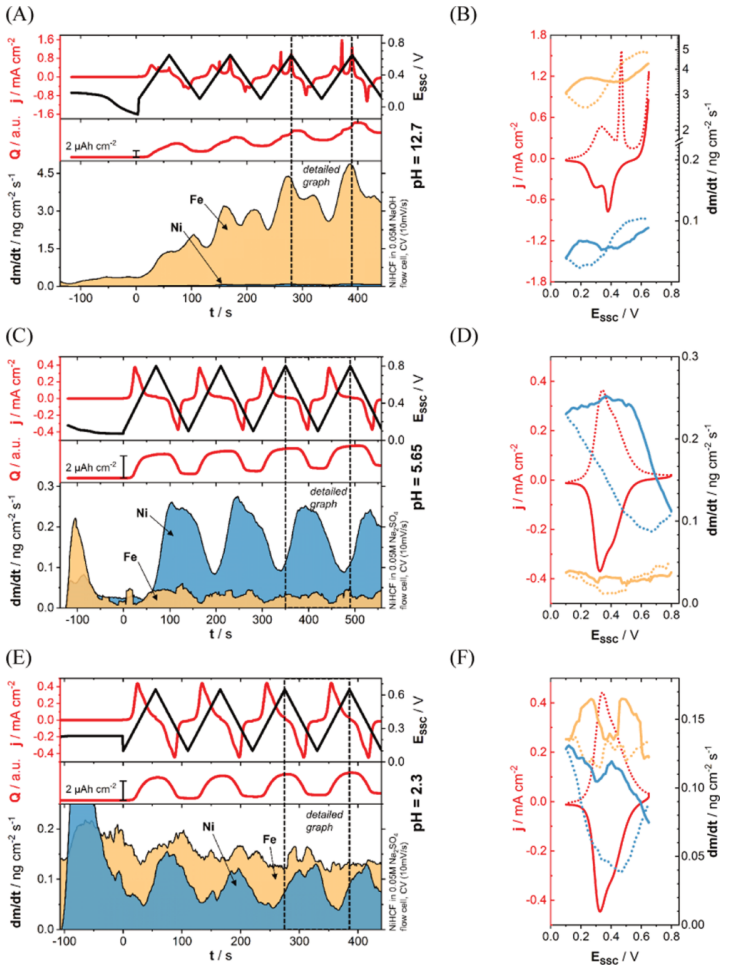

Figure 3. (A, C, E) *In operando* dissolution profiles for nickel and iron from NiHCF in the Na^+ electrolytes at varying pH during a 120 s OC period, followed by four CV cycles at 10 mV/s, as measured by the ICP-MS. (B, D, F) Dissolution rates and the ongoing electrochemical processes are correlated and shown for one exemplary cycle. The dotted curves correspond to the oxidation process, while the solid curves correspond to reduction during CVs.

eliminating the $^{40}Ar^{16}O$ interference. The ICP-MS was calibrated daily for Ni, Fe, and Co using a four-point calibration slope obtained from standard solutions (Centripur, Merck) containing 0, 0.5, 1, and 5 μg/L of each metal. As an internal standard, we used Ge (50 μg/L) to monitor the constant performance of the ICP-MS.

NiHCF and CoHCF, which were electrodeposited on gold-on-glass substrates (Arrandee Metal), were both investigated in alkaline (pH = 12.7), neutral (pH = 5.65), and acidic (pH = 2.3) conditions, following equal experimental sequences consisting of an initial 120 s open-circuit (OC) period, followed by four CV cycles at 10 mV/s. Na_2SO_4, which is a commonly used salt for ASIBs,[60] was chosen as the electrolyte, however, at a low concentration of 0.05 M due to compliance with the ICP analyzing unit. The pH of the electrolyte was adapted by adding sulfuric acid in the case of the acidic solution measurement, whereas pure NaOH was used in the alkaline case.

RESULTS AND DISCUSSION

The ability to be repetitively charged and discharged without loss of capacity is of utmost importance for any battery system. Of course, the exact load profile will critically impact the battery performance, and systems can even be tailored to specific applications. Galvanostatic cycling (i.e., constant current) at a high rate was mainly employed in this work to simulate long-term battery usage. Undoubtedly, uninterrupted superfast charging and discharging is far off any practical application but allows insights into the system's robustness under highly stressful conditions.

Long-term galvanostatic cycling was performed in 0.25 M Na_2SO_4 at 300C (12 s for complete charging or discharging)

https://doi.org/10.1021/acsami.1c21219
ACS Appl. Mater. Interfaces 2022, 14, 3515−3525

between 0.1 and 0.8 V vs SSC to examine benchmark stability of the NiHCF thin-film electrodes in aqueous electrolytes. As displayed in Figure 2A, a complete loss of capacity within 6 h of continuous cycling (1700 cycles) happening at an increasing rate indicates a severe degradation of the battery electrode. Since the (dis)charging current remains constant, each cycle passes faster and faster, which is represented in the upper cycle number axis. Furthermore, a linear mass loss at a constant rate with time was determined by EQCM, finally indicating *ca.* 75% remaining electrode material, which has lost any charge storage capability. A high coulombic efficiency of 99.6−99.8% was maintained throughout the measurement and was unaffected by the degradation progress.

The same disproportionate relation between capacity and mass loss was reproduced under similar conditions for different initially electrodeposited film masses of ∼25.4, ∼40.5, and ∼47.5 μg on the electrodes of a geometric surface area of 1.37 cm^2 (Figure 2B). Depending on the initial amount of active material, the capacity of all samples drops by an increasing absolute amount after 4 h of continuous (dis)charging at 300C, resulting in a similar relative loss of around 42% in each case. Interestingly, the amount of declined film mass is similar in absolute terms, allowing us to determine an average mass loss rate of −0.26 ng/(s cm^2). This constant mass-loss rate points toward an ongoing active material dissolution process as outlined in eqs 1 and 2. The resulting capacity fading is a commonly observed issue for PBA battery electrodes.[13,40,46] As apparent from Figure 2C, the dissolution of NiHCF appears to correlate with its oxidation state, as well as the electrochemical processes taking place. In its reduced form, no loss of active material and capacity could be observed during a period of 1 h at the open circuit conditions. In contrast, a continuous mass loss proceeds for the oxidized film at open-circuit, leading to a diminished capacity during the following cycling. The degradation process continues afterward during an extended cycling period over 2 h.

However, considering the specific capacity of NiHCF, the measured material depletion cannot solely be responsible for the observed inordinate extent of capacity fading. The electrode degradation can, in principle, occur through a continuous dissolution of active material from the electrode surface at a constant rate regardless of the initial film thickness and a disparately more substantial loss of absolute capacity with increasing rate. The latter process reflects an ongoing passivation of the remaining electrode material, which affects thicker films stronger, and diminishes their ability to intercalate Na^+ ions.

Although EQCM allows monitoring the mass of active material and (de)intercalating sodium ions during cycling for extended tests very robustly, its sensitivity cannot correlate the ongoing mass loss to the electrochemical potential and current within a single cycle (see Figure S1). This is due to both the small amount of dissolving film constituents (∼7 ng/cm^2 per cycle for 0.25 M Na_2SO_4, as calculated from the previously obtained rate) and the superimposed, significantly larger (de)intercalation signal. Furthermore, this technique can only determine the overall mass changes, neglecting the actual ratio of respective dissolution products. Therefore, a novel flow-cell setup with a highly sensitive online ICP-MS was employed in this work to overcome these drawbacks and systematically study the dissolution mechanism and detect trace concentrations of <0.1 ng/(s cm^2). The resolution in this experiment was 1.3 s. However, as the ICP-MS can only detect heavy elements properly, the analysis is restricted to the elemental transition metals from PBA materials, namely, Ni, Co, and Fe, in this study. Since the $Fe(CN)_6^{3/4-}$ complex is supposed to be highly stable, it is very likely dissolved as an entire complex, and therefore iron counts should directly translate into counts of the whole complex. "Iron" will therefore synonymously be used with the ferri/ferrocyanide.[39,41,61] As described above, the electrolyte pH significantly influences the stability of PBAs. Thus, the transition-metal dissolution profiles of NiHCF were recorded under alkaline, neutral, and acidic conditions during an initial electrode resting period and four CV cycles, as shown in Figure 3. Table 1 summarizes the corresponding integrated overall mass loss of the film constituents during the four CV cycles shown in Figure 3 compared to the total available amount of electrodeposited material.

Table 1. Cumulative Amount of Dissolved Nickel and Iron from NiHCF during the Four CV Cycles from Figure 3 for Each pH Compared to the Calculated Available Amount of the Respective Film Constituent as Obtained from the Electrodeposition[a]

dissolved mass (ng/cm^2)	pH = 2.3	pH = 5.65	pH = 12.7	total deposited mass of the film (ng/cm^2)
nickel	∼39	∼92	∼26	∼7766
iron	∼65	∼18	∼1204	∼7389

[a]It should be noted that Fe is considered without $(CN)_6$, and stoichiometry of $Na_2NiFe(CN)_6$ is assumed.

In general, the mass loss at pH = 12.7 (0.05 M NaOH) is caused by iron dissolution, which is on average 46 times larger than that of nickel (see Figure 3A and Table 1). It is well known that NiHCF is gradually transformed toward surface-confined NiO_x in the presence of abundant OH^-, which is represented by the excessive extraction of $[Fe(CN)_6]^{3/4-}$, as well as the appearance of the characteristic $Ni(OH)_2$/NiOOH peak and catalytically enhanced OER in the CV (Figure 3B).[42−44] The extraction mechanism of iron is believed to be catalyzed by OH^- adsorption at nickel sites on the crystal surface, and its rate will therefore scale with the corresponding implication on the $Fe(CN)_6$−Ni bond strength.[42] The dissolution of iron is maximal after the complete oxidation of the remaining NiHCF phases and reaches a minimum after reduction (Figure 3B). Accordingly, the adsorption of OH^- at surface nickel sites yields a fragile coexistence of distorted "$Fe^{II}(CN)_6$−Ni^{II}|···OH^-_{ads}", which is finally ruptured by oxidizing the iron centers (corresponding to Na^+ deintercalation) and leads to a simultaneous fixation of nickel and its adsorbate. The overall mechanism is schematically described by

$$Na_2Ni^{II}[Fe^{II}(CN)_6] + 2(OH^-) \rightarrow Na_2[Fe^{II}(CN)_6]Ni^{II}(OH^-)_2^{ads} \text{ (adsorption step)}$$

$$Na_2[Fe^{II}(CN)_6]Ni^{II}(OH^-)_2^{ads} \rightarrow Na^+ + e^- + Na[Fe^{III}(CN)_6]Ni^{II}(OH^-)_2^{ads} \text{ ($Fe^{II/III}$ oxidation step)}$$

https://doi.org/10.1021/acsami.1c21219
ACS Appl. Mater. Interfaces 2022, 14, 3515−3525

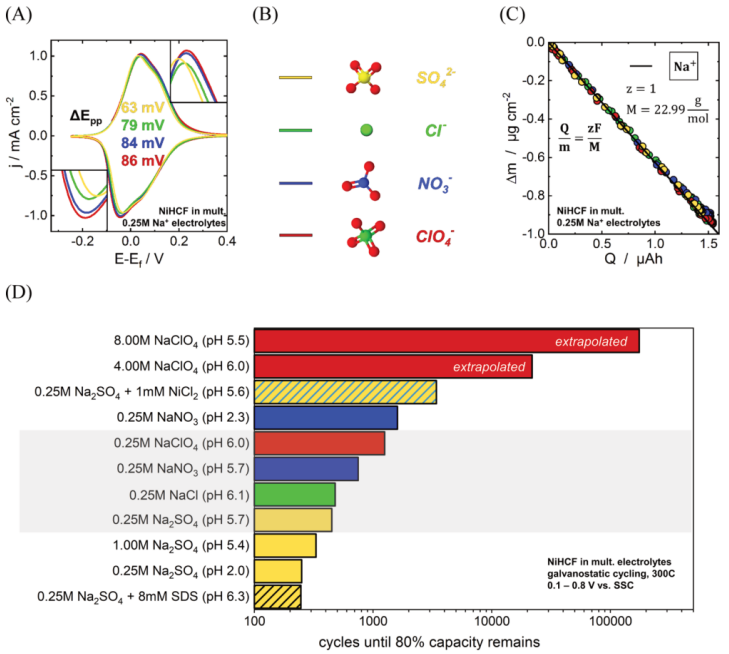

Figure 4. (A) Cyclic voltammograms and corresponding peak-to-peak separation values for NiHCF in 0.25 M Na_2SO_4, NaCl, $NaNO_3$, and $NaClO_4$ plotted vs the individual formal potentials. (B) Representation of the investigated anions. (C) Consumed charge during oxidation and reduction within one CV cycle vs the determined electrode mass change is used to calculate the apparent molar mass during the (de)intercalation process based on Faraday's law involving the transfer of one electron. (D) Stability of NiHCF during continuous galvanostatic cycling at 300C in several Na^+ electrolytes with varying anion species, concentration, pH, and additives. The values given for 4 and 8 M $NaClO_4$ are extrapolated based on the measured capacity losses of 2.6% after 2840 cycles and 1.2% after 10 500 cycles.

$$Na[Fe^{III}(CN)_6]Ni^{II}(OH^-)_2^{ads} \rightarrow Na^+ + [Fe^{III}(CN)_6]^{3-} + Ni^{II}(OH)_2$$

(dissolution and fixation step)

$$Ni^{II}(OH)_2 \rightleftarrows Ni^{III}OOH + H^+ + e^-$$

(reversible redox couple)

The accumulation of positive net charge upon cycling, as seen in the Q vs t curve in Figure 3A, furthermore reflects the dissolution of iron mainly after its oxidation toward $[Fe(CN)_6]^{3-}$ and an increasingly ongoing OER at the higher potential vertex.

Interestingly, the dissolution profile of nickel strictly follows that of iron, despite being much smaller in absolute terms. This collateral loss likely results from structural instabilities upon fast iron extraction since NiO_x is supposed to be highly stable at this pH.[56,62] The overall increase of the iron dissolution rate with proceeding time is probably caused by morphological changes due to the ongoing crystal transformation and emergence of NiO_x phases, which extends to ca. 16% after four CV cycles (see Table 1). This process yields a higher effective surface area, providing an increasing density of attack centers for OH^- adsorption on the remaining NiHCF phases. Finally, it should be mentioned that the iron dissolution profile is, besides its overall increase, not stationary, and another peak can be observed during the reduction of the electrode. In general, numerous other reaction pathways can be thought of, such as CN^- ligand exchange by OH^-.[13,40] The exact mechanisms could be further resolved by theoretical calculations on the involved binding strengths, solvation kinetics, and OH^- adsorption affinity. Since alkaline conditions have, however, proven to be very detrimental for PBAs as battery electrodes, such questions are beyond the scope of this study.

In contrast to the alkaline medium, the dissolution of nickel is much more pronounced than that of iron in the case of the close to neutral electrolyte at pH = 5.65 (see Figure 3C), with its average rate being 5 times higher (see Table 1). After an initial transient dissolution peak, once the electrode is brought into contact with the electrolyte, both rates exhibit a very repetitive and steady pattern. This was observed for all three electrolytes and is likely caused by an initial wash away of surface defects. Whereas the dissolution profile of iron does not exhibit a distinct course, the extraction of nickel strikingly correlates with the electrode current, as seen in Figure 3D. It suddenly increases upon the onset of reductive currents and is especially high throughout the entire reduction period. After switching the scanning direction toward oxidation, the dissolution rate continuously decreases, reaching a minimum in the fully oxidized state. At first glance, this conflicts with the

https://doi.org/10.1021/acsami.1c21219
ACS Appl. Mater. Interfaces 2022, 14, 3515−3525

findings by EQCM during extended resting periods, which showed a higher mass loss from the oxidized NiHCF. However, a decline of the open-circuit potential was observed during this measurement, indicating a parasitic reduction of the electrode (Figure 2C). Together with the findings from the flow cell, it can be followed that the active material dissolution is initiated by reductive processes. In general, the overall higher stability of NiHCF in neutral electrolytes compared to alkaline media is reflected in the presented results.

At pH = 2.3, the dissolution rate of nickel shows a similar trend to that in the neutral case (enhanced during reduction), whereas iron is leached from the electrode at a higher, rather constant level (see Figure 3E,F). The overall dissolution of iron is ∼1.6 times higher than nickel and 3.6 times higher than its leaching rate in the neutral electrolyte (see Table 1). Although a small amount of $Fe(CN)_6^{3/4-}$ vacancies is usually compensated with coordinated H_2O in PBA materials, an increasing extraction probably leads to quick crystal collapse and thereby accelerates the degradation process.[14,51] Since $Fe(CN)_6^{3/4-}$ is the redox-active species in NiHCF, its higher loss predicts lower capacity stability during battery operation in acidic electrolytes. However, this opposes the commonly employed method for stabilizing PBA electrodes *via* electrolyte acidification and will be discussed in a later section.

The obtained results for the dissolution of CoHCF were very similar to NiHCF (see Supporting Information, Figure S2, and Table S2), additionally showing an interesting double peak dissolution pattern associated with the two available redox steps of $Co^{II/III}$ and $Fe^{II/III}$ in CoHCF. In absolute terms, CoHCF showed to be less stable than NiHCF in neutral and acidic 0.05 M Na_2SO_4 electrolytes, and a similar transformation toward CoO_x was observed at a much faster rate in alkaline media in comparison to NiHCF. The presented results reflect an unequal constituent dissolution for $Ni^{2+}/Co^{2/3+}$ and $[Fe(CN)_6]^{3/4-}$ with a higher loss of the N-coordinated transition-metal cations, in correspondence to that previously reported for PBAs based on *ex situ* electrolyte analyses.[33,35]

Both NiHCF and CoHCF showed an increased dissolution rate of Ni and Co cations during the electrode reduction (=intercalation) under conditions relevant for PBA battery operation (neutral to acidic). At first glance, this might point toward a mechanically induced mechanism initiated by lattice strain due to Na^+ insertion into the crystal structure. However, this mechanism cannot explain the observed pH dependence of the leaching rates. In fact, considering the previously discussed OH^--induced dissolution mechanism, even higher stability would be expected for acidic conditions. As an opposite behavior was found in the previously presented flow-cell study for NiHCF and CoHCF in pH-adjusted Na_2SO_4, the possible role of electrolyte anions was further investigated. It has been presented by Ventosa et al.[58] and Yun et al.[59] that intermediary anion adsorption plays an important role in the intercalation mechanism in PBAs and many other battery materials.[63] They proposed that the net surface charge evolving from the quick electron transfer reaction (e.g., oxidation) within the solid electrode material needs to be compensated by electrolyte anions through specific adsorption until desorbing again with the slow expulsion of intercalated species (three-step mechanism). Thereby, the efficient ad/desorption of anions strongly contributes to the electrochemical reversibility of the de/intercalation reaction, as seen from the CV curves in Figure 4A for NiHCF in Na_2SO_4, NaCl, $NaNO_3$, and $NaClO_4$. The respectively obtained peak-to-peak separation (ΔE_{pp}), which is a measure of impaired reaction kinetics, increases in the order $SO_4^{2-} < Cl^- < NO_3^- < ClO_4^-$ (Figure 4B). This indicates a less efficient intermediary specific adsorption of ClO_4^- in comparison to SO_4^{2-}, revealing an opposite trend for the adsorption strength of the involved anions. Similar results were reported for PBA materials in the literature.[59,64] In general, the strength of anion adsorption is reflected by many parameters, such as the respective enthalpy of hydration and interaction energies, potential of zero charge (PZC), ion size, symmetry, and charge density.[65,66] However, especially sulfates are known as very strong adsorbents, whereas perchlorate is expected to only weakly adsorb on metal surfaces.[67] The NiHCF electrode is operated at potentials more positive than its PZC, which was determined to be in the vicinity of −0.13 V vs SSC by the laser-induced current transient technique.[68] Therefore, the positive excess surface charge probably leads to high coverage with strongly adsorbing Cl^- and SO_4^{2-} anions, especially during oxidation of the film.[69]

Figure 4C correlates the transferred charge from the cyclic voltammograms with the corresponding mass change of the NiHCF electrode, as measured by EQCM. Considering a single electron transfer redox process, the apparent molar mass of the species transported across the electrode−electrolyte interface can be calculated using Faraday's law. The obtained values confirm a "pure", highly reversible Na^+ (de)-intercalation, regardless of the employed electrolyte anion. Although the latter seems to be inevitable to foster the (de)intercalation mechanism in PBA materials, they do not participate in the overall compensation of NiHCF redox charges.

As introduced above, the cycling stability of PBAs can usually be tuned by varying the electrolyte pH, concentration, and additives. However, the influence of specific anions on the degradation speed has so far only rarely been considered. Since NiHCF showed higher overall

stability compared to CoHCF, the following study on the electrode stability in different electrolytes will focus on this PBA material. Figure 4D shows the obtained number of consecutive galvanostatic fast charge and discharge cycles at 300C for NiHCF thin-film electrodes in a series of Na^+ electrolytes until 80% of the initial capacity remains. The promoting effect of SO_4^{2-} and Cl^- in comparison to NO_3^- and ClO_4^- on the intercalation mechanism is not reflected in the electrode stability in the respective electrolytes at an equal concentration of 0.25 M and similar rather neutral pH (gray highlighted area). Especially sulfate (yellow) and chloride (green), as the strongest involved adsorbing anions, show the worst stabilities of only 450 and 480 cycles, respectively, whereas the weaker adsorbing nitrate (blue) and perchlorate (red) seem to have a less detrimental effect on the electrode stability with 750 and 1250 cycles for 20% capacity loss.

Since it was shown above that film constituent dissolution processes trigger the degradation of PBAs, this finding shows that the dissolution mechanism is highly accelerated by the affinity of the involved anion to adsorb (chemisorb) on the electrode surface specifically. The lowest overall recorded stability of only ca. 246 cycles was obtained for 0.25 M Na_2SO_4 with 8 mM $NaSO_4C_{12}H_{25}$ (sodium dodecyl sulfate, SDS). This highly polar additive is usually considered a surfactant, providing an even stronger affinity for specific adsorption regardless of its small amount. A similar effect is observed by increasing the concentration of Na_2SO_4 to 1 M, which can be explained analogously by the higher activity of sulfate anions.

https://doi.org/10.1021/acsami.1c21219
ACS Appl. Mater. Interfaces 2022, 14, 3515−3525

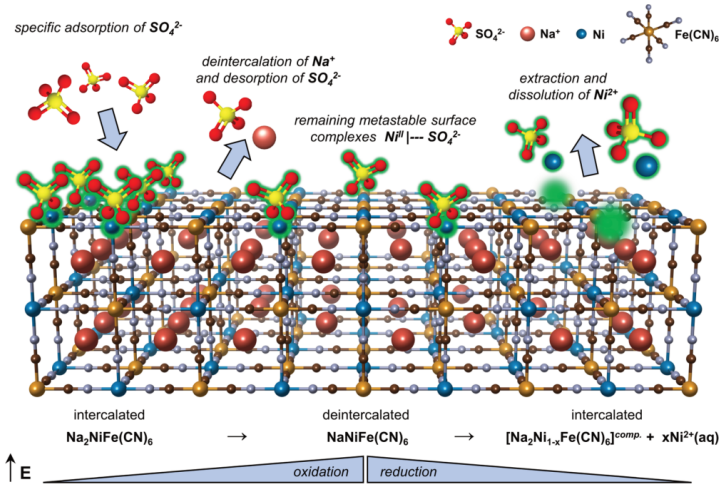

Figure 5. Anion adsorption and electrode dissolution scheme for NiHCF in Na_2SO_4 at neutral pH (atoms). Water molecules are omitted for clarity.

In contrast, the electrode lifetime is extended by a factor of more than 7 times by adding a small amount of Ni^{2+} cations to the considerably underperforming 0.25 M Na_2SO_4. Since the herein-reported real-time dissolution results identified the leaching of the N-coordinated transition metal as the driving force for PBA electrode degradation, the efficiency of this well-known stabilization measure is eventually anticipated.[46,47] Highly concentrated 4 and 8 M $NaClO_4$ yielded a negligible loss of 2.6% after 2840 cycles and 1.2% after 10 500 cycles at 300C, which can be correlated to the low affinity of perchlorate for specific adsorption, and the low uptake capability of the solvent for further dissolving film constituents due to the lack of excess H_2O. These remarkably high stabilities are in good agreement with the literature[13] and were extrapolated for Figure 4D according to the linear loss regime between 100 and 80% (see Figure 2A). In addition, the electrode was tested at lower rates from 100C to 3C in 8 M $NaClO_4$. As seen in Figure S3, the entire fractional capacity can be maintained during 100 cycles at each investigated rate without significant losses. It can therefore be concluded that this electrolyte efficiently prevents the degradation of the electrode, and a long calendar lifetime should be expectable.

Furthermore, acidification of the electrolyte to pH = 2.3 helped to more than double the lifetime of NiHCF in 0.25 M $NaNO_3$ towards 1600 cycles. Considering the low adsorption affinity of nitrate, prevention of the usual OH^--induced dissolution mechanism serves as an effective strategy to stabilize PBA materials.

In contrast, a lowered pH = 2 even impaired the stability in 0.25 M Na_2SO_4 toward 250 cycles, which agrees with the higher dissolution rates recorded during the flow-cell experiments presented above. Apparently, the detrimental chemisorption of SO_4^{2-} seems to be enhanced in the presence of H_3O^+, which corresponds to similar results obtained from soil mineral studies.[70] Although the reason for the enhanced sulfate adsorption at a lowered pH is not entirely clear yet, this finding further highlights the particular role of sulfate in comparison to other anions.

■ CONCLUSIONS

This work showed that the degradation of PBA battery electrodes is driven by active material dissolution. As demonstrated by an innovative flow-cell technique, the respective constituent leaching rates are strongly coupled to the redox activity of the electrode. The transformation of NiHCF and CoHCF to their respective TM oxides was related to the almost complete loss of iron in the case of alkaline electrolytes. Nickel and cobalt cations were mainly extracted during reduction under neutral and acidic conditions, with CoHCF being less stable than NiHCF during cycling in Na_2SO_4. The absolute values of dissolving nickel and cobalt exceeded those for iron under the battery-operation relevant neutral conditions, proving that the N-coordinated transition metals constitute the centers of attack for the degradation mechanism of PBAs.

Based on these findings, a tentative dissolution mechanism of PBA active material is schematically proposed in Figure 5 for the aqueous NiHCF–Na_2SO_4 model system, considering realistic battery conditions of neutral pH. During the electrochemical oxidation of the electrode, sulfate anions specifically adsorb on the surface to promote the deintercalation process of Na^+ ions. However, since the electrode is charged to potentials much more positive than the PZC, some of the specifically adsorbed anions remain on the surface to compensate for its excess charge and form metastable surface complexes, preferably at the positively charged nickel sites ($Ni^{II}\cdots SO_4^{2-}$). Upon the following reduction of the corresponding iron centers and the insertion of Na^+ ions into the crystal, the distorted $Fe(CN)_6$–$Ni(SO_4^{2-})^{ads}$ bond breaks and leads to the dissolution of Ni^{2+} into the electrolyte. Since electrolyte anions induce this dissolution mechanism, the degradation rate correlates with the respective chemisorption affinity. This sufficiently explains the noticeable differences in

https://doi.org/10.1021/acsami.1c21219
ACS Appl. Mater. Interfaces 2022, 14, 3515−3525

the cycling stability of NiHCF in $NaClO_4$, $NaNO_3$, NaCl, and Na_2SO_4 at equal concentrations and similar pH values. Although the nature of the involved anion strongly influences the kinetics of the (de)intercalation process, its impact on electrode stability can not be neglected. The intermediary adsorbed anions should bind "just right" to foster the (dis)charging reaction while not deteriorating the $Fe(CN)_6$–TM bonds. Therefore, $NaClO_4$ is considered a beneficial choice for aqueous battery electrolytes involving PBA materials, whereas sulfates should be avoided. Based on the consistent findings from the flow-cell-coupled ICP-MS for NiHCF and CoHCF, this mechanism probably plays an important role for transition-metal dissolution within the whole class of PBA materials. However, the overall lower stability of CoHCF might be related to lattice distortions associated with the additional $Co^{II/III}$ redox step.

It should be mentioned that the described mechanism happens statistically across the surface and is only exemplarily depicted in Figure 5. Of course, other reaction pathways during the degradation process can not be excluded, and further approaches like computational methods might be necessary to shed light on the overall composition of detrimental processes happening at the electrode–electrolyte interface. Yet, the fading capacity cannot be solely caused by active material dissolution since a high share of the initial mass loading remains on the electrode, however not showing any redox activity after all. This effect will be investigated in future studies. However, the presented flow-cell technique has been shown to provide direct access to the active material dissolution and proved to be a powerful tool for future battery research. Even though the herein performed dissolution study is unaware of long-term trends, the technique can be easily adapted to investigate the constituent dissolution profiles during more realistic battery operation scenarios like galvanostatic and potentiostatic (dis)charging profiles at varying rates and extended resting periods.

■ ASSOCIATED CONTENT

Supporting Information

The Supporting Information is available free of charge at https://pubs.acs.org/doi/10.1021/acsami.1c21219.

Time-resolved QCM data during cycling, dissolution profiles for CoHCF, and stability of NiHCF in 8 M $NaClO_4$ at low cycling rates (PDF)

■ AUTHOR INFORMATION

Corresponding Authors

Serhiy Cherevko – *Helmholtz Institute Erlangen-Nürnberg for Renewable Energy, Forschungszentrum Jülich GmbH, 91058 Erlangen, Germany;* orcid.org/0000-0002-7188-4857; Email: s.cherevko@fz-juelich.de

Aliaksandr S. Bandarenka – *Physics of Energy Conversion and Storage, Physik-Department, Technische Universität München, 85748 Garching bei München, Germany;* orcid.org/0000-0002-5970-4315; Email: bandarenka@ph.tum.de

Authors

Xaver Lamprecht – *Physics of Energy Conversion and Storage, Physik-Department, Technische Universität München, 85748 Garching bei München, Germany*

Florian Speck – *Helmholtz Institute Erlangen-Nürnberg for Renewable Energy, Forschungszentrum Jülich GmbH, 91058 Erlangen, Germany*

Philipp Marzak – *Physics of Energy Conversion and Storage, Physik-Department, Technische Universität München, 85748 Garching bei München, Germany;* orcid.org/0000-0003-3372-0816

Complete contact information is available at: https://pubs.acs.org/10.1021/acsami.1c21219

Notes

The authors declare no competing financial interest.

■ ACKNOWLEDGMENTS

Financial support from the German Research Foundation (DFG) under Germany's Excellence Strategy—EXC 2089/1-390776260, cluster of excellence "e-conversion" is gratefully acknowledged.

■ REFERENCES

(1) Schellnhuber, H. J.; Rahmstorf, S.; Winkelmann, R. Why the right climate target was agreed in Paris. *Nat. Clim. Change* **2016**, *6*, 649–653.

(2) Gallo, A. B.; Simões-Moreira, J. R.; Costa, H. K. M.; Santos, M. M.; dos Santos, E. M. Energy storage in the energy transition context: A technology review. *Renewable Sustainable Energy Rev.* **2016**, *65*, 800–822.

(3) Kittner, N.; Lill, F.; Kammen, D. M. Energy storage deployment and innovation for the clean energy transition. *Nat. Energy* **2017**, *2*, No. 17125.

(4) Vesborg, P. C.; Jaramillo, T. F. Addressing the terawatt challenge: scalability in the supply of chemical elements for renewable energy. *RSC Adv.* **2012**, *2*, 7933–7947.

(5) Choi, J. W.; Aurbach, D. Promise and reality of post-lithium-ion batteries with high energy densities. *Nat. Rev. Mater.* **2016**, *1*, No. 16013.

(6) Huang, B.; Pan, Z.; Su, X.; An, L. Recycling of lithium-ion batteries: Recent advances and perspectives. *J. Power Sources* **2018**, *399*, 274–286.

(7) Vaalma, C.; Buchholz, D.; Weil, M.; Passerini, S. A cost and resource analysis of sodium-ion batteries. *Nat. Rev. Mater.* **2018**, *3*, No. 18013.

(8) Hwang, J. Y.; Myung, S. T.; Sun, Y. K. Sodium-ion batteries: present and future. *Chem. Soc. Rev.* **2017**, *46*, 3529–3614.

(9) Wang, Q.; Mao, B.; Stoliarov, S. I.; Sun, J. A review of lithium ion battery failure mechanisms and fire prevention strategies. *Prog. Energy Combust. Sci.* **2019**, *73*, 95–131.

(10) Bin, D.; Wang, F.; Tamirat, A. G.; Suo, L.; Wang, Y.; Wang, C.; Xia, Y. Progress in aqueous rechargeable sodium-ion batteries. *Adv. Energy Mater.* **2018**, *8*, No. 1703008.

(11) Kim, H.; Hong, J.; Park, K. Y.; Kim, H.; Kim, S. W.; Kang, K. Aqueous rechargeable Li and Na ion batteries. *Chem. Rev.* **2014**, *114*, 11788–11827.

(12) Wang, B.; Han, Y.; Wang, X.; Bahlawane, N.; Pan, H.; Yan, M.; Jiang, Y. Prussian blue analogs for rechargeable batteries. *iScience* **2018**, *3*, 110–133.

(13) Pasta, M.; Wessells, C. D.; Liu, N.; Nelson, J.; McDowell, M. T.; Huggins, R. A.; Cui, Y.; et al. Full open-framework batteries for stationary energy storage. *Nat. Commun.* **2014**, *5*, No. 3007.

(14) Hurlbutt, K.; Wheeler, S.; Capone, I.; Pasta, M. Prussian Blue Analogs as battery materials. *Joule* **2018**, *2*, 1950–1960.

(15) Marzak, P.; Moser, P.; Schreier, S.; Scieszka, D.; Yun, J.; Schneider, O.; Bandarenka, A. S. A cell for controllable formation and in operando electrochemical characterization of intercalation materials for aqueous metal-ion batteries. *Small Methods* **2019**, *3*, No. 1900445.

https://doi.org/10.1021/acsami.1c21219
ACS Appl. Mater. Interfaces 2022, 14, 3515–3525

(16) Poullikkas, A. A comparative overview of large-scale battery systems for electricity storage. *Renewable Sustainable Energy Rev.* **2013**, *27*, 778−788.
(17) Edge, J. S.; O'Kane, S.; Prosser, R.; Kirkaldy, N. D.; Patel, A. N.; Hales, A.; Offer, G. J.; et al. Lithium ion battery degradation: what you need to know. *Phys. Chem. Chem. Phys.* **2021**, *23*, 8200−8221.
(18) Arora, P.; White, R. E.; Doyle, M. Capacity fade mechanisms and side reactions in lithium-ion batteries. *J. Electrochem. Soc.* **1998**, *145*, 3647.
(19) Vetter, J.; Novák, P.; Wagner, M. R.; Veit, C.; Möller, K. C.; Besenhard, J. O.; Hammouche, A. Ageing mechanisms in lithium-ion batteries. *J. Power Sources* **2005**, *147*, 269−281.
(20) Hausbrand, R.; Cherkashinin, G.; Ehrenberg, H.; Gröting, M.; Albe, K.; Hess, C.; Jaegermann, W. Fundamental degradation mechanisms of layered oxide Li-ion battery cathode materials: Methodology, insights and novel approaches. *Mater. Sci. Eng. B* **2015**, *192*, 3−25.
(21) Solchenbach, S.; Hong, G.; Freiberg, A. T. S.; Jung, R.; Gasteiger, H. A. Electrolyte and SEI decomposition reactions of transition metal ions investigated by on-line electrochemical mass spectrometry. *J. Electrochem. Soc.* **2018**, *165*, A3304.
(22) Zheng, H.; Sun, Q.; Liu, G.; Song, X.; Battaglia, V. S. Correlation between dissolution behavior and electrochemical cycling performance for $LiNi_{1/3}Co_{1/3}Mn_{1/3}O_2$-based cells. *J. Power Sources* **2012**, *207*, 134−140.
(23) Amine, K.; Chen, Z.; Zhang, Z.; Liu, J.; Lu, W.; Qin, Y.; Sun, Y. K.; et al. Mechanism of capacity fade of MCMB/$Li_{1.1}[Ni_{1/3}Mn_{1/3}Co_{1/3}]_{0.9}O_2$ cell at elevated temperature and additives to improve its cycle life. *J. Mater. Chem.* **2011**, *21*, 17754−17759.
(24) Lee, Y. K.; Park, J.; Lu, W. A comprehensive experimental and modeling study on dissolution in Li-ion batteries. *J. Electrochem. Soc.* **2019**, *166*, A1340.
(25) Berkes, B. B.; Jozwiuk, A.; Vračar, M.; Sommer, H.; Brezesinski, T.; Janek, J. Online continuous flow differential electrochemical mass spectrometry with a realistic battery setup for high-precision, long-term cycling tests. *Anal. Chem.* **2015**, *87*, 5878−5883.
(26) Strehle, B.; Solchenbach, S.; Metzger, M.; Schwenke, K. U.; Gasteiger, H. A. The effect of CO_2 on alkyl carbonate trans-esterification during formation of graphite electrodes in Li-ion batteries. *J. Electrochem. Soc.* **2017**, *164*, A2513.
(27) Jung, R.; Linsenmann, F.; Thomas, R.; Wandt, J.; Solchenbach, S.; Maglia, F.; Gasteiger, H. A.; et al. Nickel, manganese, and cobalt dissolution from Ni-rich NMC and their effects on NMC622-graphite cells. *J. Electrochem. Soc.* **2019**, *166*, A378.
(28) Wandt, J.; Freiberg, A.; Thomas, R.; Gorlin, Y.; Siebel, A.; Jung, R.; Tromp, M.; et al. Transition metal dissolution and deposition in Li-ion batteries investigated by operando X-ray absorption spectroscopy. *J. Mater. Chem. A* **2016**, *4*, 18300−18305.
(29) Hou, J.; Freiberg, A.; Shen, T. H.; Girod, R.; Gonthier, J.; Kim, S. J.; Tileli, V. Charge/discharge cycling of $Li_{1+x}(Ni_{0.6}Co_{0.2}Mn_{0.2})_{1-x}O_2$ primary particles performed in a liquid microcell for transmission electron microscopy studies. *J. Phys.: Energy* **2020**, *2*, No. 034007.
(30) Wang, L. F.; Ou, C. C.; Striebel, K. A.; Chen, J. S. Study of Mn Dissolution from $LiMn_2O_4$ Spinel Electrodes Using Rotating Ring-Disk Collection Experiments. *J. Electrochem. Soc.* **2003**, *150*, A905.
(31) Lopes, P. P.; Zorko, M.; Hawthorne, K. L.; Connell, J. G.; Ingram, B. J.; Strmcnik, D.; Markovic, N. M.; et al. Real-time monitoring of cation dissolution/deintercalation kinetics from transition-metal oxides in organic environments. *J. Phys. Chem. Lett.* **2018**, *9*, 4935−4940.
(32) Nikman, S.; Zhao, D.; Gonzalez-Perez, V.; Hoster, H. H.; Mertens, S. F. Surface or bulk? Real-time manganese dissolution detection in a lithium-ion cathode. *Electrochim. Acta* **2021**, *386*, No. 138373.
(33) Kasiri, G.; Trócoli, R.; Hashemi, A. B.; La Mantia, F. An electrochemical investigation of the aging of copper hexacyanoferrate during the operation in zinc-ion batteries. *Electrochim. Acta* **2016**, *222*, 74−83.
(34) Zhang, L.; Chen, L.; Zhou, X.; Liu, Z. Towards high-voltage aqueous metal-ion batteries beyond 1.5 V: the zinc/zinc hexacyanoferrate system. *Adv. Energy Mater.* **2015**, *5*, No. 1400930.
(35) Lee, J. H.; Ali, G.; Kim, D. H.; Chung, K. Y. Metal-organic framework cathodes based on a vanadium hexacyanoferrate Prussian blue analogue for high-performance aqueous rechargeable batteries. *Adv. Energy Mater.* **2017**, *7*, No. 1601491.
(36) Hou, Z.; Zhang, X.; Li, X.; Zhu, Y.; Liang, J.; Qian, Y. Surfactant widens the electrochemical window of an aqueous electrolyte for better rechargeable aqueous sodium/zinc battery. *J. Mater. Chem. A* **2017**, *5*, 730−738.
(37) Rai, D.; Felmy, A. R.; Smith, S. C.; Ryan, J. L. *Solubility of Ferrocyanide Compounds. Ferrocyanide Safety Project, Interim Report FY1994 No. PNL-10150*; Pacific Northwest Laboratory: Richland, WA, 1994.
(38) Shao, T.; Li, C.; Liu, C.; Deng, W.; Wang, W.; Xue, M.; Li, R. Electrolyte regulation enhances the stability of Prussian Blue Analogues in aqueous Na-ion storage. *J. Mater. Chem. A* **2019**, *7*, 1749−1755.
(39) Yang, Y.; Brownell, C.; Sadrieh, N.; May, J.; Del Grosso, A.; Place, D.; Faustino, P.; et al. Quantitative measurement of cyanide released from Prussian Blue. *Clin. Toxicol.* **2007**, *45*, 776−781.
(40) Stilwell, D. E.; Park, K. H.; Miles, M. H. Electrochemical studies of the factors influencing the cycle stability of Prussian Blue films. *J. Appl. Electrochem.* **1992**, *22*, 325−331.
(41) Mimura, H.; Lehto, J.; Harjula, R. Chemical and thermal stability of potassium nickel hexacyanoferrate (II). *J. Nucl. Sci. Technol.* **1997**, *34*, 582−587.
(42) Marzak, P.; Yun, J.; Dorsel, A.; Kriele, A.; Gilles, R.; Schneider, O.; Bandarenka, A. S. Electrodeposited $Na_2Ni[Fe(CN)_6]$ thin-film cathodes exposed to simulated aqueous Na-ion battery conditions. *J. Phys. Chem. C* **2018**, *122*, 8760−8768.
(43) Cataldi, T. R.; Guascito, R.; Salvi, A. M. XPS study and electrochemical behaviour of the nickel hexacyanoferrate film electrode upon treatment in alkaline solutions. *J. Electroanal. Chem.* **1996**, *417*, 83−88.
(44) Chen, S. M.; Liou, C. Y.; Thangamuthu, R. Preparation and characterization of mixed-valent nickel oxide/nickel hexacyanoferrate hybrid films and their electrocatalytic properties. *Electroanalysis* **2007**, *19*, 2457−2464.
(45) Wessells, C. D.; Peddada, S. V.; Huggins, R. A.; Cui, Y. Nickel hexacyanoferrate nanoparticle electrodes for aqueous sodium and potassium ion batteries. *Nano Lett.* **2011**, *11*, 5421−5425.
(46) Wang, R. Y.; Wessells, C. D.; Huggins, R. A.; Cui, Y. Highly reversible open framework nanoscale electrodes for divalent ion batteries. *Nano Lett.* **2013**, *13*, 5748−5752.
(47) Wessells, C. D.; Huggins, R. A. Stabilization of Battery Electrodes. U.S. Patent US9,130,234B22015.
(48) Wessells, C. D.; Motallebi, S. Electrolyte Additives for Electrochemical Devices. U.S. Patent US10,862,168B22020.
(49) Wessells, C. D.; Firouzi, A.; Motallebi, S.; Strohband, S. Cosolvent Electrolytes for Electrochemical Devices. U.S. Patent US9,893,3822B2018.
(50) Firouzi, A.; Qiao, R.; Motallebi, S.; Valencia, C. W.; Israel, H. S.; Fujimoto, M.; Wessells, C. D.; et al. Monovalent manganese based anodes and co-solvent electrolyte for stable low-cost high-rate sodium-ion batteries. *Nat. Commun.* **2018**, *9*, No. 861.
(51) Wu, X.; Sun, M.; Guo, S.; Qian, J.; Liu, Y.; Cao, Y.; Yang, H.; et al. Vacancy-Free Prussian Blue Nanocrystals with High Capacity and Superior Cyclability for Aqueous Sodium-Ion Batteries. *ChemNanoMat* **2015**, *1*, 188−193.
(52) Wu, X.; Wu, C.; Wei, C.; Hu, L.; Qian, J.; Cao, Y.; Yang, H.; et al. Highly crystallized $Na_2CoFe(CN)_6$ with suppressed lattice defects as superior cathode material for sodium-ion batteries. *ACS Appl. Mater. Interfaces* **2016**, *8*, 5393−5399.
(53) Wang, X.; Wang, B.; Tang, Y.; Xu, B. B.; Liang, C.; Yan, M.; Jiang, Y. Manganese hexacyanoferrate reinforced by PEDOT coating towards high-rate and long-life sodium-ion battery cathode. *J. Mater. Chem. A* **2020**, *8*, 3222−3227.

https://doi.org/10.1021/acsami.1c21219
ACS Appl. Mater. Interfaces 2022, 14, 3515−3525

(54) Wessells, C. D.; Huggins, R. A.; Cui, Y. Copper hexacyanoferrate battery electrodes with long cycle life and high power. *Nat. Commun.* **2011**, *2*, No. 550.
(55) Kasian, O.; Geiger, S.; Mayrhofer, K. J.; Cherevko, S. Electrochemical on-line ICP-MS in electrocatalysis research. *Chem. Rec.* **2019**, *19*, 2130−2142.
(56) Davydova, E. S.; Speck, F. D.; Paul, M. T.; Dekel, D. R.; Cherevko, S. Stability limits of Ni-based hydrogen oxidation electrocatalysts for anion exchange membrane fuel cells. *ACS Catal.* **2019**, *9*, 6837−6845.
(57) Speck, F. D.; Zagalskaya, A.; Alexandrov, V.; Cherevko, S. Periodicity in the electrochemical dissolution of transition metals. *Angew. Chem., Int. Ed.* **2021**, *60*, 13343−13349.
(58) Ventosa, E.; Paulitsch, B.; Marzak, P.; Yun, J.; Schiegg, F.; Quast, T.; Bandarenka, A. S. The mechanism of the interfacial charge and mass transfer during intercalation of alkali metal cations. *Adv. Sci.* **2016**, 3, No. 1600211.
(59) Yun, J.; Pfisterer, J.; Bandarenka, A. S. How simple are the models of Na intercalation in aqueous media? *Energy Environ. Sci.* **2016**, *9*, 955−961.
(60) Bin, D.; Wang, F.; Tamirat, A. G.; Suo, L.; Wang, Y.; Wang, C.; Xia, Y. Progress in aqueous rechargeable sodium-ion batteries. *Adv. Energy Mater.* **2018**, *8*, No. 1703008.
(61) Meeussen, J. C.; Keizer, M. G.; De Haan, F. A. Chemical stability and decomposition rate of iron cyanide complexes in soil solutions. *Environ. Sci. Technol.* **1992**, *26*, 511−516.
(62) Pourbaix, M. *Atlas of Electrochemical Equilibria in Aqueous Solutions*; National Association of Corrosion Engineers, 1974; p 330.
(63) Gaddam, R.; Katzenmeier, L.; Lamprecht, X.; Bandarenka, A. Review on physical impedance models in modern battery research. *Phys. Chem. Chem. Phys.* **2021**, *23*, 12926−12944.
(64) Pournaghi-Azar, M. H.; Nahalparvari, H. Electroless preparation and electrochemical behavior of a platinum-doped nickel hexacyanoferrate film−zinc modified electrode: catalytic ability of the electrode for electrooxidation of methanol. *J. Solid State Electrochem.* **2004**, *8*, 550−557.
(65) Conway, B. E. The solvation factor in specificity of ion adsorption at electrodes. *Electrochim. Acta* **1995**, *40*, 1501−1512.
(66) Wendt, H.; Riemenschneider, P. Ionenadsorption an Elektroden in wässrigen und nichtwässrigen Elektrolyten. *Chem. Ing. Tech.* **1978**, *50*, 250−258.
(67) Kasuya, M.; Sogawa, T.; Masuda, T.; Kamijo, T.; Uosaki, K.; Kurihara, K. Anion adsorption on gold electrodes studied by electrochemical surface forces measurement. *J. Phys. Chem. C* **2016**, *120*, 15986−15992.
(68) Scieszka, D.; Yun, J.; Bandarenka, A. S. What do laser-induced transient techniques reveal for batteries? Na-and K-Intercalation from aqueous electrolytes as an example. *ACS Appl. Mater. Interfaces* **2017**, *9*, 20213−20222.
(69) Malik, M. A.; Horanyi, G.; Kulesza, P. J.; Inzelt, G.; Kertesz, V.; Schmidt, R.; Czirok, E. Microgravimetric monitoring of transport of cations during redox reactions of indium (III) hexacyanoferrate (III, II): Radiotracer evidence for the flux of anions in the film. *J. Electroanal. Chem.* **1998**, *452*, 57−62.
(70) Sokolova, T. A.; Alekseeva, S. A. Adsorption of sulfate ions by soils (a review). *Eurasian Soil Sci.* **2008**, *41*, 140−148.

https://doi.org/10.1021/acsami.1c21219
ACS Appl. Mater. Interfaces 2022, 14, 3515−3525

Mechanisms of degradation of $Na_2Ni[Fe(CN)_6]$ functional electrodes in aqueous media: a combined theoretical and experimental study.

The Journal of Physical Chemistry C **2023**, *127*(5), 2204–2214.

THE JOURNAL OF PHYSICAL CHEMISTRY C
A JOURNAL OF THE AMERICAN CHEMICAL SOCIETY

pubs.acs.org/JPCC Article

Mechanisms of Degradation of $Na_2Ni[Fe(CN)_6]$ Functional Electrodes in Aqueous Media: A Combined Theoretical and Experimental Study

Xaver Lamprecht, Iman Evazzade, Iago Ungerer, Ludek Hromadko, Jan M. Macak, Aliaksandr S. Bandarenka,* and Vitaly Alexandrov*

Cite This: *J. Phys. Chem. C* 2023, 127, 2204–2214 Read Online

ACCESS | Metrics & More | Article Recommendations | Supporting Information

ABSTRACT: Prussian blue analogues (PBAs) are versatile functional materials with numerous applications ranging from electrocatalysis and batteries to sensors and electrochromic devices. Their electrochemical performance involving long-term cycling stability strongly depends on the electrolyte composition. In this work, we use density functional theory calculations and experiments to elucidate the mechanisms of degradation of model $Na_2Ni[Fe(CN)_6]$ functional electrodes in aqueous electrolytes. Next to the solution pH and cation concentration, we identify anion adsorption as a major driving force for electrode dissolution. Notably, the nature of adsorbed anions can control the mass and charge transfer mechanisms during metal cation intercalation as well as the electrode degradation rate. We find that weakly adsorbing anions, such as NO_3^-, impede the degradation, while strongly adsorbing anions, such as SO_4^{2-}, accelerate it. The results of this study provide practical guidelines for electrolyte optimization and can likely be extrapolated to the whole family of PBAs operating in aqueous media.

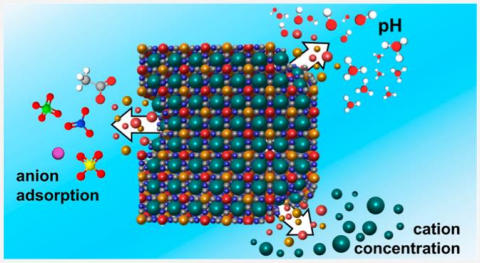

INTRODUCTION

Prussian blue analogues (PBAs) are widely used in different materials science disciplines as they provide various functionalities for battery applications,[1−3] (electro)sensorics,[6−8] heterogeneous (electro)catalysis,[9−11] desalination and selective ion removal,[12−14] as well as electrochromic devices.[15,16] PBAs can be represented by the general formula $A_xTM^1[TM^2(CN)_6]$, where A is usually Li, Na, or K, and TM is a transition metal such as Fe, Mn, Cu, Co, Ni, or Zn. The transition metals are interconnected by C≡N bridges forming $TM(CN)_6$ octahedra, which creates an open framework structure with A-site cations occupying the interstitial nanopores. These cations can be reversibly inserted and extracted from an electrolyte (which will be used synonymously with the term "intercalation" throughout this report) and diffuse through the three-dimensional channels in the structure.[4] Typically, PBAs are associated with the face-centered cubic lattice, but the monoclinic and rhombohedral structures are also commonly observed due to symmetry distortions such as octahedral tilts, Jahn−Teller distortions, hexacyanometallate vacancies, or framework hydration.[17,18] Owing to the high tunability of chemical composition, PBAs can be considered as model materials in coordination and inorganic chemistry, being analogues of the well-known metal−organic frameworks (MOFs).[19] Therefore, a basic understanding of the correlations between various functional properties of PBAs and their composition or structure is of great fundamental importance.

In the case of energy conversion and storage applications, the properties of electrified interfaces between electronically conducting PBAs and aqueous electrolytes are of central significance. So far, one fundamental property that has received very limited attention is the electrochemical stability of PBA-based electrodes. Most of the previous stability studies focused on how solution pH affects the degradation of PBA materials: it was found that PBAs are prone to degradation in both acidic (low pH)[20−24] and basic (high pH) solutions.[20,25−28] However, it was recently demonstrated that the degradation rate of aqueous sodium-ion battery electrodes based on PBAs strongly depends not only on solution pH but also on the nature of anions present in the electrolytes.[29] Specifically, for the $Na_2Ni[Fe(CN)_6]$ and $Na_2Co[Fe(CN)_6]$ model electrodes, the transition-metal dissolution during charge−discharge cycles was monitored in real time using an electrochemical flow-cell linked with an inductively coupled plasma mass

Received: November 23, 2022
Revised: January 16, 2023
Published: January 30, 2023

https://doi.org/10.1021/acs.jpcc.2c08222
J. Phys. Chem. C 2023, 127, 2204−2214

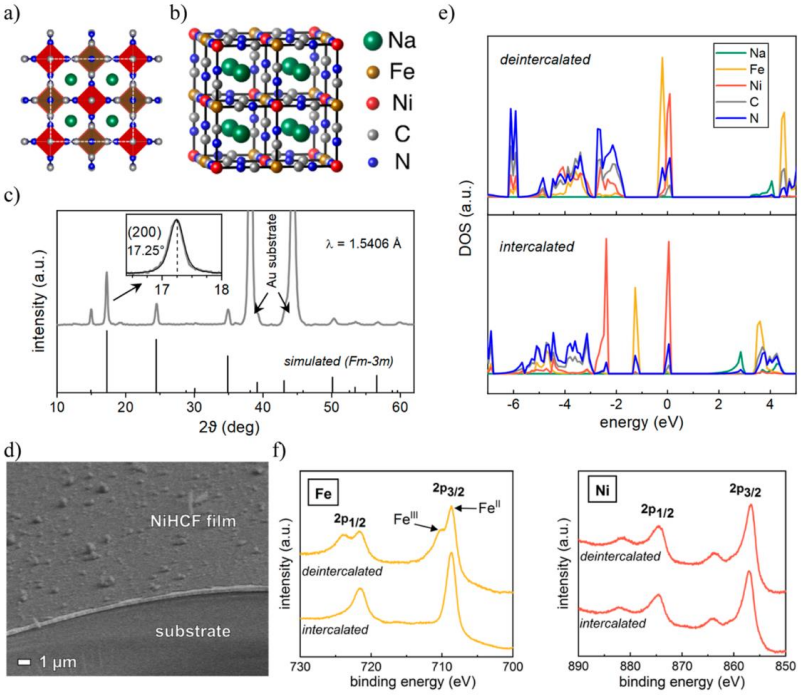

Figure 1. Polyhedral (a) and ball-and-stick (b) representations of the nickel hexacyanoferrate $Na_2Ni[Fe(CN)_6]$ crystal structure in the cubic space group $Fm\bar{3}m$. (c) XRD pattern of the NiHCF thin film together with the simulated reflections for the crystal structure given in (b). SEM image of the electrodeposited thin-film electrode (d). (e) DOS for fully intercalated and 50% deintercalated bulk NiHCF. (f) XPS spectra showing the Fe 2p and Ni 2p regions for intercalated and deintercalated NiHCF.

spectrometer. The study revealed distinct transition-metal dissolution patterns strongly correlated with the electrochemical potential and current. It was shown that the degradation rate increases in the order $ClO_4^- < NO_3^- < Cl^- < SO_4^{2-}$, revealing almost no capacity loss after 10,000 cycles for $Na_2Ni[Fe(CN)_6]$ in highly concentrated $NaClO_4$. However, the atomistic mechanisms underlying such behavior remain unclear.

In this work, we combine experiments and density functional theory calculations to elucidate the properties of the electrified interface between model nickel hexacyanoferrate {NiHCF, $Na_2Ni[Fe(CN)_6]$, and $NaNi[Fe(CN)_6]$} electrodes and aqueous electrolytes in the presence of anions commonly used in electrochemical systems. A significant affinity of the PBA surface to anionic species explains the complex mechanism of the interfacial mass and charge transfer during intercalation of alkali metal cations and drastic differences in the stability of PBA materials in the presence of different anions.[30−32] It is found that surface Fe-sites are more favorable for anion adsorption than Ni-sites. Toward the edges of the pH scale, the initial stages of the electrode degradation involve the attack of Fe-sites by OH^- (at high pH) or protonation of the CN groups of the crystal (at low pH) via intercalated H_3O^+. These findings should be of great importance for optimizing the electrochemical behavior of PBA-containing systems, interpreting experimental results, and refinement of advanced models of the electrified PBA/electrolyte interfaces.

METHODS

Experimental Section. Electrochemical experiments were performed in an electrochemical glass cell under inert argon (Ar 5.0, Westfalen) atmosphere in a three-electrode configuration. 1.37 cm^2 AT-cut Au quartz crystal wafers (Stanford Research Systems, Ti adhesive layer, 5 MHz) served as substrates for the electrochemical deposition of NiHCF thin films to monitor the mass loading and variation via electrochemical quartz crystal microbalance (EQCM). A platinum wire was used as a counter electrode, and an Ag/AgCl reference electrode (SSC, 3 M KCl, SI Analytics, "B 3420+") was used. All measurements were performed using a Bio-Logic VSP-300 potentiostat.

The synthesis of $Na_2Ni[Fe(CN)_6]$ model electrodes was performed by means of cyclic voltammetry with a scan rate of 50 mV/s in an aqueous solution of 0.25 M Na_2SO_4 (≥99%, Sigma-Aldrich), 0.5 mM $K_3[Fe(CN)_6]$ (99%, Sigma-Aldrich), and 0.5 mM $NiCl_2$ (99.3%, Alfa Aesar). The deposition method is further described in refs 29,31, and 32.

The electrochemical characteristics and stability of NiHCF were investigated in different Na^+ electrolytes as shown in Table S1. The electrolytes and precursor solutions were prepared with ultrapure water (18.2 MΩ, Merck Millipore).

https://doi.org/10.1021/acs.jpcc.2c08222
J. Phys. Chem. C 2023, 127, 2204−2214

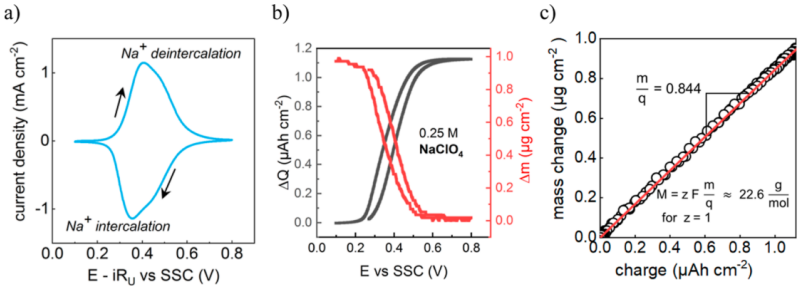

Figure 2. (a) Representative cyclic voltammogram of NiHCF in 0.25 M $NaClO_4$ showing the redox response of $Fe^{II/III}$ in the PBA complex. The electrode charge and mass change (b) during the forward and backward scan of the CV are correlated to Na^+ (de)intercalation by EQCM using Faraday's law (c).

Cyclic voltammograms were recorded with a scan rate of 50 mV/s and galvanostatic cycling (0.1−0.8 V vs SSC) was performed with a rate of 300 C, whereas 1 C generally corresponds to a (dis)charging time of 1 h. Impedance spectra were recorded at a constant potential of 0.4 V vs SSC, which equals a degree of sodiation of approximately 60%. The amplitude of the probing signal was set to 10 mV, and the scanned frequency range was between 35 kHz and 1 Hz with 10 points per decade in logarithmic spacing. All electrolytes were tested in the order of $NaClO_4$, $NaNO_3$, NaCl, Na_2SO_4, and $NaCH_3COO$ on the same sample with an unchanged electrode setup for good comparability of the results with minimal degradation between the measurements. The stationarity of the system was ensured by an appropriate waiting period before the measurement and the validity of all spectra was guaranteed by the Kramers−Kronig check (see Figure S1). The data were fitted to an electrical equivalent circuit using the software EIS Data Analysis 1.3.[33]

To study the crystallographic properties of the NiHCF thin film, grazing incidence X-ray diffraction (XRD) analysis was carried out in the range of 2θ = 5−65° (step size = 0.026°) using Panalytical Empyrean with a Cu tube (λ = 1.5406 Å, 45 kV, 40 mA) and Pixcel3D detector. The incident angle was 1°. The software VESTA (version 3.0)[34] was used to visualize crystal structures and simulate the diffraction pattern of $Na_2Ni[Fe(CN)_6]$, implying a face-centered cubic space group ($Fm\bar{3}m$) crystal structure with a lattice constant of 10.28 Å. A field-emission scanning electron microscope (SEM, JSM-7500F, JEOL) was used to characterize the thin-film electrode morphology. The elemental composition and electronic binding energies of NiHCF samples were investigated by X-ray photoelectron spectroscopy (XPS, Specs). The X-ray source was an Al K-alpha anode (1486.61 eV, 12 kV, 200 W) and photoelectrons were detected with a PHOIBOS 150 2D CCD detector.

Computational Details. All spin-polarized density functional theory (DFT) plane-wave calculations are performed using the Vienna Ab initio Simulation Package (VASP).[35,36] The revised Perdew-Burke-Ernzerhof (RPBE) generalized gradient approach (GGA) functional is employed in combination with the on-site Hubbard U parameters (U_{Fe} = 3.3 eV and U_{Ni} = 4.6 eV) and ferromagnetic ordering following previous theoretical investigations.[37,38] The D3 approach within Grimme's formalism is applied to correct for van der Waals interactions.[39,40] The core electrons are represented through the projector augmented-wave (PAW) formalism.[41] A plane-wave cutoff energy of 500 eV is used throughout the study. A Γ-centered Monkhorst−Pack k-point mesh of 5 × 5 × 5 is employed for the bulk and 5 × 5 × 1 for the slab calculations. Structural optimizations are carried out until the total energies and atomic forces are converged to within 10^{-5} eV and 0.05 eV/Å, respectively. During structural optimizations, the bottom half of the slab is kept fixed. The optimized lattice constant of $Na_2Ni[Fe(CN)_6]$ is 10.32 Å. The dimensions of the used periodic slabs are 10.32 × 10.32 × 10.32 $Å^3$ with at least a 15 Å vacuum gap. For the optimized adsorption configurations, an additional single-point calculation within the implicit solvent model is performed using the default relative permittivity of the bulk water (78.4). The calculations are carried out for both the fully intercalated $Na_2Ni[Fe(CN)_6]$ and 50% deintercalated $NaNi[Fe(CN)_6]$ slabs, which correspond to eight Na species in the former case and four Na species in the bottom layer of the slab in the latter case, respectively.

■ RESULTS AND DISCUSSION

Figure 1a,b shows the atomic structure of nickel hexacyanoferrate {$Na_2Ni[Fe(CN)_6]$} used in this study as a representative PBA to better understand its degradation properties in aqueous electrolytes. The recorded XRD pattern of the electrodeposited thin film (see Figure 1c) matches very well with the calculated pattern for the $Fm\bar{3}m$ structure. The strong (200) reflection allows us to calculate the lattice constant for the material yielding 10.28 Å. This value is in good accordance with the results of our DFT optimization (10.32 Å). It is, therefore, reasonable to use the presented atomic structure for further DFT simulations of the processes at the electrified electrode−electrolyte interface. As visible from the SEM image in Figure 1d, the NiHCF thin film obtained from the electrochemical deposition is characterized by a very homogenous coating on top of the Au substrate.

The electrochemical activity in PBAs is based on alkali metal ions, for example, sodium, (de)intercalation accompanied by the corresponding redox reaction of the host transition metals. NiHCF has only Fe(II/III) as an active redox center since Ni species are electrochemically inert in the operating window of water-based electrolytes. The corresponding redox reaction is represented by

https://doi.org/10.1021/acs.jpcc.2c08222
J. Phys. Chem. C 2023, 127, 2204−2214

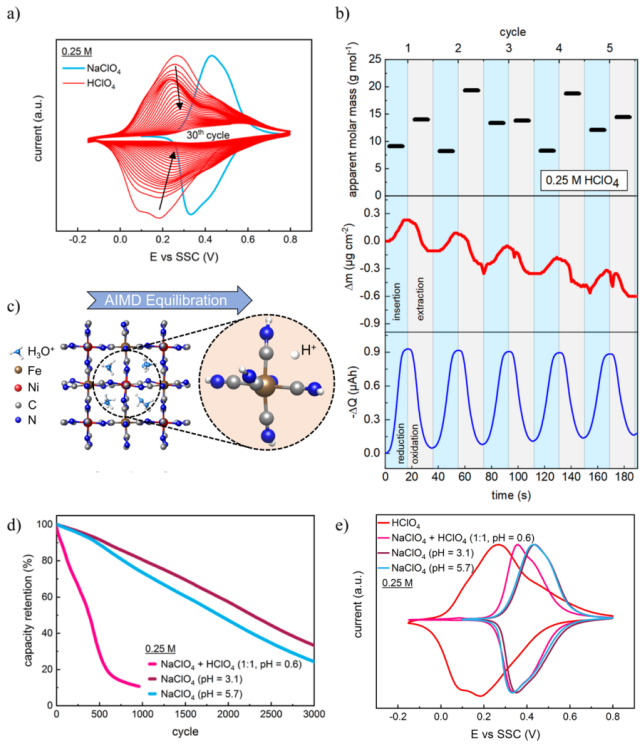

Figure 3. (a) Fast degradation of NiHCF in 0.25 M $HClO_4$ during voltametric cycling due to active material dissolution. (b) Correlation of the corresponding charge and mass change as measured via EQCM over the first five CV cycles. The apparent molar mass of the intercalate was calculated from $\Delta m/\Delta Q$ using Faraday's law. The ongoing electrode dissolution causes large fluctuations in the obtained molar mass values. (c) Ab initio molecular dynamics simulation predicts the cleavage of the [Fe−C≡N]−Ni bond due to protonation of the N-sites if Na^+ in NiHCF is replaced by H_3O^+. (d) Impact of the H^+ vs Na^+ availability on the stability of NiHCF during galvanostatic cycling and (e) respective CVs.

$$Na_2Ni^{II}[Fe^{II}(CN)_6]\ \text{(intercalated)} \rightleftharpoons Na^+ + e^- + NaNi^{II}[Fe^{III}(CN)_6]\ \text{(50\% deintercalated)} \quad (1)$$

Indeed, our Bader charge analysis based on DFT calculations of the NiHCF slabs shows that Ni ions do not change their charge upon 50% deintercalation with q(Ni) = 1.30, whereas the positive charge on Fe ions increases from q(Fe) = 1.17 for the fully intercalated case up to 1.33 for the deintercalated case. This agrees well with an analysis of the density of states (DOS), revealing that the Fe electronic states below the Fermi energy for the intercalated material shift toward the Fermi level for the deintercalated material (Figure 1e). We note here that the analysis based on Bader charges can only be considered qualitative.

This is further confirmed by XPS measurements of oxidized and reduced electrodes, which were electrochemically brought to their respective final states. NiHCF was completely reduced at a potential of 0.1 V vs SSC, whereas it was completely oxidized at 0.8 V vs SSC. As seen in Figure 1f, the samples show strongly differing spectra in the Fe 2p region. For the intercalated electrode, one sharp peak, which is observed in both regions of the spin−orbit doublet, can be associated with the Fe^{II} oxidation state as expected for fully sodiated NiHCF. Upon deintercalation, Fe^{II} is oxidized to Fe^{III}, which is well represented by the appearance of an additional peak at higher binding energies in both doublet regions.[42] On the other side, the spectra obtained for Ni 2p show identical peaks with regard to the corresponding binding energies and intensities, proving that Ni is electrochemically inert within the investigated potential window.

The electrochemical oxidation (desodiation) and reduction (sodiation) of the NiHCF electrode in 0.25 M $NaClO_4$ result in a reversible redox peak (see Figure 2a). It can be noted that the CV peak comprises a superposition of two sharp peaks at ∼0.38 and ∼0.46 V versus SSC. This double-peak structure results from the formation of two different stoichiometries of NiHCF during the electrodeposition process {$Na_2Ni^{II}[Fe^{II}(CN)_6]$ and $NaNi_{1.5}^{II}[Fe^{II}(CN)_6]$}, whereas Fe-(II/III) remains the redox-active center in both cases.[43−45] For simplicity, this work considers NiHCF as the former stoichiometry. The electrode mass change over one CV cycle, as measured by EQCM, strictly follows the consumed charge (Figure 2b). By using Faraday's law, a molar mass of 22.6 g mol^{-1} is obtained for the (de)intercalating species, from

https://doi.org/10.1021/acs.jpcc.2c08222
J. Phys. Chem. C 2023, 127, 2204−2214

which it can be confirmed that the charge compensation is achieved by the transport of Na^+ ions across the electrode−electrolyte interface (Figure 2c).

It was previously reported that the transition-metal dissolution from NiHCF is highly dependent on solution pH and anions present in the electrolyte.[29] However, the NiHCF degradation mechanism as a function of electrolyte composition remains poorly understood. This study distinguishes two degradation regimes corresponding to acidic and alkaline aqueous electrolytes.

We first analyze the mechanism of active material degradation in acidic solutions in the absence of alkali metal cations. It can be assumed that at low pH, the most abundant cationic solution species available for intercalation into the NiHCF structure are hydronium (H_3O^+) ions. An oxidized $NaNi[Fe(CN)_6]$ electrode was transferred to a 0.25 M $HClO_4$ solution and electrochemically cycled in the absence of Na^+ in the electrolyte (Figure 3a). Starting right from the first cycle, the material degrades severely, as visible from the rapidly decreasing current waves in the voltammogram. After less than 30 cycles, the redox activity has almost entirely vanished. Similarly, an instantaneous degradation was observed for desodiated NiHCF in 0.25 M H_2SO_4, which can be considered as completely degraded after already 20 cycles (Figure S2a). It should be noted that the potential range was extended toward lower potentials, as the redox peak was shifted for the acidic solutions compared to the Na^+ electrolytes. It has been reported that the nature of the intercalating cationic species strongly impacts the insertion potential (E_i) of PBA materials, with E_i decreasing when going up the periodic table from the large Cs^+ ion toward the small Li^+. This correlation generally results from the fact that the insertion potential is thermodynamically linked to the Gibbs free energy of solvation, which decreases with increasing ionic radii of the intercalate.[46−49] It is, therefore, reasonable that the intercalation of H_3O^+ in NiHCF is observed at potentials lower than that of Na^+.

To first prove that hydronium is indeed inserted into and extracted from NiHCF, Figure 3b shows the variation in the electrode mass as measured by EQCM during voltametric scans in 0.25 M $HClO_4$. A continuous mass loss indicates the dissolution of the electrode, which reflects the diminishing redox response in Figure 3a. This is overlaid with a repetitive mass increase and decrease signal, which is characteristic of the insertion of ionic species into a host electrode from the solution. By applying Faraday's law, the apparent molar mass of the intercalate is obtained between 8.2 and 19.4 g mol^{-1}. It should be noted that the large fluctuation of this value is caused by the superposition of the (de)insertion signal with the electrode dissolution, as well as the noisy EQCM data caused by the harsh degradation process. Similar results with apparent molar masses between 9.4 and 21.9 g mol^{-1} were obtained for NiHCF in 0.25 M H_2SO_4 (see Figure S2b). Even though the respective average molar masses are smaller than the expected 19 g mol^{-1} for H_3O^+, the data undoubtedly prove the intercalation and deintercalation of a cationic species associated with the reduction and oxidation of NiHCF in the $HClO_4$ and H_2SO_4 solutions. This finding strongly indicates that hydronium actively participates in the (de)intercalation process.

Due to the highly decreased cycling stability of NiHCF in the Na^+-free acidic solutions compared to pH-neutral Na^+ electrolytes, it can be assumed that the intercalation of H_3O^+ is likely responsible for the fast structure destruction. To probe the acidic dissolution mechanism by a theoretical approach, we replace Na^+ cations in the NiHCF structure with H_3O^+, maintaining the same charge of the cell, and run the ab initio molecular dynamics (AIMD) simulations. Already after 1−2 ps of AIMD equilibration, we observed spontaneous protonation of the N-sites resulting in the generation of $Fe(CN-H)_6$ moieties (see Figure 3c). This suggests that the N-sites are the primary point of attack in acidic electrolytes during the NiHCF degradation process. This should lead to the dissolution of $Fe(CN)_6^{3-}$ complexes, while the remaining Ni cations are expected to dissolve as solvated Ni^{2+} species.[29] It was reported that highly defective copper hexacyanoferrate (CuHCF, a Turnbull's blue analogue) can operate as a stable and reversible proton insertion electrode in 2 M H_2SO_4, whereas the stability deteriorated strongly when replacing Cu by Ni, Co, or Mn.[50] Our AIMD simulations predicted a similar protonation of N-sites for CuHCF, which contrasts the reported stability of this system. We hypothesize that the high content of coordination water within the defective CuHCF lattice may effectively prevent N-sites from rapid protonation, and therefore, that a high degree of crystal hydration may allow a more stable proton insertion into PBAs.

Considering this, one could erroneously conclude that the presence of H_3O^+ in general has a detrimental impact on PBA electrodes in aqueous media. However, acidification of alkali metal cation electrolytes is, overall, a well-established strategy to enhance the stability of PBAs.[29,51,52] The reason for its higher stability in slightly acidified electrolytes is usually assigned to the absence of OH^-, as it is well-known that PBA electrodes are entirely unstable in the presence of abundant hydroxide species.[26−28]Figure S3 shows the almost immediate disintegration of NiHCF upon cycling in 0.1 M NaOH (pH = 13). As previously reported, the electrode degradation at high pH is characterized by an entire loss of $[Fe(CN)_6]^{3/4-}$ and the subsequent formation of surface-confined NiO_x phases, represented by the increasing current from the Ni(II/III) redox couple.[27−29]

This stabilization strategy based on OH^- removal is represented in Figure 3d, where the reduction in the pH of a $NaClO_4$ solution from its initial value of pH = 5.7 to pH = 3.1 via the addition of $HClO_4$ leads to a significant decrease in the degradation rate during the galvanostatic cycling. If the electrolyte is, however, strongly acidified with an equal concentration of 0.25 M $HClO_4$ and $NaClO_4$, the NiHCF electrode degradation is extremely accelerated, whereas it is still more stable compared to the pure 0.25 M $HClO_4$ solution (Figure 3a). For both cases of acidified electrolytes, we assign the charge compensation mechanism mainly to the intercalation of Na^+ rather than H_3O^+. This is reflected by the respective CVs shown in Figure 3e. As the intercalation potential E_i of NiHCF for sodium is higher than that for protons in the pure $NaClO_4$ and $HClO_4$ solutions at equal concentrations, it can be deduced that sodium insertion is in general thermodynamically more favored.[47−49] For the pH-adjusted 0.25 M $NaClO_4$ electrolyte (pH = 3.1), the CV exactly resembles the one for the pH = 5.7 electrolyte. Furthermore, an apparent molar mass of ∼23 g mol^{-1} was found for the intercalating species, which shows that Na^+ is responsible for the charge compensation even in acidified electrolytes (see Figure S4). For the 0.25 M $HClO_4$ and $NaClO_4$ (1:1) mixed solution, the CV appears at a lower potential than for the pure 0.25 M $NaClO_4$ case. As the total

https://doi.org/10.1021/acs.jpcc.2c08222
J. Phys. Chem. C 2023, 127, 2204−2214

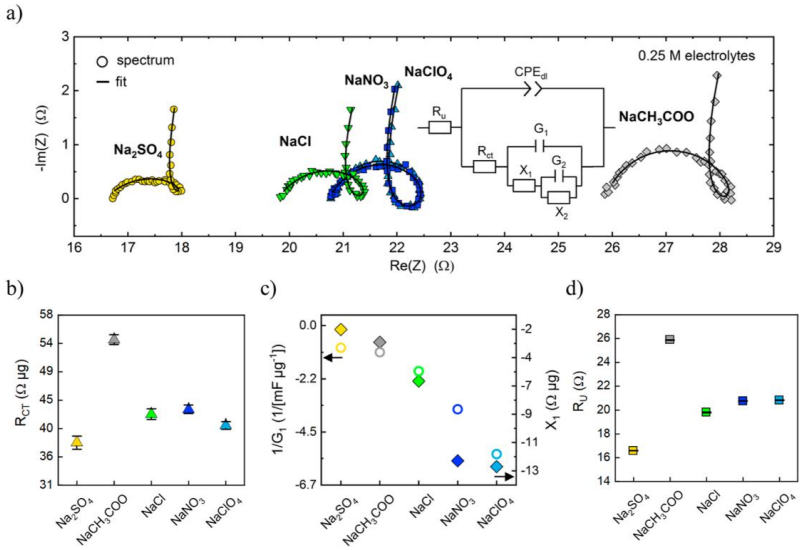

Figure 4. (a) Impedance spectra (at 0.4 V vs SSC) of NiHCF recorded in 0.25 M Na^+ electrolytes with varying anion species. The impedance spectra were fitted using the displayed equivalent circuit yielding the extracted fitting parameters for R_{CT} (b), $1/G_1$ (hollow symbols, left axis) with X_1 (filled symbols, right axis) (c), and R_u (d).

Na^+ concentration is only 0.125 M, this behavior is well described by the relation[49,53]

$$E_i = E_A^0 + \frac{RT}{F} \ln \frac{c_A}{c_0} \quad (2)$$

where E_A^0 is the standard potential of the cation intercalation reaction with c_A, the cation concentration in the solution, and c_0, the reference concentration at which E_A^0 is evaluated. R is the universal gas constant, T is the absolute temperature, and F is the Faraday constant. According to eq 2, a shift of the insertion potential of 18 mV to the left is expected for a Na^+ concentration of 0.125 M vs the original 0.25 M solution. The experimentally obtained shift of the insertion potential is ~30 mV, which can be explained by a coinsertion of H_3O^+ to a small extent. This is, furthermore, reflected by the apparent molar mass of the intercalating species, which was obtained as ~21.2 g mol^{-1} (see Figure S5). It has been reported that the insertion of two cationic species A and B in PBAs results in a single CV peak, with its E_i being between the two extrema $E_{i,A}$ and $E_{i,B}$.[49] The resulting position of E_i indicates the dominating intercalate of A and B, confirming that Na^+ is the main intercalating species even in a 1:1 mixed Na^+/H_3O^+ solution. However, it appears striking that the CV shape of NiHCF exhibits a much lower peak-to-peak separation when a high concentration of hydronium is present, which might be caused by the extremely fast kinetics associated with proton insertion.[50]

Considering the obtained stability trend, the apparent molar masses, and the CV peak positions of the Na^+/H^+ mixed solutions, we conclude that NiHCF has a higher affinity for Na^+ insertion compared to H_3O^+, and the stabilization is caused by the reduced coinsertion of hydronium when Na^+ ions are available as an intercalate. Therefore, the use of slightly acidified Na^+ electrolytes (to pH ≈ 3) should serve as a very effective strategy to enhance the stability of PBA electrodes due to the practical absence of OH^- while still providing a high Na^+/H_3O^+ ratio.

For alkaline/neutral solutions, we investigate the role of a series of common anionic species on the degradation rate of PBA materials. We have shown in our previous studies that electrolyte anions play a significant role in the interfacial charge and mass transfer processes for intercalation-type battery materials.[30−32,54] Figure 4a shows the impedance spectra for NiHCF in 0.25 M Na^+ electrolytes for varying anions, in particular, ClO_4^-, NO_3^-, Cl^-, CH_3COO^-, and SO_4^{2-}. Characteristic loop-shaped spectra were obtained for all the electrolytes, which were fitted with the equivalent electric circuit displayed in Figure 4a. Next to the "classical" elements as the uncompensated resistance (R_u), a constant phase element (CPE) represents the double-layer capacitance and the charge transfer resistance (R_{CT}) for faradaic currents, the superposition of the circuit elements X_1, G_1, X_2, and G_2 represents the intermediate adsorption of anions on the electrode surface during the alkali metal cation insertion process. This physical model describes the so-called "three-step mechanism" of intercalation, which will be briefly introduced in the following. In short, the quick electron transfer on $Fe^{II/III}$ results in the appearance of uncompensated surface charges due to the considerably slower extraction or insertion of sodium from or into the crystal structure. This excess surface charge is compensated by the intermediate adsorption of the highly mobile electrolyte anions on the electrode surface.[30−32,55] By elaborating the respective kinetic steps of the described interconnected quasireversible processes, the faradaic impedance for the (de)intercalation reaction can be modeled as

https://doi.org/10.1021/acs.jpcc.2c08222
J. Phys. Chem. C 2023, 127, 2204−2214

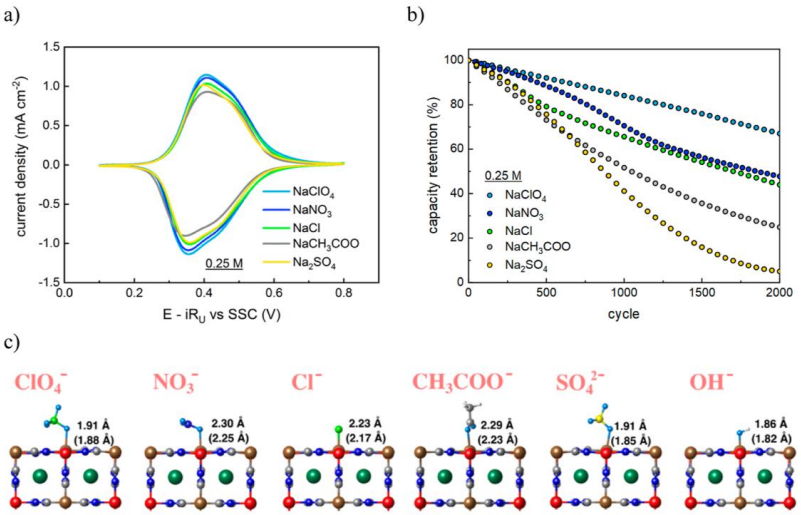

Figure 5. (a) Cyclic voltammograms (50 mV/s) and (b) cycling stability (galvanostatic oxidation and reduction at a rate of 300 C) of NiHCF recorded in 0.25 M Na^+ electrolytes with varying anion species. (c) DFT optimized structures of a series of anions adsorbed on Fe surface sites of the NiHCF surface along with the Fe−O and Fe−Cl distances. The values are for the fully intercalated and 50% deintercalated (in parentheses) cases. The corresponding adsorption energies are presented in Table 1.

$$\tilde{Z} = R_{ct} + \cfrac{1}{j\omega G_1 + \cfrac{1}{X_1 + \cfrac{1}{j\omega G_2 + \cfrac{1}{X_2}}}} \quad (3)$$

The parameters G_1, G_2, X_1, and X_2 are formed by combinations of the complex kinetic parameters of the charge transfer and individual ad/desorption steps associated with the three-step mechanism. Importantly, these parameters can take on both positive and negative values.[31,32] For a more detailed derivation of the general impedance model for faradaic reactions involving surface adsorbed species, the reader is referred to ref 56.

From Figure 4b, it is apparent that the nature of the anions has, as expected, no significant impact on the charge transfer resistance and thereby the corresponding rate constants of the redox reaction. In contrast, the model elements G_1 and X_1, which represent the anion adsorption, strongly deviate among the different anions (Figure 4c). From this, we can conclude that the complex interfacial mechanism of alkali metal cation intercalation strongly depends on the respective adsorption affinity of the involved anions. The different ionic conductivities of the salt solutions are represented by the varying uncompensated resistance values (Figure 4d), which are nevertheless in a comparable range.

Following this argumentation, the anion nature should determine the electrochemical performance of PBA electrodes. Figure 5a shows the CVs of NiHCF in 0.25 M Na^+ electrolytes with ClO_4^-, NO_3^-, Cl^-, CH_3COO^-, and SO_4^{2-} as the respective anionic species. The potential was corrected for the uncompensated resistance to eliminate any effects stemming from the different ionic conductivities of the solutions. Apparently, the peak shape and position are highly symmetric in all cases and remain unaffected by the present anion. Furthermore, the apparent molar mass of the intercalating species was determined to be very close to the expected 22.99 g mol^{-1} for all investigated electrolytes, showing that only sodium is inserted into the host structure (see Figure S6). From the consistently reversible CV curves, it can be concluded that all the tested anionic species effectively compensate for the intermediate excess surface charges during the redox process and that the corresponding adsorption and desorption steps proceed fast enough to not be rate limiting. While this process is supposed to be fully reversible in theory, we observed a significant impact from the involved anion on the electrode stability in our previous study.[29]

To correlate the degradation rates to the specific anions, we repetitively cycled NiHCF thin-film model electrodes in equally concentrated Na^+ electrolytes with comparable neutral pH = 5.7−6.2 (see Table S1), as shown in Figure 5b. The electrode stability was found to decrease in the order of ClO_4^- > NO_3^- > Cl^- > CH_3COO^- > SO_4^{2-}, with the capacity retention after 2000 cycles ranging from 67% for perchlorate to only 5% for sulfate. This finding strongly indicates the detrimental effect of some anions and their notable role in promoting electrode dissolution. The order of electrode stability as a function of the involved anion is also in great agreement with previous findings for other PBA materials, namely, $NaIn[Fe(CN)_6]$ and $K_2Cr[Fe(CN)_6]$.[57,58]

Hypothesizing that the degradation process is initiated by the adsorption of anions from the electrolyte on the metal centers of the NiHCF surface, the adsorption strength and, therefore, the impact of the individual anions should differ considering their distinct geometry, size, charge density, and polarity. To quantify this effect, we examine the adsorption energetics for ClO_4^-, NO_3^-, Cl^-, CH_3COO^-, SO_4^{2-}, and OH^-. Table 1 lists the computed binding energies for the anions adsorbed at the Fe and Ni surface sites of NiHCF. It is seen that the surface affinity for anions is very strong, assuming

https://doi.org/10.1021/acs.jpcc.2c08222
J. Phys. Chem. C 2023, 127, 2204−2214

Table 1. DFT Computed Adsorption Energies (E_{ads}) for a Series of Electrolyte Anions Adsorbed Over Fe and Ni Surface Sites of Intercalated and 50% Deintercalated NiHCF[a]

	intercalated		50% deintercalated	
adsorbate	E_{ads} (Fe), eV	E_{ads} (Ni), eV	E_{ads} (Fe), eV	E_{ads} (Ni), eV
OH^-	−2.87	−1.41	−2.91	−1.58
Cl^-	−2.73	−2.04	−2.52	−1.74
SO_4^{2-}	−3.54	−1.84	−3.55	−2.49
ClO_4^-	−2.65	−2.35	−2.47	−2.25
NO_3^-	−1.29	−1.35	−1.57	−1.23
CH_3COO^-	−1.89	−1.26	−1.57	−1.28

[a]The corresponding distances between the adsorbates and the surface metal centers are provided in Figure 5c.

specific adsorption with preferential binding to Fe centers in both intercalated and deintercalated NiHCF. To confirm that these results do not depend on a particular choice of the *U* values in our computational scheme, we also ran a series of plain DFT calculations (see Table S2). It appears striking to see that even perchlorate, which is known as a weak adsorbate on metals,[59] yields considerably high adsorption energies when adsorbed over Fe. Figure 5c shows the atomic configurations of the anions adsorbed on the Fe-sites of the NiHCF surface. It can be observed that the stronger adsorbed anions (SO_4^{2-} and OH^-) are characterized by shorter interfacial distances than the weaker adsorbed species. Also, the distances are decreased upon deintercalation, in agreement with the overall more positive charge on the host Fe-sites after Na removal (see Table S3). Endorsing our experimental studies, these computational results support the proposed mechanism of anions dictating the kinetics of the interfacial charge and mass transport by adsorption on the electrode surface during (de)intercalation of alkali metal cations in PBAs.[30−32]

It is also seen from Table 1 that SO_4^{2-} and OH^- anions are characterized by the strongest and CH_3COO^-, NO_3^-, and ClO_4^- by the weakest adsorption to the NiHCF surface. The calculated adsorption energetics appears to qualitatively correlate with the decreasing stability of NiHCF from the perchlorate to sulfate electrolytes upon cycling. Furthermore, the strong interaction of OH^- with the electrode material reflects its fast deterioration in the presence of hydroxide. We, therefore, reason that the low stability of PBAs in high pH media, as well as in the presence of some anionic species in the solution, can be described by a generalized degradation mechanism involving the specific adsorption of anions. The exact dissolution pathways of the specific electrode constituents are certainly too complicated to be entirely unveiled by our simplified approach, but it clearly identifies anion attack to catalyze the degradation process via specific adsorption and subsequent metal extraction by breaking the lattice bonds. Considering the obtained strong (chemi)/adsorption energies in the order of 2−3.5 eV, ligand exchange leading to the formation and dissolution of, for example, $[Fe^{III}(CN)_5OH]^{3-}$ in the alkaline case cannot be excluded.

However, these DFT results cannot explain the experimentally observed low stability of NiHCF in 0.25 M sodium acetate, as one should in fact expect the slowest degradation rate according to the weak anion adsorption in this case. We suppose that the unexpected detrimental role of CH_3COO^- is related to its considerably higher basic strength (pK_b = 9.2) compared to the other investigated anions (see Table S4).[60,61] Even though the sodium acetate electrolyte was adjusted to a neutral pH = 6.2, this only reflects an overall statistical quantity. On a molecular level, hydrolysis due to deprotonation of H_2O and subsequent CH_3COOH formation will result in the local appearance of free OH^-. This in turn accelerates the degradation of the electrode if the process occurs close to its surface. In contrast to the pure NaOH case, this will not lead to the formation of NiO_x (as it is not stable at medium pH) but to the dissolution of active material. Extrapolating these findings, low stability of PBAs in electrolytes involving other (carboxylic) anions corresponding to weak acids should be expected. Furthermore, this argument allows for the explanation of the previously published low stability observed for PBA electrodes in 1 M $Mg(ClO_4)_2$ solutions.[62] Besides Mg^{2+}, the initial dissolution of NiHCF electrodes was also observed in other divalent metal nitrate electrolytes (Ca^{2+} and Sr^{2+}).[63] Assuming a similar mechanism, local hydrolysis and $X(OH)_2$ precipitation (with X = Mg, Ca, and Sr) might result in free H_3O^+, which can in turn initiate the acidic degradation pathway. Other authors discussed the substitution of lattice Ni(II) by intercalated divalent cations like Mg^{2+}, which was assumed to result in the collapse of the framework.[64] It should, however, be mentioned that the coinsertion of H_3O^+ cannot be ruled out in divalent cation solutions.[63,65] In contrast to the mixed H_3O^+/Na^+ electrolyte, we expect that H_3O^+ is a preferred intercalate over Mg^{2+} due to the selectivity of PBAs favoring the insertion of low hydration energy/small radius species over large divalent cations.[47,48] Further research will be necessary to assess the impact of different degradation pathways in the case of PBAs in divalent cation solutions.

Lastly, we investigate the effect of the electrolyte concentration on electrode stability. It has been shown in previous works on PBAs that the dissolution of active material can be suppressed by increasing the concentration of the electrolyte toward the so-called water-in-salt electrolytes.[29,57,66] $NaClO_4$ has proven to be a promising candidate for this approach as concentrations beyond 10 M are feasible for this salt.[66,67] Figure 6 shows the stability of NiHCF electrodes in varying concentrations from 0.25 to 8 M $NaClO_4$. The stability slightly decreases when raising the concentration from 0.25 to 1 M, while a significant stabilization of the material can be observed above 2 M with almost no degradation for an 8 M

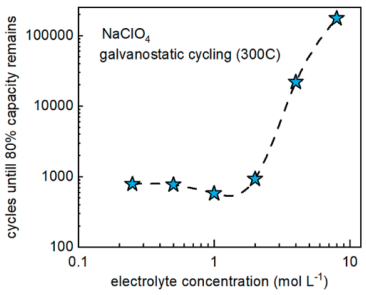

Figure 6. Stability of NiHCF in varying concentrations of $NaClO_4$ during galvanostatic cycling (300 C). The data points show the number of cycles after a loss of 20% capacity. For the 4 and 8 M solutions, the stability was extrapolated based on the measured capacity losses of 2.6% after 2840 cycles and 1.2% after 10,500 cycles.[29] The dashed line serves as a guide to the eye.

https://doi.org/10.1021/acs.jpcc.2c08222
J. Phys. Chem. C 2023, 127, 2204−2214

$NaClO_4$ solution. For the superconcentrated electrolytes, the material hydrolysis is effectively suppressed through the absence of free water molecules, as these are excessively incorporated into the ions' solvation shells due to the strong hydration of the salt. In fact, only a very few water molecules exist per one sodium perchlorate molecule causing a vanishing uptake capability for dissolved electrode constituents.[68] Furthermore, the sluggish diffusion dynamics for dissolved electrode constituents in the electrolyte bulk strongly inhibit electrode degradation in such water-in-salt systems.[69] For the low-to-medium concentrated solutions, we assign the slight decrease in the stability to the effect of the ClO_4^- anion. Even though this species was found to adsorb on the electrode surface only weakly, its increased activity at higher concentrations could lead to a stronger degradation of the active material. However, beyond a concentration of 2 M, the stabilizing crowding effect of the electrolyte prevails.

CONCLUSIONS

In this work, the governing mechanisms driving the degradation of model $Na_2Ni[Fe(CN)_6]$ electrodes based on the electrolyte composition were elucidated by a combined experimental and theoretical approach. DFT calculations for the anions commonly used in electrochemical systems showed that the NiHCF surface has a significant affinity for anion adsorption with binding energies up to ~3.5 eV. This finding emphasizes a non-negligible role of anion-specific adsorption in the complex mechanism of interfacial mass and charge transfer during the intercalation of alkali metal cations. It is shown that the surface Fe-sites are more favorable for anion adsorption than Ni-sites, forming the following trend for the adsorption strength of anions on Fe (surface layer atoms): $SO_4^{2-} > OH^- > Cl^- > ClO_4^- > CH_3COO^- > NO_3^-$. The anion adsorption characteristics allow us to explain the drastic differences in the stability of PBA electrodes, confirming the experimentally determined higher stability in the presence of weakly adsorbing anions like ClO_4^- and NO_3^- compared to the strongly adsorbing SO_4^{2-} and OH^-. Considering the special role of hydroxide on PBA decomposition, the respective basic strength of the anions also has to be taken into account, excluding the acetate anion from stable electrode cycling. Whereas benign acidification (pH ~ 2−3) of the electrolyte generally helps to increase the stability due to the decreased OH^- activity, an overwhelming availability and intercalation of H_3O^+ cause a fast deterioration of the Ni−[N≡C−Fe] bond due to protonation of the N-sites within the crystal structure and subsequent electrode dissolution.

We point out, however, that it is not straightforward to predict the stability of PBAs in aqueous environments by a single generalized mechanism. Overall, the material stability is determined by a complex interplay of competing processes involving anion attack via strong adsorption on the electrified interface, specifically OH^--induced hydrolysis, and protonation of the CN group in the presence of hydronium. Therefore, the exact composition of the electrolyte should be carefully considered for achieving a long material lifetime as the solution pH, salt concentration, and the involved anion determine its resistance against degradation. These findings should be of great importance in optimizing electrochemical systems based on PBA materials, interpreting experimental results, and elucidating the advanced models of the electrified PBA/electrolyte interfaces.

ASSOCIATED CONTENT

Supporting Information

The Supporting Information is available free of charge at https://pubs.acs.org/doi/10.1021/acs.jpcc.2c08222.

Used sodium salt solutions with suppliers and respective pH values; computed anion binding energies via plain DFT calculations; computed local charge on Fe- and Ni-sites; list of acid and basic strength of investigated species; characterization of NiHCF in 0.25 M H_2SO_4, 0.1 M NaOH, and a mixed 0.25 M $HClO_4$ and $NaClO_4$ (1:1) electrolytes; apparent molar mass of the (de)-intercalating species during cycling of NiHCF in different Na^+ electrolytes; and Kramers−Kronig check for the impedance spectra of NiHCF (PDF)

AUTHOR INFORMATION

Corresponding Authors

Aliaksandr S. Bandarenka − *Physics of Energy Conversion and Storage, Physik-Department, Technische Universität München, Garching bei München 85748, Germany;* orcid.org/0000-0002-5970-4315; Email: bandarenka@ph.tum.de

Vitaly Alexandrov − *Department of Chemical and Biomolecular Engineering and Nebraska Center for Materials and Nanoscience, University of Nebraska−Lincoln, Lincoln, Nebraska 68588, United States;* orcid.org/0000-0003-2063-6914; Email: valexandrov2@unl.edu

Authors

Xaver Lamprecht − *Physics of Energy Conversion and Storage, Physik-Department, Technische Universität München, Garching bei München 85748, Germany*

Iman Evazzade − *Department of Chemical and Biomolecular Engineering and Nebraska Center for Materials and Nanoscience, University of Nebraska−Lincoln, Lincoln, Nebraska 68588, United States*

Iago Ungerer − *Physics of Energy Conversion and Storage, Physik-Department, Technische Universität München, Garching bei München 85748, Germany*

Ludek Hromadko − *Central European Institute of Technology, Brno University of Technology, Brno 61200, Czech Republic; Center of Materials and Nanotechnologies, Faculty of Chemical Technology, University of Pardubice, Pardubice 53002, Czech Republic*

Jan M. Macak − *Central European Institute of Technology, Brno University of Technology, Brno 61200, Czech Republic; Center of Materials and Nanotechnologies, Faculty of Chemical Technology, University of Pardubice, Pardubice 53002, Czech Republic*

Complete contact information is available at: https://pubs.acs.org/10.1021/acs.jpcc.2c08222

Notes

The authors declare no competing financial interest.

ACKNOWLEDGMENTS

We want to thank the German Research Foundation (DFG) under Germany's excellence strategy—EXC 2089/1-390776260, Germany's excellence cluster "e-conversion". We acknowledge funding support from the National Science Foundation (NSF) through the CBET-1929810 award. This research used the Extreme Science and Engineering Discovery

https://doi.org/10.1021/acs.jpcc.2c08222
J. Phys. Chem. C 2023, 127, 2204−2214

Environment (XSEDE), which is supported by NSF grant number ACI-1548562, as well as the Leibniz Supercomputing Center (LRZ). XRD and SEM analyses were carried out with the support of the CEMNAT Research Infrastructure funded by the Ministry of Education, Youth and Sports of the Czech Republic (projects LM2018103)

REFERENCES

(1) Han, J.; Varzi, A.; Passerini, S. The Emergence of Aqueous Ammonium-Ion Batteries. *Angew. Chem., Int. Ed.* **2022**, *61*, No. e202115046.
(2) Hurlbutt, K.; Wheeler, S.; Capone, I.; Pasta, M. Prussian Blue Analogs as Battery Materials. *Joule* **2018**, *2*, 1950−1960.
(3) Xie, B.; Sun, B.; Gao, T.; Ma, Y.; Yin, G.; Zuo, P. Recent progress of Prussian blue analogues as cathode materials for nonaqueous sodium-ion batteries. *Coord. Chem. Rev.* **2022**, *460*, 214478.
(4) Wang, B.; Han, Y.; Wang, X.; Bahlawane, N.; Pan, H.; Yan, M.; Jiang, Y. Prussian Blue Analogs for Rechargeable Batteries. *iScience* **2018**, *3*, 110−133.
(5) Yi, H.; Qin, R.; Ding, S.; Wang, Y.; Li, S.; Zhao, Q.; Pan, F. Structure and properties of prussian blue analogues in energy storage and conversion applications. *Adv. Funct. Mater.* **2021**, *31*, 2006970.
(6) Karyakin, A. A. Prussian blue and its analogues: electrochemistry and analytical applications. *Electroanalysis* **2001**, *13*, 813−819.
(7) Avila, Y.; Acevedo-Peña, P.; Reguera, L.; Reguera, E. Recent progress in transition metal hexacyanometallates: From structure to properties and functionality. *Coord. Chem. Rev.* **2022**, *453*, 214274.
(8) Matos-Peralta, Y.; Antuch, M. Prussian blue and its analogs as appealing materials for electrochemical sensing and biosensing. *J. Electrochem. Soc.* **2019**, *167*, 037510.
(9) Chen, S. M.; Liou, C. Y.; Thangamuthu, R. Preparation and characterization of mixed-valent nickel oxide/nickel hexacyanoferrate hybrid films and their electrocatalytic properties. *Electroanalysis* **2007**, *19*, 2457−2464.
(10) Su, X.; Wang, Y.; Zhou, J.; Gu, X.; Li, J.; Zhang, S. Operando spectroscopic identification of active sites in NiFe Prussian Blue Analogues as electrocatalysts: activation of oxygen atoms for oxygen evolution reaction. *J. Am. Chem. Soc.* **2018**, *140*, 11286−11292.
(11) Zhang, H.; Li, P.; Chen, S.; Xie, F.; Riley, D. J. Anodic transformation of a core-shell Prussian Blue Analogue to a bifunctional electrocatalyst for water splitting. *Adv. Funct. Mater.* **2021**, *31*, 2106835.
(12) Rassat, S. D.; Sukamto, J. H.; Orth, R. J.; Lilga, M. A.; Hallen, R. T. Development of an electrically switched ion exchange process for selective ion separations. *Sep. Purif. Technol.* **1999**, *15*, 207−222.
(13) Kim, T.; Gorski, C. A.; Logan, B. E. Ammonium removal from domestic wastewater using selective battery electrodes. *Environ. Sci. Technol. Lett.* **2018**, *5*, 578−583.
(14) Reale, E. R.; Regenwetter, L.; Agrawal, A.; Dardón, B.; Dicola, N.; Sanagala, S.; Smith, K. C. Low porosity, high areal-capacity Prussian blue analogue electrodes enhance salt removal and thermodynamic efficiency in symmetric faradaic deionization with automated fluid control. *Water Res.: X* **2021**, *13*, 100116.
(15) Shibata, T.; Moritomo, Y. Quick response of all solid electrochromic device. *Appl. Phys. Express* **2009**, *2*, 105502.
(16) Assis, L. M. N.; Leones, R.; Kanicki, J.; Pawlicka, A.; Silva, M. M. Prussian blue for electrochromic devices. *J. Electroanal. Chem.* **2016**, *777*, 33−39.
(17) Cattermull, J.; Pasta, M.; Goodwin, A. L. Structural complexity in Prussian blue analogues. *Mater. Horiz.* **2021**, *8*, 3178−3186.
(18) Boström, H. L. B.; Brant, W. R. Octahedral tilting in Prussian blue analogues. *J. Mater. Chem. C* **2022**, *10*, 13690−13699.
(19) Zhang, W.; Wu, Y.; Li, Z.; Dong, H.; Zhang, Y.; Gu, N.. *Nanozymology*; Springer: Singapore, 2020; pp 141−170.
(20) Yang, Y.; Brownell, C.; Sadrieh, N.; May, J.; Del Grosso, A.; Place, D.; Leutzinger, E.; Duffy, E.; He, R.; Houn, F.; et al. Quantitative measurement of cyanide released from Prussian Blue. *Environ. Sci. Technol. Lett.* **2007**, *45*, 776−781.
(21) Zhang, W.; Zhao, Y.; Malgras, V.; Ji, Q.; Jiang, D.; Qi, R.; Ariga, K.; Yamauchi, Y.; Liu, J.; Jiang, M.; et al. Synthesis of monocrystalline nanoframes of prussian blue analogues by controlled preferential etching. *Angew. Chem., Int. Ed.* **2016**, *55*, 8228−8234.
(22) Zhu, Y.; Wang, B.; Gan, Q.; Wang, Y.; Wang, Z.; Xie, J.; Gu, S.; Li, Z.; Li, Y.; Ji, Z.; et al. Selective edge etching to improve the rate capability of Prussian blue analogues for sodium ion batteries. *Inorg. Chem. Front.* **2019**, *6*, 1361−1366.
(23) Hu, M.; Furukawa, S.; Ohtani, R.; Sukegawa, H.; Nemoto, Y.; Reboul, J.; Kitagawa, S.; Yamauchi, Y. Synthesis of Prussian blue nanoparticles with a hollow interior by controlled chemical etching. *Angew. Chem., Int. Ed.* **2012**, *51*, 984−988.
(24) Hu, M.; Belik, A. A.; Imura, M.; Yamauchi, Y. Tailored design of multiple nanoarchitectures in metal-cyanide hybrid coordination polymers. *J. Am. Chem. Soc.* **2013**, *135*, 384−391.
(25) Stilwell, D. E.; Park, K. H.; Miles, M. H. Electrochemical studies of the factors influencing the cycle stability of Prussian Blue films. *J. Appl. Electrochem.* **1992**, *22*, 325−331.
(26) Mimura, H.; Lehto, J.; Harjula, R. Chemical and thermal stability of potassium nickel hexacyanoferrate(II). *J. Nucl. Sci. Technol.* **1997**, *34*, 582−587.
(27) Marzak, P.; Yun, J.; Dorsel, A.; Kriele, A.; Gilles, R.; Schneider, O.; Bandarenka, A. S. Electrodeposited $Na_2Ni[Fe(CN)_6]$ thin-film cathodes exposed to simulated aqueous Na-ion battery conditions. *J. Phys. Chem. C* **2018**, *122*, 8760−8768.
(28) Cataldi, T. R.; Guascito, R.; Maria Salvi, A. M. XPS study and electrochemical behaviour of the nickel hexacyanoferrate film electrode upon treatment in alkaline solutions. *J. Electroanal. Chem.* **1996**, *417*, 83−88.
(29) Lamprecht, X.; Speck, F.; Marzak, P.; Cherevko, S.; Bandarenka, A. S. Electrolyte effects on the stabilization of Prussian blue analog electrodes in aqueous sodium-ion batteries. *ACS Appl. Mater. Interfaces* **2022**, *14*, 3515−3525.
(30) Scieszka, D.; Sohr, C.; Scheibenbogen, P.; Marzak, P.; Yun, J.; Liang, Y.; Fichtner, J.; Bandarenka, A. S. Multiple potentials of maximum entropy of a $Na_2Co[Fe(CN)_6]$ battery electrode material: does the electrolyte composition control the interface? *ACS Appl. Mater. Interfaces* **2018**, *10*, 21688−21695.
(31) Ventosa, E.; Paulitsch, B.; Marzak, P.; Yun, J.; Schiegg, F.; Quast, T.; Bandarenka, A. S. The mechanism of the interfacial charge and mass transfer during intercalation of alkali metal cations. *Adv. Sci.* **2016**, *3*, 1600211.
(32) Yun, J.; Pfisterer, J.; Bandarenka, A. S. How simple are the models of Na-intercalation in aqueous media? *Energy Environ. Sci.* **2016**, *9*, 955−961.
(33) Bandarenka, A. S. Development of hybrid algorithms for EIS data fitting. *Lect. Notes Impedance Spectrosc.* **2013**, *4*, 29−36.
(34) Momma, K.; Izumi, F. VESTA 3 for three-dimensional visualization of crystal, volumetric and morphology data. *J. Appl. Crystallogr.* **2011**, *44*, 1272−1276.
(35) Kresse, G.; Furthmüller, J. Efficient iterative schemes for ab initio total-energy calculations using a plane-wave basis set. *Phys. Rev. B: Condens. Matter Mater. Phys.* **1996**, *54*, 11169−11186.
(36) Kresse, G.; Furthmüller, J. Efficiency of ab-initio total energy calculations for metals and semiconductors using a plane-wave basis set. *Comput. Mater. Sci.* **1996**, *6*, 15−50.
(37) Perdew, P.; Burke, K.; Ernzerhof, M. Generalized gradient approximation made simple. *Phys. Rev. Lett.* **1996**, *77*, 3865−3868.
(38) Zhang, Y.; Yang, W. Comment on "Generalized gradient approximation made simple". *Phys. Rev. Lett.* **1998**, *80*, 890.
(39) Grimme, S.; Antony, J.; Ehrlich, S.; Krieg, H. A consistent and accurate ab initio parametrization of density functional dispersion correction (DFT-D) for the 94 elements H-Pu. *J. Chem. Phys.* **2010**, *132*, 154104.
(40) Grimme, S.; Ehrlich, S.; Goerigk, L. Effect of the damping function in dispersion corrected density functional theory. *J. Comput. Chem.* **2011**, *32*, 1456−1465.

https://doi.org/10.1021/acs.jpcc.2c08222
J. Phys. Chem. C 2023, 127, 2204−2214

(41) Blöchl, P. E. Projector augmented-wave method. *Phys. Rev. B: Condens. Matter Mater. Phys.* **1994**, *50*, 17953−17978.
(42) Gerber, S. J.; Erasmus, E. Electronic effects of metal hexacyanoferrates: An XPS and FTIR study. *Mater. Chem. Phys.* **2018**, *203*, 73−81.
(43) Bácskai, J.; Martinusz, K.; Czirók, E.; Inzelt, G.; Kulesza, P. J.; Malik, M. A. Polynuclear nickel hexacyanoferrates: monitoring of film growth and hydrated counter-cation flux/storage during redox reactions. *J. Electroanal. Chem.* **1995**, *385*, 241−248.
(44) Chen, W.; Tang, J.; Xia, X. H. Composition and shape control in the construction of functional nickel hexacyanoferrate nano-interfaces. *J. Phys. Chem. C* **2009**, *113*, 21577−21581.
(45) Hao, X.; Yan, T.; Wang, Z.; Liu, S.; Liang, Z.; Shen, Y.; Pritzker, M. Unipolar pulse electrodeposition of nickel hexacyanoferrate thin films with controllable structure on platinum substrates. *Thin Solid Films* **2012**, *520*, 2438−2448.
(46) Paulitsch, B.; Yun, J.; Bandarenka, A. S. Electrodeposited $Na_2VO_x[Fe(CN)_6]$ films as a cathode material for aqueous Na-ion batteries. *ACS Appl. Mater. Interfaces* **2017**, *9*, 8107−8112.
(47) Lee, H. W.; Pasta, M.; Wang, R. Y.; Ruffo, R.; Cui, Y. Effect of the alkali insertion ion on the electrochemical properties of nickel hexacyanoferrate electrodes. *Faraday Discuss.* **2014**, *176*, 69−81.
(48) Gamaethiralalage, J. G.; Singh, K.; Sahin, S.; Yoon, J.; Elimelech, M.; Suss, M. E.; Liang, P.; Biesheuvel, P. M.; Zornitta, R. L.; de Smet, L. C. P. M. Recent advances in ion selectivity with capacitive deionization. *Energy Environ. Sci.* **2021**, *14*, 1095−1120.
(49) Erinmwingbovo, C.; Palagonia, M. S.; Brogioli, D.; La Mantia, F. Intercalation into a Prussian blue derivative from solutions containing two species of cations. *ChemPhysChem* **2017**, *18*, 917−925.
(50) Wu, X.; Hong, J. J.; Shin, W.; Ma, L.; Liu, T.; Bi, X.; Yuan, Y.; Qi, Y.; Surta, T. W.; Huang, X.; et al. Diffusion-free Grotthuss topochemistry for high-rate and long-life proton batteries. *Nat. Energy* **2019**, *4*, 123−130.
(51) Wessells, C. D.; Peddada, S. V.; Huggins, R. A.; Cui, Y. Nickel hexacyanoferrate nanoparticle electrodes for aqueous sodium and potassium ion batteries. *Nano Lett.* **2011**, *11*, 5421−5425.
(52) Wessells, C. D.; Huggins, R. A.; Cui, Y. Copper hexacyanoferrate battery electrodes with long cycle life and high power. *Nat. Commun.* **2011**, *2*, 550.
(53) Doménech, A.; Montoya, N.; Scholz, F. Estimation of individual Gibbs energies of cation transfer employing the insertion electrochemistry of solid Prussian blue. *J. Electroanal. Chem.* **2011**, *657*, 117−122.
(54) Dinkelacker, F.; Marzak, P.; Yun, J.; Liang, Y.; Bandarenka, A. S. Multistage mechanism of lithium intercalation into graphite anodes in the presence of the solid electrolyte interface. *ACS Appl. Mater. Interfaces* **2018**, *10*, 14063−14069.
(55) Gaddam, R. R.; Katzenmeier, L.; Lamprecht, X.; Bandarenka, A. S. Review on physical impedance models in modern battery research. *Phys. Chem. Chem. Phys.* **2021**, *23*, 12926−12944.
(56) Lasia, A.*Electrochemical Impedance Spectroscopy and its Applications*; Springer: New York, 2014; Chapter 5.
(57) Lamprecht, X.; Marzak, P.; Wieczorek, A.; Thomsen, N.; Kim, J.; Garlyyev, B.; Liang, Y.; Bandarenka, A. S.; Yun, J. High voltage and superior cyclability of indium hexacyanoferrate cathodes for aqueous Na-ion batteries enabled by superconcentrated $NaClO_4$ electrolytes. *Energy Adv.* **2022**, *1*, 623−631.
(58) Bors, R.; Yun, J.; Marzak, P.; Fichtner, J.; Scieszka, D.; Bandarenka, A. S. Chromium(II) hexacyanoferrate-based thin films as a material for aqueous alkali metal cation batteries. *ACS Omega* **2018**, *3*, 5111−5115.
(59) Kasuya, M.; Sogawa, T.; Masuda, T.; Kamijo, T.; Uosaki, K.; Kurihara, K. Anion adsorption on gold electrodes studied by electrochemical surface forces measurement. *J. Phys. Chem. C* **2016**, *120*, 15986−15992.
(60) Trummal, A.; Lipping, L.; Kaljurand, I.; Koppel, I. A.; Leito, I. Acidity of strong acids in water and dimethyl sulfoxide. *J. Phys. Chem. A* **2016**, *120*, 3663−3669.
(61) Dean, J.*Lange's Handbook of Chemistry*, 15th ed.; McGraw-Hill, 1999; Section 8.
(62) Marzak, P.; Kosiahn, M.; Yun, J.; Bandarenka, A. S. Intercalation of Mg^{2+} into electrodeposited Prussian Blue Analogue thin films from aqueous electrolytes. *Electrochim. Acta* **2019**, *307*, 157−163.
(63) Wang, R. Y.; Wessells, C. D.; Huggins, R. A.; Cui, Y. Highly reversible open framework nanoscale electrodes for divalent ion batteries. *Nano Lett.* **2013**, *13*, 5748−5752.
(64) Shrivastava, A.; Liu, S.; Smith, K. C. Linking capacity loss and retention of nickel hexacyanoferrate to a two-site intercalation mechanism for aqueous Mg^{2+} and Ca^{2+} ions. *Phys. Chem. Chem. Phys.* **2019**, *21*, 20177−20188.
(65) Komayko, A. I.; Ryazantsev, S. V.; Trussov, I. A.; Arkharova, N. A.; Presnov, D. E.; Levin, E. E.; Nikitina, V. A. The Misconception of Mg^{2+} Insertion into Prussian Blue Analogue Structures from Aqueous Solution. *ChemSusChem* **2021**, *14*, 1574−1585.
(66) Pasta, M.; Wessells, C. D.; Liu, N.; Nelson, J.; McDowell, M. T.; Huggins, R. A.; Toney, M. F.; Cui, Y. Full open-framework batteries for stationary energy storage. *Nat. Commun.* **2014**, *5*, 3007.
(67) Reber, D.; Grissa, R.; Becker, M.; Kühnel, R. S.; Battaglia, C. Anion selection criteria for water-in-salt electrolytes. *Adv. Energy Mater.* **2021**, *11*, 2002913.
(68) Tomiyasu, H.; Shikata, H.; Takao, K.; Asanuma, N.; Taruta, S.; Park, Y. Y. An aqueous electrolyte of the widest potential window and its superior capability for capacitors. *Sci. Rep.* **2017**, *7*, 45048.
(69) Chen, L.; Sun, W.; Xu, K.; Dong, Q.; Zheng, L.; Wang, J.; Lu, D.; Shen, Y.; Zhang, J.; Fu, H.; et al. How Prussian Blue Analogues can be stable in concentrated aqueous electrolytes. *ACS Energy Lett.* **2022**, *7*, 1672−1678.

https://doi.org/10.1021/acs.jpcc.2c08222
J. Phys. Chem. C 2023, 127, 2204−2214

Fast charging capability of thin-film Prussian blue analogue electrodes for aqueous sodium-ion batteries.

ACS Applied Materials and Interfaces **2023**, *15(19)*, 23951–23962.

ACS APPLIED MATERIALS & INTERFACES

www.acsami.org Research Article

Fast-Charging Capability of Thin-Film Prussian Blue Analogue Electrodes for Aqueous Sodium-Ion Batteries

Xaver Lamprecht, Philipp Zellner, Göktug Yesilbas, Ludek Hromadko, Philipp Moser, Philipp Marzak, Shujin Hou, Richard Haid, Florian Steinberger, Tim Steeger, Jan M. Macak, and Aliaksandr S. Bandarenka*

Cite This: *ACS Appl. Mater. Interfaces* 2023, 15, 23951−23962 Read Online

ACCESS | Metrics & More | Article Recommendations | Supporting Information

ABSTRACT: Prussian blue analogues are considered as promising candidates for aqueous sodium-ion batteries providing a decently high energy density for stationary energy storage. However, suppose the operation of such materials under high-power conditions could be facilitated. In that case, their application might involve fast-response power grid stabilization and enable short-distance urban mobility due to fast re-charging. In this work, sodium nickel hexacyanoferrate thin-film electrodes are synthesized *via* a facile electrochemical deposition approach to form a model system for a robust investigation. Their fast-charging capability is systematically elaborated with regard to the electroactive material thickness in comparison to a "traditional" composite-type electrode. It is found that quasi-equilibrium kinetics allow extremely fast (dis)charging within a few seconds for sub-micron film thicknesses. Specifically, for a thickness below ≈ 500 nm, 90% of the capacity can be retained at a rate of 60C (1 min for full (dis)charge). A transition toward mass transport control is observed when further increasing the rate, with thicker films being dominated by this mode earlier than thinner films. This can be entirely attributed to the limiting effects of solid-state diffusion of Na^+ within the electrode material. By presenting a PBA model cell yielding 25 Wh kg^{-1} at up to 10 kW kg^{-1}, this work highlights a possible pathway toward the guided design of hybrid battery−supercapacitor systems. Furthermore, open challenges associated with thin-film electrodes are discussed, such as the role of parasitic side reactions, as well as increasing the mass loading.

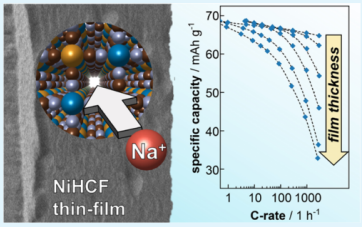

KEYWORDS: *Na-ion aqueous batteries, Prussian blue analogues, sodium nickel hexacyanoferrate, fast-charging capability, thin-film electrochemical deposition, hybrid battery−supercapacitors*

INTRODUCTION

Over the last years, rechargeable batteries have been regarded as an essential enabler for the transition of the world's energy provision scheme toward sustainability. Today, the market is dominated by "traditional" lithium-ion batteries due to the demand for high energy densities in electric vehicles.[1,2] However, alternative battery technologies are inevitably needed, especially considering the increasing adoption of stationary energy storage applications in the power grid, where resource availability, safety, and durability outweigh energy density.[2−4] Aqueous sodium-ion batteries (ASIBs) could play a substantial role in replacing LIBs for such applications in the future.[5]

The material class of Prussian blue analogues (PBA) has gained increasing attention for being a promising candidate for scalable, cost-efficient, and ecologically friendly ASIB electrodes.[6,7] In general, the stoichiometry of these transition metal coordination compounds is described by $AM_xTM^{(1)}[TM^{(2)}(CN)_6]$, where AM is an alkali metal cation, like Li^+, Na^+, or K^+, and $TM^{(1,2)}$ are transition metals interconnected by cyanide ligands.[8] The AM-cations can reversibly intercalate into the PBA open-framework structure to compensate for the charge from the TM redox activity. Ionic charge propagation within the PBA lattice is enabled *via* solid-state diffusion along the wide channels of the nanoporous three-dimensional network.[8]

While an extremely long cycle life of several thousand cycles is enabled by so-called water-in-salt electrolytes,[9,10] also decent energy densities in the order of tens of Wh kg^{-1} have been reported for entirely PBA-based ASIBs.[9,11,12] Traditionally, PBAs are synthesized *via* coprecipitation, followed by casting a slurry containing the active material powder, conductive carbon, and a polymeric binder on a current collector to form a composite electrode.[6] Even though being the standard up-to-date method, it bears several disadvantages, such as holding a significant share of inactive material and impaired

Received: February 23, 2023
Accepted: April 26, 2023
Published: May 5, 2023

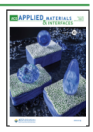

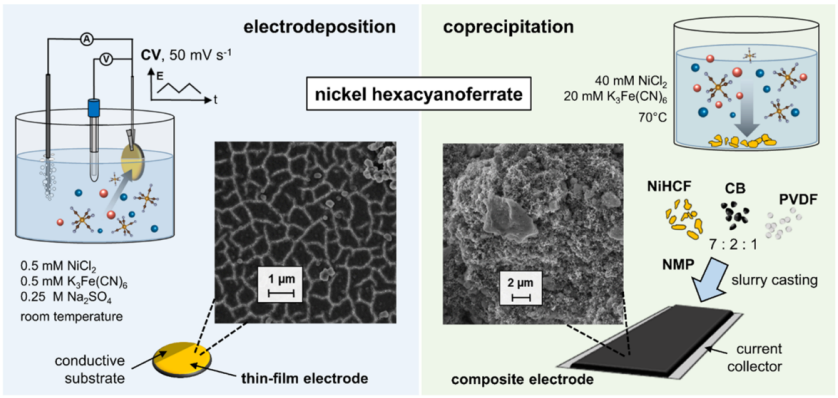

Figure 1. Routines for the preparation of NiHCF electrodes. (Left) Direct electrodeposition of a pure active material thin film on a conductive substrate from an aqueous precursor solution. (Right) Synthesis of NiHCF nanoparticles *via* coprecipitation. The active material is mixed with carbon black and a polymeric binder, followed by preparing a slurry with an organic solvent. A high-mass loading, porous composite electrode coating is obtained on the current collector.

intercalation kinetics due to limited access of ions to the active material surface.[13−15] Furthermore, without optimized and controlled synthesis conditions, the coprecipitation method commonly yields primary and secondary particles of imperfect and detrimental crystallinity and morphology resulting in unfavorable mass transport properties and kinetics.[16−19] These effects negatively impact the available capacity and give rise to a potential hysteresis of the electrodes when charged and discharged at high rates.[20]

In contrast, binder-free nano/microstructured PBA electrodes can possibly hold great potential for high-rate ASIBs.[12,21−23] Such hybrid battery−supercapacitor systems, which combine a decent energy density with high power density, could not only serve the energy transition by stationary usage for fast-response power grid stabilization but also open opportunities for short-distance transportation use-cases like urban buses.[24−26] It has been known for over 40 years that microstructured thin-film PBA electrodes can be easily synthesized by a single-step electrodeposition process on top of a conductive template.[27−29] Yet, a fundamental understanding of their inherent rate-limiting processes is indispensable for application as high-power electrodes and to reasonably benchmark their performance against the "classic" composite electrode configuration.[30] This work comprises a systematic study of the fast-charging capability of sodium nickel hexacyanoferrate (NiHCF) thin-film electrodes prepared *via* the electrodeposition method as a function of the mass loading and film thickness. The electrochemical behavior of the thin-film electrodes is compared to a composite-type one, and their performance is analyzed with regard to the rate-determining steps during the (dis)charging process. The findings are extrapolated to ASIB full cell configurations by providing characterization data of two solely PBA-based systems. Overall, this report presents a model system aiming to provide a mechanistic understanding of the potential benefits and open challenges for thin-film PBA electrodes and thereby determine the principles for a guided design of fast-charging microstructured batteries in the future.

EXPERIMENTAL SECTION

Preparation and Electrochemical Characterization of Battery Electrodes. Thin-film electrodes were prepared by direct electrodeposition, whereas composite-type electrodes were obtained from active material powder *via* slurry casting. The two differing routines are presented in Figure 1. A list of used chemicals and their suppliers is provided in Table S1.

The electrodeposition of NiHCF was carried out in a three-electrode configuration in a custom glass setup under argon atmosphere (5.0, Westfalen AG).[12] An Ag/AgCl (SSC, 3 M KCl, B3420+, SI Analytics) reference electrode was used along with a Pt wire as a counter electrode. 1.37 cm^2 gold-on-quartz crystals (in a QCM200 microbalance, AT-cut, Au on Ti adhesive layer, Stanford Research Systems) served as the substrates for determining the mass of deposited electrode material. Alternatively, gold-on-glass substrates (Arrandee Metal) were used to prepare samples for the morphological and crystallographic examination. A VSP-300 potentiostat (Bio-Logic) was used to control and measure the electrode potentials and current.

Au substrates were rinsed with ultrapure water (18.2 MΩ, Evoqua), followed by a cleaning step using cyclic voltammetry (CV) scans (0 ↔ 1.3 V vs SSC at 50 mV s^{-1}) in 0.1 M H_2SO_4 and rinsing with ultrapure water again. The electrodeposition method was adopted from refs 31, 32, cycling the Au substrates (CV, 50 mV s^{-1}, 0 ↔ 0.9 V vs SSC) in an aqueous precursor solution consisting of 0.5 mM $NiCl_2$, 0.5 mM $K_3Fe(CN)_6$, and 0.25 M Na_2SO_4. The latter served as a supporting electrolyte to guarantee sufficient ionic conductivity of the plating solution. The process was stopped after reaching the desired mass loading as obtained from the in operando QCM measurement, terminating the CV scan at the lower potential vertex. As this yields a fully reduced electrode, the indicated mass loadings refer to intercalated NiHCF (i.e., $Na_2NiFe(CN)_6$). The samples were washed with argon-purged ultrapure water, followed by drying under a continuous argon stream for at least 1 h.

Bulky electrodes with a mass loading of 1.49 mg cm^{-2} (active material) were obtained following the routine as described by Wessells et al.[33] NiHCF nanoparticles were synthesized from an aqueous solution of 40 mM $NiCl_2$ and 20 mM $K_3Fe(CN)_6$ at 70 °C under continuous stirring. The reagents were added dropwise in equal quantities from stock solutions, and the mixture was allowed to rest for 10 min. The orange precipitate was centrifuged, washed with ultrapure water several times, and dried at 70 °C under ambient conditions. NiHCF electrodes were prepared by mixing the

https://doi.org/10.1021/acsami.3c02633
ACS Appl. Mater. Interfaces 2023, 15, 23951−23962

ACS Applied Materials & Interfaces www.acsami.org Research Article

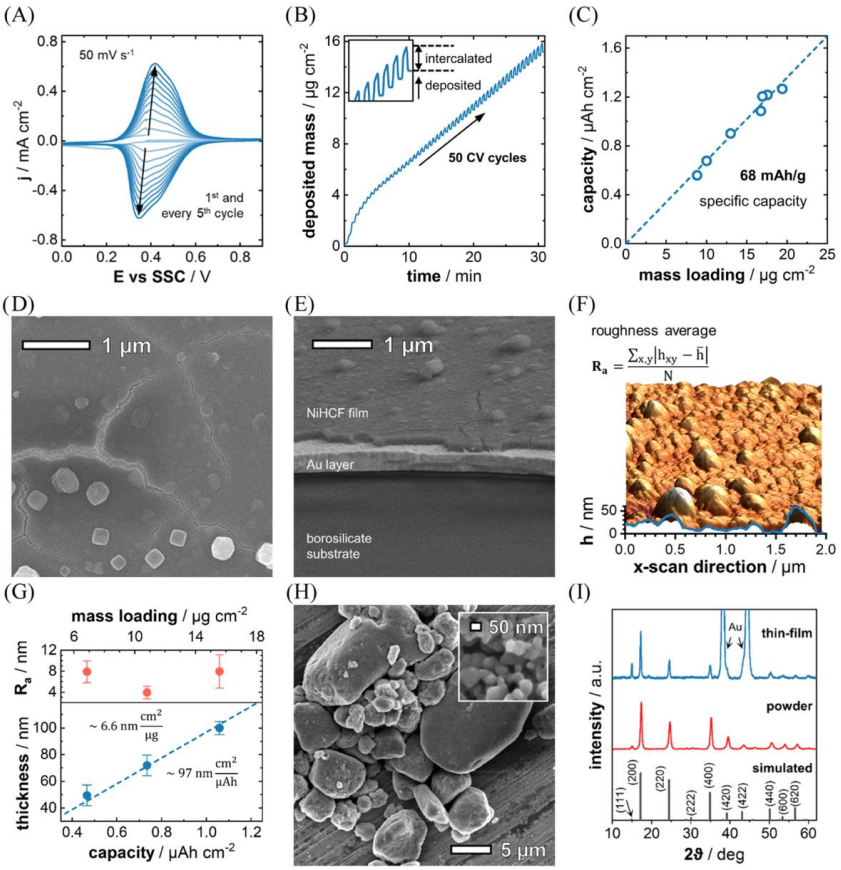

Figure 2. (A) CVs showing the electrodeposition of a NiHCF thin film and (B) the corresponding deposited mass determined *via* EQCM on an Au substrate. (C) Areal capacity obtained for different mass loadings of electrodeposited thin-film electrodes allows for the extraction of the specific capacity of NiHCF. (D) Top-view and (E) cross-sectional SEM and (F) AFM images of a NiHCF thin film show a homogeneous coating of the active material. (G) Thickness and surface roughness of the deposited electrodes as a function of the areal capacity and mass loading. (H) SEM image of NiHCF powder obtained *via* coprecipitation shows large secondary particles. (I) XRD patterns of NiHCF thin film and powder confirm their crystallographic similarity.

synthesized active material, carbon black, and poly(vinylidene fluoride) (PVDF) in a 7:2:1 weight ratio, using *N*-methyl-2-pyrrolidone (NMP) as a solvent, and coating the slurry on stainless steel foil.

The electrochemical characterization of battery electrodes was performed under an argon atmosphere in the three-electrode setup described above in 8 M $NaClO_4$, as this water-in-salt electrolyte allows a degradation-free operation of the electrodes over long cycling intervals.[9] As exemplarily shown in Figure S1, stable performance of the thin-film electrodes is obtained at low and high C-rates along with a coulombic efficiency close to 100%. A more detailed analysis and discussion of the stability of PBAs in aqueous electrolytes is available in our previous work.[10,34] Since the composite electrode had a much higher absolute capacity compared to the thin-film electrodes, a symmetric WE-CE configuration was set up using a largely oversized CE, which was previously brought to 50% state-of-charge. The measurement protocols involved CV scans at different rates and galvanostatic cycling with potential limitations at varying C-rates. Furthermore, staircase-potential electrochemical impedance spectroscopy (EIS) was performed with a probing AC amplitude of 10 mV in a frequency range between 100 kHz and 100 mHz. System stationarity was guaranteed by an appropriate waiting period before the impedance spectra acquisition, and the validity of all data within the analysis interval was verified by the Kramers−Kronig check. The spectra were fitted using the software EIS Data Analysis 1.3[35] using the electrical equivalent circuit presented in the Supporting Information.

Full Cell Battery Assemblies. Full cell prototypes were assembled in the glass cell setup described in ref 12. The respective cathode and anode thin-film electrodes were previously electrodeposited on Au-QCM substrates. The experimental details for the preparation of sodium manganese hexacyanomanganate (MnHCM) and sodium cobalt hexacyanoferrate (CoHCF) are given in the Supporting Information. After the deposition of the individual cathode and anode thin-film electrodes, the respective glass cells were connected ionically by opening the closures of an electrolyte

https://doi.org/10.1021/acsami.3c02633
ACS Appl. Mater. Interfaces 2023, 15, 23951−23962

bridge. The large spatial distance between the cathode and anode results in a high uncompensated resistance across the electrolyte bridge of ≈ 153.5 Ω in 8 M $NaClO_4$, as determined by EIS. As this setup allows the use of a reference electrode in the full cell configuration, the potential limits of the individual electrodes could be precisely controlled during cycling and were as follows: NiHCF [0.8 V ↔ 0.1 V vs SSC]−MnHCM [−1.2 V ↔ −0.6 V vs SSC] and CoHCF [1.2 V ↔ 0.6 V vs SSC]−NiHCF [0.1 V ↔ 0.6 V vs SSC].

Crystallographic and Morphological Characterization. The grazing incidence X-ray diffraction (XRD) pattern of the thin-film electrodes was acquired in the range of 2θ = 5−65° (step size = 0.026°, incident angle 1°) using PANalytical Empyrean with a Ni-filtered Cu tube (λ = 1.5406 Å, 45 kV, 40 mA) and a Pixcel3D detector. The powder XRD pattern of the synthesized NiHCF precipitate was collected on a Rigaku Miniflex (Rigaku) with a Ni-filtered Cu Kα radiation (λ = 1.5406 Å). The procedure used for powder XRD measurements consisted of a 2θ range from 10 to 62.5° and a slow-scanning step of 2° per minute. The crystal visualization and simulated diffraction pattern were obtained by modeling $Na_2NiFe(CN)_6$ with a face-centered cubic $Fm\bar{3}m$ crystal structure (see Figure S2) and a lattice constant of 10.28 Å using the software VESTA (version 3.0).[36]

The surface was scanned by atomic force microscopy (AFM) in tapping mode (scan rate 0.5 Hz) to evaluate the morphology of the films. For this purpose, an EC-STM/AFM multimode device (Veeco Instruments) with a Nanoscope IIID controller and the Nanoscope 5.31r1 software was utilized. The AFM probes were made from silicon (RTESP-300, purchased from Bruker). The roughness of the surface was analyzed by using the WSxM software.[37]

Top-view and cross-sectional images of the thin films were obtained from a field emission scanning electrode microscope (SEM, JSM-7500F, JEOL). Samples were prepared for cross-sectional imaging by mechanical rupture. All samples were directly visualized (i.e., without any coating to increase the samples' conductivity) using either in-lens (top-views) or lower (cross sections) secondary electron detector. The morphologies of NiHCF powders were acquired on an NVision40 FE-SEM (Zeiss) with a working voltage of 5.0 kV and a working distance of 7.4 mm.

The thickness of the electrodeposited NiHCF thin films was determined using a DekTak profilometer (Bruker).

■ RESULTS AND DISCUSSION

The electrodeposition method leads to a homogeneous coating of the current collector with pure additive- and binder-free active material. In general, the deposition of NiHCF thin films from the available solvated precursor ions (Na^+, $Fe(CN)_6^{3-}$, Ni^{2+}) on the electrified substrate can follow two different pathways:[38−40] (chemical) precipitation on the substrate

$$2Fe(CN)_6^{3-} + 3Ni^{2+} \rightarrow 2Ni_{1.5}Fe(CN)_6 \quad (1)$$

as well as *via* an electrochemical process involving the preceding reduction of $Fe(CN)_6^{3-}$

$$Fe(CN)_6^{3-} + e^- \rightarrow Fe(CN)_6^{4-} \quad (2)$$

$$Fe(CN)_6^{4-} + Ni^{2+} + 2Na^+ \rightarrow Na_2NiFe(CN)_6 \quad (3)$$

and

$$2Fe(CN)_6^{4-} + 3Ni^{2+} + 2Na^+ \rightarrow 2NaNi_{1.5}Fe(CN)_6 \quad (4)$$

According to Bácskai, the chemical step (eq 1) can be neglected due to its slow rate compared to the electrodeposition process (eqs 3 and 4).[38] In conclusion, the film growth occurs mainly during the cathodic scan of the CV, yielding a compound with mixed stoichiometry explaining the usually observed double- or shouldered-peak structure of NiHCF (see text in the Supporting Information and Figure S3 for further details).[38−40] The growth of NiHCF thin films on the Au-QCM substrate can be directly observed by its increasing redox current response in the CV (see Figure 2A). The respective Na^+ (de)intercalation redox reactions can be written as follows

$$Na_2NiFe^{II}(CN)_6 \rightleftarrows Na^+ + e^- + NaNiFe^{III}(CN)_6 \quad (5)$$

$$NaNi_{1.5}Fe^{II}(CN)_6 \rightleftarrows Na^+ + e^- + Ni_{1.5}Fe^{III}(CN)_6 \quad (6)$$

Without the restriction of generality, this work will consider NiHCF as the stoichiometry described in eqs 3 and 5.

The simultaneous EQCM measurement allows monitoring of the deposited electrode mass loading, which can be directly controlled by the number of CV cycles. Figure 2B shows the continuous plating of NiHCF next to a repetitive and increasing mass variation of the electrode stemming from (de)intercalating Na^+ ions. Figure 2C displays the obtained areal capacity over the respective mass loading for a series of NiHCF depositions up to 20 μg cm^{-2}. The specific capacity of the electrode material was determined to be ≈ 68 mAh g^{-1} (based on sodiated material), which matches with usually reported values.[17] The deviation from the theoretically available 85 mAh g^{-1} can be explained by defects and the nonstoichiometry of the compound due to $Fe(CN)_6^{3/4-}$ vacancies, as well as the incorporation of zeolitic and coordination water in the crystal structure.[7] The determined specific capacity was extrapolated to calculate the mass loading for thicker films (>20 μg cm^{-2}), as the QCM signal showed an increasing impact from viscous coupling for higher loadings. This can possibly damp the quartz oscillation and thereby lead to an overestimation of the deposited mass by the Sauerbrey equation. Nevertheless, there is no apparent physical or chemical reason why thicker films should have a different stoichiometry and correspondingly altered specific capacity.

The SEM images shown in Figure 2D,E reveal a uniform and rigid deposition of the battery film on the substrate surface. A repetitive crack pattern separates the film into ≈ 1 μm^2 sized segments, which might result from drying the film after deposition.[39] Sub-micron-sized particles on top of the film surface probably constitute precipitated NiHCF, which might have formed from the remains of the deposition solution precursors during the drying period, e.g., according to eq 1. The film surface is very homogeneous and comparably smooth with a roughness in the range of 5−10 nm and a horizontal structure size of around 100 nm, as shown by AFM measurements (Figure 2F,G). Therefore, it can be assumed that the film consists of continuous vertical grains with an approximate diameter of ≈ 100 nm, which might be inherited from the gold substrate. As expected, Figure 2G confirms a linear relationship between the film thickness and the mass loading with a 6.6 nm/(μg cm^{-2}) slope. Our experiments yielded maximum possible mass loadings on plain gold substrates of approximately 100 μg cm^{-2}, which corresponds to ≈ 660 nm thick films. Thicker films showed low mechanical stability and even detached from the substrate in some cases.

As usually reported for the chemical synthesis routine, NiHCF precipitates as irregular nanoparticles with a size in the order of 50 nm (see Figure 2H).[33,41] However, these particles agglomerated to form bulky chunks extending several micrometers. This structure was maintained after the fabrication of the composite electrodes *via* slurry casting (see Figure S4). NiHCF powder and thin-film material yield a similar X-ray diffraction pattern matching very well with that of simulated

https://doi.org/10.1021/acsami.3c02633
ACS Appl. Mater. Interfaces 2023, 15, 23951−23962

ACS Applied Materials & Interfaces www.acsami.org Research Article

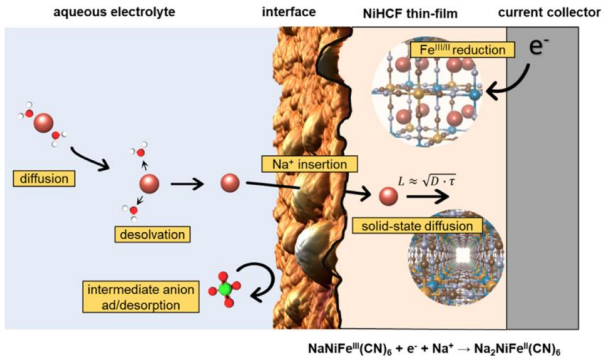

Figure 3. Scheme of the individual steps involved during the insertion of Na^+ ions from the electrolyte into the NiHCF electrode as a result of $Fe^{III/II}$ reduction. It should be noted that the solvation shell only consists of a small number of H_2O molecules due to the strong hydration of the highly concentrated salt solution (8 M $NaClO_4$).

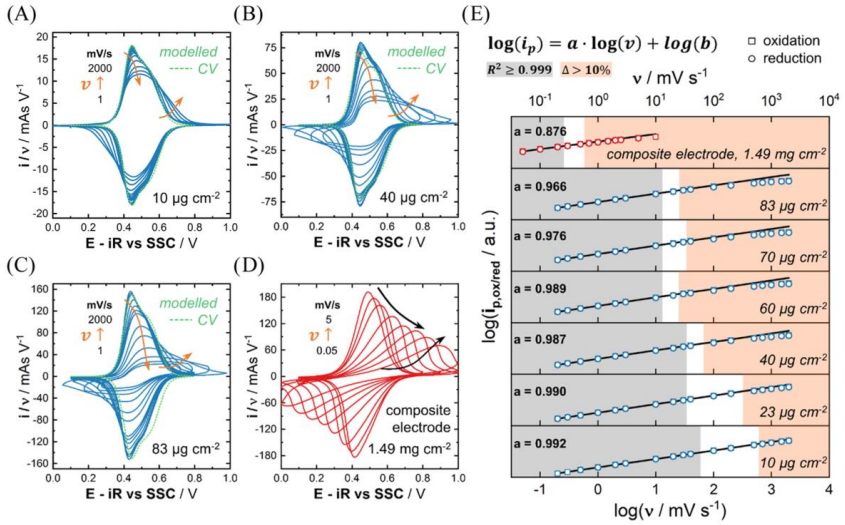

Figure 4. Normalized CVs of (A−C) NiHCF thin films with varying mass loadings along with their respective modeled curves and (D) as composite electrode at different scan rates. (E) Resulting dependence of the peak currents on the scan rate. For low to medium scan rates (gray-shaded area), the peak current depends linearly on the scan rate as seen from the fitting lines, indicating fast kinetic control of the Na^+ de/insertion.

$Na_2NiFe(CN)_6$ with a face-centered cubic $Fm\bar{3}m$ structure (see Figure 2I). Lattice constants of 10.27 and 10.21 Å were obtained from the (200) reflections from the thin film and powder, respectively, which agrees with previously reported values.[17,33,41] The absence of diffraction peaks deviating from the simulated pattern confirms the chemical purity of the synthesized thin-film and powder samples. In conclusion, the electrodeposition and coprecipitation routine result in a similar material without any undesired deviating side products. The higher intensity of the (111) peak obtained for the thin film might come from a preferential growth direction of the polycrystalline grains on the substrate.

Figure 3 shows a schematic representation of the different charge and mass transport processes involved in the intercalation of sodium into NiHCF thin-film electrodes. We have shown in previous works that a simple single-step reaction cannot describe these holistically, but they rather follow a complex multistep reaction with different time constants. These involve the reduction of $Fe^{III/II}$, the intermediate ad/desorption of electrolyte anions, and the insertion of Na^+ across the electrode−electrolyte interface.[31,32,42] This so-called "three-step mechanism" is further explained in the Supporting Information. The charge propagation of the intercalated Na^+ ions within the NiHCF lattice happens *via* solid-state diffusion to entirely fill up all available sites of the active material. In general, a Na^+ desolvation step precedes the intercalation of the ion into the host material. As 8 M $NaClO_4$ was used as the electrolyte in this work to allow a degradation-free cycling of

https://doi.org/10.1021/acsami.3c02633
ACS Appl. Mater. Interfaces 2023, 15, 23951−23962

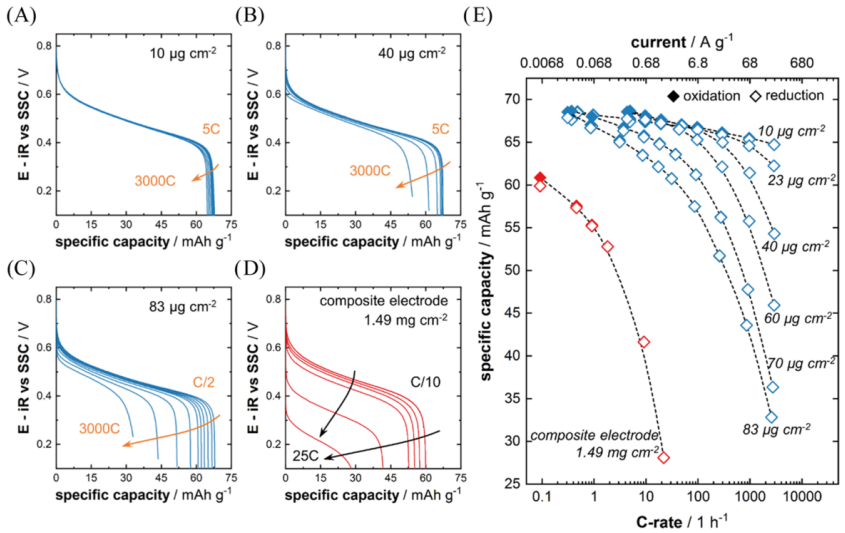

Figure 5. Galvanostatic discharge curves at different C-rates obtained for (A–C) NiHCF thin films with varying mass loadings and (D) composite electrode. Horizontal arrows indicate the decreasing capacity, whereas the vertical arrow additionally shows the increasing hysteresis in the case of the composite electrode. (E) Capacity retention for a wide range of tested C-rates for the different mass loadings. The dashed lines serve as a guide to the eye.

the active material,[9,10] only ≈ 2 H_2O molecules exist for each Na^+ ion. This results from the fact that the volume ratio of H_2O:solution drops to ≈ 62% due to the high amount of $NaClO_4$ salt. However, it should be mentioned that the actual structure of the solvation sheath is much more complicated than in this simplified sketch, as such "water-in-salt" electrolytes somewhat resemble a liquified salt rather than a classical salt solution.[43−45] The availability of sodium ions at the electrode surface is replenished by diffusion from the bulk electrolyte. In general, the achievable (dis)charging speed of the battery material is determined by the individual rates and complex interplay of the presented processes. In this work, we performed CV scans, galvanostatic cycling at different rates, and impedance spectroscopy to investigate the kinetics of charge and mass transport during (de)intercalation and thereby identify the rate-limiting steps for battery operation of NiHCF thin-film vs composite electrodes.

Figure 4 shows the CVs of NiHCF thin-film electrodes with mass loadings of 10 μg cm^{-2} (A), 40 μg cm^{-2} (B), and 83 μg cm^{-2} (C) at scan rates between 1 and 2000 mV s^{-1}. The voltammograms were corrected to compensate for the ohmic drop stemming from the uncompensated resistance, which is mostly associated with the ionic conductivity of the electrolyte. In general, the CV shape is characterized by a very reversible redox peak with $\Delta E_{peak-peak}$ in the range of a few mV for all mass loadings. From the scan-rate-normalized current curves, a linear relationship between the scan rate ν and the peak current $i_{p,ox/red}$ is observed for low to medium cycling rates. The dependence of the peak current on the scan rate can, in general, be described by the empirical relation given in eq 7, where the exponent a yields information on the processes governing the current response of the investigated system[46]

$$i_{p,ox/red} = b \cdot \nu^a \rightarrow \log(i_{p,ox/red}) = a \log(\nu) + \log(b) \quad (7)$$

As shown in Figure 4E, a value of $a \approx 1$ is obtained over the entire range of mass loadings for the thin films up to considerably high scan rates (gray-shaded area). This linear dependency of $i(\nu)$ is similar to the capacitive response usually associated with the adsorption of surface-near ionic species in liquid electrolytes.[47] For the case of the herein investigated thin-film electrodes, it can be concluded that the charge transfer kinetics and the mass transport (i.e., diffusion of Na^+) are very fast and therefore do not affect the shape of CV.[48] This implies that the coupled ion and electron transfer dynamics are governed by fast reversible kinetics which require a negligible driving force, i.e., the intercalation isotherm can be used to describe them.[47,49,50] This is reflected by the great accordance of the CVs at slow scan rates with the modeled response of the NiHCF thin-film electrodes in quasi-equilibrium regardless of the mass loading. The theoretical background of the modeling approach is elaborated in detail in the Supporting Information along with employed parameters. It should be noted that the calculated $i(E)/\nu$ characteristics were linearly extrapolated from the one at 10 μg cm^{-2} for higher mass loadings, confirming uniform applicability of the quasi-equilibrium approach even at high electrode thicknesses.

The linear dependency breaks down (red-shaded area) once higher scan rates are reached. This is reflected by the contraction of the normalized CV curves and the emergence of a "tail"-like current decay after the peak potential (see arrows in Figure 4A–C). The proportionality factor of eq 7 approaches $a \approx 0.5$, whereas $\Delta E_{peak-peak}$ increases significantly toward 50–60 mV for higher scan rates, as exemplarily shown for the 40 μg cm^{-2} film in Figure S5. Such CV characteristics indicate the transition from kinetic to mass transport control when increasing the scan rate, where the Na^+ concentration

https://doi.org/10.1021/acsami.3c02633
ACS Appl. Mater. Interfaces 2023, 15, 23951−23962

gradient in the NiHCF thin-film electrode can no longer be neglected.[48,50−53]

Remarkably, the deviation from $i \propto \nu$ is observed at lower scan rates when increasing the mass loadings of the thin-film electrodes. Considering the propagation of intercalated Na^+ ions within the host structure, it can be easily understood that solid-state diffusion constitutes the limiting process for the charging speed based on the active material geometry and imposed rate (see Figure 3). Supposing that the thin-film electrode must be entirely filled up with Na^+ ions during the reduction of NiHCF, the characteristic time constant can be described by

$$\tau = \frac{L^2}{D_{Na^+,\,NiHCF}} \tag{8}$$

where L is the diffusion length, specified by the film thickness, and $D_{Na^+,\,NiHCF}$ is the apparent diffusion coefficient of Na^+ inside NiHCF.[50] At sufficiently high rates, the available reaction time becomes too short to maintain a uniform Na^+ concentration within the NiHCF film as the diffusion length becomes smaller than the film thickness.[39] Approximating τ by the duration of a half-cycle of the CV for the different mass loadings at the respective scan rate, where $i(\nu)$ shows a significant deviation from the kinetic regime (red-shaded area in Figure 4E), $D_{Na^+,\,NiHCF} \approx 10^{-11}-10^{-10}$ cm^2 s^{-1} is obtained (see Figure S6A). Mass transport limitations stemming from the diffusion of sodium in the electrolyte can be neglected, as $D_{Na^+,\,solution} \approx 10^{-6}-10^{-5}$ cm^2 s^{-1} in 8 M $NaClO_4$,[45] and therefore, no build-up of a Na^+ concentration gradient is expected due to its fast diffusion in the liquid phase. Furthermore, the highly concentrated solution provides an excess reservoir of Na^+ ions for intercalation in the electrode vicinity.

Analogously, we performed a set of galvanostatic cycling experiments at different rates. Figure 5 shows the discharge curves of NiHCF thin-film electrodes with mass loadings of 10 μg cm^{-2} (A), 40 μg cm^{-2} (B), and 83 μg cm^{-2} (C). The potentials were corrected for the uncompensated resistance. In general, all discharge curves show almost no potential hysteresis up to very high rates of 3000C. Generally, a rate of 1C corresponds to a (dis)charging time of 1 h. This proves that the interfacial charge transfer kinetics is fast enough to not pose a limiting factor to the system. Sufficiently thin NiHCF film electrodes can be fully (dis)charged within a few seconds without significant capacity losses. At a very high rate of 3000C (1.2 s for full (dis)charge) a capacity retention of 95% is achieved for a mass loading of 10 μg cm^{-2}, which corresponds to a film thickness of ≈ 66 nm. For higher mass loadings and, thus, thicker films, the achievable intercalation capacity drops systematically if higher C-rates are applied during (dis)-charging (Figure 5E). At a mass loading of 70 μg cm^{-2} with an approximate film thickness of ≈ 460 nm, 95% of the capacity remains at a rate of 18C (200 s), while > 80% is obtained at 270C (≈13 s).

Again, this characteristic is typical for the transition to diffusional rate control beyond "too high" (dis)charging rates.[50,54] Taking a capacity threshold of C/C_0 = 95% as the transition point, where the solid-state diffusion of intercalated Na^+ ions proceeds too slowly to keep up with the imposed cycling rate, eq 8 yields $D_{Na^+,\,NiHCF} \approx 10^{-12}-10^{-10}$ cm^2 s^{-1} (see Figure S6B), which is consistent with the values obtained from the CV data. Certainly, such treatment reflects an over-simplified model of the thin-film system. It can, therefore, only serve as an approximation, but the obtained results agree very well with diffusion coefficients reported in the literature for PBAs.[50] It should be mentioned that the fast-charging capability of the thin films does not result from the high-speed diffusion properties of Na^+ within the PBA lattice but rather from the short diffusion length provided by the microstructured electrode material.[30] In summary, we found that NiHCF thin-film electrodes with a thickness below ≈ 500 nm can be fully (dis)charged within 1 min (60C) while retaining 90% of their capacity. The charge-discharge characteristics of the thin-film electrodes can be described by quasi-equilibrium kinetics up to very high rates until mass transport limitations set in. Accordingly, the diffusion-time approach reflected in eq 8 can serve as a practical guideline to predict the limits of the fast-charging capability of PBA thin films, or in turn, define the maximum thickness for a desired rate performance ($L < \sqrt{\tau \cdot D}$).[20]

In contrast to the fast cycling behavior of the NiHCF thin films, an inferior performance is found for the slurry-casted composite electrode with a probably more commercially relevant mass loading of 1.49 mg cm^{-2}. As shown in Figure 4D,E, the CVs at different scan rates are characterized by a nonproportionality of $i(\nu)$ and a high $\Delta E_{peak-peak}$, which increases strongly with ν. Such behavior can be ascribed to a "mixed" rate control where both diffusion and charge transfer are slow enough to constitute limiting processes for the intercalation dynamics.[50] Similarly, the galvanostatic discharge curves at different rates exhibit severe hysteresis with increasing currents (see Figure 5D). The iR-corrected polarization curves shown in Figure S7 represent a dependence of the overpotential similar to the one expected for a process controlled by charge transfer kinetics (CT, η_{CT}). However, since the total overpotential is $\eta - \eta_{iR} = \eta_{CT} + \eta_{diffusion}$, the individual contributions to the electrode polarization from charge transfer and mass transport cannot be differentiated without supplementary techniques.[55] Therefore, impedance spectroscopy was performed to isolate and quantify the effect of the charge transfer on the overall system limitation. Figure S8 shows the obtained impedance spectra of a NiHCF thin-film electrode (Figure S8A) and composite electrode (Figure S8B), which were fitted with a physical model describing the multistep ion de/insertion mechanism of intercalation-type battery electrodes (Figure S8C, see Supporting Information text for further information). The mass-normalized charge transfer resistance was found to be two orders of magnitude higher for the composite electrode over the entire electrochemically active region of NiHCF (Figure S8D), consistently explaining the strong polarization of the composite electrode by η_{CT} compared to the hysteresis-free performance of the thin-film samples.

Besides the strong hysteresis, the available capacity drops significantly for higher rates (see Figure 5E). A much higher rate capability would be expected, considering that the primary NiHCF particles have a size of ≈ 50 nm, which is in the order of the investigated thin-film thicknesses. Taking an approximate solid-state diffusion coefficient for intercalated sodium in the order of 10^{-11} cm^2 s^{-1}, the diffusion length is in the order of a few μm at a rate of 1C. Therefore, Na^+ should be able to penetrate the active material entirely. However, micrometer-sized agglomerated secondary NiHCF particles were observed for both the precipitate and the composite electrodes (see Figures 2H and S4), which sufficiently explains its inferior

https://doi.org/10.1021/acsami.3c02633
ACS Appl. Mater. Interfaces 2023, 15, 23951−23962

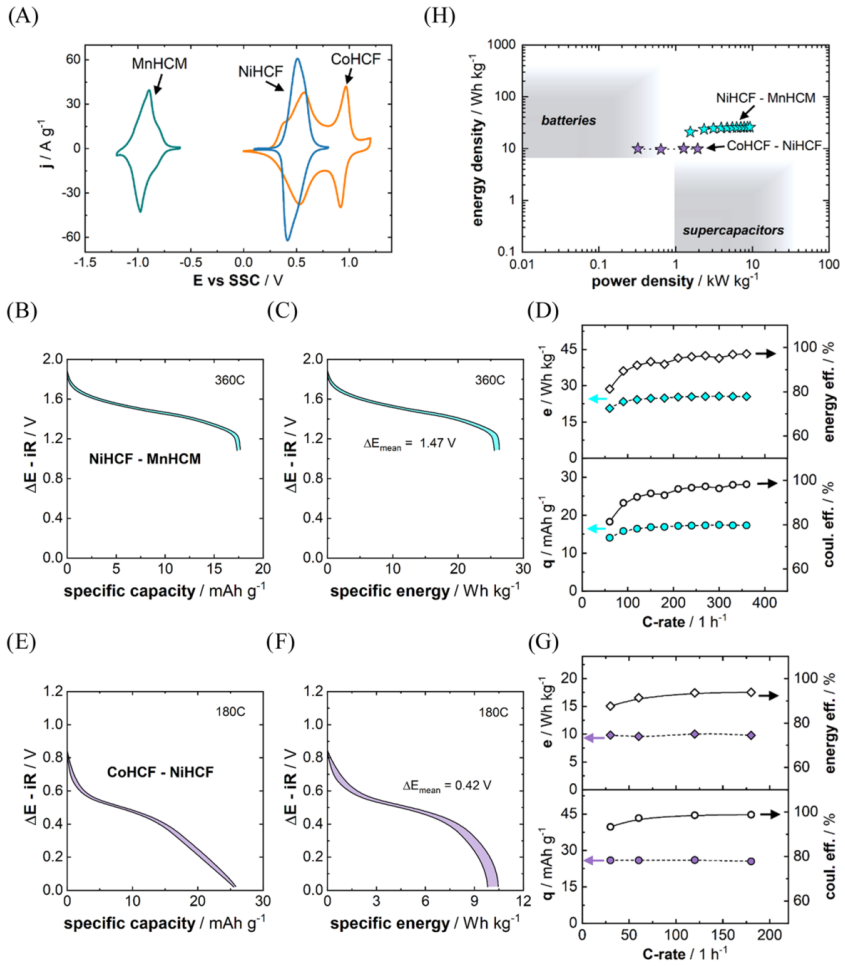

Figure 6. (A) Individual CVs of the PBA thin-film electrodes employed for assembling the two entirely PBA-based model ASIBs presented in this work. iR-corrected full cell voltage versus the specific capacity and specific energy for the NiHCF–MnHCM (B, C) and CoHCF–NiHCF (E, F) batteries at a selected high (dis)charging rate in galvanostatic mode. (D, G) Respective rate capabilities of the specific discharge capacity with the corresponding coulombic efficiencies (bottom) and specific energy with the corresponding energy efficiencies (top) of the model batteries up to very high C-rates. The dashed and solid lines serve as a guide to the eye. The resulting power and energy density qualifies the presented full cells as hybrid battery–supercapacitor systems as visible from the schematic Ragone plot (H).

performance as the effective diffusion pathway is extremely increased. Furthermore, these large agglomerates have a lower surface area to mass ratio compared to smaller sub-micron-sized geometries or thin films, which results in a higher mass-normalized charge transfer resistance due to the lower specific surface area available for ion de/insertion.[17,56] Therefore, the strong polarization of the composite electrode is in accordance with its low rate capability. This effect could be further aggravated by blocking of active sites for ion transfer at NiHCF particles within the composite electrode, as well as poor contact with the current collector metal foil.

Two full cell configurations were set up and characterized to extrapolate the fast-charging properties of PBA thin-film electrodes to a battery model system. Next to NiHCF, which was used as a model system in this study, Figure 6A shows the CVs of sodium manganese hexacyanomanganate (MnHCM) and sodium cobalt hexacyanoferrate (CoHCF), which were obtained as thin-film electrodes *via* electrodeposition similar to NiHCF, as described in the literature.[31,57] The very low redox potential of the $Na_xMn^{II}Mn^{I/II}(CN)_6$ transition makes MnHCM a promising anode material for ASIBs.[57−60] Similar to NiHCF, we found fast Na^+ insertion, which enables a high rate capability of MnHCM thin-film anodes (see Figure S9).

https://doi.org/10.1021/acsami.3c02633
ACS Appl. Mater. Interfaces 2023, 15, 23951−23962

Paired with a NiHCF cathode, a full cell discharge voltage of 1.47 V and a specific capacity of ≈ 17.3 mAh g^{-1} is achieved based on the total active material masses of both cathode and anode, which yields an energy density of 25.5 Wh kg^{-1} (see Figure 6B,C). The full cell reaction of the NiHCF−MnHCM battery is shown in eq 9

$$Na_2NiFe^{II}(CN)_6 + Na_2Mn^{II}Mn^{II}(CN)_6(\text{discharged}) \rightleftarrows NaNiFe^{III}(CN)_6 + Na_3Mn^{II}Mn^{I}(CN)_6(\text{charged}) \quad (9)$$

As shown in Figure 6D, the specific capacity remains constant even up to very fast rates of 360C, which corresponds to only 10 s for a full (dis)charge. Although the coulombic efficiency is ≈ 98% for higher rates, it significantly drops when reducing the charging speed, which is reflected by a drop in the discharging capacity. We assign this detrimental behavior to parasitic HER and self-discharge reactions of the MnHCM thin-film electrode in the presence of trace amounts of oxygen in the electrolyte (see Figure S10A−E and corresponding discussion in the Supporting Information). Since the available surface area strictly controls the rate of both of these processes, its relative impact was observed to decrease with higher film thicknesses as the specific surface area decreases (see Figure S10F). Furthermore, faster (dis)charging rates leave less time for such parasitic processes, which explains why they are only observed toward lower C-rates. It should be mentioned that such extraordinarily high voltage for an aqueous system is only enabled by the employed "water-in-salt" electrolyte.[44] Parasitic reactions at the low-potential anode could be even more suppressed by further electrolyte modifications to enhance its stable operation window.[61] However, further research will be necessary to optimize the reversibility of the MnHCM electrode. Nevertheless, the beneficial fast-charging behavior of the individual electrodes is maintained in the full cell configuration. The energy density remains unaffected even at high rates, with the energy efficiency approaching 98% due to the almost negligible (dis)charge curves' hysteresis.

As another example of an ASIB based on thin-film PBAs, a CoHCF cathode was paired with NiHCF, which served as the anode in this case. In general, the CV of CoHCF features a set of two redox peaks, which are associated with the activity of both $Co^{II/III}$ and $Fe^{II/III}$ in the lattice.[16]

In order to maintain the full cell driving force, only the $Na_xCo^{III}Fe^{II/III}(CN)_6$ transition was allowed by restricting the individual electrode potential ranges of CoHCF and NiHCF. The mean discharge voltage of this system is 0.42 V, and a specific capacity of 26 mAh g^{-1} is obtained based on the active materials (see Figure 6E). As shown in Figure 6F, the resulting energy density is 10 Wh kg^{-1} at 180C, which results from the lower working voltage compared to the NiHCF−MnHCM cell. Nevertheless, the discharge capacity, as well as the energy density remain stable at high rates (see Figure 6G). Although a high coulombic efficiency of 98.8% is achieved at high rates, the energy efficiency is below 94%, which can be explained by chemically irreversible processes toward the higher potential limit of the CoHCF cathode. Similar to the MnHCM anode, this effect is stronger at lower C-rates. The cell reaction is given in eq 10

$$NaCo^{III}Fe^{II}(CN)_6 + NaNiFe^{III}(CN)_6(\text{discharged}) \rightleftarrows Co^{III}Fe^{III}(CN)_6 + Na_2NiFe^{II}(CN)_6(\text{charged}) \quad (10)$$

Since the presented model cells can be operated at very high C-rates, the resulting power density reaches 1−10 kW kg^{-1} without any drop in the energy density. As visible from Figure 6H, this behavior qualifies such thin-film PBA materials as a hybrid battery−supercapacitor system.[24,62] Remarkably, they combine the beneficial properties of batteries, which are the provision of a stable operating voltage next to a decent energy density for an aqueous system, with the extremely high rate capability of supercapacitors.

We are aware of the fact that the achieved mass loadings of the thin-film electrodes presented in this work (<100 $\mu g\ cm^{-2}$) are too low for commercially competitive batteries (several mg cm^{-2}).[63,64] However, it should be kept in mind that the employed gold substrates for the electrodeposition had a planar geometry to allow an unambiguous characterization of the model system. By using a lightweight, conductive, and microporous material as the substrate for the electrodeposition technique, the achievable total mass loading might be increased significantly by offering a real surface largely exceeding its geometric footprint.[13,14,65] First studies identified carbon cloth as a suitable template for the preparation of binder-free PBA electrodes.[15,66−70] Dedicated studies will be needed in the future to scale up the mass loading while preserving the fast-charging capability of PBA-based thin-film electrodes.

■ SUMMARY AND CONCLUSIONS

This work aimed at introducing a model system to elaborate the high-power properties of thin-film Prussian blue analogue electrodes prepared *via* a facile, single-step electrodeposition method in comparison to "traditional" composite electrodes. Their fast-charging capability was investigated by systematically varying the mass loading and, therefore, the thickness of the active material. It was found that their superior cycling performance originates from very fast quasi-equilibrium kinetics. This allows a loss-free increase of the charging speed up to extremely high rates until the diffusional ion transport in the PBA lattice is no longer fast enough to fill up the entire active material. The respective rate where the electrode behavior transits to mass transport limited mode can be approximated from the diffusion coefficient and the film thickness. This relation can also be used as a practical guideline for the future design of thin-film electrodes with a desired rate capability. It was found that NiHCF electrodes with a thickness below ≈ 500 nm can be fully charged within 1 min (60C) with a capacity retention above 90%. Entirely thin-film PBA-based ASIBs were assembled as model systems, showing a hysteresis- and loss-free performance even when (dis)charging the cells in less than a minute. The full cells delivered energy densities in the range of 10−25 Wh kg^{-1} at extremely high power densities of up to 10 kW kg^{-1}, which motivates their design as a hybrid battery−supercapacitor system.

However, further research will be necessary to increase the overall mass loading of such electrodes toward a commercially relevant scale while maintaining their beneficial fast-charging properties based on the limitations presented herein. Such endeavors should also improve cycling reversibility toward lower imposed rates by suppressing parasitic reactions, a common challenge in high-voltage aqueous batteries. Microstructured, conductive templates with a high intrinsic surface area could be a promising research direction for increasing the mass loading obtained from the electrodeposition technique.

https://doi.org/10.1021/acsami.3c02633
ACS Appl. Mater. Interfaces 2023, 15, 23951−23962

Nevertheless, the presented model systems serve as proof that thin-film PBA-based ASIBs might have great potential for high-power applications that only require a decent energy density, such as power grid stabilization or short-distance electric mobility.

■ ASSOCIATED CONTENT

Supporting Information

The Supporting Information is available free of charge at https://pubs.acs.org/doi/10.1021/acsami.3c02633.

Information on used chemicals; experimental details on the synthesis of CoHCF and MnHCM thin-film electrodes; cycling stability data; crystal structure of NiHCF; modeling of charge-discharge characteristics in quasi-equilibrium; SEM image of composite electrode; additional CV analysis; apparent solid-state diffusion coefficients; polarization analysis of composite electrode; impedance analysis; and detailed characterization of MnHCM (PDF)

■ AUTHOR INFORMATION

Corresponding Author

Aliaksandr S. Bandarenka − *Physics of Energy Conversion and Storage, Physik-Department, Technische Universität München, 85748 Garching bei München, Germany;* orcid.org/0000-0002-5970-4315; Email: bandarenka@ph.tum.de

Authors

Xaver Lamprecht − *Physics of Energy Conversion and Storage, Physik-Department, Technische Universität München, 85748 Garching bei München, Germany*

Philipp Zellner − *Physics of Energy Conversion and Storage, Physik-Department, Technische Universität München, 85748 Garching bei München, Germany*

Göktug Yesilbas − *Physics of Energy Conversion and Storage, Physik-Department, Technische Universität München, 85748 Garching bei München, Germany*

Ludek Hromadko − *Central European Institute of Technology, Brno University of Technology, 61200 Brno, Czech Republic; Center of Materials and Nanotechnologies, Faculty of Chemical Technology, University of Pardubice, 53002 Pardubice, Czech Republic*

Philipp Moser − *Physics of Energy Conversion and Storage, Physik-Department, Technische Universität München, 85748 Garching bei München, Germany*

Philipp Marzak − *Physics of Energy Conversion and Storage, Physik-Department, Technische Universität München, 85748 Garching bei München, Germany;* orcid.org/0000-0003-3372-0816

Shujin Hou − *Physics of Energy Conversion and Storage, Physik-Department, Technische Universität München, 85748 Garching bei München, Germany*

Richard Haid − *Physics of Energy Conversion and Storage, Physik-Department, Technische Universität München, 85748 Garching bei München, Germany*

Florian Steinberger − *Physics of Energy Conversion and Storage, Physik-Department, Technische Universität München, 85748 Garching bei München, Germany*

Tim Steeger − *Physics of Energy Conversion and Storage, Physik-Department, Technische Universität München, 85748 Garching bei München, Germany*

Jan M. Macak − *Central European Institute of Technology, Brno University of Technology, 61200 Brno, Czech Republic; Center of Materials and Nanotechnologies, Faculty of Chemical Technology, University of Pardubice, 53002 Pardubice, Czech Republic*

Complete contact information is available at: https://pubs.acs.org/10.1021/acsami.3c02633

Author Contributions

X.L.: conceptualization, methodology, laboratory research (general), data analysis (general), data curation, visualization of data, writing the draft of the manuscript. P.Z.: methodology, laboratory research on NiHCF thin films, analysis of corresponding data, review and editing of the manuscript. G.Y.: laboratory research on NiHCF composite electrodes, analysis of impedance data. L.H.: laboratory research (SEM, XRD). P.M.: laboratory research on full cells, analysis of corresponding data. P.M.: laboratory research on full cells, analysis of corresponding data, review and editing of the manuscript. S.H.: laboratory research (SEM, XRD), analysis of corresponding data, review and editing of the manuscript. R.H.: laboratory research (AFM), analysis of corresponding data, review and editing of the manuscript. F.S.: laboratory research on MnHCM thin films, analysis of corresponding data. T.S.: laboratory research on MnHCM thin films, analysis of corresponding data, review and editing of the manuscript. J.M.M.: funding acquisition, resources, reviewing of the manuscript. A.S.B.: conceptualization, funding acquisition, resources, reviewing and editing of manuscript, supervision.

Notes

The authors declare no competing financial interest.

■ ACKNOWLEDGMENTS

Financial support from German Research Foundation (DFG) under Germany's Excellence Strategy-EXC 2089/1-390776260, cluster of excellence "e-conversion" is gratefully acknowledged. SEM and XRD analyses were carried out with the support of CEMNAT open-access Infrastructure (the Ministry of Education, Youth and Sports of the Czech Republic, LM2018103, 2020−2022).

■ REFERENCES

(1) Li, M.; Lu, J.; Chen, Z.; Amine, K. 30 years of lithium-ion batteries. *Adv. Mater.* **2018**, *30*, No. 1800561.

(2) Zu, C.; Ren, Y.; Guo, F.; Yu, H.; Li, H. A Reflection on lithium-ion batteries from a lithium-resource perspective. *Adv. Energy Sustainability Res.* **2021**, *2*, No. 2100062.

(3) Peters, I. M.; Breyer, C.; Jaffer, S. A.; Kurtz, S.; Reindl, T.; Sinton, R.; Vetter, M. The role of batteries in meeting the PV terawatt challenge. *Joule* **2021**, *5*, 1353−1370.

(4) Sawicki, M.; Shaw, L. L. Advances and challenges of sodium ion batteries as post lithium-ion batteries. *RSC Adv.* **2015**, *5*, 53129−53154.

(5) Bin, D.; Wang, F.; Tamirat, A. G.; Suo, L.; Wang, Y.; Wang, C.; Xia, Y. Progress in aqueous rechargeable sodium-ion batteries. *Adv. Energy Mater.* **2018**, *8*, No. 1703008.

(6) Peng, J.; Zhang, W.; Liu, Q.; Wang, J.; Chou, S.; Liu, H.; Dou, S. Prussian blue analogues for sodium-ion batteries: past, present, and future. *Adv. Mater.* **2022**, *34*, No. 2108384.

(7) Wang, B.; Han, Y.; Wang, X.; Bahlawane, N.; Pan, H.; Yan, M.; Jiang, Y. Prussian blue analogs for rechargeable batteries. *iScience* **2018**, *3*, 110−133.

(8) Yi, H.; Qin, R.; Ding, S.; Wang, Y.; Li, S.; Zhao, Q.; Pan, F. Structure and properties of Prussian blue analogues in energy storage

and conversion applications. *Adv. Funct. Mater.* **2021**, *31*, No. 2006970.
(9) Pasta, M.; Wessells, C. D.; Liu, N.; Nelson, J.; McDowell, M. T.; Huggins, R. A.; Toney, M. F.; Cui, Y. Full open-framework batteries for stationary energy storage. *Nat. Commun.* **2014**, *5*, No. 4007.
(10) Lamprecht, X.; Speck, F.; Marzak, P.; Cherevko, S.; Bandarenka, A. S. Electrolyte effects on the stabilization of Prussian blue analog electrodes in aqueous sodium-ion batteries. *ACS Appl. Mater. Interfaces* **2022**, *14*, 3515−3525.
(11) Wang, B.; Wang, X.; Liang, C.; Yan, M.; Jiang, Y. An all-Prussian-blue-based aqueous sodium-ion battery. *ChemElectroChem* **2019**, *6*, 4848−4853.
(12) Marzak, P.; Moser, P.; Schreier, S.; Scieszka, D.; Yun, J.; Schneider, O.; Bandarenka, A. S. A cell for controllable formation and in operando electrochemical characterization of intercalation materials for aqueous metal-ion batteries. *Small Methods* **2019**, *3*, No. 1900445.
(13) Zhou, G.; Li, F.; Cheng, H. M. Progress in flexible lithium batteries and future prospects. *Energy Environ. Sci.* **2014**, *7*, 1307−1338.
(14) Jin, T.; Han, Q.; Jiao, L. Binder-free electrodes for advanced sodium-ion batteries. *Adv. Mater.* **2020**, *32*, No. 1806304.
(15) Zhang, L.; Qin, X.; Zhao, S.; Wang, A.; Luo, J.; Wang, Z. L.; Kang, F.; Lin, Z.; Li, B. Advanced matrixes for binder-free nanostructured electrodes in lithium-ion batteries. *Adv. Mater.* **2020**, *32*, No. 1908445.
(16) Wu, X.; Wu, C.; Wei, C.; Hu, L.; Qian, J.; Cao, Y.; Ai, X.; Wang, J.; Yang, H. Highly crystallized $Na_2CoFe(CN)_6$ with suppressed lattice defects as superior cathode material for sodium-ion batteries. *ACS Appl. Mater. Interfaces* **2016**, *8*, 5393−5399.
(17) Park, S.; Kim, J.; Yi, S. H.; Chun, S. E. Coprecipitation temperature effects of morphology-controlled nickel hexacyanoferrate on the electrochemical performance in aqueous sodium-ion batteries. *ChemSusChem* **2021**, *14*, 1082−1093.
(18) Camacho, P. S.; Wernert, R.; Duttine, M.; Wattiaux, A.; Rudola, A.; Balaya, P.; Croguennec, L.; et al. Impact of synthesis conditions in Na-Rich Prussian blue analogues. *ACS Appl. Mater. Interfaces* **2021**, *13*, 42682−42692.
(19) Chen, R.; Huang, Y.; Xie, M.; Wang, Z.; Ye, Y.; Li, L.; Wu, F. Chemical inhibition method to synthesize highly crystalline Prussian blue analogs for sodium-ion battery cathodes. *ACS Appl. Mater. Interfaces* **2016**, *8*, 31669−31676.
(20) Weiss, M.; Ruess, R.; Kasnatscheew, J.; Levartovsky, Y.; Levy, N. R.; Minnmann, P.; Stolz, L.; Waldmann, T.; Wohlfahrt-Mehrens, M.; Aurbach, D.; Winter, M.; Ein-Eli, Y.; Janek, J. Fast charging of lithium-ion batteries: a review of materials aspects. *Adv. Energy Mater.* **2021**, *11*, No. 2101126.
(21) He, B.; Zhang, Q.; Pan, Z.; Li, L.; Li, C.; Ling, Y.; Wang, Z.; Chen, M.; Wang, Z.; Yao, Y.; Ling, Q.; Sun, L.; Wang, J.; Wie, L. Freestanding metal−organic frameworks and their derivatives: an emerging platform for electrochemical energy storage and conversion. *Chem. Rev.* **2022**, *122*, 10087−10125.
(22) Lin, Y.; Zhang, L.; Xiong, Y.; Wei, T.; Fan, Z. Toward the design of high-performance supercapacitors by Prussian blue, its analogues and their derivatives. *Energy Environ. Mater.* **2020**, *3*, 323−345.
(23) Zhang, F.; Qi, L. Recent progress in self-supported metal oxide nanoarray electrodes for advanced lithium-ion batteries. *Adv. Sci.* **2016**, *3*, No. 1600049.
(24) Zuo, W.; Li, R.; Zhou, C.; Li, Y.; Xia, J.; Liu, J. Battery-supercapacitor hybrid devices: recent progress and future prospects. *Adv. Sci.* **2017**, *4*, No. 1600539.
(25) Şahin, M.; Blaabjerg, F.; Sangwongwanich, A. A comprehensive review on supercapacitor applications and developments. *Energies* **2022**, *15*, 674.
(26) Shin, J.; Choi, J. W. Opportunities and reality of aqueous rechargeable batteries. *Adv. Energy Mater.* **2020**, *10*, No. 2001386.
(27) Neff, V. D. Electrochemical oxidation and reduction of thin films of Prussian blue. *J. Electrochem. Soc.* **1978**, *125*, 886.
(28) Itaya, K.; Uchida, I.; Neff, V. D. Electrochemistry of polynuclear transition metal cyanides: Prussian blue and its analogues. *Acc. Chem. Res.* **1986**, *19*, 162−168.
(29) Karyakin, A. A. Prussian blue and its analogues: electrochemistry and analytical applications. *Electroanalysis* **2001**, *13*, 813−819.
(30) Komayko, A. I.; Arkharova, N. A.; Presnov, D. E.; Levin, E. E.; Nikitina, V. A. Resolving the seeming contradiction between the superior rate capability of Prussian blue analogues and the extremely slow ionic diffusion. *J. Phys. Chem. Lett.* **2022**, *13*, 3165−3172.
(31) Ventosa, E.; Paulitsch, B.; Marzak, P.; Yun, J.; Schiegg, F.; Quast, T.; Bandarenka, A. S. The mechanism of the interfacial charge and mass transfer during intercalation of alkali metal cations. *Adv. Sci.* **2016**, *3*, No. 1600211.
(32) Yun, J.; Pfisterer, J.; Bandarenka, A. S. How simple are the models of Na intercalation in aqueous media? *Energy Environ. Sci.* **2016**, *9*, 955−961.
(33) Wessells, C. D.; Peddada, S. V.; Huggins, R. A.; Cui, Y. Nickel hexacyanoferrate nanoparticle electrodes for aqueous sodium and potassium ion batteries. *Nano Lett.* **2011**, *11*, 5421−5425.
(34) Lamprecht, X.; Evazzade, I.; Ungerer, I.; Hromadko, L.; Macak, J. M.; Bandarenka, A. S.; Alexandrov, V. Mechanisms of degradation of $Na_2Ni[Fe(CN)_6]$ functional electrodes in aqueous media: A combined theoretical and experimental study. *J. Phys. Chem. C* **2023**, *127*, 2204−2214.
(35) Bandarenka, A. S.Development of Hybrid Algorithms for EIS Data Fitting. In *Lecture Notes on Impedance Spectroscopy*; CRC Press, 2013; Vol. *4*, p 29.
(36) Momma, K.; Izumi, F. VESTA 3 for three-dimensional visualization of crystal, volumetric and morphology data. *J. Appl. Crystallogr.* **2011**, *44*, 1272−1276.
(37) Horcas, I.; Fernández, R.; Gomez-Rodriguez, J. M.; Colchero, J.; Gómez-Herrero, J.; Baro, A. M. WSXM: a software for scanning probe microscopy and a tool for nanotechnology. *Rev. Sci. Instrum.* **2007**, *78*, No. 013705.
(38) Bácskai, J.; Martinusz, K.; Czirok, E.; Inzelt, G.; Kulesza, P. J.; Malik, M. A. Polynuclear nickel hexacyanoferrates: monitoring of film growth and hydrated counter-cation flux/storage during redox reactions. *J. Electroanal. Chem.* **1995**, *385*, 241−248.
(39) Hao, X.; Yan, T.; Wang, Z.; Liu, S.; Liang, Z.; Shen, Y.; Pritzker, M. Unipolar pulse electrodeposition of nickel hexacyanoferrate thin films with controllable structure on platinum substrates. *Thin Solid Films* **2012**, *520*, 2438−2448.
(40) Chen, W.; Tang, J.; Xia, X. H. Composition and shape control in the construction of functional nickel hexacyanoferrate nano-interfaces. *J. Phys. Chem. C* **2009**, *113*, 21577−21581.
(41) Lee, H. W.; Pasta, M.; Wang, R. Y.; Ruffo, R.; Cui, Y. Effect of the alkali insertion ion on the electrochemical properties of nickel hexacyanoferrate electrodes. *Faraday Discuss.* **2014**, *176*, 69−81.
(42) Gaddam, R. R.; Katzenmeier, L.; Lamprecht, X.; Bandarenka, A. S. Review on physical impedance models in modern battery research. *Phys. Chem. Chem. Phys.* **2021**, *23*, 12926−12944.
(43) Suo, L.; Borodin, O.; Wang, Y.; Rong, X.; Sun, W.; Fan, X.; Xu, S.; Schroeder, M. A.; Cresce, A. V.; Wang, F.; Yang, C.; Hu, Y. S.; Xu, K.; Wang, C. "Water-in-salt" electrolyte makes aqueous sodium-ion battery safe, green, and long-lasting. *Adv. Energy Mater.* **2017**, *7*, No. 1701189.
(44) Tomiyasu, H.; Shikata, H.; Takao, K.; Asanuma, N.; Taruta, S.; Park, Y. Y. An aqueous electrolyte of the widest potential window and its superior capability for capacitors. *Sci. Rep.* **2017**, *7*, No. 45048.
(45) da Silva, D. A.; Messias, A.; Fileti, E. E.; Pascon, A.; Franco, D. V.; Da Silva, L. M.; Zanin, H. G. Effect of conductivity, viscosity, and density of water-in-salt electrolytes on the electrochemical behavior of supercapacitors: molecular dynamics simulations and in situ characterization studies. *Mater. Adv.* **2022**, *3*, 611−623.
(46) Lindström, H.; Södergren, S.; Solbrand, A.; Rensmo, H.; Hjelm, J.; Hagfeldt, A.; Lindquist, S. E. Li^+ ion insertion in TiO_2 (anatase). 2. Voltammetry on nanoporous films. *J. Phys. Chem. B* **1997**, *101*, 7717−7722.

https://doi.org/10.1021/acsami.3c02633
ACS Appl. Mater. Interfaces 2023, 15, 23951−23962

(47) Bard, A. J.; Faulkner, L. R.; White, H. S. *Electrochemical Methods: Fundamentals and Applications*; John Wiley & Sons, 2022.
(48) Vassiliev, S. Y.; Levin, E. E.; Nikitina, V. A. Kinetic analysis of lithium intercalating systems: cyclic voltammetry. *Electrochim. Acta* **2016**, *190*, 1087−1099.
(49) Levi, M. D.; Aurbach, D. Frumkin intercalation isotherm - a tool for the description of lithium insertion into host materials: a review. *Electrochim. Acta* **1999**, *45*, 167−185.
(50) Nikitina, V. A.; Vassiliev, S. Y.; Stevenson, K. J. Metal-ion coupled electron transfer kinetics in intercalation-based transition metal oxides. *Adv. Energy Mater.* **2020**, *10*, No. 1903933.
(51) Kondratiev, V. V.; Tikhomirova, A. V.; Malev, V. V. Study of charge transport processes in Prussian-blue film modified electrodes. *Electrochim. Acta* **1999**, *45*, 751−759.
(52) Augustyn, V.; Come, J.; Lowe, M. A.; Kim, J. W.; Taberna, P. L.; Tolbert, S. H.; Abruña, H. D.; Simon, P.; Dunn, B. High-rate electrochemical energy storage through Li^+ intercalation pseudocapacitance. *Nat. Mater.* **2013**, *12*, 518−522.
(53) Come, J.; Taberna, P. L.; Hamelet, S.; Masquelier, C.; Simon, P. Electrochemical kinetic study of $LiFePO_4$ using cavity microelectrode. *J. Electrochem. Soc.* **2011**, *158*, A1090.
(54) Dokko, K.; Nakata, N.; Kanamura, K. High rate discharge capability of single particle electrode of $LiCoO_2$. *J. Power Sources* **2009**, *189*, 783−785.
(55) Heubner, C.; Schneider, M.; Michaelis, A. Investigation of charge transfer kinetics of Li-Intercalation in $LiFePO_4$. *J. Power Sources* **2015**, *288*, 115−120.
(56) Ariyoshi, K.; Tanimoto, M.; Yamada, Y. Impact of particle size of lithium manganese oxide on charge transfer resistance and contact resistance evaluated by electrochemical impedance analysis. *Electrochim. Acta* **2020**, *364*, No. 137292.
(57) Yun, J.; Schiegg, F. A.; Liang, Y.; Scieszka, D.; Garlyyev, B.; Kwiatkowski, A.; Wagner, T.; Bandarenka, A. S. Electrochemically formed $Na_xMn[Mn(CN)_6]$ thin film anodes demonstrate sodium intercalation and deintercalation at extremely negative electrode potentials in aqueous media. *ACS Appl. Energy Mater.* **2018**, *1*, 123−128.
(58) Scholz, F.; Dostal, A. The formal potentials of solid metal hexacyanometalates. *Angew. Chem., Int. Ed.* **1996**, *34*, 2685−2687.
(59) Firouzi, A.; Qiao, R.; Motallebi, S.; Valencia, C. W.; Israel, H. S.; Fujimoto, M.; Wray, L. A.; Chuang, Y. D.; Yang, W.; Wessells, C. D. Monovalent manganese based anodes and co-solvent electrolyte for stable low-cost high-rate sodium-ion batteries. *Nat. Commun.* **2018**, *9*, No. 861.
(60) Hurlbutt, K.; Giustino, F.; Volonakis, G.; Pasta, M. Origin of the high specific capacity in sodium manganese hexacyanomanganate. *Chem. Mater.* **2022**, *34*, 4336−4343.
(61) Xie, J.; Liang, Z.; Lu, Y. C. Molecular crowding electrolytes for high-voltage aqueous batteries. *Nat. Mater.* **2020**, *19*, 1006−1011.
(62) Simon, P.; Gogotsi, Y.; Dunn, B. Where do batteries end and supercapacitors begin? *Science* **2014**, *343*, 1210−1211.
(63) Mathis, T. S.; Kurra, N.; Wang, X.; Pinto, D.; Simon, P.; Gogotsi, Y. Energy storage data reporting in perspective - guidelines for interpreting the performance of electrochemical energy storage systems. *Adv. Energy Mater.* **2019**, *9*, No. 1902007.
(64) Lin, Z.; Liu, T.; Ai, X.; Liang, C. Aligning academia and industry for unified battery performance metrics. *Nat. Commun.* **2018**, *9*, No. 5262.
(65) Ellis, B. L.; Knauth, P.; Djenizian, T. Three-dimensional self-supported metal oxides for advanced energy storage. *Adv. Mater.* **2014**, *26*, 3368−3397.
(66) Zhang, G.; Yao, H.; Zhang, F.; Gao, Z.; Li, Q.; Yang, Y.; Lu, X. A high over-potential binder-free electrode constructed of Prussian blue and MnO_2 for high performance aqueous supercapacitors. *Nano Res.* **2019**, *12*, 1061−1069.
(67) He, B.; Man, P.; Zhang, Q.; Wang, C.; Zhou, Z.; Li, C.; Wei, L.; Yao, Y. Conversion synthesis of self-standing potassium zinc hexacyanoferrate arrays as cathodes for high-voltage flexible aqueous rechargeable sodium-ion batteries. *Small* **2019**, *15*, No. 1905115.
(68) Yang, Y. J.; Li, Y.; Ding, X.; Zhang, C.; Ren, H.; Guo, F.; Dong, J. Synthesis of nickel hexacyanoferrate nanostructure on carbon cloth with predeposited nickel nanoparticles as precursor for binder-free high-performance supercapacitor electrodes. *J. Alloys Compd.* **2021**, *871*, No. 159510.
(69) Zhang, X.; Dutta, J. X-Fe (X = Mn, Co, Cu) Prussian blue analogue-modified carbon cloth electrodes for capacitive deionization. *ACS Appl. Energy Mater.* **2021**, *4*, 8275−8284.
(70) Lu, K.; Song, B.; Li, K.; Zhang, J.; Ma, H. Cobalt hexacyanoferrate nanoparticles and MoO_3 thin films grown on carbon fiber cloth for efficient flexible hybrid supercapacitor. *J. Power Sources* **2017**, *370*, 98−105.

https://doi.org/10.1021/acsami.3c02633
ACS Appl. Mater. Interfaces 2023, 15, 23951−23962

References

1. S. Arrhenius. On the influence of carbonic acid in the air upon the temperature of the ground. *Philosophical Magazine and Journal of Science* **1896**, *5*(41), 237-276.

2. G. S. Callendar. The artificial production of carbon dioxide and its influence on temperature. *Quarterly Journal of the Royal Meteorological Society* **1938**, *64*(275), 223-240.

3. G. N. Plass. The carbon dioxide theory of climatic change. *Tellus* **1956**, *8*(2), 140-154.

4. S. Manabe. Role of greenhouse gas in climate change. *Tellus A: Dynamic Meteorology and Oceanography* **2019**, *71*(1), 1620078.

5. IPCC 2021, V. Masson-Delmotte, P. Zhai, A. Pirani, S. L. Connors, C. Péan, S. Berger, N. Caud, Y. Chen, L. Goldfarb, M. I. Gomis, M. Huang, K. Leitzell, E. Lonnoy, J. B. R. Matthews, T. K. Maycock, T. Waterfield, O. Yelekçi, R. Yu, B. Zhou (eds.). Climate change 2021: the physical science basis. Contribution of working group I to the sixth assessment report of the intergovernmental panel on climate change. *Cambridge University Press* **2021**, doi:10.1017/9781009157896.

6. H. Ritchie, M. Roser, P. Rosado. CO_2 and greenhouse gas emissions. Published online at *OurWorldInData.org* **2020**. Retrieved from *https://ourworldindata.org/co2-and-greenhouse-gas-emissions* on 13. July 2023. Based on original research from P. Friedlingstein, *et al*. Global Carbon Budget 2022. *Earth System Science Data* **2022**, *14*, 4811-4900.

7. H. Ritchie, M. Roser, P. Rosado. CO_2 and greenhouse gas emissions. Published online at *OurWorldInData.org* **2020**. Retrieved from *https://ourworldindata.org/co2-and-greenhouse-gas-emissions* on 13. July 2023. Based on original research from C. P. Morice, J. J. Kennedy, N. A. Rayner, J. P. Winn, E. Hogan, R. E. Killick, R. J. H. Dunn, T. J. Osborn, P. D. Jones and I. R. Simpson. An updated assessment of near-surface temperature change from 1850: the HadCRUT5 dataset. *Journal of Geophysical Research: Atmospheres* **2021**. *126*(3), e2019JD032361.

8. W. J. Ripple, C. Wolf, T. M. Newsome, P. Barnard, W. R. Moomaw and 11,258 signatories from 153 countries. World scientists' warning of a climate emergency. *BioScience* **2020**, *70*(1), 8-12.

9. M. Lynas, B. Z. Houlton, S. Perry. Greater than 99% consensus on human caused climate change in the peer-reviewed scientific literature. *Environmental Research Letters* **2021**, *16*(11), 114005.

10. IPCC 2022, H. O. Pörtner, D.C. Roberts, M. Tignor, E. S. Poloczanska, K. Mintenbeck, A. Alegría, M. Craig, S. Langsdorf, S. Löschke, V. Möller, A. Okem, B. Rama (eds.). Climate change 2022: impacts, adaptation, and vulnerability. Contribution of working group II to the sixth assessment report of the intergovernmental panel on climate change. *Cambridge University Press* **2022**, doi:10.1017/9781009325844.

11. D. Steel, C. T. DesRoches, K. Mintz-Woo. Climate change and the threat to civilization. *Proceedings of the National Academy of Sciences* **2022**, *119*(42), e2210525119.

12. J. Tollefson. Top climate scientists are sceptical that nations will rein in global warming. *Nature* **2021**, *599*.

13. Paris Agreement. *United Nations* **2015**.

14. M. Crippa, D. Guizzardi, M. Banja, E. Solazzo, M. Muntean, E. Schaaf, F. Pagani, F. Monforti-Ferrario, J. Olivier, R. Quadrelli, A. Risquez Martin, P. Taghavi-Moharamli, G. Grassi, S. Rossi, D. Jacome Felix Oom, A. Branco, J. San-Miguel-Ayanz, E. Vignati. CO_2 emissions of all world countries - 2022 Report. *Publications Office of the European Union* **2022**, EUR 31182 EN, JRC130363, doi:10.2760/730164.

15. Emissionsdaten nach §5 Bundesklimaschutzgesetz (KSG). *Umweltbundesamt*, *umweltbundesamt.de*. Accessed online on 22. December 2022.

16. Gesamtausgabe der Energiedaten – Datensammlung des *Bundesministeriums für Wirtschaft und Klimaschutz* 2022, *bmwk.de/Redaktion/DE/Artikel/Energie/energiedaten-gesamtausgabe.html*. Accessed online on 23. December 2022.

17. Unsere Energiewende: sicher, sauber, bezahlbar. *Bundesministeriums für Wirtschaft und Klimaschutz*, *bmwk.de/Redaktion/DE/Dossier/energiewende.html*. Accessed online on 23. December 2022.

18. Prognos, Öko-Institut, Wuppertal-Institut. Klimaneutrales Deutschland 2045. Wie Deutschland seine Klimaziele schon vor 2050 erreichen kann. *Studie im Auftrag von Stiftung Klimaneutralität, Agora Energiewende und Agora Verkehrswende* **2021**.

19. H. Ritchie, M. Roser, P. Rosado. Energy. Published online at *OurWorldInData.org* **2022**. Retrieved from *https://ourworldindata.org/energy* on 27. December 2022. Based on original publication from BP Statistical Review of World Energy, *bp.com/en/global/corporate/energy-economics/statistical-review-of-world-energy.html* **2022** and V. Smil. Energy Transitions: Global and National Perspectives, 2nd ed. *Praeger* **2017**.

20. *Bundesnetzagentur*, *smard.de*. Accessed online on 27. December 2022.

21. S. R. Sinsel, R. L. Riemke, V. H. Hoffmann. Challenges and solution technologies for the integration of variable renewable energy sources—a review. *Renewable Energy* **2020**, *145*, 2271-2285.

22. D. Hajek, K. Hofbauer. Die Herausforderung des grünen Stroms. *Frankfurter Allgemeine Zeitung* **2021**. *faz.net/aktuell/wirtschaft/schneller-schlau/energiewende-die-herausforderung-des-gruenen-stroms-17473677.html*. Accessed online on 27. December 2022.

23. P. S. Georgilakis. Technical challenges associated with the integration of wind power into power systems. *Renewable and Sustainable Energy Reviews* **2008**, *12*(3), 852-863.

24. M. Joos, I. Staffell. Short-term integration costs of variable renewable energy: Wind curtailment and balancing in Britain and Germany. *Renewable and Sustainable Energy Reviews* **2018**, *86*, 45-65.

25. Bericht: Netzengpassmanagement Gesamtes Jahr 2021. *Bundesnetzagentur*.

26. W. P. Schill. Electricity storage and the renewable energy transition. *Joule* **2020**, *4*(10), 2059-2064.

27. Z. Yang, J. Zhang, M. C. Kintner-Meyer, X. Lu, D. Choi, J. P. Lemmon, J. Liu. Electrochemical energy storage for green grid. *Chemical Reviews* **2011**, *111*(5), 3577-3613.

28. A. Malhotra, B. Battke, M. Beuse, A. Stephan, T. Schmidt. Use cases for stationary battery technologies: A review of the literature and existing projects. *Renewable and Sustainable Energy Reviews* **2016**, *56*, 705-721.

29. Bayerisches Staatsministerium für Wirtschaft, Landesentwicklung und Energie. Press Release Nr. 28/23 on 27.01.2023. *stmwi.bayern.de/presse/pressemeldungen/pressemeldung/28-2023/.* Accessed online on 30. January 2023.

30. X. Luo, J. Wang, M. Dooner, J. Clarke. Overview of current development in electrical energy storage technologies and the application potential in power system operation. *Applied Energy* **2015**, *137*, 511-536.

31. B. Dunn, H. Kamath, J. M. Tarascon. Electrical energy storage for the grid: a battery of choices. *Science* **2011**, *334*(6058), 928-935.

32. Stromspeicher in der Energiewende. *Agora Energiewende* **2014.**

33. H. Chen, T. N. Cong, W. Yang, C. Tan, Y. Li, Y. Ding. Progress in electrical energy storage system: A critical review. *Progress in Natural Science* **2009**, *19*(3), 291-312.

34. M. Müller, L. Viernstein, C. N. Truong, A. Eiting, H. C. Hesse, R. Witzmann, A. Jossen. Evaluation of grid-level adaptability for stationary battery energy storage system applications in Europe. *Journal of Energy Storage* **2017**, *9*, 1-11.

35. J. Brandes, M. Haun, D. Wrede, P. Jürgens, C. Kost, H. M. Henning. Wege zu einem klimaneutralen Energiesystem. Die deutsche Energiewende im Kontext gesellschaftlicher Verhaltensweisen. Update November 2021: Klimaneutralität 2045. *Fraunhofer-Institut für Solare Energiesysteme ISE* **2021**.

36. A. A. Kebede, T. Kalogiannis, J. Van Mierlo, M. Berecibar. A comprehensive review of stationary energy storage devices for large scale renewable energy sources grid integration. *Renewable and Sustainable Energy Reviews* **2022**, *159*, 112213.

37. I. M. Peters, C. Breyer, S. A. Jaffer, S. Kurtz, T. Reindl, R. Sinton, M. Vetter. The role of batteries in meeting the PV terawatt challenge. *Joule* **2021**, *5*(6), 1353-1370.

38. C. J. Barnhart, M. Dale, A. R. Brandt, S. M. Benson. The energetic implications of curtailing versus storing solar-and wind-generated electricity. *Energy & Environmental Science* **2013**, *6*(10), 2804-2810.

39. Y. Zhao, O. Pohl, A. I. Bhatt, G. E. Collis, P. J. Mahon, T. Rüther, A. F. Hollenkamp. A review on battery market trends, second-life reuse, and recycling. *Sustainable Chemistry* **2021**, *2*(1), 167-205.

40. J. Figgener, P. Stenzel, K. P. Kairies, J. Linßen, D. Haberschusz, O. Wessels, D. U. Sauer, *et al*. The development of stationary battery storage systems in Germany – A market review. *Journal of Energy Storage* **2020**, *29*, 101153.

41. A. Masias, J. Marcicki, W. A. Paxton. Opportunities and challenges of lithium ion batteries in automotive applications. *ACS Energy Letters* **2021**, *6*(2), 621-630.

42. M. D. Slater, D. Kim, E. Lee, C. S. Johnson. Sodium-ion batteries. *Advanced Functional Materials* **2013**, *23*(8), 947-958.

43. H. S. Hirsh, Y. Li, D. H. Tan, M. Zhang, E. Zhao, Y. S. Meng. Sodium-ion batteries paving the way for grid energy storage. *Advanced Energy Materials* **2020**, *10*(32), 2001274.

44. X. Sun, H. Hao, P. Hartmann, Z. Liu, F. Zhao. Supply risks of lithium-ion battery materials: An entire supply chain estimation. *Materials Today Energy* **2019**, *14*, 100347.

45. P. C. Vesborg, T. F. Jaramillo. Addressing the terawatt challenge: scalability in the supply of chemical elements for renewable energy. *RSC Advances* **2012**, *2*(21), 7933-7947.

46. J. D. Graham, J. A. Rupp, E. Brungard. Lithium in the Green Energy Transition: The Quest for Both Sustainability and Security. *Sustainability* **2021**, *13*(20), 11274.

47. R. B. Kaunda. Potential environmental impacts of lithium mining. *Journal of Energy & Natural Resources Law* **2020**, *38*(3), 237-244.

48. B. K. Sovacool. The precarious political economy of cobalt: Balancing prosperity, poverty, and brutality in artisanal and industrial mining in the Democratic Republic of the Congo. *The Extractive Industries and Society* **2019**, *6*(3), 915-939.

49. Website of the *Hornsdale Power Reserve, hornsdalepowerreserve.com.au.* Accessed online on 22. December 2022.

50. D. Peper, S. Längle, M. Muhr, T. Reuther, C. Kost. Photovoltaik- und Batteriespeicherzubau in Deutschland in Zahlen: Auswertung des Markstammdatenregisters. *Fraunhofer-Institut für Solare Energiesysteme ISE* **2022.**

51. Q. Wang, B. Mao, S. I. Stoliarov, J. Sun. A review of lithium ion battery failure mechanisms and fire prevention strategies. *Progress in Energy and Combustion Science* **2019**, *73*, 95-131.

52. Creative Commons CC BY-SA 4.0 (*creativecommons.org/licenses/by-sa/4.0*). Downloaded from *commons.wikimedia.org (Image propriété Neoen*). Accessed online on 22. December 2022.

53. D. Bin, F. Wang, A. G. Tamirat, L. Suo, Y. Wang, C. Wang, Y. Xia. Progress in aqueous rechargeable sodium-ion batteries. *Advanced Energy Materials* **2018**, *8*(17), 1703008.

54. H. Kim, J. Hong, K. Y. Park, H. Kim, S. W. Kim, K. Kang. Aqueous rechargeable Li and Na ion batteries. *Chemical Reviews* **2014**, *114*(23), 11788-11827.

55. H. Zhang, X. Liu, H. Li, I. Hasa, S. Passerini. Challenges and strategies for high-energy aqueous electrolyte rechargeable batteries. *Angewandte Chemie International Edition* **2021**, *60*(2), 598-616.

56. J. Y. Hwang, S. T. Myung, Y. K. Sun. Sodium-ion batteries: present and future. *Chemical Society Reviews* **2017**, *46*(12), 3529-3614.

57. C. Delmas. Sodium and sodium-ion batteries: 50 years of research. *Advanced Energy Materials* **2018**, *8*(17), 1703137.

58. Y. Wang, D. Liu, M. Sun, J. Liu. Recent progress in electrode materials for aqueous sodium and potassium ion batteries. *Materials Chemistry Frontiers* **2021**, *5*, 7384-7402.

59. D. Pahari, S. Puravankara. Greener, safer, and sustainable batteries: an insight into aqueous electrolytes for sodium-ion batteries. *ACS Sustainable Chemistry & Engineering* **2020**, *8*(29), 10613-10625.

60. D. Chao, W. Zhou, F. Xie, C. Ye, H. Li, M. Jaroniec, S. Z. Qiao. Roadmap for advanced aqueous batteries: From design of materials to applications. *Science Advances* **2020**, *6*(21), eaba4098.

61. K. Hurlbutt, S. Wheeler, I. Capone, M. Pasta. Prussian blue analogs as battery materials. *Joule* **2018**, *2*, 1950-1960.

62. B. Wang, Y. Han, X. Wang, N. Bahlawane, H. Pan, M. Yan, Y. Jiang. Prussian blue analogs for rechargeable batteries. *iScience* **2018**, *3*, 110-133.

63. H. Yi, R. Qin, S. Ding, Y. Wang, S. Li, Q. Zhao, F. Pan. Structure and properties of Prussian blue analogues in energy storage and conversion applications. *Advanced Functional Materials* **2021**, *31*(6), 2006970.

64. J. Peng, W. Zhang, Q. Liu, J. Wang, S. Chou, H. Liu, S. Dou. Prussian blue analogues for sodium-ion batteries: past, present, and future. *Advanced Materials* **2022**, *34*(15), 2108384.

65. S. Qiu, Y. Xu, X. Wu, X. Ji. Prussian blue analogues as electrodes for aqueous monovalent ion batteries. *Electrochemical Energy Reviews* **2021**, *5*(2), 242-262.

66. K. Roth. Berliner Blau – Entdecker und Verräter: Tatort Berlin. *Chemie in Unserer Zeit* **2022**, *56*(1), 34-49.

67. Public Domain. Downloaded from *commons.wikimedia.org (Dcoetzee/Google Arts and Culture. Museum of Modern Arts, New York City).* Accessed online on 22. December 2022.

68. F. Scholz, A. Dostal. The formal potentials of solid metal hexacyanometalates. *Angewandte Chemie International Edition* **1996**, *34*(23-24), 2685-2687.

69. W. J. Li, C. Han, G. Cheng, S. L. Chou, H. K. Liu, S. X. Dou. Chemical properties, structural properties, and energy storage applications of Prussian blue analogues. *Small* **2019**, *15*(32), 1900470.

70. J. Han, Y. Lin, Y. Yang, D. Zuo, C. Wang, X. Liu. Dominant role of M element on the stability and properties of Prussian blue analogues $Na_xMFe(CN)_6$ (M= 3d transition metal) as cathode material for the sodium-ion batteries. *Journal of Alloys and Compounds* **2021**, *870*, 159533.

71. X. Bie, K. Kubota, T. Hosaka, K. Chihara, S. Komaba. Synthesis and electrochemical properties of Na-rich Prussian blue analogues containing Mn, Fe, Co, and Fe for Na-ion batteries. *Journal of Power Sources* **2018**, *378*, 322-330.

72. K. Hurlbutt, F. Giustino, M. Pasta, G. Volonakis. Electronic structure and electron-transport properties of three metal hexacyanoferrates. *Chemistry of Materials* **2021**, *33*(17), 7067-7074.

73. A. A. Karyakin. Prussian blue and its analogues: electrochemistry and analytical applications. *Electroanalysis* **2001**, *13*(10), 813-819.

74. Y. Avila, P. Acevedo-Peña, L. Reguera, E. Reguera. Recent progress in transition metal hexacyanometallates: From structure to properties and functionality. *Coordination Chemistry Reviews* **2022**, *453*, 214274.

75. Y. Matos-Peralta, M. Antuch. Prussian blue and its analogs as appealing materials for electrochemical sensing and biosensing. *Journal of the Electrochemical Society* **2019**, *167*(3), 037510.

76. S. M. Chen, C. Y. Liou, R. Thangamuthu. Preparation and characterization of mixed-valent nickel oxide/nickel hexacyanoferrate hybrid films and their electrocatalytic properties. *Electroanalysis: An International Journal Devoted to Fundamental and Practical Aspects of Electroanalysis* **2007**, *19*(23), 2457-2464.

77. X. Su, Y. Wang, J. Zhou, S. Gu, J. Li, S. Zhang. Operando spectroscopic identification of active sites in NiFe Prussian blue analogues as electrocatalysts: activation of oxygen atoms for oxygen evolution reaction. *Journal of the American Chemical Society* **2018**, *140*, 11286–11292.

78. H. Zhang, P. Li, S. Chen, F. Xie, D.J. Riley. Anodic Transformation of a core-shell Prussian blue analogue to a bifunctional electrocatalyst for water splitting. *Advanced Functional Materials* **2021**, *31*, 2106835.

79. S. D. Rassat, J. H. Sukamto, R. J. Orth, M. A. Lilga, R. T. Hallen. Development of an electrically switched ion exchange process for selective ion separations. *Separation and Purification Technology* **1999**, *15*(3), 207-222.

80. T. Kim, C. A. Gorski, B. E. Logan. Ammonium removal from domestic wastewater using selective battery electrodes. *Environmental Science & Technology Letters* **2018**, *5*(9), 578-583.

81. E. R. Reale, L. Regenwetter, A. Agrawal, B. Dardón, N. Dicola, S. Sanagala, K. C. Smith. Low porosity, high areal-capacity Prussian blue analogue electrodes enhance salt removal and thermodynamic efficiency in symmetric Faradaic deionization with automated fluid control. *Water Research X* **2021**, *13*, 100116.

82. T. Shibata, Y. Moritomo. Quick response of all solid electrochromic device. *Applied Physics Express* **2009**, *2*, 105502.

83. L. M. N. Assis, R. Leones, J. Kanicki, A. Pawlicka, M. M. Silva. Prussian blue for electrochromic devices. *Journal of Electroanalytical Chemistry* **2016**, *777*, 33-39.

84. C. D. Wessells, S. V. Peddada, R. A. Huggins, Y. Cui. Nickel hexacyanoferrate nanoparticle electrodes for aqueous sodium and potassium ion batteries. *Nano Letters* **2011**, *11*(12), 5421-5425.

85. J. Han, A. Varzi, S. Passerini. The emergence of aqueous ammonium-ion batteries. *Angewandte Chemie International Edition* **2022**, *61*, e202115046.

86. B. Xie, B. Sun, T. Gao, Y. Ma, G. Yin, P. Zuo. Recent progress of Prussian blue analogues as cathode materials for nonaqueous sodium-ion batteries. *Coordination Chemistry Reviews* **2022**, *460*, 214478.

87. Q. Liu, Z. Hu, M. Chen, C. Zou, H. Jin, S. Wang, S. L. Chou, Y. Liu, S. X. Dou. The cathode choice for commercialization of sodium-ion batteries: layered transition metal oxides versus Prussian blue analogs. *Advanced Functional Materials* **2020**, *30*(14), 1909530.

88. Y. Lu, L. Wang, J. Cheng, J. B. Goodenough. Prussian blue: a new framework of electrode materials for sodium batteries. *Chemical Communications* **2012**, *48*(52), 6544-6546.

89. CATL unveils its latest breakthrough technology by releasing its first generation of sodium-ion batteries, *catl.com/en/news/665.html*. Accessed online on 20. December 2022.

90. J. Peng, W. Zhang, Q. Liu, J. Wang, S. Chou, H. Liu, S. Dou. Prussian blue analogues for sodium-ion batteries: past, present, and future. *Advanced Materials* **2022**, *34*(15), 2108384.

91. Q. Liu, Z. Hu, M. Chen, C. Zou, H. Jin, S. Wang, S. L. Chou, Y. Liu, S. X. Dou. The cathode choice for commercialization of sodium-ion batteries: layered transition metal oxides versus Prussian blue analogs. *Advanced Functional Materials* **2020**, *30*(14), 1909530.

92. Information available on the website of the company *Natron Energy*, *natron.energy/technology/*. Accessed online on 20. December 2022.

93. L. Mauler, F. Duffner, W. G. Zeier, J. Leker. Battery cost forecasting: a review of methods and results with an outlook to 2050. *Energy & Environmental Science* **2021**, *14*, 4712-4739.

94. J. T. Frith, M. J. Lacey, U. Ulissi. A non-academic perspective on the future of lithium-based batteries. *Nature Communications* **2023**, *14*(1), 1-17.

95. A. Firouzi, R. Qiao, S. Motallebi, C. W. Valencia, H. S. Israel, M. Fujimoto, L. A. Wray, Y. D. Chuang, W. Yang, C. D. Wessells. Monovalent manganese based anodes and co-solvent electrolyte for stable low-cost high-rate sodium-ion batteries. *Nature Communications* **2018**, *9*(1), 1-10.

96. C. J. Barnhart, S. M. Benson. On the importance of reducing the energetic and material demands of electrical energy storage. *Energy & Environmental Science* **2013**, *6*(4), 1083-1092.

97. Warranty of LFP-based LIB provided by the company *Sonnen. sonnen.com.au/technical-documents/.* Accessed online on 20. December 2022.

98. Warranty of LFP-based LIB provided by the company *BYD, bydbatterybox.com/downloads.* Accessed online on 20. December 2022.

99. Warranty of LFP-based LIB provided by the company *CATL*, *catl.com/en/ess/*. Accessed online on 20. December 2022.

100. Y. Preger, H. M. Barkholtz, A. Fresquez, D. L. Campbell, B. W. Juba, J. Romàn-Kustas, S. R. Ferreira, B. Chalamala. Degradation of commercial lithium-ion cells as a function of chemistry and cycling conditions. *Journal of The Electrochemical Society* **2020**, *167*(12), 120532.

101. C. Kost, S. Shammugam, V. Fluri, D. Peper, A. Davoodi Memar, T. Schlegl. Levelized cost of electricity – Renewable energy technologies. *Fraunhofer-Institut für Solare Energiesysteme ISE* **2021**.

102. S. Howell, Y. Rezgui, J. L. Hippolyte, B. Jayan, H. Li. Towards the next generation of smart grids: Semantic and holonic multi-agent management of distributed energy resources. *Renewable and Sustainable Energy Reviews* **2017**, *77*, 193-214.

103. A. Q. Al-Shetwi, M. A. Hannan, K. P. Jern, M. Mansur, T. M. I. Mahlia. Grid-connected renewable energy sources: Review of the recent integration requirements and control methods. *Journal of Cleaner Production* **2020**, *253*, 119831.

104. S. Mischinger, H. Seidl, E. L. Limbacher, S. Fasbender, F. Stalleicken. dena-Innovationsreport Systemdienstleistungen: Aktueller Handlungsbedarf und Roadmap für einen stabilen Betrieb des Stromsystems bis 2030. *Deutsche Energie-Agentur GmbH (dena)* **2017**.

105. D. Choi, N. Shamim, A. Crawford, Q. Huang, C. K. Vartanian, V. V. Viswanathan, M. D. Paiss, M. J. E. Alam, D. M. Reed, V. L. Sprenkle. Li-ion battery technology for grid application. *Journal of Power Sources* **2021**, *511*, 230419.

106. Potential benefits of high-power, high-capacity batteries. *U.S. Department of Energy* **2020**.

107. J. Shin, J. W. Choi. Opportunities and reality of aqueous rechargeable batteries. *Advanced Energy Materials* **2020**, *10*(28), 2001386.

108. W. Zuo, R. Li, C. Zhou, Y. Li, J. Xia, J. Liu. Battery-supercapacitor hybrid devices: recent progress and future prospects. *Advanced Science* **2017**, *4*(7), 1600539.

109. D. P. Dubal, O. Ayyad, V. Ruiz, P. Gomez-Romero. Hybrid energy storage: the merging of battery and supercapacitor chemistries. *Chemical Society Reviews* **2015**, *44*(7), 1777-1790.

110. M. E. Şahin, F. Blaabjerg, A. Sangwongwanich. A comprehensive review on supercapacitor applications and developments. *Energies* **2022**, *15*(3), 674.

111. A. Hnatov, S. Arhun. Energy saving technologies for urban bus transport. *International Journal of Automotive and Mechanical Engineering* **2017**, 14(*4*), 4649–4664.

112. F. L. Mapelli, D. Tarsitano, D. Annese, M. Sala, G. Bosia. A study of urban electric bus with a fast charging energy storage system based on lithium battery and supercapacitors. *Eighth International Conference and Exhibition on Ecological Vehicles and Renewable Energies, IEEE* **2013**, doi: 10.1109/EVER.2013.6521614.

113. S. Majumder, K. De, P. Kumar, R. Rayudu. A green public transportation system using E-buses: A technical and commercial feasibility study. *Sustainable Cities and Society* **2019**, *51*, 101789.

114. Ultracapacitor busses from the Shanghai-based company *Aowei* running in several cities, *aowei.com/en/program/applicationinfo-16.html*. Accessed online on 14. March 2023.

115. Announced and ongoing projects of the company *Electreon*, *electreon.com/projects*. Accessed online on 14. March 2023.

116. C. Daniel, J. O. Besenhard (editors). Handbook of battery materials, 2nd ed. *Wiley-VCH* **2011**.

117. T. B. Reddy, D. Linden (editors). Linden's handbook of batteries, 2nd ed. *McGraw-Hill* **2011**.

118. C. H. Hamann, W. Vielstich. Elektrochemie, 4th ed. *Wiley-VCH* **2005**.

119. A. J. Bard, L. R. Faulkner. Electrochemical methods: fundamentals and applications. *John Wiley & Sons* **2001**.

120. S. Trasatti. The absolute electrode potential: an explanatory note (Recommendations 1986). *Pure and Applied Chemistry* **1968**, *58*(7), 955-966.

121. D. R. Lide (editor). Handbook of chemistry and physics, 84th ed. *CRC Press* **2004**.

122. R. D. Mountain. Solvation structure of ions in water. *International Journal of Thermophysics* **2007**, *28*(2), 536-543.

123. B. Garlyyev, S. Xue, S. Watzele, D. Scieszka, A. S. Bandarenka. Influence of the nature of the alkali metal cations on the electrical double-layer capacitance of model Pt(111) and Au(111) electrodes. *The Journal of Physical Chemistry Letters* **2018**, *9*(8), 1927-1930.

124. O. Stern. Zur Theorie der elektrolytischen Doppelschicht. *Zeitschrift für Elektrochemie und Angewandte Physikalische Chemie* **1924**, *30*(21-22), 508-516.

125. D. C. Grahame. The electrical double layer and the theory of electrocapillarity. *Chemical Reviews* **1947**, *41*(3), 441-501.

126. J. M. Bockris, M. A. V. Devanathan, K. Müller. On the structure of charged interfaces. *Proceedings of the Royal Society of London. Series A. Mathematical and Physical Sciences* **1963**, *274*, 55-79.

127. P. Vanýsek. *In* Handbook of chemistry and physics, 84th ed, D. R. Lide (editor). *CRC Press* **2004**.

128. M. Pourbaix. Atlas of electrochemical equilibria in aqueous solutions. *National Association of Corrosion Engineers* **1974**.

129. A. Yoshino. The birth of the lithium-ion battery. *Angewandte Chemie International Edition* **2012**, *51*(24), 5798-5800.

130. M. Winter, B. Barnett, K. Xu. Before Li ion batteries. *Chemical Reviews* **2018**, *118*(23), 11433-11456.

131. H. Kawamura, M. LaFleur, K. Iversen H. W. J. Cheng. Frontier Technology Issues: Lithium-ion batteries: a pillar for a fossil fuel-free economy? *United Nations – Department of Economic and Social Affairs* **2021**. *un.org/development/desa/dpad/publication/frontier-technology-issues-lithium-ion-batteries-a-pillar-for-a-fossil-fuel-free-economy/*. Accessed online on 29. January 2023.

132. The Nobel prize in chemistry 2019. *The Royal Swedish Academy of Sciences*, *nobelprize.org/prizes/chemistry/2019/popular-information/*. Accessed online on 28. January 2023.

133. M. Li, J. Lu, Z. Chen, K. Amine. 30 years of lithium-ion batteries. *Advanced Materials* **2018**, *30*(33), 1800561.

134. F. R. M. McDonnell, R. C. Pink, A. R. Ubbelohde. Some physical properties associated with “aromatic” electrons. Part III. The pseudo-metallic properties of potassium–graphite and graphite–bromine. *Journal of the Chemical Society* **1951**, 191-197.

135. W. Rüdorff. Graphite intercalation compounds. *Advances in Inorganic Chemistry and Radiochemistry* **1959**, *1*, 223-266.

136. A. Lerf. Storylines in intercalation chemistry. *Dalton Transactions* **2014**, *43*(27), 10276-10291.

137. A. S. Bandarenka. Energy materials – a short introduction to functional materials for energy conversion and storage. *CRC Press* **2022**.

138. A. Yoshino, K. Sanechika, T. Nakajima. *Patent JP1989293* **1985**.

139. A. Yoshino, K. Sanechika, T. Nakajima. Secondary battery. *Patent US4,668,595* **1985**.

140. J. B. Goodenough, K. S. Park. The Li-ion rechargeable battery: a perspective. *Journal of the American Chemical Society* **2013**, *135*(4), 1167-1176.

141. M. D. Levi, D. Aurbach. Frumkin intercalation isotherm - a tool for the description of lithium insertion into host materials: a review. *Electrochimica Acta* **1999**, *45*(1-2), 167-185.

142. V. A. Nikitina, S. Y. Vassiliev, K. J. Stevenson. Metal-ion coupled electron transfer kinetics in intercalation-based transition metal oxides. *Advanced Energy Materials* **2020**, *10*(22), 1903933.

143. D. A. Aksyonov, V. A. Nikitina. Charge transfer through interfaces in metal-ion intercalation systems. *Reference Module in Chemistry, Molecular Sciences and Chemical Engineering. Elsevier* **2021**.

144. M. Weiss, R. Ruess, J. Kasnatscheew, Y. Levartovsky, N. R. Levy, P. Minnmann, L. Stolz, T. Waldmann, M. Wohlfahrt-Mehrens, D. Aurbach, M. Winter, Y. Ein-Eli, J. Janek. Fast charging of lithium-ion batteries: a review of materials aspects. *Advanced Energy Materials* **2021**, *11*(33), 2101126.

145. M. Doyle, J. Newman. Analysis of capacity–rate data for lithium batteries using simplified models of the discharge process. *Journal of Applied Electrochemistry* **1997**, *27*, 846-856.

146. P. Peljo, H. H. Girault. Electrochemical potential window of battery electrolytes: the HOMO–LUMO misconception. *Energy & Environmental Science* **2018**, *11*(9), 2306-2309.

147. J. S. Edge, S. O’Kane, R. Prosser, N. D. Kirkaldy, A. N. Patel, A. Hales, G. J. Offer, ***et al***. Lithium ion battery degradation: what you need to know. *Physical Chemistry Chemical Physics* **2021**, *23*(14), 8200-8221.

148. P. Verma, P. Maire, P. Novák. A review of the features and analyses of the solid electrolyte interphase in Li-ion batteries. *Electrochimica Acta* **2010**, *55*(22), 6332-6341.

149. K. Liu, Y. Liu, D. Lin, A. Pei, Y. Cui. Materials for lithium-ion battery safety. *Science Advances* **2018**, *4*(6), eaas9820.

150. M. Liu, H. Ao, Y. Jin, Z. Hou, X. Zhang, Y. Zhu, Y. Qian. Aqueous rechargeable sodium ion batteries: developments and prospects. *Materials Today Energy* **2020**, *17*, 100432.

151. Y. Yokoyama, T. Fukutsuka, K. Miyazaki, T. Abe. Origin of the electrochemical stability of aqueous concentrated electrolyte solutions. *Journal of the Electrochemical Society* **2018**, *165*(14), A3299-A3303.

152. W. G. Nunes, B. G. Freitas, R. M. Beraldo, R. M. Filho, L. M. Da Silva, H. Zanin. A rational experimental approach to identify correctly the working voltage window of aqueous-based supercapacitors. *Scientific Reports* **2020**, *10*(1), 19195.

153. C. Wessells, R. Ruffo, R. A. Huggins, Y. Cui. Investigations of the electrochemical stability of aqueous electrolytes for lithium battery applications. *Electrochemical and Solid-State Letters* **2010**, *13*(5), A59.

154. N. T. Suen, S. F. Hung, Q. Quan, N. Zhang, Y. J. Xu, H. M. Chen. Electrocatalysis for the oxygen evolution reaction: recent development and future perspectives. *Chemical Society Reviews* **2017**, *46*(2), 337-365.

155. L. Suo, O. Borodin, T. Gao, M. Olguin, J. Ho, X. Fan, C. Luo, C. Wang, K. Xu. "Water-in-salt" electrolyte enables high-voltage aqueous lithium-ion chemistries. *Science* **2015**, *350*(6263), 938-943.

156. L. Suo, O. Borodin, Y. Wang, X. Rong, W. Sun, X. Fan, S. Xu, M. A. Schroeder, A. V. Cresce, F. Wang, C. Yang, Y. S. Hu, K. Xu, C. Wang. "Water-in-salt" electrolyte makes aqueous sodium-ion battery safe, green, and long-lasting. *Advanced Energy Materials* **2017**, *7*(21), 1701189.

157. Y. Wang, X. Meng, J. Sun, Y. Liu, L. Hou. Recent progress in "water-in-salt" electrolytes toward non-lithium based rechargeable batteries. *Frontiers in Chemistry* **2020**, *8*, 595.

158. D. Reber, R. Grissa, M. Becker, R. S. Kühnel, C. Battaglia. Anion selection criteria for water-in-salt electrolytes. *Advanced Energy Materials* **2021**, *11*(5), 2002913.

159. R. Sakamoto, M. Yamashita, K. Nakamoto, Y. Zhou, N. Yoshimoto, K. Fujii, T. Yamaguchi, A. Kitajou, S. Okada. Local structure of a highly concentrated $NaClO_4$ aqueous solution-type electrolyte for sodium ion batteries. *Physical Chemistry Chemical Physics* **2020**, *22*(45), 26452-26458.

160. K. Nakamoto, R. Sakamoto, Y. Sawada, M. Ito, S. Okada. Over 2 V aqueous sodium-ion battery with Prussian blue-type electrodes. *Small Methods* **2019**, *3*(4), 1800220.

161. K. Nakamoto, R. Sakamoto, M. Ito, A. Kitajou, S. Okada. Effect of concentrated electrolyte on aqueous sodium-ion battery with sodium manganese hexacyanoferrate cathode. *Electrochemistry* **2017**, *85*(4), 179-185.

162. H. Tomiyasu, H. Shikata, K. Takao, N. Asanuma, S. Taruta, Y. Y. Park. An aqueous electrolyte of the widest potential window and its superior capability for capacitors. *Scientific Reports* **2017**, *7*(1), 1-12.

163. M. H. Lee, S. J. Kim, D. Chang, J. Kim, S. Moon, K. Oh, K. Y. Park, W. M. Seong, H. Park, G. Kwon, B. Lee, K. Kang. Toward a low-cost high-voltage sodium aqueous rechargeable battery. *Materials Today* **2019**, *29*, 26-36.

164. D. A. da Silva, A. Messias, E. E. Fileti, A. Pascon, D. V. Franco, L. M. Da Silva, H. G. Zanin. Effect of conductivity, viscosity, and density of water-in-salt electrolytes on the electrochemical behavior of supercapacitors: molecular dynamics simulations and in situ characterization studies. *Materials Advances* **2022**, *3*(1), 611-623

165. J. Zheng, G. Tan, P. Shan, T. Liu, J. Hu, Y. Feng, F. Pan, *et al*. Understanding thermodynamic and kinetic contributions in expanding the stability window of aqueous electrolytes. *Chem* **2018**, *4*(12), 2872-2882.

166. Y. Zhang, J. Xu, Z. Li, Y. Wang, S. Wang, X. Dong, Y. Wang. All-climate aqueous Na-ion batteries using “water-in-salt” electrolyte. *Science Bulletin* **2022**, *67*(2), 161-170.

167. J. Xie, Z. Liang, Y. C. Lu. Molecular crowding electrolytes for high-voltage aqueous batteries. *Nature Materials* **2022**, *19*(9), 1006-1011.

168. A. Grasser. Molecular crowding electrolytes as a way towards high-energy aqueous sodium-ion batteries. *MSc Thesis, Technische Universität München* **2022**.

169. M. Park, X. Zhang, M. Chung, G. B. Less, A. M. Sastry. A review of conduction phenomena in Li-ion batteries. *Journal of Power Sources* **2010**, *195*(24), 7904-7929.

170. W. Wu, S. Shabhag, J. Chang, A. Rutt, J. F. Whitacre. Relating electrolyte concentration to performance and stability for $NaTi_2(PO_4)_3/Na_{0.44}MnO_2$ aqueous sodium-ion batteries. *Journal of The Electrochemical Society* **2015**, *162*(6), A803.

171. E. R. Logan, E. M. Tonita, K. L. Gering, J. Li, X. Ma, L. Y. Beaulieu, J. R. Dahn. A study of the physical properties of Li-ion battery electrolytes containing esters. *Journal of The Electrochemical Society* **2018**, *165*(2), A21.

172. S. I. Lee, U. H. Jung, Y. S. Kim, M. H. Kim, D. J. Ahn, H. S. Chun. A study of electrochemical kinetics of lithium ion in organic electrolytes. *Korean Journal of Chemical Engineering* **2002**, *19*, 638-644.

173. R. Borah, F. R. Hughson, J. Johnston, T. Nann. On battery materials and methods. *Materials Today Advances* **2020**, *6*, 100046.

174. S. T. Myung, Y. Hitoshi, Y. K. Sun. Electrochemical behavior and passivation of current collectors in lithium-ion batteries. *Journal of Materials Chemistry* **2011**, *21*(27), 9891-9911.

175. C. Dong, F. Xu, L. Chen, Z. Chen, Y. Cao. Design strategies for high-voltage aqueous batteries. *Small Structures* **2021**, *2*(7), 2100001.

176. U. Mittal, D. Kundu. Electrochemical stability of prospective current collectors in the sulfate electrolyte for aqueous Zn-ion battery application. *Journal of The Electrochemical Society* **2021**, *168*(9), 090560.

177. L. Zhang, X. Qin, S. Zhao, A. Wang, J. Luo, Z. L. Wang, F. Kang, Z. Lin, B. Li. Advanced matrixes for binder-free nanostructured electrodes in lithium-ion batteries. *Advanced Materials* **2020**, *32*(24), 1908445.

178. H. Shi, G. Wen, Y. Nie, G. Zhang, H. Duan. Flexible 3D carbon cloth as a high-performing electrode for energy storage and conversion. *Nanoscale* **2020**, *12*(9), 5261-5285.

179. J. Betz, G. Bieker, P. Meister, T. Placke, M. Winter, R. Schmuch. Theoretical versus practical energy: a plea for more transparency in the energy calculation of different rechargeable battery systems. *Advanced Energy Materials* **2019**, *9*(6), 1803170.

180. C. Heubner, K. Voigt, P. Marcinkowski, S. Reuber, K. Nikolowski, M. Schneider, A. Michaelis, *et al*. From active materials to battery cells: a straightforward tool to determine performance metrics and support developments at an application-relevant level. *Advanced Energy Materials* **2021**, *11*(46), 2102647.

181. N. Elgrishi, K. J. Rountree, B. D. McCarthy, E. S. Rountree, T. T. Eisenhart, J. L. Dempsey. A practical beginner's guide to cyclic voltammetry. *Journal of Chemical Education* **2018**, *95*(2), 197-206.

182. H. Lindström, S. Södergren, A. Solbrand, H. Rensmo, J. Hjelm, A. Hagfeldt, S. E. Lindquist. Li^+ ion insertion in TiO_2 (anatase). 2. Voltammetry on nanoporous films. *The Journal of Physical Chemistry B* **1997**, *101*(39), 7717-7722.

183. W. van den Bergh, M. Stefik. Understanding rapid intercalation materials one parameter at a time. *Advanced Functional Materials* **2022**, 2204126.

184. S. Y. Vassiliev, E. E. Levin, V. A. Nikitina. Kinetic analysis of lithium intercalating systems: cyclic voltammetry. *Electrochimica Acta* **2016**, *190*, 1087-1099.

185. P. Keil, A. Jossen. Charging protocols for lithium-ion batteries and their impact on cycle life – An experimental study with different 18650 high-power cells. *Journal of Energy Storage* **2016**, *6*, 125-141.

186. K. Dokko, N. Nakata, K. Kanamura. High rate discharge capability of single particle electrode of $LiCoO_2$. *Journal of Power Sources* **2009**, *189*(1), 783-785.

187. A. Lasia. Electrochemical impedance spectroscopy and its applications. *Springer* **2014**.

188. M. E. Orazem, B. Tribollet. Electrochemical impedance spectroscopy. *John Wiley & Sons* **2008**.

189. E. Barsoukov, J. R. Macdonald. Impedance spectroscopy: theory, experiment, and applications, 2nd ed. *John Wiley and Sons* **2005**.

190. R. R. Gaddam, L. Katzenmeier, X. Lamprecht, A. S. Bandarenka. Review on physical impedance models in modern battery research. *Physical Chemistry Chemical Physics* **2021**, *23*(23), 12926-12944.

191. A. S. Bandarenka. Exploring the interfaces between metal electrodes and aqueous electrolytes with electrochemical impedance spectroscopy. *Analyst* **2013**, *138*(19), 5540-5554.

192. A. S. Bondarenko. Analysis of large experimental datasets in electrochemical impedance spectroscopy. *Analytica Chimica Acta* **2012**, *743*, 41-50.

193. V. Vivier, M. E. Orazem. Impedance analysis of electrochemical systems. *Chemical Reviews* **2022**, *122*(12), 11131-11168.

194. C. Heubner, M. Schneider, A. Michaelis. Investigation of charge transfer kinetics of Li-intercalation in $LiFePO_4$. *Journal of Power Sources* **2015**, *288*, 115-120.

195. J. E. B. Randles. Kinetics of rapid electrode reactions. *Discussions of the Faraday Society* **1947**, *1*, 11-19.

196. A. Lasia. The origin of the constant phase element. *The Journal of Physical Chemistry Letters* **2022**, *13*(2), 580-589.

197. J. Yun, J. Pfisterer, A. S. Bandarenka. How simple are the models of Na intercalation in aqueous media? *Energy & Environmental Science* **2016**, *9*(3), 955-961.

198. J. Yun. Prussian blue analogs for aqueous Na-ion batteries: identification, understanding and optimization. *Dissertation, Technische Universität München* **2020**.

199. E. Ventosa, B. Paulitsch, P. Marzak, J. Yun, F. Schiegg, T. Quast, A. S. Bandarenka. The mechanism of the interfacial charge and mass transfer during intercalation of alkali metal cations. *Advanced Science* **2016**, *3*(12), 1600211.

200. J. Yun, F. A. Schiegg, Y. Liang, D. Scieszka, B. Garlyyev, A. Kwiatkowski, T. Wagner, A. S. Bandarenka. Electrochemically formed $Na_xMn[Mn(CN)_6]$ thin film anodes demonstrate sodium intercalation and deintercalation at extremely negative electrode potentials in aqueous media. *ACS Applied Energy Materials* **2017**, *1*(1), 123-128.

201. D. Scieszka, C. Sohr, P. Scheibenbogen, P. Marzak, J. Yun, Y. Liang, J. Fichtner, A.S. Bandarenka. Multiple potentials of maximum entropy of a $Na_2Co[Fe(CN)_6]$ battery electrode material: does the electrolyte composition control the interface? *ACS Applied Materials and Interfaces* **2018**, *10*, 21688–21695.

202. P. Marzak, M. Kosiahn, J. Yun, A.S. Bandarenka. Intercalation of Mg^{2+} into electrodeposited Prussian blue analogue thin films from aqueous electrolytes. *Electrochimica Acta* **2019**, *307*, 157-163.

203. D. Scieszka, J. Yun, A. S. Bandarenka. What do laser-induced transient techniques reveal for batteries? Na- and K-intercalation from aqueous electrolytes as an example. *ACS Applied Materials and Interfaces* **2017**, *9*(23), 20213-20222.

204. B. Paulitsch, Y. Yun, A. S. Bandarenka. Electrodeposited $Na_2VO_x[Fe(CN)_6]$ films as a cathode material for aqueous Na-ion batteries. *ACS Applied Materials and Interfaces* **2017**, *9*(9), 8107-8112.

205. X. Lamprecht, P. Marzak, A. Wieczorek, N. Thomsen, J. Kim, B. Garlyyev, Y. Liang, A. S. Bandarenka, J. Yun. High voltage and superior cyclability of indium hexacyanoferrate cathodes for aqueous Na-ion batteries enabled by superconcentrated $NaClO_4$ electrolytes. *Energy Advances* **2022**, *1*, 623-631.

206. F. Dinkelacker, P. Marzak, J. Yun, Y. Liang, A. S. Bandarenka. Multistage mechanism of lithium intercalation into graphite anodes in the presence of the solid electrolyte interface. *ACS Applied Materials and Interfaces* **2018**, *10*(16), 14063-14069.

207. D. Zhang, B. S. Haran, A. Durairajan, R. E. White, Y. Podrazhansky, B. N. Popov. Studies on capacity fade of lithium-ion batteries. *Journal of Power Sources* **2000**, *91*(2), 122-129.

208. A. I. Komayko, N. A. Arkharova, D. E. Presnov, E. E. Levin, V. A. Nikitina. Resolving the seeming contradiction between the superior rate capability of Prussian blue analogues and the extremely slow ionic diffusion. *The Journal of Physical Chemistry Letters* **2022**, *13*(14), 3165-3172.

209. J. Song, M. Z. Bazant. Effects of nanoparticle geometry and size distribution on diffusion impedance of battery electrodes. *Journal of The Electrochemical Society* **2012**, *160*(1), A15.

210. D. A. Buttry, M. D. Ward. Measurement of interfacial processes at electrode surfaces with the electrochemical quartz crystal microbalance. *Chemical Reviews* **1992**, *92*(6), 1355-1379.

211. G. Inzelt. Characterization of modified electrodes by electrochemical quartz crystal microbalance, radiotracer technique and impedance spectroscopy. *Electroanalysis* **1995**, *7*(9), 895-903.

212. G. Sauerbrey. Verwendung von Schwingquarzen zur Wägung dünner Schichten und zur Mikrowägung. *Zeitschrift für Physik* **1959**, *155*(2), 206-222.

213. QCM200 – Operation and service manual, Rev. 2.5. *Stanford Research Systems* **2018**.

214. K. K. Kanazawa, J. G. Gordon. Frequency of a quartz microbalance in contact with liquid. *Analytical Chemistry* **1985**, *57*(8), 1770-1771.

215. L. Daikhin, M. Urbakh. Influence of surface roughness on the quartz crystal microbalance response in a solution new configuration for QCM studies. *Faraday Discussions* **1997**, *107*, 27-38.

216. J. F. Moulder, J. Chastain (editor). Handbook of X-ray photoelectron spectroscopy: a reference book of standard spectra for identification and interpretation of XPS data. *Perkin-Elmer Corporation* **1992**.

217. G. H. Major, T. G. Avval, B. Moeini, G. Pinto, D. Shah, V. Jain, M. R. Linford *et al*. Assessment of the frequency and nature of erroneous X-ray photoelectron spectroscopy analyses in the scientific literature. *Journal of Vacuum Science & Technology A* **2020**, *38*(6), 061204.

218. G. H. Major, N. Fairley, P. M. Sherwood, M. R. Linford, J. Terry, V. Fernandez K. Artyushkova. Practical guide for curve fitting in x-ray photoelectron spectroscopy. *Journal of Vacuum Science & Technology A* **2020**, *38*(6), 061203.

219. S. Hunklinger. Festkörperphysik. *Oldenbourg Wissenschaftsverlag* **2011**.

220. Y. Waseda, E. Matsubara, K. Shinoda. X-ray diffraction crystallography. *Springer* **2011**.

221. A. Ul-Hamid. A beginners‘ guide to scanning electron microscopy. *Springer* **2018**.

222. B. Voigtländer. Atomic force microscopy. *Springer Nature* **2019**.

223. J. C. Myland, K. B. Oldham. Uncompensated resistance. 1. The effect of cell geometry. *Analytical Chemistry* **2000**, *72*(17), 3972-3980.

224. P. Marzak, P. Moser, S. Schreier, D. Scieszka, J. Yun, O. Schneider, A. S. Bandarenka. A cell for controllable formation and in operando electrochemical characterization of intercalation materials for aqueous metal-ion batteries. *Small Methods* **2019**, *3*(12), 1900445.

225. X. Lamprecht, P. Zellner, G. Yesilbas, L. Hromadko, P. Moser, P. Marzak, S. Hou, R. W. Haid, F. Steinberger, T. Steeger, J. M. Macak, A. S. Bandarenka. Fast charging capability of thin-film Prussian blue analogue electrodes for aqueous sodium-ion batteries. *ACS Applied Materials and Interfaces* **2023**, *15(19)*, 23951–23962.

226. P. Marzak. Influence of the alkali metal cation Solvation on their intercalation into battery cathode materials. *MSc Thesis, Technische Universität München* **2016**.

227. T. R. Cataldi, R. Guascito, A. M. Salvi. XPS study and electrochemical behaviour of the nickel hexacyanoferrate film electrode upon treatment in alkaline solutions. *Journal of Electroanalytical Chemistry* **1996**, *417*(1-2), 83-88.

228. P. Marzak, J. Yun, A. Dorsel, A. Kriele, R. Gilles, O. Schneider, A. S. Bandarenka. Electrodeposited $Na_2Ni[Fe(CN)_6]$ thin-film cathodes exposed to simulated aqueous Na-ion battery conditions. *The Journal of Physical Chemistry C* **2018**, *122*(16), 8760-8768.

229. Safety data sheet for NMP provided by the company *Merck*, *merckmillipore.com*. Accessed online on 09. January 2023.

230. *Adapted from the answer letter to the reviewers during the peer-review process for the article*: X. Lamprecht, F. Speck, P. Marzak, S. Cherevko, A.S. Bandarenka. Electrolyte effects on the stabilization of Prussian blue analog electrodes in aqueous sodium-ion batteries. *ACS Applied Materials and Interfaces* **2022**, *14*, 3515-3525.

231. A. S. Bandarenka. Development of hybrid algorithms for EIS data fitting. *Lecture Notes on Impedance Spectroscopy* **2013**, *4*, 29.

232. K. Momma, F. Izumi. VESTA 3 for three-dimensional visualization of crystal, volumetric and morphology data. *Journal of Applied Crystallography* **2011**, 44, 1272-1276.

233. M. Pasta, C. D. Wessells, N. Liu, J. Nelson, M. T. McDowell, R. A. Huggins, M. F. Toney, Y. Cui. Full open-framework batteries for stationary energy storage. *Nature Communications* **2014**, *5*(1), 1-9.

234. W. Zhang, Y. Wu, Z. Li, H. Dong, Y. Zhang, N. Gu. Prussian blue and other metal-organic framework-based nanozymes *in* Nanozymology (editor X. Yan). *Springer Nature* **2020**, 141-170.

235. J. Cattermull, M. Pasta, A. L. Goodwin. Structural complexity in Prussian blue analogues. *Materials Horizons.* **2021**, *8*, 3178-3186.

236. H. L. Boström, W. R. Brant. Octahedral tilting in Prussian blue analogues. *Journal of Materials Chemistry C* **2022**, *10*, 13690-13699.

237. F. Herren, P. Fischer, A. Ludi, W. Hälg. Neutron diffraction study of Prussian blue, $Fe_4[Fe(CN)_6]_3 \cdot xH_2O$. Location of water molecules and long-range magnetic order. *Inorganic Chemistry* **1980**, *19*(4), 956-959.

238. H. W. Lee, M. Pasta, R. Y. Wang, R. Ruffo, Y. Cui. Effect of the alkali insertion ion on the electrochemical properties of nickel hexacyanoferrate electrodes. *Faraday Discussions* **2014**, *176*, 69-81.

239. J. G. Gamaethiralalage, K. Singh, S. Sahin, J. Yoon, M. Elimelech, M. E. Suss, P. Liang, P. M. Biesheuvel, R. L. Zornitta, L. C. P. M. De Smet. Recent advances in ion selectivity with capacitive deionization. *Energy Environental Science* **2021**, *14*, 1095-1120.

240. C. Erinmwingbovo, M. S. Palagonia, D. Brogioli, F. La Mantia. Intercalation into a Prussian blue derivative from solutions containing two species of cations. *ChemPhysChem* **2017**, *18*, 917-925.

241. W. Li, F. Zhang, X. Xiang, X. Zhang. High-efficiency Na-storage performance of a nickel-based ferricyanide cathode in high-concentration electrolytes for aqueous sodium-ion batteries. *ChemElectroChem* **2017**, *4*(11), 2870-2876.

242. A. Doménech, N. Montoya, F. Scholz. Estimation of individual Gibbs energies of cation transfer employing the insertion electrochemistry of solid Prussian blue. *Journal of Electroanalytical Chemistry* **2011**, *657*, 117-122.

243. V. D. Neff. Electrochemical oxidation and reduction of thin films of Prussian blue. *Journal of the Electrochemical Society* **1978**, *125*(6), 886.

244. K. Itaya, I. Uchida, V. D. Neff. Electrochemistry of polynuclear transition metal cyanides: Prussian blue and its analogues. *Accounts of Chemical Research* **1986**, *19*(6), 162-168

245. K. Itaya, H. Akahoshi, S. Toshima. Electrochemistry of Prussian blue modified electrodes: an electrochemical preparation method. *Journal of the Electrochemical Society* **1982**, *129*(7), 1498.

246. N. R. De Tacconi, K. Rajeshwar, R. O. Lezna. Metal hexacyanoferrates: electrosynthesis, in situ characterization, and applications. *Chemistry of Materials* **2003**, *15*(16), 3046-3062.

247. J. Bacskai, K. Martinusz, E. Czirok, G. Inzelt, P. J. Kulesza, M. A. Malik. Polynuclear nickel hexacyanoferrates: monitoring of film growth and hydrated counter-cation flux/storage during redox reactions. *Journal of Electroanalytical Chemistry* **1995**, *385*(2), 241-248.

248. X. Hao, T. Yan, Z. Wang, S. Liu, Z. Liang, Y. Shen, M. Pritzker. Unipolar pulse electrodeposition of nickel hexacyanoferrate thin films with controllable structure on platinum substrates. *Thin Solid Films* **2012**, *520*(7), 2438-2448.

249. W. Chen, J. Tang, X. H. Xia. Composition and shape control in the construction of functional nickel hexacyanoferrate nanointerfaces. *The Journal of Physical Chemistry C* **2009**, *113*(52), 21577-21581.

250. S. J. Gerber, E. Erasmus. Electronic effects of metal hexacyanoferrates: An XPS and FTIR study. *Materials Chemistry and Physics* **2018**, *203*, 73-81.

251. X. Lamprecht, I. Evazzade, I. Ungerer, L. Hromadko, J. M. Macak, A. S. Bandarenka, V. Alexandrov. Mechanisms of degradation of $Na_2Ni[Fe(CN)_6]$ functional electrodes in aqueous media: a combined theoretical and experimental study. *The Journal of Physical Chemistry C* **2023**, *127*(5), 2204–2214.

252. S. Park, J. Kim, S. H. Yi, S. E. Chun. Coprecipitation temperature effects of morphology-controlled nickel hexacyanoferrate on the electrochemical performance in aqueous sodium-ion batteries. *ChemSusChem* **2021**, *14*(4), 1082-1093.

253. J. Vetter, P. Novák, M. R. Wagner, C. Veit, K. C. Möller, J. O. Besenhard, M. Winter, M. Wohlfahrt-Mehrens, C. Vogler, A. Hammouche. Ageing mechanisms in lithium-ion batteries. *Journal of Power Sources* **2005**, *147*(1-2), 269-281.

254. C. R. Birkl, M. R. Roberts, E. McTurk, P. G. Bruce, D. A. Howey. Degradation diagnostics for lithium ion cells. *Journal of Power Sources* **2017**, *341*, 373-386.

255. M. M. Kabir, D. E. Demirocak. Degradation mechanisms in Li-ion batteries: a state-of-the-art review. *International Journal of Energy Research* **2017**, *41*(14), 1963-1986.

256. Y. Yang, C. Brownell, N. Sadrieh, J. May, A. Del Grosso, D. Place, P. Faustino, *et al*. Quantitative measurement of cyanide released from Prussian blue. *Clinical Toxicology* **2007**, *45*(7), 776-781.

257. W. Zhang, Y. Zhao, V. Malgras, Q. Ji, D. Jiang, R. Qi, M. Hu, *et al*. Synthesis of monocrystalline nanoframes of Prussian blue analogues by controlled preferential etching. *Angewandte Chemie International Edition* **2016**, *55*(29), 8228-8234.

258. Y. Zhu, B. Wang, Q. Gan, Y. Wang, Z. Wang, J. Xie, Z. Lu, *et al*. Selective edge etching to improve the rate capability of Prussian blue analogues for sodium ion batteries. *Inorganic Chemistry Frontiers* **2019**, *6*(6), 1361-1366.

259. M. Hu, S. Furukawa, R. Ohtani, H. Sukegawa, Y. Nemoto, J. Reboul, Y. Yamauchi, *et al*. Synthesis of Prussian blue nanoparticles with a hollow interior by controlled chemical etching. *Angewandte Chemie International Edition* **2012**, *51*(4), 984-988.

260. M. Hu, A. A. Belik, M. Imura, Y. Yamauchi. Tailored design of multiple nanoarchitectures in metal-cyanide hybrid coordination polymers. *Journal of the American Chemical Society* **2013**, *135*(1), 384-391.

261 D. E. Stilwell, K. H. Park, M. H. Miles. Electrochemical studies of the factors influencing the cycle stability of Prussian blue films. *Journal of Applied Electrochemistry* **1992**, *22*(4), 325-331.

262. H. Mimura, J. Lehto, R. Harjula. Chemical and thermal stability of potassium nickel hexacyanoferrate(II). *Journal of Nuclear Science and Technology* **1997**, *34*(6), 582-587.

263. X. H. Liu, J. Peng, W. H. Lai, Y. Gao, H. Zhang, L. Li, Y. Qiao, S. L. Chou. Advanced characterization techniques paving the way for commercialization of low-cost Prussian blue analog cathodes. *Advanced Functional Materials* **2022**, *32*(7), 2108616.

264. C. D. Wessells, R. A. Huggins. Stabilization of battery electrodes. *Patent US9,130,234B2* **2015**.

265. R. Y. Wang, C. D. Wessells, R. A. Huggins, Y. Cui. Highly reversible open framework nanoscale electrodes for divalent ion batteries. *Nano Letters* **2013**, *13*, 5748-5752.

266. C. D. Wessells, S. Motallebi. Electrolyte additives for electrochemical devices. *Patent US10,862,168B2* **2020**.

267. C. D. Wessells, A. Firouzi, S. Motallebi, S. Strohband. Cosolvent electrolytes for electrochemical devices. *Patent US9,287,589B2* **2016**.

268. C. D. Wessells, R. A. Huggins, Y. Cui. Copper hexacyanoferrate battery electrodes with long cycle life and high power. *Nature Communications* **2011**, *2*(1), 550.

269. L. Jiang, Y. Lu, C. Zhao, L. Liu, J. Zhang, Q. Zhang, Y. S. Hu, *et al*. Building aqueous K-ion batteries for energy storage. *Nature Energy* **2019**, *4*(6), 495-503.

270. L. Chen, W. Sun, K. Xu, Q. Dong, L. Zheng, J. Wang, D. Lu, Y. Shen, J. Zhang, H. Chen, *et al*. How Prussian blue analogues can be stable in concentrated aqueous electrolytes. *ACS Energy Letters* **2022**, *7*, 1672-1678.

271. W. J. Li, S. L. Chou, J. Z. Wang, J. L. Wang, Q. F. Gu, H. K. Liu, S. X. Dou. Multifunctional conducing polymer coated $Na_{1+x}MnFe(CN)_6$ cathode for sodium-ion batteries with superior performance via a facile and one-step chemistry approach. *Nano Energy* **2015**, *13*, 200-207.

272. D. Asakura, C. H. Li, Y. Mizuno, M. Okubo, H. Zhou, D. R. Talham. Bimetallic cyanide-bridged coordination polymers as lithium ion cathode materials: core@shell nanoparticles with enhanced cyclability. *Journal of the American Chemical Society* **2013**, *135*(7), 2793-2799.

273. T. U. Choi, G. Baek, S. G. Lee, J. H. Lee. Hierarchically designed cathodes composed of vanadium hexacyanoferrate@copper hexacyanoferrate with enhanced cycling stability. *ACS Applied Materials and Interfaces* **2020**, *12*(22), 24817-24826.

274. X. Wu, M. Sun, S. Guo, J. Qian, Y. Liu, Y. Cao, X. Ai, H. Yang. Vacancy-free Prussian blue nanocrystals with high capacity and superior cyclability for aqueous sodium-ion batteries. *ChemNanoMat* **2015**, *1*(3), 188-193.

275. X. Wu, C. Wu, C. Wei, L. Hu, J. Qian, Y. Cao, X. Ai, J. Wang, H. Yang. Highly crystallized $Na_2CoFe(CN)_6$ with suppressed lattice defects as superior cathode material for sodium-ion batteries. *ACS Applied Materials and Interfaces* **2016**, *8*(8), 5393-5399.

276. X. Wu, Y. Luo, M. Sun, J. Qian, Y. Cao, X. Ai, H. Yang. Low-defect Prussian blue nanocubes as high capacity and long life cathodes for aqueous Na-ion batteries. *Nano Energy* **2015**, *13*, 117-123.

277. Y. You, X. L. Wu, Y. X. Yin, Y. G. Guo. High-quality Prussian blue crystals as superior cathode materials for room-temperature sodium-ion batteries. *Energy & Environmental Science* **2014**, *7*(5), 1643-1647.

278. W. J. Li, S. L. Chou, J. Z. Wang, Y. M. Kang, J. L. Wang, Y. Liu, S. X. Duo, *et al*. Facile method to synthesize Na-enriched $Na_{1+x}FeFe(CN)_6$ frameworks as cathode with superior electrochemical performance for sodium-ion batteries. *Chemistry of Materials* **2015**, *27*(6), 1997-2003.

279. D. Yang, J. Xu, X. Z. Liao, Y. S. He, H. Liu, Z. F. Ma. Structure optimization of Prussian blue analogue cathode materials for advanced sodium ion batteries. *Chemical Communications* **2014**, *50*(87), 13377-13380.

280. X. Lamprecht. Degradation mechanisms of thin film electrodes in aqueous sodium ion batteries. *MSc Thesis, Technische Universität München* **2019**.

281. X. Lamprecht, F. Speck, P. Marzak, S. Cherevko, A.S. Bandarenka. Electrolyte effects on the stabilization of Prussian blue analog electrodes in aqueous sodium-ion batteries. *ACS Applied Materials and Interfaces* **2022**, *14*, 3515-3525.

282. P. P. Lopes. A framework for the relationships between stability and functional properties of electrochemical energy materials. *ACS Materials Au* **2023**, 2023, *3*(1), 8–17.

283. T. Waldmann, A. Iturrondobeitia, M. Kasper, N. Ghanbari, F. Aguesse, E. Bekaert, M. Wohlfahrt-Mehrens, *et al*. Post-mortem analysis of aged lithium-ion batteries: Disassembly methodology and physico-chemical analysis techniques. *Journal of the Electrochemical Society* **2016**, *163*(10), A2149.

284. H. Zheng, Q. Sun, G. Liu, X. Song, V. S. Battaglia. Correlation between dissolution behavior and electrochemical cycling performance for $LiNi_{1/3}Co_{1/3}Mn_{1/3}O_2$-based cells. *Journal of Power Sources* **2012**, *207*, 134-140.

285. K. Amine, Z. Chen, Z. Zhang, J. Liu, W. Lu, Y. Qin, Y. K. Sun, *et al*. Mechanism of capacity fade of MCMB/$Li_{1.1}[Ni_{1/3}Mn_{1/3}Co_{1/3}]_{0.9}O_2$ cell at elevated temperature and additives to improve its cycle life. *Journal of Materials Chemistry* **2011**, *21*(44), 17754-17759.

286. Y. K. Lee, J. Park, W. A. Lu. A comprehensive experimental and modeling study on dissolution in Li-ion batteries. *Journal of the Electrochemical Society* **2019**, *166*(8), A1340.

287. J. Xie, L. Ma, J. Li, X. Yin, Z. Wen, Y. Zhong, C. Li, Y. Liu, Z. Shen, W. Mai, G. Hong, W. Zhang. Self-healing of Prussian blue analogues with electrochemically driven morphological rejuvenation. *Advanced Materials* **2022**, *34*(44), 2205625.

288. F. Feng, S. Chen, S. Zhao, W. Zhang, Y. Miao, H. Che, Z. F. Ma, *et al*. Enhanced electrochemical performance of MnFe@NiFe Prussian blue analogue benefited from the inhibition of Mn ions dissolution for sodium-ion batteries. *Chemical Engineering Journal* **2021**, *411*, 128518.

289. G. Kasiri, R. Trócoli, A. B. Hashemi, F. La Mantia. An electrochemical investigation of the aging of copper hexacyanoferrate during the operation in zinc-ion batteries. *Electrochimica Acta* **2016**, *222*, 74-83.

290. T. Shao, C. Li, C. Liu, W. Deng, W. Wang, M. Xue, R. Li. Electrolyte regulation enhances the stability of Prussian blue analogues in aqueous Na-ion storage. *Journal of Materials Chemistry A* **2019**, *7*(4), 1749-1755.

291. J. H. Lee, G. Ali, D. H. Kim, K. Y. Chung. Metal-organic framework cathodes based on a vanadium hexacyanoferrate Prussian blue analogue for high-performance aqueous rechargeable batteries. *Advanced Energy Materials* **2017**, *7*(2), 1601491.

292. L. Zhang, L. Chen, X. Zhou, Z. Liu. Towards high-voltage aqueous metal-ion batteries beyond 1.5 V: the zinc/zinc hexacyanoferrate system. *Advanced Energy Materials* **2015**, *5*(2), 1400930.

293. N. Tapia-Ruiz, A. R. Armstrong, H. Alptekin, M. A. Amores, H. Au, J. Barker, R. Younesi, *et al*. 2021 roadmap for sodium-ion batteries. *Journal of Physics: Energy* **2021**, *3*(3), 031503.

294. S. Solchenbach, G. Hong, A. T. S. Freiberg, R. Jung, H. A. Gasteiger. Electrolyte and SEI decomposition reactions of transition metal ions investigated by on-line electrochemical mass spectrometry. *Journal of the Electrochemical Society* **2018**, *165*(14), A3304.

295. B. B. Berkes, A. Jozwiuk, M. Vračar, H. Sommer, T. Brezesinski, J. Janek. Online continuous flow differential electrochemical mass spectrometry with a realistic battery setup for high-precision, long-term cycling tests. *Analytical Chemistry* **2015**, *87*(12), 5878-5883.

296. B. Strehle, S. Solchenbach, M. Metzger, K. U. Schwenke, H. A. Gasteiger. The effect of CO_2 on alkyl carbonate trans-esterification during formation of graphite electrodes in Li-ion batteries. *Journal of The Electrochemical Society* **2017**, *164*(12), A2513.

297. R. Jung, F. Linsenmann, R. Thomas, J. Wandt, S. Solchenbach, F. Maglia, H. A. Gasteiger, *et al*. Nickel, manganese, and cobalt dissolution from Ni-rich NMC and their effects on NMC622-graphite cells. *Journal of the Electrochemical Society* **2019**, *166*(2), A378.

298. J. Wandt, A. Freiberg, R. Thomas, Y. Gorlin, A. Siebel, R. Jung, H. A. Gasteiger, M. Tromp. Transition metal dissolution and deposition in Li-ion batteries investigated by operando X-ray absorption spectroscopy. *Journal of Materials Chemistry A* **2016**, *4*(47), 18300-18305.

299. R. Hausbrand, G. Cherkashinin, H. Ehrenberg, M. Gröting, K. Albe, C. Hess, W. Jaegermann. Fundamental degradation mechanisms of layered oxide Li-ion battery cathode materials: Methodology, insights and novel approaches. *Materials Science and Engineering: B* **2015**, *192*, 3-25.

300. S. E. Lee, O. C. Harris, T. Siboonruang, M. Tang. A reaction engineering approach to non-aqueous battery lifetime. *Joule* **2021**, *5*(3), 551-563.

301. L. F. Wang, C. C. Ou, K. A. Striebel, J. S. Chen. Study of Mn dissolution from $LiMn_2O_4$ spinel electrodes using rotating ring-disk collection experiments. *Journal of the Electrochemical Society* **2003**, *150*(7), A905.

302. P. P. Lopes, M. Zorko, K. L. Hawthorne, J. G. Connell, B. J. Ingram, D. Strmcnik, N. M. Markovic, *et al*. Real-time monitoring of cation dissolution/deintercalation kinetics from transition-metal oxides in organic environments. *The Journal of Physical Chemistry Letters* **2018**, *9*(17), 4935-4940.

303. S. Nikman, D. Zhao, V. Gonzalez-Perez, H. H. Hoster, S. F. Mertens. Surface or bulk? Real-time manganese dissolution detection in a lithium-ion cathode. *Electrochimica Acta* **2021**, *386*, 138373.

304. S. J. Wachs, C. Behling, J. Ranninger, J. Möller, K. J. Mayrhofer, B. B. Berkes. Online monitoring of transition-metal dissolution from a high-Ni-content cathode material. *ACS Applied Materials and Interfaces* **2021**, *13*(28), 33075-33082.

305. J. Lüchtefeld, H. Hemmelmann, S. Wachs, K. J. Mayrhofer, M. T. Elm, B. B. Berkes. Effect of water contamination on the transition metal dissolution in water-enriched electrolyte: A mechanistic insight into a new type of dissolution. *The Journal of Physical Chemistry C* **2022**, *126*(40), 17204-17211.

306. S. O. Klemm, A. A. Topalov, C. A. Laska, K. J. Mayrhofer. Coupling of a high throughput microelectrochemical cell with online multielemental trace analysis by ICP-MS. *Electrochemistry Communications* **2011**, *13*(12), 1533-1535.

307. O. Kasian, S. Geiger, K. J. Mayrhofer, S. Cherevko. Electrochemical on-line ICP-MS in electrocatalysis research. *The Chemical Record* **2019**, *19*(10), 2130-2142.

308. J. Ranninger, S. J. Wachs, J. Möller, K. J. Mayrhofer, B. B. Berkes. On-line monitoring of dissolution processes in nonaqueous electrolytes - a case study with platinum. *Electrochemistry Communications* **2020**, *114*, 106702.

309. A. A. Topalov, I. Katsounaros, M. Auinger, S. Cherevko, J. C. Meier, S. O. Klemm, K .J. Mayrhofer. Dissolution of platinum: limits for the deployment of electrochemical energy conversion? *Angewandte Chemie International Edition* **2012**, *51*(50), 12613-12615.

310. S. Cherevko, A. R. Zeradjanin, G. P. Keeley, K. J. Mayrhofer. A comparative study on gold and platinum dissolution in acidic and alkaline media. *Journal of the Electrochemical Society* **2014**, *161*(12), H822.

311. S. Cherevko, N. Kulyk, K. J. Mayrhofer. Durability of platinum-based fuel cell electrocatalysts: Dissolution of bulk and nanoscale platinum. *Nano Energy* **2016**, *29*, 275-298.

312. M. Ledendecker, S. J. Mondschein, O. Kasian, S. Geiger, D. Göhl, M. Schalenbach, K. J. Mayrhofer, *et al*. Stability and activity of non-noble-metal-based catalysts toward the hydrogen evolution reaction. *Angewandte Chemie International Edition* **2017**, *56*(33), 9767-9771.

313. F. D. Speck, A. Zagalskaya, V. Alexandrov, S. Cherevko. Periodicity in the electrochemical dissolution of transition metals. *Angewandte Chemie International Edition* **2021**, *60*(24), 13343-13349.

314. E. S. Davydova, F. D. Speck, M. T. Paul, D. R. Dekel, S. Cherevko. Stability limits of Ni-based hydrogen oxidation electrocatalysts for anion exchange membrane fuel cells. *ACS Catalysis* **2019**, *9*(8), 6837-6845.

315. J. C. Meeussen, M. G. Keizer, F. A. De Haan. Chemical stability and decomposition rate of iron cyanide complexes in soil solutions. *Environmental Science & Technology* **1992**, *26*(3), 511-516.

316. M. Pasta, R. Y. Wang, R. Ruffo, R. Qiao, H. W. Lee, B. Shyam, Y. Cui, *et al*. Manganese-cobalt hexacyanoferrate cathodes for sodium-ion batteries. *Journal of Materials Chemistry A* **2016**, *4*(11), 4211-4223.

317. J. K. Nørskov, T. Bligaard, J. Rossmeisl, C. H. Christensen. Towards the computational design of solid catalysts. *Nature Chemistry* **2009**, *1*(1), 37-46.

318. F. Calle-Vallejo, J. Tymoczko, V. Colic, Q. H. Vu, M. D. Pohl, K. Morgenstern, D. Loffreda, P. Sautet, W. Schuhmann, A. S. Bandarenka. Finding optimal surface sites on heterogeneous catalysts by counting nearest neighbors. *Science* **2015**, *350*(6257), 185-189.

319. Z. W. Seh, J. Kibsgaard, C. F. Dickens, I. B. Chorkendorff, J. K. Nørskov, T. F. Jaramillo. Combining theory and experiment in electrocatalysis: Insights into materials design. *Science* **2017**, *355*(6321), eaad4998.

320. A. Jain, S. P. Ong, G. Hautier, W. Chen, W. D. Richards, S. Dacek, K .A. Persson, *et al*. Commentary: The Materials Project: A materials genome approach to accelerating materials innovation. *APL Materials* **2013**, *1*(1), 011002.

321. Y. S. Meng, M. E. Arroyo de Dompablo. First principles computational materials design for energy storage materials in lithium ion batteries. *Energy & Environmental Science* **2009**, *2*(6), 589-609.

322. W. T. Hong, M. Risch, K. A. Stoerzinger, A. Grimaud, J. Suntivich, Y. Shao-Horn. Toward the rational design of non-precious transition metal oxides for oxygen electrocatalysis. *Energy & Environmental Science* **2015**, *8*(5), 1404-1427.

323. J. Hafner, C. Wolverton, G. Ceder. Toward computational materials design: the impact of density functional theory on materials research. *MRS Bulletin* **2006**, *31*(9), 659-668.

324. Q. Wang, L. Velasco, B. Breitung, V. Presser. High-entropy energy materials in the age of big data: a critical guide to next-generation synthesis and applications. *Advanced Energy Materials* **2021**, *11*(47), 2102355.

325. A. Urban, D. H. Seo, G. Ceder. Computational understanding of Li-ion batteries. *npj Computational Materials* **2016**, *2*(1), 1-13.

326. I. Ungerer Fraga. Role of the electrolyte composition on the stability of NiHCF electrodes for aqueous sodium-ion batteries. *BSc Thesis, Technische Universität München* **2022**.

327. X. Wu, J. J. Hong, W. Shin, L. Ma, T. Liu, X. Bi, X. Ji, *et al*. Diffusion-free Grotthuss topochemistry for high-rate and long-life proton batteries. *Nature Energy* **2019**, *4*(2), 123-130.

328. R. Bors, Y. Yun, P. Marzak, J. Fichtner, D. Scieszka, A. S. Bandarenka. Chromium(II) hexacyanoferrate-based thin films as a material for aqueous alkali metal cation batteries. *ACS Omega* **2018**, *3*(5), 5111-5115.

329. J. A. Dean. Lange's handbook of chemistry, 15th ed. *McGraw-Hill* **1999**. Section 8.

330. A. Trummal, L. Lipping, I. Kaljurand, I. A. Koppel, I. Leito. Acidity of strong acids in water and dimethyl sulfoxide. *The Journal of Physical Chemistry A* **2016**, *120*(20), 3663-3669.

331. Y. Yamada, J. Wang, S. Ko, E. Watanabe, A. Yamada. Advances and issues in developing salt-concentrated battery electrolytes. *Nature Energy* **2019**, *4*(4), 269-280.

332. W. Hu, Y. Peng, Y. Wei, Y. Yang. Application of electrochemical impedance spectroscopy to degradation and aging research of lithium-ion batteries. *The Journal of Physical Chemistry C* **2023**. *127*(9), 4465-4495.

333. P. Iurilli, C. Brivio, V. Wood. On the use of electrochemical impedance spectroscopy to characterize and model the aging phenomena of lithium-ion batteries: a critical review. *Journal of Power Sources* **2021**, *505*, 229860.

334. W. Waag, S. Käbitz, D. U. Sauer. Experimental investigation of the lithium-ion battery impedance characteristic at various conditions and aging states and its influence on the application. *Applied Energy* **2013**, *102*, 885-897.

335. M. Dubarry, C. Truchot, B. Y. Liaw, K. Gering, S. Sazhin, D. Jamison, C. Michelbacher. Evaluation of commercial lithium-ion cells based on composite positive electrode for plug-in hybrid electric vehicle applications. Part II. Degradation mechanism under 2 C cycle aging. *Journal of Power Sources* **2011**, *196*(23), 10336-10343.

336. X. Han, L. Lu, Y. Zheng, X. Feng, Z. Li, J. Li, M. Ouyang. A review on the key issues of the lithium ion battery degradation among the whole life cycle. *ETransportation* **2019**, *1*, 100005.

337. D. Aurbach, B. Markovsky, I. Weissman, E. Levi, Y. Ein-Eli. On the correlation between surface chemistry and performance of graphite negative electrodes for Li ion batteries. *Electrochimica Acta* **1999**, *45*(1-2), 67-86.

338. J. Guo, S. Jin, X. Sui, X. Huang, Y. Xu, Y. Li, D. Stroe. Unravelling and quantifying the aging processes of commercial $Li(Ni_{0.5}Co_{0.2}Mn_{0.3})O_2$/graphite lithium-ion batteries under constant current cycling. *Journal of Materials Chemistry A* **2023**, *11*(1), 41-52.

339. M. G. S. R. Thomas, P. G. Bruce, J. B. Goodenough. AC impedance analysis of polycrystalline insertion electrodes: application to $Li_{1-x}CoO_2$. *Journal of the Electrochemical Society* **1985**, 132(7), 1521.

340. Y. Xu, M. Ou, Y. Liu, J. Xu, S. Sun, C. Fang, Y. Huang, *et al*. Crystallization-induced ultrafast Na-ion diffusion in nickel hexacyanoferrate for high-performance sodium-ion batteries. *Nano Energy* **2020**, *67*, 104250.

341. C. Heubner, M. Schneider, A. Michaelis. Diffusion-limited C-rate: a fundamental principle quantifying the intrinsic limits of Li-ion batteries. *Advanced Energy Materials* **2020**, *10*(2), 1902523.

342. H. Ruan, J. V. Barreras, T. Engstrom, Y. Merla, R. Millar, B. Wu. Lithium-ion battery lifetime extension: a review of derating methods. *Journal of Power Sources* **2023**, *563*, 232805.

343. D. Kim, S. Park, O. B. Chae, J. H. Ryu, Y. U. Kim, R. Z. Yin, S. M. Oh. Re-deposition of manganese species on spinel $LiMn_2O_4$ electrode after Mn dissolution. *Journal of the Electrochemical Society* **2011**, *159*(3), A193.

344. D. Aurbach, B. Markovsky, G. Salitra, E. Markevich, Y. Talyossef, M. Koltypin, D. Kovacheva, *et al*. Review on electrode–electrolyte solution interactions, related to cathode materials for Li-ion batteries. *Journal of Power Sources* **2007**, *165*(2), 491-499.

345. J. Huang, P. Xu, T. Gao, J. Huangfu, X. J. Wang, S. Liu, B. Song, *et al*. Controlled synthesis of hollow bimetallic Prussian blue analog for conversion into efficient oxygen evolution electrocatalyst. *ACS Sustainable Chemistry & Engineering* **2019**, *8*(2), 1319-1328.

346. M. Qin, W. Ren, J. Meng, X. Wang, X. Yao, Y. Ke, L. Mai, *et al*. Realizing superior Prussian blue positive electrode for potassium storage via ultrathin nanosheet assembly. *ACS Sustainable Chemistry & Engineering* **2019**, *7*(13), 11564-11570.

347. J. Nai, X. W. Lou. Hollow structures based on Prussian blue and its analogs for electrochemical energy storage and conversion. *Advanced Materials* **2019**, *31*(38), 1706825.

348. A. Dostal, B. Meyer, F. Scholz, U. Schroeder, A. M. Bond, F. Marken, S. J. Shaw. Electrochemical study of microcrystalline solid Prussian blue particles mechanically attached to graphite and gold electrodes: electrochemically induced lattice reconstruction. *The Journal of Physical Chemistry* **1995**, *99*(7), 2096-2103.

349. J. Ge, L. Fan, A. M. Rao, J. Zhou, B. Lu. Surface-substituted Prussian blue analogue cathode for sustainable potassium-ion batteries. *Nature Sustainability* **2022**, *5*(3), 225-234.

350. J. Xie, L. Ma, J. Li, X. Yin, Z. Wen, Y. Zhong, W. Zhang. Self-Healing of Prussian blue analogues with electrochemically driven morphological rejuvenation. *Advanced Materials* **2022**, *34*(44), 2205625.

351. S. Kjeldgaard, I. Dugulan, A. Mamakhel, M. Wagemaker, B. B. Iversen, A. Bentien. Strategies for synthesis of Prussian blue analogues. *Royal Society Open Science* **2021**, *8*(1), 201779.

352. R. Rehman, J. Peng, H. Yi, Y. Shen, J. Yin, C. Li, J. Han, *et al*. Highly crystalline nickel hexacyanoferrate as a long-life cathode material for sodium-ion batteries. *RSC Advances* **2020**, *10*(45), 27033-27041.

353. R. Chen, Y. Huang, M. Xie, Z. Wang, Y. Ye, L. Li, F. Wu. Chemical inhibition method to synthesize highly crystalline Prussian blue analogs for sodium-ion battery cathodes. *ACS Applied Materials and Interfaces* **2016**, *8*(46), 31669-31676.

354. J. Asenbauer, T. Eisenmann, M. Kuenzel, A. Kazzazi, Z. Chen, D. Bresser. The success story of graphite as a lithium-ion anode material – fundamentals, remaining challenges, and recent developments including silicon (oxide) composites. *Sustainable Energy & Fuels* **2020**, *4*(11), 5387-5416.

355. A. Kraytsberg, Y. Ein-Eli. Conveying advanced Li-ion battery materials into practice - the impact of electrode slurry preparation skills. *Advanced Energy Materials* **2016**, *6*(21), 1600655.

356. T. Jin, Q. Han, L. Jiao. Binder-free electrodes for advanced sodium-ion batteries. *Advanced Materials* **2020**, *32*(3), 1806304.

357. G. Zhou, F. Li, H. M. Cheng. Progress in flexible lithium batteries and future prospects. *Energy & Environmental Science* **2014**, *7*(4), 1307-1338.

358. C. Heubner, K. Nikolowski, S. Reuber, M. Schneider, M. Wolter, A. Michaelis. Recent insights into rate performance limitations of Li-ion batteries. *Batteries & Supercaps* **2021**, *4*(2), 268-285.

359. P. S. Camacho, R. Wernert, M. Duttine, A. Wattiaux, A. Rudola, P. Balaya, L. Croguennec. Impact of synthesis conditions in Na-rich Prussian blue analogues. *ACS Applied Materials and Interfaces* **2021**, *13*(36), 42682-42692

360. F. Zhang, L. Qi. Recent progress in self-supported metal oxide nanoarray electrodes for advanced lithium-ion batteries. *Advanced Science* **2016**, *3*(9), 1600049.

361. P. Simon, Y. Gogotsi, B. Dunn. Where do batteries end and supercapacitors begin? *Science* **2014**, *343*(6176), 1210-1211.

362. J. Jiang, Y. Li, J. Liu, X. Huang, C. Yuan, X. W. Lou. Recent advances in metal oxide-based electrode architecture design for electrochemical energy storage. *Advanced Materials* **2012**, *24*(38), 5166-5180.

363. Y. Sun, N. Liu, Y. Cui. Promises and challenges of nanomaterials for lithium-based rechargeable batteries. *Nature Energy* **2016**, *1*(7), 1-12.

364. L. Ji, Z. Lin, M. Alcoutlabi, X. Zhang. Recent developments in nanostructured anode materials for rechargeable lithium-ion batteries. *Energy & Environmental Science* **2011**, *4*(8), 2682-2699.

365. P. G. Bruce, B. Scrosati, J. M. Tarascon. Nanomaterials for rechargeable lithium batteries. *Angewandte Chemie International Edition* **2008**, *47*(16), 2930-2946.

366. B. He, Q. Zhang, Z. Pan, L. Li, C. Li, Y. Ling, Z. Wang, M. Chen, Z. Wang, Y. Yao, Q. Ling, L. Sun, J. Wang, L. Wei. Freestanding metal – organic frameworks and their derivatives: an emerging platform for electrochemical energy storage and conversion. *Chemical Reviews* **2022**, *122*, 11, 10087–10125.

367. Y. Lin, L. Zhang, Y. Xiong, T. Wei, Z. Fan, Z. Toward the design of high-performance supercapacitors by Prussian blue, its analogues and their derivatives. *Energy & Environmental Materials* **2020**, *3*(3), 323-345.

368. X. Tang, H. Liu, D. Su, P. H. Notten, G. Wang. Hierarchical sodium-rich Prussian blue hollow nanospheres as high-performance cathode for sodium-ion batteries. *Nano Research* **2018**, *11*, 3979-3990.

369. W. Ren, M. Qin, Z. Zhu, M. Yan, Q. Li, L. Zhang, L. Mai, *et al*. Activation of sodium storage sites in Prussian blue analogues via surface etching. *Nano Letters* **2017**, *17*(8), 4713-4718.

370. J. Pu, Z. Shen, C. Zhong, Q. Zhou, J. Liu, J. Zhu, H. Zhang. Electrodeposition technologies for Li-based batteries: New frontiers of energy storage. *Advanced Materials* **2020**, *32*(27), 1903808.

371. Y. Pang, Y. Cao, Y. Chu, M. Liu, K. Snyder, D. MacKenzie, C. Cao. Additive manufacturing of batteries. *Advanced Functional Materials* **2020**, *30*(1), 1906244.

372. C. Zhu, T. Liu, F. Qian, W. Chen, S. Chandrasekaran, B. Yao, Y. Li, *et al*. 3D printed functional nanomaterials for electrochemical energy storage. *Nano Today* **2017**, *15*, 107-120.

373. P. Zellner. Scalability of fast-charging properties in aqueous sodium-ion batteries. *BSc Thesis*, *Technische Universität München* **2021**.

374. V. V. Kondratiev, A. V. Tikhomirova, V. V. Malev. Study of charge transport processes in Prussian-blue film modified electrodes. *Electrochimica Acta* **1999**, *45*(4-5), 751-759.

375. K. Dokko, N. Nakata, Y. Suzuki, K. Kanamura. High-rate lithium deintercalation from lithiated graphite single-particle electrode. *The Journal of Physical Chemistry C* **2010**, *114*(18), 8646-8650.

376. M. Lovrić, M. Hermes, F. Scholz. The effect of the electrolyte concentration in the solution on the voltammetric response of insertion electrodes. *Journal of Solid State Electrochemistry* **1998**, *2*, 401-404.

377. C. Heubner, C. Lämmel, A. Nickol, T. Liebmann, M. Schneider, A. Michaelis. Comparison of chronoamperometric response and rate-performance of porous insertion electrodes: towards an accelerated rate capability test. *Journal of Power Sources* **2018**, *397*, 11-15.

378. B. E. Conway. Transition from "supercapacitor" to "battery" behavior in electrochemical energy storage. *Journal of the Electrochemical Society* **1991**, *138*(6), 1539.

379. V. Augustyn, J. Come, M. A. Lowe, J. W. Kim, P. L. Taberna, S. H. Tolbert, H. D. Abruña, P. Simon, B. Dunn. High-rate electrochemical energy storage through Li^+ intercalation pseudocapacitance. *Nature Materials* **2013**, *12*(6), 518-522.

380. J. Come, P. L. Taberna, S. Hamelet, C. Masquelier, P. Simon. Electrochemical kinetic study of $LiFePO_4$ using cavity microelectrode. *Journal of The Electrochemical Society* **2011**, *158*(10), A1090.

381. H. Munakata, B. Takemura, T. Saito, K. Kanamura. Evaluation of real performance of $LiFePO_4$ by using single particle technique. *Journal of Power Sources* **2012**, *217*, 444-448.

382. K. Ariyoshi, M. Tanimoto, Y. Yamada. Impact of particle size of lithium manganese oxide on charge transfer resistance and contact resistance evaluated by electrochemical impedance analysis. *Electrochimica Acta* **2020**, *364*, 137292.

383. K. Hurlbutt, F. Giustino, G. Volonakis, M. Pasta. Origin of the high specific capacity in sodium manganese hexacyanomanganate. *Chemistry of Materials* **2022**, *34*(10), 4336-4343.

384. F. Steinberger. Aqueous sodium ion batteries: Stability and self-discharge of manganese hexacyanomanganate (MnHCMn) electrodes. *MSc Thesis, Technische Universität München* **2021**.

385. T. Steeger. Self-discharge, degradation and characterization of manganese hexacyanomanganate thin films in aqueous sodium ion batteries. *BSc Thesis, Technische Universität München* **2022**.

386. P. Moser. High-performance model aqueous Na-ion batteries. *MSc Thesis, Technische Universität München* **2018**.

387. J. Y. Luo, W. J. Cui, P. He, Y. Y. Xia. Raising the cycling stability of aqueous lithium-ion batteries by eliminating oxygen in the electrolyte. *Nature Chemistry* **2010**, *2*(9), 760-765.

388. W. Xing, M. Yin, Q. Lv, Y. Hu, C. Liu, J. Zhang. Oxygen solubility, diffusion coefficient, and solution viscosity. In *Rotating Electrode Methods and Oxygen Reduction Electrocatalysts*. *Elsevier* **2014**.

389. L. Chen, L. Cao, X. Ji, S. Hou, Q. Li, J. Chen, C. Wang, *et al*. Enabling safe aqueous lithium ion open batteries by suppressing oxygen reduction reaction. *Nature Communications* **2020**, *11*(1), 2638.

390. G. Plečkaitytė, M. Petrulevičienė, L. Staišiūnas, D. Tediashvili, J. Pilipavičius, J. Juodkazytė, L. Vilčiauskas. Understanding and mitigation of $NaTi_2(PO_4)_3$ degradation in aqueous Na-ion batteries. *Journal of Materials Chemistry A* **2021**, *9*(21), 12670-12683.

391. J. F. Whitacre, S. Shanbhag, A. Mohamed, A. Polonsky, K. Carlisle, J. Gulakowski, C. Truchot, *et al*. A polyionic, large-format energy storage device using an aqueous electrolyte and thick-format composite $NaTi_2(PO_4)_3$/activated carbon negative electrodes. *Energy Technology* **2015**, *3*(1), 20-31.

392. M. Ujvári, G. G. Lang. On the stability of perchlorate ions against reductive attacks in electrochemical systems and in the environment. *Journal of Electrochemical Science and Engineering* **2011**, *1*(1), 1-26.

393. S. Chen, C. Niu, H. Lee, Q. Li, L. Yu, W. Xu, J. Liu, *et al*. Critical parameters for evaluating coin cells and pouch cells of rechargeable Li-metal batteries. *Joule* **2019**, *3*(4), 1094-1105.

394. B. Wang, X. Wang, C. Liang, M. Yan, Y. Jiang. An all-Prussian-blue-based aqueous sodium-ion battery. *ChemElectroChem* **2019**, *6*(18), 4848-4853.

395. J. C. Liu, Z. H. Huang, T. Y. Ma. Aqueous supercapacitor with ultrahigh voltage window beyond 2.0 volt. *Small Structures* **2020**, *1*(1), 2000020.

396. T. S. Mathis, N. Kurra, X. Wang, D. Pinto, P. Simon, Y. Gogotsi. Energy storage data reporting in perspective - guidelines for interpreting the performance of electrochemical energy storage systems. *Advanced Energy Materials* **2019**, *9*(39), 1902007.

397. Z. Lin, T. Liu, X. Ai, C. Liang. Aligning academia and industry for unified battery performance metrics. *Nature Communications* **2018**, *9*(1), 1-5.

398. L. S. Kremer, A. Hoffmann, T. Danner, S. Hein, B. Prifling, D. Westhoff, M. Wohlfahrt-Mehrens, *et al*. Manufacturing process for improved ultra-thick cathodes in high-energy lithium-ion batteries. *Energy Technology* **2020**, *8*(2), 1900167.

399. B. L. Ellis, P. Knauth, T. Djenizian. Three-dimensional self-supported metal oxides for advanced energy storage. *Advanced Materials* **2014**, *26*(21), 3368-3397.

400. G. Zhou, L. Xu, G. Hu, L. Mai, Y. Cui. Nanowires for electrochemical energy storage. *Chemical Reviews* **2019**, *119*(20), 11042-11109.

401. S. Ferrari, M. Loveridge, S. D. Beattie, M. Jahn, R. J. Dashwood, R. Bhagat. Latest advances in the manufacturing of 3D rechargeable lithium microbatteries. *Journal of Power Sources* **2015**, *286*, 25-46.

402. S. Moitzheim, J. E. Balder, R. Ritasalo, S. Ek, P. Poodt, S. Unnikrishnan, P. M. Vereecken. Toward 3D thin-film batteries: optimal current-collector design and scalable fabrication of TiO_2 thin-film electrodes. *ACS Applied Energy Materials* **2019**, *2*(3), 1774-1783.

403. Y. Yue, H. Liang. 3D current collectors for lithium-ion batteries: a topical review. *Small Methods* **2018**, *2*(8), 1800056.

404. X. Liu, W. Xu, D. Zheng, Z. Li, Y. Zeng, X. Lu. Carbon cloth as an advanced electrode material for supercapacitors: progress and challenges. *Journal of Materials Chemistry A* **2020**, *8*(35), 17938-17950.

405. A. Mishra, N. P. Shetti, S. Basu, K. Raghava Reddy, T. M. Aminabhavi. Carbon cloth-based hybrid materials as flexible electrochemical supercapacitors. *ChemElectroChem* **2019**, *6*(23), 5771-5786.

406. G. Zhang, H. Yao, F. Zhang, Z. Gao, Q. Li, Y. Yang, X. Lu. A high over-potential binder-free electrode constructed of Prussian blue and MnO_2 for high performance aqueous supercapacitors. *Nano Research* **2019**, *12*(5), 1061-1069.

407. J. Quan, E. Xu, Y. Chang, Y. Zhu, P. Li, L. Wang, Y. Jiang, *et al*. Interface engineering of a sandwich flexible electrode PAn@CoHCF rooted in carbon cloth for enhanced sodium-ion storage. *ACS Applied Materials and Interfaces* **2021**, *13*(20), 23794-23802.

408. B. He, P. Man, Q. Zhang, C. Wang, Z. Zhou, C. Li, L. Wei, Y. Yao. Conversion synthesis of self-standing potassium zinc hexacyanoferrate arrays as cathodes for high-voltage flexible aqueous rechargeable sodium-ion batteries. *Small* **2019**, *15*(52), 1905115.

409. P. Nie, L. Shen, G. Pang, Y. Zhu, G. Xu, Y. Qing, X. Zhang, *et al*. Flexible metal–organic frameworks as superior cathodes for rechargeable sodium-ion batteries. *Journal of Materials Chemistry A* **2015**, *3*(32), 16590-16597.

410. J. Gu, K. Cui, S. Niu, Y. Ge, Y. Liu, Z. Ma, X. Wang, *et al*. Smart configuration of cobalt hexacyanoferrate assembled on carbon fiber cloths for fast aqueous flexible sodium ion pseudocapacitor. *Journal of Colloid and Interface Science* **2021**, *594*, 522-530.

411. K. Lu, B. Song, K. Li, J. Zhang, H. Ma. Cobalt hexacyanoferrate nanoparticles and MoO_3 thin films grown on carbon fiber cloth for efficient flexible hybrid supercapacitor. *Journal of Power Sources* **2017**, *370*, 98-105.

412. Y. J. Yang, Y. Li, X. Ding, C. Zhang, H. Ren, F. Guo, J. Dong. Synthesis of nickel hexacyanoferrate nanostructure on carbon cloth with predeposited nickel nanoparticles as precursor for binder-free high-performance supercapacitor electrodes. *Journal of Alloys and Compounds* **2021**, *871*, 159510.

413. H. Yao, F. Zhang, G. Zhang, Y. Yang. A new hexacyanoferrate nanosheet array converted from copper oxide as a high-performance binder-free energy storage electrode. *Electrochimica Acta* **2019**, *294*, 286-296.

414. X. Zhang, J. Dutta. X-Fe (X= Mn, Co, Cu) Prussian blue analogue-modified carbon cloth electrodes for capacitive deionization. *ACS Applied Energy Materials* **2021**, *4*(8), 8275-8284.

415. S. Wang, X. Ge, C. Lv, C. Hu, H. Guan, J. Wu, J. Cai, *et al*. Oxygen vacancy-rich amorphous porous NiFe(OH)x derived from $Ni(OH)_x$/Prussian blue as highly efficient oxygen evolution electrocatalysts. *Nanoscale* **2020**, *12*(17), 9557-9568.

416. N. M. Thomsen. Aqueous sodium ion batteries: conceptualizing the commercial uptake of a scalable energy storage system. *MSc Thesis, Technische Universität München* **2021**.

417. R. List. Carbon cloth as a high-area current collector for thin-film electrodes in aqueous sodium ion batteries. *BSc Thesis, Technische Universität München* **2022**.

418. A. Tóth, K. László. Water adsorption by carbons. Hydrophobicity and hydrophilicity. In *Novel Carbon Adsorbents*. *Elsevier* **2012**.

419. H. Kim, Y. J. Lee, D. C. Lee, G. G. Park, Y. Yoo. Fabrication of the carbon paper by wet-laying of ozone-treated carbon fibers with hydrophilic functional groups. *Carbon* **2013**, *60*, 429-436.

420. K. Kordek, L. Jiang, K. Fan, Z. Zhu, L. Xu, M. Al-Mamun, H. Zhao, *et al*. Two-step activated carbon cloth with oxygen-rich functional groups as a high-performance additive-free air electrode for flexible zinc–air batteries. *Advanced Energy Materials* **2019**, *9*(4), 1802936.

421. K. Kordek, H. Yin, P. Rutkowski, H. Zhao. Cobalt-based composite films on electrochemically activated carbon cloth as high performance overall water splitting electrodes. *International Journal of Hydrogen Energy* **2019**, *44*(1), 23-33.

422. K. Kordek-Khalil, I. Walendzik, P. Rutkowski. Low-overpotential full water splitting with metal-free self-supported electrodes obtained by amination of oxidised carbon cloth. *Sustainable Energy Technologies and Assessments* **2022**, *53*, 102569.

423. D. Ye, Y. Yu, J. Tang, L. Liu, Y. Wu. Electrochemical activation of carbon cloth in aqueous inorganic salt solution for superior capacitive performance. *Nanoscale* **2016**, *8*(19), 10406-10414.

424. Datasheet of Carbon Cloth AvCarb "1071 HCB plain carbon cloth fabric" *AvCarb Material Solutions*, *avcarb.com/wp-content/uploads/2014/01/3063-AvCarb-Carbon-Fabrics.pdf*. Accessed online on 21. May 2023.

425. R. Streng. Investigation of alizarin and its derivatives as anode materials for aqueous sodium ion batteries. *MSc Thesis, Technische Universität München* **2022**.